Titre: Title:	Effect of nanoparticles on the fatigue behavior of a semicrystalline polymer
Auteur: Author:	Simon C. Bellemare
Date:	2002
Type:	Mémoire ou thèse / Dissertation or Thesis
Référence: Citation:	Bellemare, S. C. (2002). Effect of nanoparticles on the fatigue behavior of a semicrystalline polymer [Master's thesis, École Polytechnique de Montréal]. PolyPublie. https://publications.polymtl.ca/26857/

URL de PolyPublie: PolyPublie URL:	https://publications.polymtl.ca/26857/
Directeurs de recherche: Advisors:	J. Ivan Dickson, & Martin Bureau
Programme: Program:	Unspecified

UNIVERSITÉ DE MONTRÉAL

EFFECT OF NANOPARTICLES ON THE FATIGUE BEHAVIOR OF A SEMICRYSTALLINE POLYMER

SIMON C. BELLEMARE
PROGRAMME DE GÉNIE DES MATÉRIAUX
ÉCOLE POLYTECHNIQUE DE MONTRÉAL

MÉMOIRE PRÉSENTÉ EN VUE DE L'OBTENTION
DU DIPLÔME DE MAÎTRISE ÈS SCIENCES APPLIQUÉES
(génie métallurgique)
JUILLET 2002

UNIVERSITÉ DE MONTRÉAL

ÉCOLE POLYTECHNIQUE

Ce mémoire intitulé:

EFFECT OF NANOPARTICLES ON THE FATIGUE BEHAVIOR OF A SEMICRYSTALLINE POLYMER

Présenté par: BELLEMARE Simon C.
En vue de l'obtention du diplôme de: Maîtrise ès sciences appliquées
a été dûment accepté par le jury d'examen constitué de:

M. FISA Bohuslav, Ph.D., membre
M. DICKSON J. Ivan, Ph.D., membre et directeur de recherche
M. BUREAU Martin N., Ph.D., membre et codirecteur de recherche
M. KAMAL Musa R., Ph.D., membre

REMERCIEMENTS

Je tiens d'abord à exprimer ma gratitude envers mes parents. Ceux-ci ont été les principaux acteurs dans le développement de mes habilités et aptitudes. Je tiens tout aussi à remercier ma conjointe pour son soutien et ses encouragements.

Ma reconnaissance va également au professeur J. Ivan Dickson et au docteur Martin N. Bureau qui m'ont accordé de la latitude dans la réalisation des travaux et qui m'ont justement conseillé. Je remercie aussi la docteure Johanne Denault pour son intérêt envers le projet et pour ses conseils.

Plusieurs personnes m'ont conseillé et/ou assisté dans la réalisation de mes travaux expérimentaux à l'Institut des matériaux industriels (IMI) du Conseil national de recherches du Canada (CNRC). Je tiens à souligner les contributions de mesdames Manon Plourde, Florence Perrin et Chantale Coulombe ainsi que celles de messieurs Yves Simard, Pierre Sammut et Patrick Gagnon.

Finalement, je remercie l'IMI pour l'accès aux laboratoires, locaux et équipements ainsi que le Conseil de recherche en sciences naturelles et génie du Canada (CRSNG) pour son support financier.

Simon C. Bellemare

RÉSUMÉ

Plusieurs types de renforts ont été traditionnellement ajoutés aux polymères de façon à améliorer leur rigidité. Ces dernières années, un nouveau type de renfort à base de couches de cristaux minéraux exfoliés a commencé à être employé commercialement. Chacun de ces cristaux a la forme d'un feuillet ayant des dimensions typiques d'approximativement 100 nm en longueur et 1 nm en épaisseur. Typiquement, l'ajout de 2% massique de ces nanoparticules dans un polymère semicristallin tel que le polyamide 6 (PA6) augmente le module Young de 50% mais diminue de façon marquée la ductilité et la ténacité.

Avec l'objectif de recherche principal de déterminer l'effet de l'ajout de nanoparticules sur le comportement en fatigue d'une matrice de PA6 séché, des essais de fatigue axiale et de résistance à la propagation d'une fissure de fatigue (PFF) ont été réalisés en employant des éprouvettes avec et sans entaille du nanocomposite polymérique (NCP) et de la matrice de PA6 homologue non renforcée. Les éprouvettes ont été moulées par injection. Puisque le comportement en fatigue des polymères semicristallins dépend d'une grande variété de paramètres de la structure des matériaux et qu'il peut être corrélé avec d'autres aspects du comportement mécanique, une revue de la littérature sur la structure des matériaux considérés ainsi que sur leur comportement en chargement monotone ou constant a été réalisée et présentée avant la revue reliée à la fatigue. L'information et les connaissances obtenues de ces revues ont été employées pour l'interprétation des résultats.

Les deux types de résultats quantitatifs qui ont été obtenus étaient la réponse macroscopique en contrainte-déformation-temps et la vie en fatigue. Étant donné l'absence de corrélation entre ces deux types de résultats, les mesures de la réponse macroscopique en contrainte-déformation-temps ne sont pas sensibles aux événements reliés à l'initiation d'une fissure de fatigue à partir d'une inclusion. L'interruption d'essais et le changement du mode de chargement a permis d'obtenir de l'information additionnelle sur la nature des processus d'endommagement par fatigue ayant lieu de

façon homogène à travers l'entière section calibrée de l'éprouvette. À partir de l'évolution des différents paramètres employés pour caractériser cette réponse, une succession de trois régimes de réponse a été observée.

L'accumulation de déformation macroscopique était partiellement réversible et largement réduite lorsque le mode de chargement était changé de tension-tension à tension-compression. L'accumulation de déformation est probablement le résultat d'un alignement viscoélastique des segments de chaînes moléculaires, par la migration de plis moléculaires ou par reptation, selon la direction de tension. Les transitions dans la déformation macroscopique accumulée qui ont été mesurées lors des essais pourraient correspondre à une augmentation du volume d'activation pour un événement moléculaire. Dans le régime final, le taux d'accumulation de déformation devient constant, ce qui suggère clairement que la reptation des chaînes devient le mécanisme dominant.

Les autres paramètres employés pour caractériser la réponse étaient l'évolution de la variation de volume accumulée, du module de conservation (E') et de la tangente de l'angle de perte (tan δ). La diminution irréversible et contrôlée par l'amplitude de contrainte de E' qui a été enregistrée durant le premier régime de la réponse pourrait être attribuée à des événements de déformation menant à une distribution plus homogène de la contrainte entre les segments moléculaires. Ce processus proposé de redistribution des contraintes pourrait être complété lorsque la structure atteint un certain arrangement, ce qui pourrait constituer le commencement du second régime au cours duquel l'orientation des segments moléculaires ou la cristallisation pourrait devenir prédominante. D'autre part, l'évolution du paramètre tan δ paraît largement réversible et non affectée par la contrainte moyenne au moins dans le premier régime, où une compétition entre l'accumulation d'énergie de déformation réversible et l'augmentation du volume libre pourrait expliquer l'inflexion positive des courbes. Dans le régime final de la réponse, d'importantes diminutions de E` et augmentations de tan δ ont été mesurées. Aussi, un changement d'inflexion de négative à positive a été noté sur les courbes de l'évolution de la variation de volume accumulée. La germination et croissance de vides peut devenir un processus dominant dans le régime final.

L'ajout de nanoparticules a réduit le taux d'accumulation de déformation dans les régimes initiaux de la réponse, ce qui peut être expliqué par la diminution de l'amplitude de déformation résultant de l'augmentation de la rigidité. Cependant, cet effet de renforcement des nanoparticules n'a pas été observé dans le régime final où la densité d'enchevêtrements, la masse moléculaire et la fraction volumique de la phase amorphe sont probablement les principaux paramètres du matériau contrôlant la résistance à l'accumulation de déformation.

À partir de la corrélation trouvée entre la taille des inclusions au site d'initiation de fissure et la vie en fatigue, cette vie caractérise probablement la résistance de l'éprouvette à l'initiation d'une fissure de fatigue. Cette résistance est augmentée par l'addition de nanoparticules, ce qui pourrait avoir pour origine l'augmentation de la résistance du matériau à l'initiation extrinsèque d'une fissure ou le changement dans la position du site d'initiation d'une fissure.

Une couche relativement très déformée d'approximativement 4 µm en épaisseur et dans laquelle le matériau apparaissait uniformément allongé suivant la direction de propagation de la fissure a été observée sous la surface de rupture d'un échantillon de PFF du NCP. Il est proposé que la PFF dans NCP soit accompagnée par le déplacement d'une interface entre le volume de la matrice relativement non déformé et une couche relativement très déformée. Puisque des fibrilles très étirées ayant une morphologie similaire à celles reportées dans d'autres polymères semicristallins ont été observées sur la surface de rupture, le développement et la croissance d'une zone de fibrillation survient également à l'avant du fond de fissure et près du plan de séparation des surfaces.

L'addition de nanoparticules a induit une réduction de la résistance à la PFF ainsi qu'un changement dans le mécanisme de PFF. La séparation des surfaces a eu lieu par le développement et la rupture d'une zone de fibrillation au lieu d'avoir lieu par cisaillement sans cavitation importante. Il est proposé que cette transition soit un effet indirect des nanoparticules sur la contrainte d'écoulement puisque cette contrainte détermine la contrainte locale près du plan de séparation des surfaces, ce qui est la position où des vides peuvent germiner et croître si une contrainte statique ou cyclique est appliquée au cours d'une période de temps suffisante. Réduire la contrainte d'écoulement du NCP par une diminution de la résistance de l'interface nanoparticule-matrice ou par l'ajout de particules de caoutchouc pourrait probablement améliorer la ductilité et la ténacité du NCP, mais pas nécessairement la résistance à la PFF, laquelle pourrait plutôt être améliorée en promouvant des effets de pontage de la fissure.

ABSTRACT

Several types of reinforcement have been traditionally added to polymers in order to enhance their stiffness. In recent years, a new type of reinforcement based on exfoliated mineral layered crystals has begun to be employed commercially. Each such crystal has a sheet-like form, with typical dimensions of approximately 100 nm in length and 1 nm in thickness. Typically, adding 2-wt% of these nanoparticles into a semicrystalline polymer such as dried polyamide 6 (PA6) increases Young's modulus by 50% but decreases markedly the ductility and fracture toughness.

With the main research objective of determining the effect of the addition of nanoparticles on the fatigue behavior of a dried PA6 matrix, axial fatigue and fatigue crack propagation (FCP) tests were carried out employing non-notched and pre-cracked injection-molded specimens of the polymer nanocomposite (PNC) studied and of the corresponding non-filled PA6 matrix. Since the fatigue behavior of semicrystalline polymers depends on a wide variety of material structure parameters and have correlations with other aspects of the mechanical behavior, a detailed literature review on the structure of the materials under consideration and on their behavior under monotonic or constant loading was carried out and is presented before the review related to fatigue. The information and knowledge obtained from these reviews were employed for the interpretation of the results.

The two types of quantitative results obtained from the axial fatigue tests were the macroscopic stress-strain-time response and the fatigue life. Because of the absence of correlation between these two types of results, the measurements of the macroscopic stress-strain-time response are not sensitive to the events related to fatigue crack initiation from an inclusion. Test interruption and a change in the loading mode enabled to obtain additional information on the nature of the fatigue damage processes occurring macroscopically homogeneously throughout the whole gauge section of the specimens. From the evolution of the different parameters employed to characterize this response, a succession of three regimes of response has been observed.

The accumulation of macroscopic strain was partially reversible and largely reduced when the loading mode was changed from tension-tension to tension-compression. Strain accumulation is expected to result from the viscoelastic alignment of molecular segments, by migration of molecular kinks or reptation, along the tensile direction. The transitions in the accumulated strain response measured during the tests could correspond to an increase in the activation volume for a molecular event. In the final regime, the rate of accumulation of strain became constant, which clearly suggests that chain reptation becomes a dominant mechanism.

The three other parameters employed to characterize the response were the evolution of the accumulated volume variation, the storage modulus (E') and the loss tangent (tan δ). The irreversible decrease in E', which was stress amplitude-controlled recorded during the first regime of the response, could be attributed to deformation events leading to a more homogeneous distribution of the stress between the chain segments. This proposed process of stress redistribution may be completed when the structure reaches a certain arrangement, which may constitute the beginning of the second regime where the reorientation of chain segments or crystallization could become dominant. On the other hand, the evolution of the parameter tan δ appeared largely reversible and non-affected by the mean stress at least in the first regime, where a competition between the accumulation of reversible strain energy and the increase in the free volume could explain the positive inflection of the curves. In the final regime of the response, important decreases in E' and increases in tan δ were measured. Also, a change from a negative to a positive inflection was noted on the curves of the evolution of the accumulated volume variation. Void nucleation and growth may become a dominant process in the final regime.

The addition of nanoparticles was found to reduce the rate of strain accumulation in the initial regimes of response, which was explained by a decrease in the strain amplitude resulting from the increase in stiffness. However, no such reinforcing effect of the nanoparticles was observed in the final regime where entanglement density, molecular weight and volume fraction of the amorphous phase are expected to be the principal material parameters controlling the resistance to strain accumulation.

From the correlation found between the size of the inclusions at the crack initiation site and the fatigue life, this life is expected to characterize the resistance of the specimen to fatigue crack initiation. This resistance increased as a result of the addition of nanoparticles, which could originate from an increase in the resistance of the material to extrinsic crack nucleation or to a change in the position of the crack initiation site.

A relatively highly deformed layer of approximately 4 μm in thickness in which the material structure appeared uniformly stretched along the crack propagation direction has been observed just below the fracture surface. It is proposed that FCP in the PNC studied is accompanied by the displacement of an interface between a relatively non-deformed matrix and a relatively highly deformed layer. Since highly stretched fibrils with similar morphology to those reported in other semicrystalline polymers were observed on the fracture surface, the development and growth of a fibrillated deformation zone also occurred in front of the crack tip and near the surface separation plane.

As measured and observed, the addition of nanoparticles induced a reduction in the FCP resistance and a change in the mechanism of FCP from surface separation by shear to surface separation by the development and breakdown of a fibrillated deformation zone. This transition is proposed to be an indirect effect of the nanoparticles on the yield stress since this stress determines the local stress near the surface separation plane. This plane is a site where voids can nucleate and grow if a substantial static or cyclic stress is applied over a sufficient period of time. Reducing the yield stress of PNC by decreasing the strength of the nanoparticle-matrix interface or by adding rubber particles would probably enhance the ductility and fracture toughness of PNC but not necessarily the resistance to FCP, which could rather be enhanced by promoting bridging effects.

CONDENSÉ EN FRANÇAIS

1. *Introduction*

En science et ingénierie des matériaux, le terme fatigue réfère au phénomène de perte de propriétés importantes résultant d'une sollicitation en contrainte appliquée au cours d'une période de temps et généralement de façon intermittente. En fatigue, des changements microstructuraux importants peuvent survenir localement même si il n'y a pas de changement dans les dimensions et le comportement macroscopique du matériau.

Plusieurs efforts en recherche et développement ont été et sont dédiés à l'amélioration des propriétés mécaniques des matériaux. Les polymères sont des matériaux légers qui présentent généralement une bonne ductilité. Leur rigidité a souvent été augmentée par l'incorporation d'un renfort minéral ou de verre. Pour diminuer les coûts de production, plusieurs pièces en polymères sont renforcées de particules ou de fibres discontinues et elles sont moulées par injection.

Ces dernières années, un nouveau type de renfort à base de couches de cristaux minéraux exfoliées a commencé à être employé commercialement. Chacun de ces cristaux a la forme d'un feuillet ayant des dimensions typiques d'approximativement 100 nm en longueur et 1 nm en épaisseur. Typiquement, l'ajout de 2% massique de ces nanoparticules dans un polymère semicristallin tel que le polyamide 6 (PA6) augmente le module d'Young de 50% mais diminue de façon marquée la ductilité et la ténacité. L'objectif principal du projet de recherche était de déterminer l'effet de l'ajout de nanoparticules sur le comportement en fatigue d'une matrice de PA6 séché.

2. *Revue de la littérature*

Puisque le comportement en fatigue d'un polymère semicristallin dépend une grande variété de paramètres de structure du matériau et qu'il peut être corrélé avec d'autres aspects du comportement mécanique, une revue de la littérature sur la structure des matériaux considérés ainsi que sur leur comportement en chargement monotone ou constant a été réalisée et présentée avant la revue reliée à la fatigue.

À l'intérieur de la phase amorphe d'un polymère semicristallin, les concepts sur la structure et le comportement en déformation devraient être applicables. Pour la phase cristalline, la résistance au cisaillement dépend de la structure des cristaux et des défauts. Un polymère semicristallin est généralement composé d'un arrangement de sphérulites, lesquels contiennent chacune des micro-domaines. Ces micro-domaines sont constitués de quelques cristallites allongées parallèlement aux rayons des sphérulites et séparées par des couches de polymère amorphe. Lors d'une cristallisation assez rapides, les enchevêtrements sont sensés se concentrer dans la phase amorphe. La déformation de chacune des sphérulites commence dans la phase amorphe et est très affectée par les anisotropies locales, notamment par l'angle entre la direction de la longueur des cristallites et l'axe de traction principal. La déformation est sensée s'initier dans les domaines à 45° par une déformation en cisaillement entre les cristallites. De par la redistribution des contraintes résultantes et de par la microstructure dans les disques équatoriaux des sphérulites, ces dernières régions sont les plus susceptibles à l'initiation de cavités.

Lors d'un étirement important, la structure sphérulite peut être transformée en une structure orientée. Selon l'orientation locale, cette transformation peut impliquer la fragmentation des cristallites et la rotation des fragments ou la destruction des cristallites et la recristallisation. Lors de l'étirage en tension, la micro-striction n'est pas nécessairement une étape essentielle au processus de transformation mais elle peut probablement le faciliter et l'accélérer. Cette micro-striction produit un arrangement de fibrilles dont chacune contient des micro-fibrilles. Il est crû qu'une déformation additionnelle de cette structure a lieu par un mouvement relatif entre les fibrilles ou les micro fibrilles.

Comme pour les polymères amorphes, les mécanismes principaux de déformation hétérogène des polymères semicristallins sont la déformation en cisaillement localisé et le développement de craquelures. Comme pour les polymères amorphes, la déformation en cisaillement localisé peut probablement avoir lieu par le déplacement d'un interface entre une matrice non-déformée et une zone ayant un rapport d'allongement constant.

Dans les polymères semicristallins, les structures similaires aux craquelures peuvent être classées en deux catégories. Les craquelures de basse température sont probablement formées par un mécanisme similaire à celui applicable dans les polymères amorphes. Par compte, les zones fibrillées de déformation sont probablement formées par un mécanisme similaire à celui ayant lieu lors de l'étirement en traction. Il a été trouvé que le rapport d'allongement de ces fibrilles est contrôlé par le réseau d'enchevêtrements. Dans plusieurs cas, la croissance de craquelures et de zones fibrillées de déformation a lieu préférentiellement suivant les disques équatoriaux des sphérulites.

Dans la catégorie de nanocomposites où une seule des dimensions est dans l'ordre de grandeur du nanomètre, l'ajout de nanoparticules peut mener à trois différent types de morphologies : celles où les feuillets empilés demeurent en contact, celles où du polymère s'insère entre les feuillets empilés mais où la structure demeure ordonnée et celles où les feuillets sont dispersés uniformément dans une matrice continue. Les composites ayant ces morphologies sont appelés respectivement microcomposites, nanocomposite intercalé et nanocomposite exfolié. Un paramètre important de la structure des nanocomposites qui affecte les propriétés mécaniques est le niveau d'exfoliation. Pour les nanocomposites à base de PA6, l'augmentation de la contrainte d'écoulement est généralement attribuée à la forte interaction entre les feuillets et la matrice. L'ajout de nanoparticules change la proportion des phases cristallines et diminue légèrement l'indice de cristallinité. Ces changements peuvent expliquer l'augmentation de la contrainte d'écoulement. Aussi, l'ajout de nanoparticules change le gradient de structure entre celle dans la peau de l'échantillon et celle à cœur. Après l'injection du polyamide 12, un alignement des nanoparticules dans le plan de cisaillement ainsi que l'alignement des cristallites dans une direction perpendiculaire à ce plan ont été observés. La ductilité et la ténacité du PA6 sont fortement diminués par l'ajout de nanoparticules exfoliées.

3. *Matériaux et métholodogie expérimentale*

Les deux matériaux étudiés étaient une matrice de PA6 contenant 2% massique de nanoparticules de montmorillonite, qui sera référée ici comme NCP, et la matrice non-renforcée de PA6. Une fois séché, ces deux matériaux avaient une température de transition vitreuse d'approximativement 65°C. Les échantillons sans et avec entaille ont tous été moulés par injection et séché sous vide avant d'être utilisés pour les essais. Des observations de la microstructure ont suggéré l'absence de structure sphérulitique dans le PFF, alors que cette structure a été très clairement mise en évidence dans le PA6. Des essais de traction reportés pour des échantillons similaires à ceux utilisés pour les essais de fatigue ont indiqué des valeurs de module d'Young, résistance en traction et déformation à la rupture de respectivement 4.1 GPa, 100 MPa et moins de 10% pour le PFF et de respectivement 2.7 GPa, 74 MPa et 175% pour le PA6.

Des essais de fatigue axiale et de résistance à la propagation d'une fissure de fatigue (PFF) ont été réalisés à température ambiante sur chacun de ces matériaux. Les essais de fatigue axiale ont été réalisés à une fréquence de chargement de 5 Hz, en contrainte imposée et en tension-tension à l'exception des essais où l'effet de ces paramètres a été spécifiquement étudié. Des paramètres ont été définis et utilisés pour caractériser la réponse macroscopique en contrainte-déformation-temps des éprouvettes de fatigue axiale. Les surfaces de rupture et une section transverse, intersectant le fond de fissure ayant été préparée par ultramicrotomie à basse température, ont été observées par microscopie électronique à balayage.

4. *Résultats et discussion*

Les deux types de résultats quantitatifs qui ont été obtenus étaient la réponse macroscopique en contrainte-déformation-temps et la vie en fatigue. Aucune corrélation n'est apparût entre ces types de résultats. Donc, les mesures de la réponse macroscopique en contrainte-déformation-temps ne sont pas sensibles aux événements reliés à l'initiation d'une fissure de fatigue à partir d'une des inclusions présente dans la matrice.

Cette réponse caractérise des événements ayant lieu dans le volume de l'échantillon. Les paramètres utilisés pour caractériser ces événements ont été l'accumulation de la déformation macroscopique, la variation de volume accumulée, le module de conservation (E') et la tangente de l'angle de phase (tan δ). À partir de l'évolution de ces paramètres, une succession de trois régimes de réponse a été observée au cours de chaque essai.

L'accumulation de déformation macroscopique en fonction du nombre de cycles de chargement tracée sur une échelle log-log a donné une courbe approximativement linéaire dans le régime I. Cette courbe avait une inflexion négative dans le régime II et une inflexion positive dans le régime III, où le taux d'accumulation de la déformation est devenu constant. Lorsque les essais ont été interrompus dans le régime II, la déformation accumulée était partiellement recouverte. Lorsque le mode de chargement a été changé de tension-tension à tension-compression, la déformation accumulée devenait très négligeable dans le régime I.

L'accumulation de déformation est probablement le résultat d'un alignement viscoélastique des segments de chaînes moléculaires, par la migration de plis moléculaires ou par reptation, selon la direction de traction. Les transitions dans la déformation macroscopique accumulée qui ont été mesurées lors des essais pourraient correspondre à une augmentation du volume d'activation pour un événement moléculaire. Dans le régime final, la reptation des chaînes contrôlée le désenchevêtrement devient probablement le processus dominant. Un des mécanismes contrôlant cette reptation est le désenchevêtrement des chaînes.

Pour les paramètres E' et tan δ, la transition entre les régimes I et II correspond aussi à des changements d'inflexion sur des courbes d'évolution en fonction du logarithme du nombre de cycles : la courbe de E' passe de négative à positive alors que celle de tan δ passe de positive à négative. Lorsque les essais ont été interrompus au début du régime II, aucune recouvrance de E' n'a été observé alors que tan δ a montré une recouvrance presque complète. Lorsque le mode de chargement a été changé de tension-tension à tension-compression, la variation dans ces deux paramètres est demeurée la même, indiquant que les processus causant les variations sont contrôlés par l'amplitude de contrainte et non par la contrainte maximale.

La diminution de E' dans le régime I pourrait être attribuée à des événements de déformation menant à une distribution plus homogène de la contrainte entre les segments moléculaires. Ce processus proposé de redistribution des contraintes pourrait être complété lorsque la structure atteint un certain arrangement, ce qui pourrait constituer le commencement du régime II où l'orientation des segments moléculaires ou la cristallisation pourrait expliquer l'augmentation de E'. D'autre part, une compétition entre l'accumulation d'énergie de déformation réversible et l'augmentation dans le volume libre pourrait expliquer l'inflexion positive des courbes de tan δ dans le régime I.

Dans le régime III de la réponse, d'importantes diminutions de E` et augmentations de tan δ ont été mesurées. Aussi, un changement d'inflexion de négative à positive a été noté sur les courbes de l'évolution de la variation de volume accumulée. La germination et croissance de microvides pourrait devenir un processus dominant dans le régime III.

L'ajout de nanoparticules a réduit le taux d'accumulation de déformation dans les régimes I et II, ce qui peut être expliqué par la diminution de l'amplitude de déformation résultant de l'augmentation de la rigidité. Dans le régime III, il n'y a eu aucun effet de renfort des nanoparticules sur le taux d'accumulation de la déformation. Cette perte de l'effet de renfort peut s'expliquer par un changement dans la nature des principaux événements de déformation qui deviennent contrôlés par l'amplitude de contrainte et/ou la contrainte maximale.

Par ailleurs, une corrélation a été trouvée entre la taille des inclusions au site d'initiation de fissure et la vie en fatigue. Donc, cette vie caractérise probablement la résistance de l'éprouvette à l'initiation d'un fissure de fatigue à partir d'une zone de concentration de contrainte microscopique. Lorsque comparée à la même amplitude de contrainte, la vie en fatigue a augmenté par l'ajout de nanoparticules. Aussi, l'initiation de fissures a eu toujours lieu à l'intérieur des éprouvettes du NCP alors que cette initiation est survenue beaucoup plus près des surfaces latérales de l'éprouvette dans le cas du PA6. L'augmentation de la durée de vie pourrait provenir de l'augmentation de la résistance du matériau à l'initiation extrinsèque de fissures ou du changement dans la position du site d'initiation de fissures.

Les observations microscopiques ont révélé la présence d'une couche d'approximativement 4 µm en épaisseur dans laquelle le matériau apparaissait uniformément allongé suivant la direction de propagation de la fissure. Cette couche était située juste au dessous de la surface de rupture et elle était séparée du volume de la matrice relativement non déformé par une interface mince et poreuse. Aussi, des fibrilles très étirées ayant une morphologie similaire à celles reportées dans d'autres polymères semicristallins ont été observées sur la surface de rupture. Basé sur ces observations, il est proposé que la PFF dans le NCP soit accompagnée par le déplacement d'une interface entre le volume de la matrice relativement non déformé et une couche relativement très déformée ainsi que par le développement et la croissance d'une zone de fibrillation à l'avant du fond de fissure et près du plan de séparation des surfaces.

Tel que mesuré par des essais de PFF et tel qu'observé sur la surface de rupture, l'addition de nanoparticules a induit une réduction de la résistance à la PFF ainsi qu'un changement dans le mécanisme de PFF. La séparation des surfaces a eu lieu par le développement et la rupture d'une zone de déformation plutôt que d'avoir lieu simplement par cisaillement. Il est proposé que cette transition soit un effet indirect des nanoparticules sur la contrainte d'écoulement, puisque cette contrainte détermine la contrainte locale près du plan de séparation des surfaces, ce qui est la position où des vides peuvent germiner et croître si une contrainte substantielle statique ou cyclique est appliquée au cours d'une période de temps suffisante.

Réduire la contrainte d'écoulement du NCP par une diminution de la résistance de l'interface nanoparticule-matrice ou par l'ajout de particules de caoutchouc pourrait probablement améliorer la ductilité et la ténacité du NCP mais pas nécessairement la résistance à la PFF. Tel que reporté dans la littérature, les effets de ponts peuvent augmenter la résistance à la PFF de certains polymères. Ces effets ont lieu lorsque des ligaments situés en arrière du fond de fissure retiennent ensemble les surfaces de rupture. Bien que des restrictions, tel que la taille et la résistance des particules de renfort ainsi que la ductilité de la matrice, peuvent limiter les conditions où ces effets peuvent être observés, promouvoir des effet de pontage de la fissure est probablement l'une des bonnes manières d'augmenter la résistance à la PFF des polymères.

5. Conclusion

Les principales conclusions tirées des travaux réalisés sont les suivantes :

- La réponse en contrainte-déformation-temps mesurée lors des essais de fatigue axiale caractérise des transitions dans les processus de changements microstructuraux qui ont lieu dans l'ensemble de la section de l'éprouvette.
- Les nanoparticules font augmenter le module d'Young, ce qui fait diminuer l'amplitude de déformation et donc le taux d'accumulation de déformation dans les régimes initiaux.
- Dans le régime final, la réponse en déformation accumulée devient visqueuse et les processus menant à cette déformation sont contrôlés par la contrainte maximale et/ou l'amplitude de contrainte.
- Dans ce régime final, le taux d'accumulation de la déformation devient indépendant de la présence de nanoparticules. La densité d'enchevêtrements, la masse moléculaire et la fraction volumique de la phase amorphe sont probablement les principaux paramètres contrôlant la résistance à l'accumulation de déformation dans ce régime final.
- L'augmentation de la vie en fatigue causée par l'addition de nanoparticules pourrait correspondre à une augmentation de la résistance du PA6 à

l'initiation hétérogène de fissures ou à une augmentation de la résistance des éprouvettes à l'initiation de fissures près des surfaces.

- La propagation d'une fissure dans le NCP et le PA6 est probablement devancée par la propagation d'une interface, entre la matrice relativement peu déformée et une couche relativement très déformée, où la déformation aurait lieu en cisaillement et où le rapport d'élongation serait contrôlé par le réseau d'enchevêtrements.
- L'ajout de nanoparticules a engendré le développement d'une mince zone de fibrillation en avant du fond de fissure et près du plan de séparation des surfaces, ce qui peut expliquer la diminution de la résistance à la PFF. Le développement d'une zone de fibrillation est probablement une conséquence de l'augmentation de la contrainte d'écoulement, qui devient alors supérieure à la contrainte critique de fibrillation.
- Dans le système considéré, l'effet bénéfique de l'ajout de nanoparticules exfoliées est apparût être limité à l'augmentation de la rigidité. L'ajout de nanoparticules pourrait difficilement augmenter la résistance à la propagation de fissures. Une façon d'augmenter cette résistance pourrait être d'engendrer des effets de pontage de la fissure.

TABLE OF CONTENTS

LIST OF TABLES

LIST OF FIGURES

LIST OF SYMBOLS AND ABBREVIATIONS

AFM	Atomic force microscopy
ALA	Aminolauric acid
$b_{50\%,increase}$	Ordinate at zero strain of the linear regression between stress and strain employing the seven data points from the increasing part of the cycle that were the nearest to $\sigma_{Min} + 50\%*2\sigma_{Amp}$
$b_{i,decrease}$	Ordinate at zero strain of the linear regression between stress and strain employing the seven data points from the decreasing part of the cycle that were the nearest to the stress target
$b_{i,increase}$	Ordinate at zero strain of the linear regression between stress and strain employing the seven data points from the increasing part of the cycle that were the nearest to the stress target
$b_{t,decrease}$	Ordinate at zero time of the linear regression between stress and time employing the seven data points from the decreasing part of the cycle that were the nearest to the stress target
$b_{t,increase}$	Ordinate at zero time of the linear regression between stress and time employing the seven data points from the increasing part of the cycle that were the nearest to the stress target
β	Activation volume for the molecular event
	Constant for a given molecular structure
C_∞	Characteristic ratio of the macromolecular chain
Ca	Calcium
CR	Compression ratio
da/dN	Macroscopic fatigue crack propagation rate
D	Final thickness of a fibril
D_o	Distance between the center of the fibrils
$D1_{Max}$	Measured length in the long axis
$D2_{Max}$	Measured length in the short axis

DSC	Differential scanning calorimetry
δ	Phase lag
ΔG	Range of strain energy release rate
ΔH	Potential energy barrier
ΔK	Range of stress intensity factor
Δt	Time delay of the strain relative to the stress calculated from the symmetry points for the curves
$\Delta V/V$	Volume strain
$\Delta V/V_0$	Instantaneous volume strain
$\Delta V/V_{0,\ Acc}$	Accumulated volume strain
$\Delta V/V_{0,\ Min}$	Minimum volume strain in a single cycle
$\Delta V_{DEV}/V$	Deviatoric component
$\Delta V_{DIL}/V$	Dilatational component
$\Delta V_{EL}/V$	Elastic component
e	Strain
$\dot{e}$	Rate of change of strain
e_0	Initial strain
$\dot{e}_0$	Constant pre-exponential factor
E	Young's modulus
E'	Storage modulus
E''	Loss modulus
EDS	Energy dispersive spectrometer
ε_{Acc}	Longitudinal accumulated strain
ε_{Amp}	Longitudinal strain amplitude Strain amplitude
ε_{DEV}	Deviatoric component

ε_{DIL}	Dilatational component
ε_{EL}	Elastic component of the axial strain
$\dot{\varepsilon}_f$	Strain rate of a non-Newtonian fluid
ε_L	Longitudinal strain
ε_L	Instantaneous longitudinal strain
ε_{Max}	Maximum longitudinal strain in a single cycle
ε_{Min}	Minimum longitudinal strain in a single cycle
$\varepsilon_{Pl}MaxInc$	Apparent plastic strain
ε_t	Rate of strain accumulation
ε_W	Long-transverse strain
ε_W	Instantaneous transverse strain
$\dot{\varepsilon}_y$	Constant
f	Frequency
FCP	Fatigue crack propagation
FD	Flow direction
FEGSEM	Field emission gun SEM
FS	Fracture surface
G^o_N	Shear modulus at the rubbery plateau
G_{Ic}	Critical energy release rate in mode I
Γ	Surface tension of the void surface
Γ^*	Specific enthalpies of damage
H	Thickness of that active zone
HDPE	High density polyethylene
kcyc	kilocycles
K_I	Stress intensity factor in the crack opening mode or mode I
K_{Ic}	Critical stress intensity factor in the crack opening mode or mode I

$K_{I,Max}$	Maximum cyclic stress intensity factor in the crack opening mode or mode I
$K_{I,mean}$	Average cyclic stress intensity factor in the crack opening mode or mode I
l_o	Length of the projection of the monomer unit on the chain axis
$<l^2_v>$	Mean square length of such a unit
LAED	Low angle electron diffraction
LDPE	Low density polyethylene
L_N	End-to-end distance of a sequence of a sequence of entanglement points
λ	Aspect ratio of the internal voids
λ_e	Maximum extension ratio of the entanglement network
l_e	Length of a completely elongated segment
$m_{20\%,increase}$	Slope from a linear regression between the stress and strain at stress targets of $\sigma_{Min} + 20\%*2\sigma_{Amp}$
$m_{50\%, increase}$	Slope at zero strain of the linear regression between stress and strain employing the seven data points from the increasing part of the cycle that were the nearest to $\sigma_{Min} + 50\%*2\sigma_{Amp}$
$m_{80\%,increase}$	Slope from a linear regression between the stress and strain at stress targets of $\sigma_{Min} + 80\%*2\sigma_{Amp}$).
$m_{i, decrease}$	Slope at zero strain of the linear regression between stress and strain employing the seven data points from the decreasing part of the cycle that were the nearest to the stress target
$m_{i, increase}$	Slope at zero strain of the linear regression between stress and strain employing the seven data points from the increasing part of the cycle that were the nearest to the stress target
$m_{t,decrease}$	Slope at zero time of the linear regression between stress and time employing the seven data points from the decreasing part of the cycle that were the nearest to the stress target

$m_{t,increase}$	Slope at zero time of the linear regression between stress and time employing the seven data points from the increasing part of the cycle that were the nearest to the stress target
M	Molecular weight of the macromolecules or chain segments
M_o	Molecular weight of the monomer unit
M.A.Sc.	Master of Applied Science
M_c	Critical molecular weight
MDPE	Medium density polyethylene
M_e	Molecular weight between entanglements
Mg	Magnesium
M_w	Weight-average molecular weight
n	Constant exponential factor (characteristic of material in active zone)
n_v	Number of statistical skeletal units in a chain
	Constant exponential factor (characteristic of bulk material)
N	Measure of the sensitivity of the material to fatigue
ω	Angular speed
PA6	Polyamide 6
PA6NC	Polyamide 6 / organo-modified montmorillonite nanocomposite
PA12	Polyamide 12
PA66	Polyamide 66
PBT	Polybutylene terephthalalte
PC	Polycarbonate
PE	Polyethylene
PEEK	Polyetheretherketone
PEI	Polyetherimide
PET	Polyethylene terephthalalte
PLCNC	Polymer-layered crystals nanocomposites
PMMA	Polymethylmethacrylate
POM	Polyoxymethylene

PNC	Polymer nanocomposite employed in the experimental study (matrix of PA6 filled with 2-wt% montmorillonite and prepared by *in-situ* polymerization)
PP	Polypropylene
PS	Polystyrene
PSU	Polysulphone
PTA	Phosphotungstic acid
PVDF	Polyvinylidene fluoride
$<r^2>$	Mean square end-to-end distance
$<r^2>^{1/2}$	Square root of the mean square end-to-end distance
r_s	Root-mean-square chain end-to-end distance
R	Loading ratio (minimum stress / maximum stress)
	Universal gas constant
R_e	Distance between entanglement points
	Root-mean-square end-to-end distance of unperturbed segments
Re	Reynolds's number
R_g	Radius of gyration between entanglement points
RH	Relative humidity
RHB	Region of higher brightness
ρ	Density of the polymer
s	Length of the plastic zone
S	stress required for a craze to grow
SEM	Scanning electron microscopy
Si	Silicon
SLS	standard linear solid
SMD	Shear microdomain
S-N	Stress versus number of loading cycles to fracture
SS	Specimen surfaces
σ	Stress

σ_0	Stress amplitude
σ_{Amp}	Stress amplitude
σ_c	Uniform internal compressive stress
σ_{fc}	Flow stress of a non-Newtonian fluid at a strain rate of $\dot{\varepsilon}_f$
σ_{max}	Maximum stress
σ_{min}	Minimum stress
σ_{Min}	Minimum cyclic stress
σ_y	Yield stress
σ_{yo}	Yield stress at a strain rate of $\dot{\varepsilon}_y$
t	time
tan δ	Tangent of the phase lag or simply loss tangent
t_{max}	Time under maximum stress
T	Temperature
T_2	T_g – 52.6°C
T_A	Absolute temperature
TEM	Transmission electron microscopy
T_g	Glass transition temperature
UTS	Ultimate tensile strength
v	Velocity of displacement of the surface of the active zone of the craze
ν	Poisson's ratio
ν_0	Constant pre-exponential factor
ν_1	Number of chain segments moving in one direction
ν_2	Number of chain segments moving in the opposite direction
w_{Hyst}	Average width of the hysteresis loops
x	Ratio of its length located on one side of the separation plane to its total length

XRD	X-ray diffraction
Ø	Orientation of the long axis of the pores relative to the crack propagation direction

LIST OF APPENDICES

1 INTRODUCTION

1.1 BASIC PHENOMENOLOGY OF FATIGUE

In materials science and engineering, the term fatigue refers to the phenomenon of loss of strength or other important properties as a result of stressing over a period of time. Even if fracture resulting from the application of a monotonic or static stress is not excluded from the definition, the term fatigue usually refers to the loss of properties as a result of intermittent stressing. Fatigue can occur when the maximum cyclic stress applied on the material is below the yield stress, which is the stress at which the macroscopic strain of a material starts to be incompletely recovered after loading and unloading.

In order to account for the observed changes in properties, intermittent stressing leading to fatigue must induce microstructural changes. These changes occur during fatigue as a result of irreversible relative movement of many atoms or molecules. The average displacement of the atoms upon unloading can be of equal magnitude and opposite in the direction to the average displacement upon loading. However, each atom does not necessary return exactly to its original position. An accumulation of microstructural changes may eventually induce the initiation and propagation of crack(s). The final effect of fatigue is the loss of functionality and/or fracture of the specimen or component even if the stress applied was well below the yield stress.

1.2 MATERIAL DEVELOPMENT CONTEXT

Much research and development effort has been and is being devoted to the improvement of mechanical properties of materials. From an engineering point of view, an improvement in the properties of a material without increasing its density allows either to increase the load applied on a geometrical component or to decrease the size of that component. For motorized vehicles, both mechanical design changes enable to decrease the amount of energy required to carry a given load. According to Newton's acceleration law, the mechanical power required to accelerate a vehicle decreases linearly as the total weight of that vehicle decreases.

Polymers are lightweight materials (density between 0.9 and 1.5 g/cm^3) that usually present good ductility. However, when compared to metals and ceramics, their stiffness and strength are low and highly sensitive to temperature. Many polymers deform under load by creep at room temperature. Accordingly, polymers are good alternatives to other materials for many but not all transportation vehicle applications. Metals, polymers and ceramics will always have their own field of application in which they are the most advantageous choice.

The stiffness and strength of polymers have been increased by the incorporation of mineral or glass reinforcement. In the case of reinforcement by continuous fibers, the polymer composite generally has significantly higher mechanical properties than its non-reinforced matrix. However, the density of this composite is increased, typically by 50%. Also, parts made of continuous fiber reinforced polymer composites are much more expensive to produce. Polymers that are not reinforced with continuous fibers also find industrial applications. Those polymers can be basically classed into the following categories: polymer blends, particle-filled polymers and non-reinforced polymers. All of these polymers can be molded, which results in relatively low manufacturing costs. Although their stiffness/weight ratio is not necessarily competitive with most of the other materials, other characteristics such as their low production costs, low thermal conductivity, high damping capacity and good corrosion resistance make them suitable for a variety of structural applications.

In recent years, a new category of polymer reinforced with mineral particles has begun to be employed commercially: polymer-layered crystals nanocomposites (PLCNC). The addition of mineral layered crystals, having a thickness in the nanometer range, into non-reinforced polymer matrixes can induce an increase in stiffness much higher than that encountered with the same volume fraction of microparticles. These improvements in mechanical properties have resulted in considerable research interest in PLCNC.

Typically, adding 2-wt% of mineral layered crystals into a semicrystalline polymer such as dry polyamide 6 (PA6) increases Young's modulus (E) and ultimate tensile strength (UTS) by 50% and 35%, respectively. Structural materials also often need to have sufficient ductility, toughness and fatigue resistance. Very few studies have been published so far of the effect on the fatigue behavior and fatigue resistance of adding mineral layered crystals into a semicrystalline polymer matrix.

1.3 THE MASTER DEGREE PROJECT

The main objective of this Master of Applied Science (M.A.Sc.) research project was to determine the effect of the addition of mineral layered crystals on the fatigue behavior of a PA6 matrix. This thesis covers the three principal aspects of the project: the literature review, the experimental methodology and results, and a general discussion.

The main objective of the literature review presented in this thesis was to only cover the aspects potentially helpful for the interpretation of the results. An important part of this review focused on the microstructure and the deformation behavior of amorphous and semicrystalline polymers. This part is followed by a review of the known effects of the addition of mineral layered crystals on the microstructure and on the mechanical behavior of the matrix as well as by a review of the fatigue behavior of polymers.

The microstructure and mechanical properties of the specimens produced are presented before the description of the methodology employed for the characterization of the fatigue behavior. The first results presented have been obtained employing non-notched specimens. They describe the effect of the testing and material conditions on the macroscopic stress-strain-time response and on the fatigue life. The subsequent results were obtained employing pre-cracked specimens. They indicate the resistance of the materials to fatigue crack propagation. The last results presented are the observations of the fracture surface and of the deformed microstructure located near the crack plan. Some basis interpretation and references to literature data are included with the presentation of the experimental results.

For this reason, the discussion presented in the last section of this thesis is relatively general. The main objective of this general discussion was to integrate the results and to establish relationships between the experimental results and concepts presented in the literature review. The mechanisms leading to the accumulation of homogeneous and heterogeneous fatigue damage are discussed. A discussion is also made regarding the effect of the addition of mineral layered crystals on the fitigue life of non-notched specimens and on the mechanisms of fatigue damage.

2 LITERATURE REVIEW

Fatigue properties and fatigue behavior depend on a wide variety of material structure parameters and have some correlation with other aspects of the material mechanical behavior. Hence, in this literature review, a summary of the structure of the materials under consideration and of their behavior under monotonic or constant loading precedes the summary related to fatigue. For generalities on polymeric materials and for a literature review on the inelastic deformation cracking mechanisms in amorphous polymers, the reader is referred to the appendix.

2.1 SEMICRYSTALLINE POLYMERS

In semicrystalline polymers, there are three different levels of structure which have an important effect on the material properties (Schultz, 1984).

2.1.1 Structure of Semicrystalline Polymers

2.1.1.1 Molecular Level

At the first structural level, which will be called the molecular level (with a 0.1-1 nm scale range), interactions between neighboring chain segments occur. This first structural level controls the behavior within the amorphous phase and the crystallized phase. The concepts on the structure and deformation behavior of amorphous polymers presented in appendix (section A.2) are likely to apply to the structure and behavior within the amorphous phase. The α crystal structure of PA6 is shown in Figure 2.1. The macromolecules are aligned parallel to each other and retained together by hydrogen bonds. The shear strength of such a structure depends on the crystalline structure but also on the form and density of the crystal defects. As observed through dark field transmission electron microscopy (TEM), some of these defects are linear and present the characteristics of screw and edge dislocations (Lin and Argon, 1994), which where originally defined for metallic crystals. The molecular structure level is of importance in determining the intrinsic resistance to deformation of the amorphous and crystallized phases.

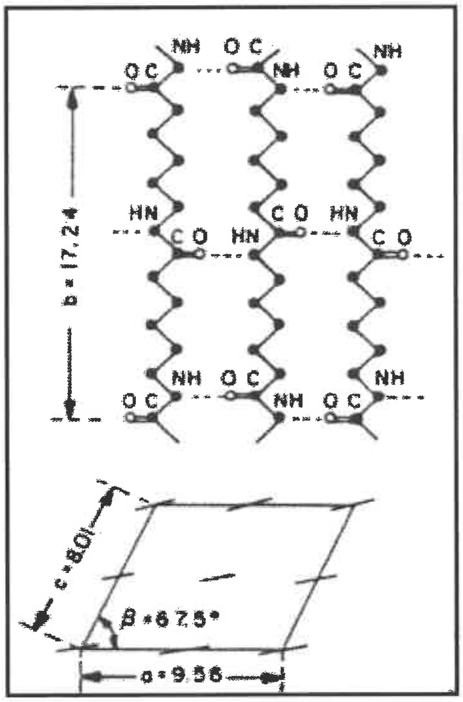

Figure 2.1: Crystalline α phase structure of PA6 (Galeski, Argon and Cohen, 1991a).

2.1.1.2 Phase Level

The second structural level will be called the phase level. Unless crystallization occurs under extremely high strain conditions, the crystalline phase is a distribution of thin plates or ribbons, which are stacked parallel to each other and are separated by thin amorphous layers. A schematic view of such a structure is shown in Figure 2.2(a). The thickness of the crystallized plates or ribbons as well as that of the amorphous layers are of the order of 10 nm (Schultz, 1984). The crystallized plates are often called crystallites. Within each crystallite, the chain axis is oriented along the crystallite thickness direction

(Schultz, 1984). This preferential orientation leads to anisotropy of the elastic and inelastic deformation properties of the crystallites.

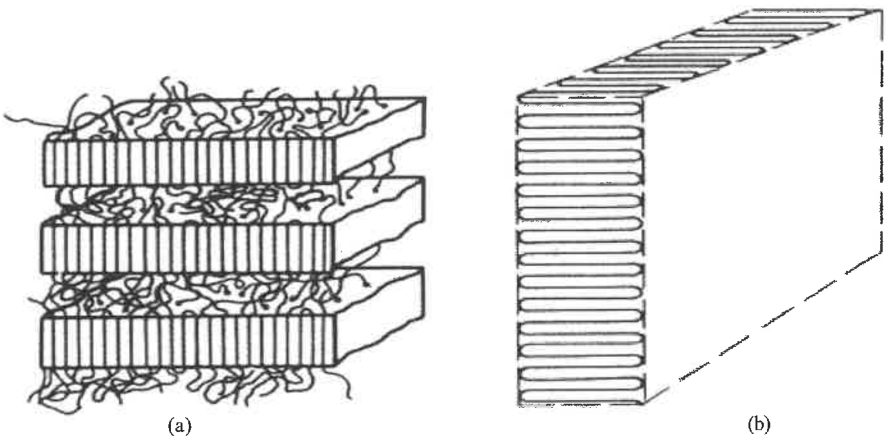

Figure 2.2: (a) Phase level of the semicrystalline polymer structure (from Schultz, 1984) and (b) Folded macromolecular chains in a crystal formed in a dilute solution (from Ward and Hadley, 1993).

At this structural level, the strength of the interface between the crystallized phase and the amorphous phase is of primary importance. Poor interface strength facilitates the formation of cavities and cracks, thus directly affecting the overall resistance to inelastic deformation. This can be related to the morphology of that interface. The interface between the amorphous zone and the crystallites in bulk-solidified crystallites is difficult to characterize (Ward and Hadley, 1993). However, the crystal external surface of crystallites formed in dilute solutions can be more easily observed by microscopy. Those observations reveal that, for these idealized crystallization conditions, most of the macromolecular chains are folded at the crystal external surfaces as shown schematically in Figure 2.2(b). The situation however appears different when the polymer is crystallized from a melt. Lin and Argon (1994) have extensively reviewed the structure and inelastic deformation of semicrystalline polymers, while taking the case of high-density polyethylene (HDPE) as a specific example (review paper of 30 pages with 301 references). In their discussion, they claimed as experimental evidence that crystallites in bulk-solidified spherulites are more the result of chain association than of chain folding.

A chain that is not folded at the interface has the following characteristic: one or many of its segments are in the crystallized phase while one or many other segments are situated in the amorphous phase. Those chains are called tie molecules. They provide continuity between the crystallites and the amorphous layers, which explains the stability of the interfaces and the usual relatively high ductility of semicrystalline polymers. Therefore, their concentration directly influences the elastic modulus and the yield strength of semicrystalline polymers (Schultz, 1984).

2.1.1.3 Entanglement Network

By comparing the rate of crystal growth and the relaxation time of the molecules in rapidly solidified melts, Flory and Yoon (1978) concluded that complete rearrangement of a macromolecule is unlikely to occur. They proposed that the formation of crystals involves only local conformational changes and that the entanglements present in the melt are concentrated in the amorphous phase. This view is shared by another group of researchers (Plummer, Menu, Cudre-Mauroux and Kausch, 1995). One can imagine an intermediate situation where partial disentanglement would occur during crystallization.

2.1.1.4 Spherulite Level

After bulk solidification, semi-crystalline thermoplastics usually contain spherulites, which is the third and the roughest structural level. The size of a spherulite in non-oriented semicrystalline polymers varies in the range of 0.1 to 1000 μm (Schultz, 1984). Thus, spherulites can be considered as similar to grains in metallic polycrystals because of their size range and because they are the coarsest level of structural arrangement. However, a spherulite is not a single ordered atomic structure. The central zone of each spherulite corresponds to a nucleation site for crystallization. As one can expect, the crystallites are generally preferentially oriented along the spherulite radius.

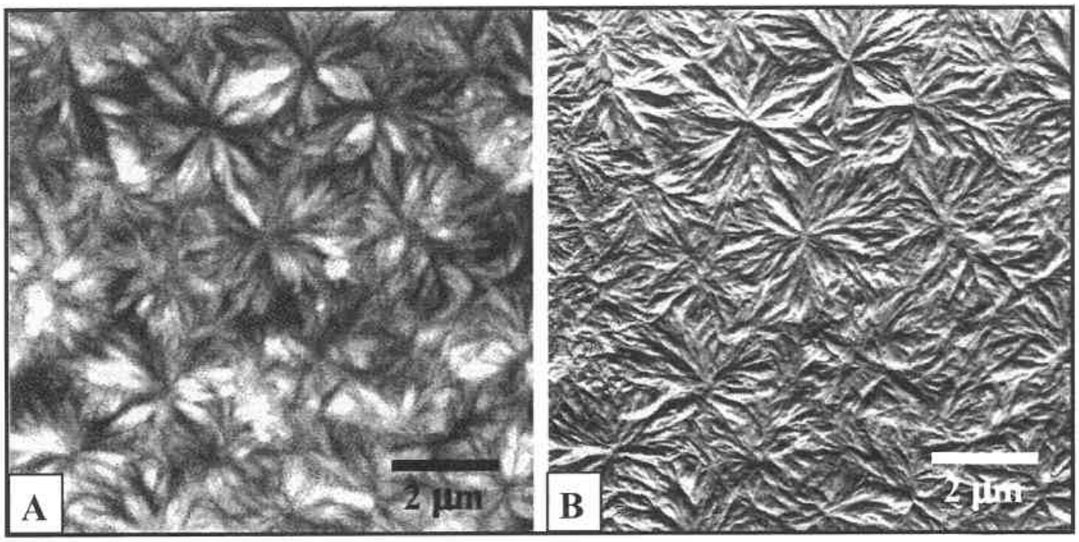

Figure 2.3: Spherulites at the native surface of PA6 films observed by atomic force microscopy (AFM) where A is a topographic and B is an amplitude image (adapted from Ferreiro, Pennec, Seguela and Coulon, 2000).

Galeski, Argon and Cohen (1987) employed TEM observations on samples stained with heavy metal ions (e.g. from OsO_4 in solution) to characterize the arrangement of the crystallites within the spherulites within a bulk solidified PA6. They have established that each crystallite has a thickness and a width in the range of 5-6 nm and 15-60 nm, respectively. They have also determined that the length of some crystallites is relatively large and approaches the dimension of the spherulites radius while their orientation is often along the local spherulite radii. Figure 2.4 is a schematic representation of their model for the arrangement of crystallites within spherulites. The two-labeled squares are observation planes which are both perpendicular to the same spherulite radius. The difference between the two observation planes is that the one labeled “2” is farther from the nucleus than the one labeled “1”. The back color filled crystallites shown in the square labeled “2” are the same as that shown in the square labeled “1”. This schematic representation is based on the observation that the crystallites often extend from the point of their origin up to the spherulite borders. The white color filled crystallites shown in the square labeled “2” are not present in the square labeled “1”. Thus, these crystallites have their point of origin between the two observation planes. An increase in the number of crystallites over a same radial scanned angle occurs because of the increasing volume available for crystallization when moving away from the nuclei. In both observation planes, three or four neighboring crystallites are stacked parallel to each other. Each of these stacks can be called a crystalline domain.

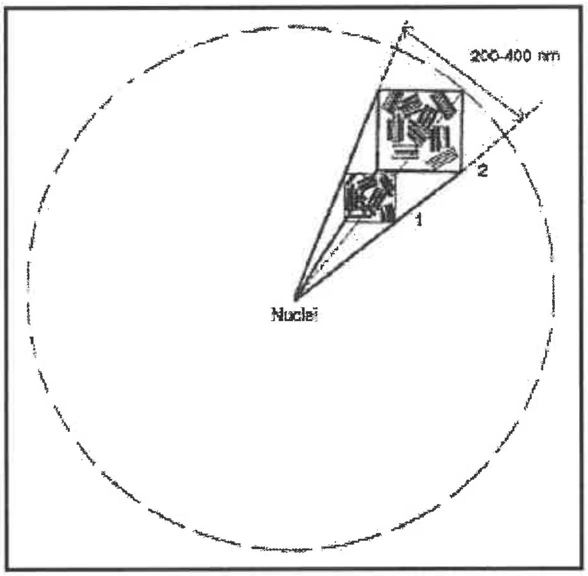

Figure 2.4 **Model for the arrangement of crystallites within bulk solidified PA6 spherulites (adapted from Ferreiro, Pennec, Seguela and Coulon, 2000).**

In their extensive review, Lin and Argon (1994) have reported some generally accepted features for bulk solidified HDPE spherulites. These are that crystallites grow out from a common central nucleus, that crystallites may branch by developing adjacent crystallites making a small angle with each other to satisfy the necessity of filling the space, that the macromolecular chains within the crystallites are perpendicular to the spherulite local radial direction and that the crystallites are present between two thin disordered layers. These generally accepted features are similar to the conclusions of Galeski, Argon and Cohen (1987) regarding the structure of PA6. A potential difference between the PA6 and the HDPE resides in the form of the crystallites. The S-shaped form is the most prevalent form in HDPE (Lin and Argon, 1994); while in PA6, crystallites are plate-like and form crystalline domains (Galeski, Argon and Cohen, 1987). Although much material particularity certainly exists, the above description should be representative of the general supermolecular structure of semicrystalline polymers.

The manner in which spherulites grow upon crystallization and the effect of the processing parameters on the spherulite morphology remains a subject on which many experimental results are controversial (Lin and Argon, 1994). Varga (1992), in an extensive review of the supermolecular structure of isotactic polypropylene, has clarified some of these controversial features. However, the knowledge about the semicrystalline polymer structure summarized above should be sufficient in the context of the present project. This brief summary will serve as background for the description of the deformation and cracking behavior.

2.1.2 Inelastic Deformation Mechanisms in Semicrystalline Polymers

2.1.2.1 Local Inelastic Deformation Mechanisms

Experimental results employed in support of the following brief review of the local deformation mechanisms in the crystalline and in the amorphous phases were taken from the review by Lin and Argon (1994). In the crystalline phase, the deformation mechanisms can be classed into two categories: crystallographic slip and twinning/stress induced martensitic transformation. These categories are the same as for metallic crystals. In polymers, the slip plane always contains the chain direction. In PE, crystallographic slip can occur along the chain axis (chain slip) and/or along another close packing direction (transverse slip). For PA6, the lattice resistance to (001)[010] chain slip is the lowest (Lin and Argon, 1992). When crystallographic slip occurs in a crystallite segment, there is a tendency for the crystal to orient the slip direction parallel to the tensile direction. Thus, a preferential alignment in the crystalline phase of the chain axis parallel to the tensile direction results from the deformation, which has been measured experimentally for PA6 by X-ray diffraction (Galeski, Argon and Cohen, 1991a).

Since the amorphous phase has lower strength than the crystalline phase, the deformation is initially localized in the amorphous phase. In the amorphous layers located between the crystallites, three deformation modes have received some experimental support: intercrystallite slip, intercrystallite separation and stack rotation. A schematic representation of each of these is shown in Figure 2.5. For HDPE, it has been reported that intercrystallite shear is dominant in the early stage of deformation at room temperature and that the deformation which occurs by this mechanism is fully reversible. This complete reversibility is probably limited to a certain range of accumulated strain. There appears to be two categories of intercrystallite separation deformation processes based upon reported results for polyethylene (PE). These are processes in which cavitation occurs and processes in which it does not. The latter category has been demonstrated experimentally in single-texture low density polyethylene (LDPE) where the intercrystallite separation was reversible. Cavitation during intercrystallite separation can be expected from the presence of hydrostatic stresses in the amorphous phase. This hydrostatic tension results from the high resistance of the crystalline phase to contraction. Stack rotation has received much less experimental evidence in PE than the two other mechanisms. In conclusion, the effective mode of deformation of the amorphous layers depends on the relative orientation between the layer planes and the local stress orientation on these planes.

The proportion of the local deformation which occurs in the amorphous zone depends on the deformation mechanism and on the local amorphous phase content. After approximately 25% of true strain, the plastic deformation of HDPE is very well characterized by the deformation of the crystalline component alone (Lin and Argon, 1994). To conclude, the effective local deformation mechanism depends on the amount of accumulated strain and on the relative orientation between the microstructural features and the stress.

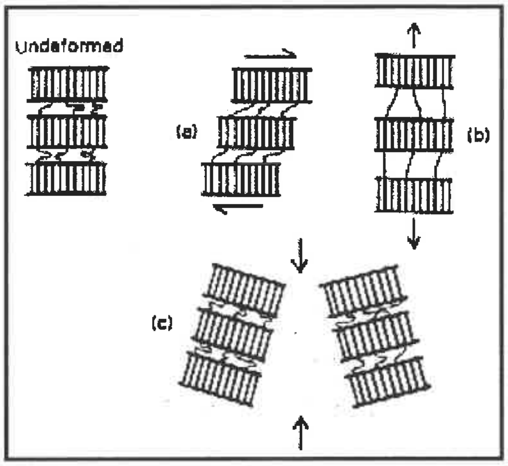

Figure 2.5: **Three deformation modes of the inter-crystallite amorphous layers with some experimental support (from Lin and Argon, 1994): (a) intercrystallite slip, (b) intercrystallite separation, and (c) stack rotation.**

2.1.2.2 Heterogeneity of the Inelastic Deformation

The fact that a semicrystalline polymer is a made up of a three-dimensional array of entities which are initially roughly spherical and internally mechanically anisotropic has a primary effect on the overall deformation process. Basically, the two factors that should control the magnitude and the nature of the deformation in a given region within a spherulite are the local stress field and the orientation of the microstructure with respect to this stress field. The local stress is affected by the deformation of the other regions of the same spherulite and also by the necessity of maintaining geometrical compatibility at the spherulite boundaries, since observations have shown that this compatibility is maintained. In metals, compatibility at the grain boundaries must also be maintained but the microstructure within each grain is more homogenous than in each spherulite. The microstructure of the spherulite can be simplified as a reinforced composite in which the crystallites act as the reinforcement. The length of the crystallites is locally oriented along the radial direction of the spherulite (c.f. section 2.1.1.4). Hence, the angle between the reinforcement material orientation and the direction of the principal tensile stress varies from region to region. As a consequence, the effective local deformation mechanisms also vary from region to region within a spherulite.

2.1.2.3 Deformation-Induced Localized Cavitation

For the following discussion, three regions of each spherulite in which the effective local deformation mechanisms are different will be defined: the equatorial disk, the 45° domains and the polar fans. The equatorial disk is the region where the local principal tensile stress is almost perpendicular to the spherulite radius. The polar fans are the two regions where the local principal tensile stress and the spherulite radius are almost parallel. The 45° domains are located between the equatorial disk and the polar fans. Galeski, Argon and Cohen (1988) have performed a detailed study in which dried and humidity conditioned PA6 drawn samples were soaked under stress in a solution containing osmium ions (OsO_4 in solution), sectioned and further stained with phosphotungstic acid (PTA) prior to TEM observations. The procedure of soaking under stress was employed in order to prevent strain recovery of the samples as well as to reveal the damage produced upon deformation. The most relevant result from their TEM work is the observation on transverse cross-sections of dark features mainly situated in the equatorial disks but also found in the interspherulitic regions where three spherulites meet. These dark features were not observed when the drawn samples were not soaked under stress. Also, no dark spots were found in non-deformed specimens stained with OsO_4. The dark features, observed due to preferential fixation of osmium ions, are probably zones of localized deformation.

This postulate is also supported by the observation that immersion in trifluoroethanol dissolved the deformed PA6 but not the dark features. Their structure was observed by deposition on a carbon film of the isolated dark features obtained after centrifugation of the solutions in which the remaining PA6 was dissolved. This structure was composed of 3 or 4 parallel rods of dimensions and arrangement clearly suggesting that they were crystallite segments coming from the same crystallite domain (c.f. section

2.1 for definition and representation of the microstructural features) surrounded by chemically cross-linked PA6. This indicates that the local plastic deformation process in the regions where dark features were observed introduced chemical changes to the PA6 macromolecules so that the deformed product reacted with OsO_4.

These experimental results clearly suggest that the dark features correspond to regions where the material presents a high concentration of deformation-induced free radicals. Also, since the concentration of dark spots was high in the interspherulitic regions in which three spherulites meet and since those latter regions are known to be regions where voids are formed during the latter stages of crystallization (Galeski and Piorkowska, 1983a and 1983b; Way, Atkinson and Nutting, 1974; Muccigresso and Phillips, 1978), localized cavitation most probably occurred in these regions upon deformation. The dark features observed in the micrographs will be called dark spots. Dark spots are distinct entities of the deformed spherulite structure.

These dark spots have an elongated shape with their preferential orientation being along the local spherulite radius. Their aspect ratio observed on an equatorial plane was approximately two or three, as estimated from stereographic observations of the dark features. The concentration of the dark spots in the equatorial disks of the spherulites was higher in the case of the dried specimens then in the case of the 60% humidity conditioned specimens. Water-soaked conditioned samples revealed only very few and smaller dark spots. The glass transition temperature (T_g) shifts from below to above the tensile stretching temperature when the humidity condition of the specimens is varied from dried to water-soaked (Koham, 1995). Hence, the mechanism for dark spot formation is progressively inhibited as the ductility of the amorphous phase increases. The formation of dark spots therefore can be attributed to insufficient ductility of the glassy amorphous matrix to accommodate the local deformation without losing its microstructural integrity.

2.1.2.4 Deformation of the Spherulite Array

In the necking region of dried PA6 tensile specimen where the drawing ratio was approximately 2, Galeski, Argon and Cohen (1988) have reported that the spherulitic structure was still observable. Similar observations have been made in PE (references in Lin and Argon, 1994). Spherulites become elongated in the loading direction during deformation but the interspherulitic boundaries are maintained. Therefore, the deformation of the spherulite arrays occurs by maintaining geometrical compatibility at these interfaces.

Galeski, Argon and Cohen (1988) have presented a possible sequence of events for the early stage of deformation within spherulites (Figure 2.6). The non-deformed spherulite (Figure 2.6a) undergoes shear deformation in the 45° domains, which promotes an intercrystallite shear deformation mechanism in the amorphous phase and chain slip in the crystallites. As a result, there is a reorientation and elongation of the crystallites in the 45° domain and stress redistribution to the polar fans and the equatorial disk regions (Figure 2.6b). Early deformation processes localized in the 45° domain appears to be a reasonable assumption when considering that constant volume deformation must locally occur through a shear mechanism, that the shear deformation mechanism having the lowest yielding shear resistance is intercrystallite slip (at sufficiently low strains and strain rates) and that intercrystallite slip is favored by a local orientation of the crystallite length parallel to the local direction of maximum resolved shear stress. Before deformation, all crystallites in the 45° domains have their length parallel to the local direction of maximum resolved shear stress. Therefore, the assumption that early inelastic deformation processes are localized in the 45° domains will be considered as a fact in the following discussion. After a certain deformation in the 45° domains, stress redistribution occurs because the geometrical compatibility between the spherulites must be maintained. That stress redistribution affects the deformation mechanisms occurring in the other regions of the spherulite.

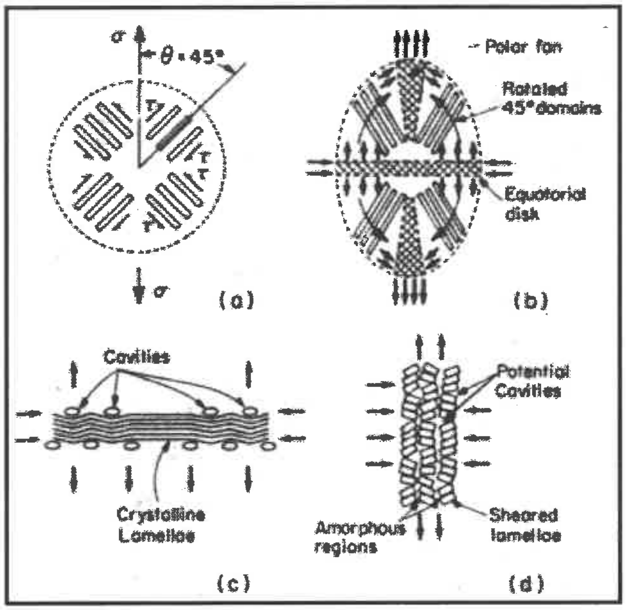

Figure 2.6: Possible sequence of events upon the early stage of PA6 spherulite deformation: (a) un-deformed material where the 45° domains are schematized; (b) reorientation and elongation of the crystallites in the 45° domain due to shear deformation and stress redistribution to the polar fans and the equatorial disk regions with the external stresses acting on each spherulite region indicated by the arrows; (c) kinking of the crystallites in the equatorial disk due to radial compression; (d) shear instability due to chain slip in crystallites in polar regions (from Galeski, Argon and Cohen,1988).

In the equatorial disk (Figure 2.6c), the radial compression stresses as well as the tensile stress in the loading direction are driving forces for lateral contraction of the spherulite. However, the material is particularly rigid along the radial directions since these directions correspond to the preferential orientation of the crystallites. It appears reasonable to assume that the crystallites which have a length almost equal to the spherulite radius will not conserve their structural integrity upon lateral contraction. Galeski, Argon and Cohen (1988) have proposed, by analogy with the behavior of continuous fiber composites, that the crystallites accommodate the required contraction by giving rise to unstable kinking. However, other processes such as transverse slip could be considered.

As pointed out by Galeski, Argon and Cohen (1988), the amorphous regions in the equatorial disk are not expected to have a high resistance to the initiation of cavities since these regions must sustain the stress triaxiality induced by the intercrystallite separation deformation process. Independently of the exact mechanism which leads to the formation of cavities in the equatorial disk, the final effect of the perpendicularity between the applied principal tensile stress and the spherulite radial local orientation remains a high potential for the initiation and growth of cavities. This behavior can be expected to have a strong effect on the cracking mechanisms.

In the polar fans (Figure 2.6d), the stress redistribution coming from deformation in the 45° domains also induces the presence of a lateral compression stress field. In these regions, the chain fold plane is parallel to the applied principal tensile stress. Galeski, Argon and Cohen (1988) proposed as a potential deformation process the radial extension of the crystallites by segmentation. This segmentation of the crystallites could induce cavitation, as in the case of segmentation in the equatorial disk. However, since one cannot expect stress triaxiality in the amorphous phase located in the polar fans, the amorphous phase can be expected to heal any formed cavity during the segmentation process. Therefore, the polar fans are not expected to be regions of preferential crack initiation.

Heterogeneous deformation by shear banding in thin films of PA6 strained above and below T_g (c.f. section 2.1.3.1) have been observed by atomic force microscopy (AFM) by Ferreiro, Pennec, Seguela and Coulon (2000). They reported that "Below the glass transition temperature $T_g = 32^oC$ [], the spreading of the shear bands within the spherulites is heterogeneous. The number of shear bands per unit area is maximum near the equatorial zone and decreases regularly towards the polar zones.". Their observations were carried out on 10% strained films. No figures were included in their paper. The observed deformed spherulites were those native from the heterogeneous crystallization initiation at the mold-melt interface. Thus, most of the spherulites had their nuclei located in the observation plane (Figure 2.3). Shear bands were observed but their contribution to the overall deformation appears unknown.

Assuming that Ferreiro, Pennec, Seguela and Coulon (2000) have the same definition of the equatorial zone, it is of interest to determine if their observations conflict with the possible sequence of deformation events in bulk deformed PA6 proposed by Galeski, Argon and Cohen (1988). Although both materials were made of PA6 spherulites in which the crystallites were oriented along the spherulite radius, the geometrical constraints for the deformation of a given spherulite located in the bulk and at the surface are quite different. In the experiments performed by Ferreiro, Pennec, Seguela and Coulon (2000), there is no compressive stress along the film thickness direction since there is no geometrical constraint along this direction at the free surface. Also, shear banding may occur in the 45° domains without being observable microscopically since the deformation process does not, at a low drawing ratio, destroy the low magnification appearance of the original crystallites. The results of Ferreiro, Pennec, Seguela and Coulon (2000) on thin films do not rule out the sequence of deformation events in bulk deformed PA6 proposed by Galeski, Argon and Cohen (1988).

2.1.2.5 Transformation during Drawing

In the previous section, the discussion was mainly oriented towards the initiation of plastic deformation. Although the spherulite boundaries are maintained up to a certain point upon deformation, high drawing ratios are known to destroy almost completely the original spherulitic structure. As measured by X-ray diffraction (XRD), deformation induces an alignment of the chain direction in the crystals parallel to the tensile or flow direction (e.g. studies on uniaxial extension and compression of PA6 by Galeski, Argon and Cohen, 1991a and 1991b).

Peterlin (1973, 1975) was among the first to study extensively the microstructural transformation in a propagating neck zone during uniaxial extension. He proposed a general model in which drawing induces micro-necking that results in fibrillation of the originally spherulitic structure. In this model, the crystallites are broken-up during micronecking and incorporated into the micro-fibrils, which therefore consist of alternating crystallites and amorphous regions. Peterlin (1973) observed fibrils with a width of approximately 1μm on surface replicas of drawn PA6 specimens. Each of these fibrils was thought to contain several micro-fibrils. Further deformation of drawn specimens was believed to occur by a relative displacement of the micro-fibrils along the tensile direction. This displacement requires shear deformation at the interfaces between the fibrils (Peterlin, 1975).

Zhou and Wilkes (1998) studied the deformation of melt-extruded HDPE specimens in which the crystallites were all oriented perpendicularly to the melt flow direction. Depending on the angle between the melt flow and the tensile loading direction, they observed different stress-strain behavior (Figure 2.7). Based on this behavior, on XRD measurements and on TEM observations, they suggested that three different previously developed models were likely to describe adequately the orientation processes in bulk crystallized spherulitic samples: intercrystallite separation and crystallite fragmentation by chain slip when the angle between the chain axis and the tensile axis is 0^o (Figure 2.7a), break up of the crystallites and re-crystallization when the angle is 90^o (Figure 2.7e), and an intermediate deformation mechanism when the angle is 45^o (Figure 2.7c). Adams, Yang and Thomas (1986) provided strong experimental evidence for the process of intercrystallite separation and crystallite fragmentation by chain slip in oriented thin films of PE.

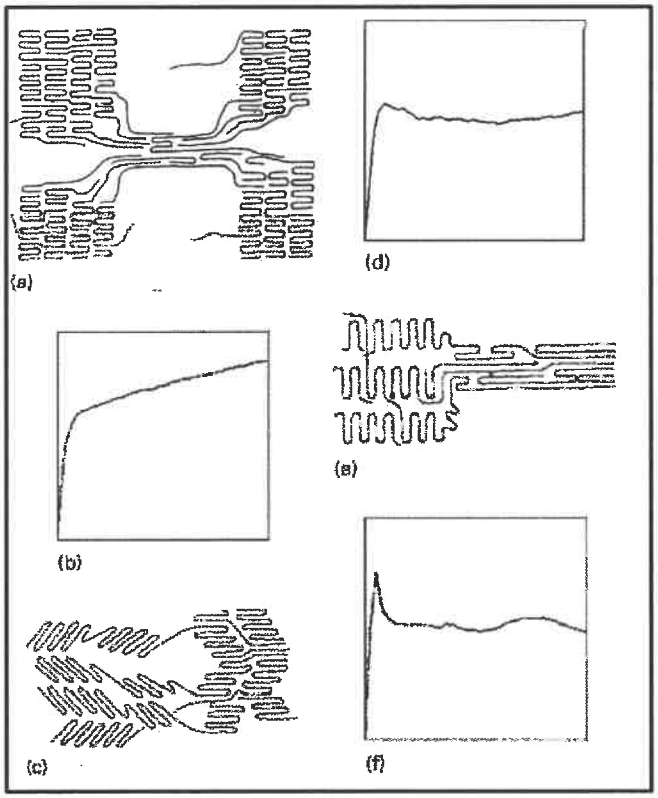

Figure 2.7: **Stress-strain response (b, d and f) associated with models of transformation during uniaxial extension when the angle between the chain axis and the tensile axis is (a) 0°, (c) 45° and (e) 90 °, respectively (from Zhou and Wilkes, 1998).**

Galeski, Bartczak, Argon and Cohen (1992) observed a sequence of events in which high amplitude deformation occurs when the crystallite thickness direction is at an angle to the principal elongation direction during plane strain compression. As shown in Figure 2.8, the sequence involves: intercrystallite shear and intra-crystallite slip, fragmentation of the crystallite into blocks, rotation, and recombination of the blocks. From this mechanism observed in plane strain compression, fibrillation is not observed on the micrometer scale so it cannot be considered as an essential step in producing a highly oriented structure (Galeski, Bartczak, Argon and Cohen, 1992).

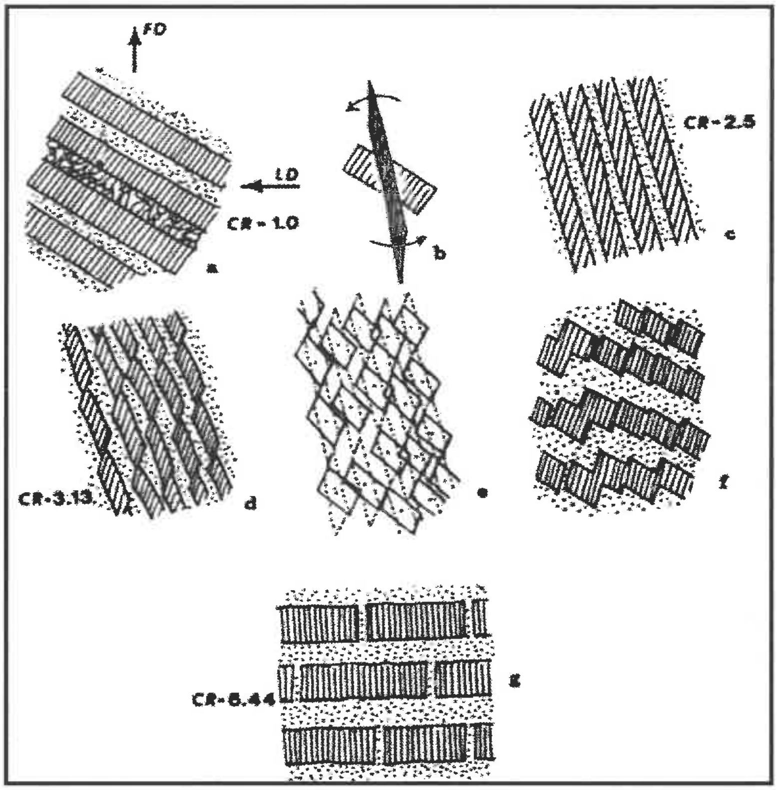

Figure 2.8: Sequence of events for high amplitude deformation in semicrystalline polymers when, as shown in a), the initial orientation between the flow direction (FD) and the crystallite orientation is 45°: b) and c) intercrystallite shear and intra-crystallite slip, d) fragmentation, e) rotation and f) recombination of crystallite blocks. The process in HDPE is completed in g) at a compression ratio (CR) of 6.44 where the newly formed crystallites have their length perpendicular to the flow direction (based upon experiments in plane strain compression, from Galeski, Bartczak, Argon and Cohen, 1992).

The models summarized in this section were obtained from experiments mostly carried out on HDPE. At relatively small tensile strain in bulk solidified semicrystalline polymers in which the amorphous phase is in a glassy state, the regions of a spherulite most susceptible to the initiation of cavitation are the equatorial disk and the interspherulitic regions. These relatively weak regions could have an effect on the cracking mechanisms.

2.1.3 Heterogeneous Deformation

2.1.3.1 Shear Banding

Shear bands similar to those found in glassy polymers have been observed after compressive deformation well below T_g in semicrystalline polypropylene (PP) and in HDPE (Friedrich, 1983). These bands can either follow he spherulite boundaries or be present in the spherulites. In PP, coarse shear bands are formed at a notch tip only well below –70°C ($T/T_g = 0.75$). However, diffuse shear zones are observed in PP at higher temperatures. Shear bands have also been observed by AFM at the surfaces of PA6 specimens (Ferreiro, Pennec, Seguela and Coulon, 2000). Shear bands intersecting each other can promote void nucleation.

2.1.3.2 Crazing

As in amorphous polymers, heterogeneous deformation localized in a planar area nearly perpendicular to the tensile direction has been reported in semicrystalline polymers. These planar areas also contain voids and fibrils in which the entanglement network is highly strained. Unlike crazes in amorphous polymers (c.f. appendix, section A.2.4.1), these planar areas can be classified into two categories (Friedrich, 1983; Narisawa and Ishikawa, 1990). Under conditions where amorphous polymers would generally form crazes through chain scission (craze thickening mechanism applicable at low temperature), the morphology of the crazes in semicrystalline polymers are generally similar to those formed in amorphous polymers. This type of crazes are designated here as low temperature crazes. Unlike in amorphous polymers, craze-like features are also formed in semicrystalline polymers under conditions of relatively high ductility and at temperatures well above T_g. These craze-like features are designated here as fibrillated deformation zones. Before the proposed growth mechanisms of low temperature crazes and of fibrillated deformation zones are presented, the potential effect of crystallinity on the mechanism of chain disentanglement will be outlined.

a) Effect of Strain-Induced Crystallization

In polymers presenting a certain tendency to crystallize, it has been suggested that strain-induced crystallization could inhibit crazing. This suggestion is supported by experimental results reported by Gensler, Plummer, Kausch and Munstedt (1997) on blends of polyether ether ketone (PEEK) and polyether imide (PEI). PEEK is a semicrystalline polymer that can be amorphous if rapidly solidified; whereas, PEI is an amorphous polymer. The addition of PEI in a melt of PEEK reduces the rate of crystallization. Tensile testing over a wide range of temperatures on amorphous thin films of different PEI/PEEK blends showed that the temperature range over which crazing occurred decreased from approximately 100°C to 30°C as the PEEK content increased from 0 to 60%. For a PEEK content equal to or greater than 80%, crazing was completely inhibited. A similar inhibition of crazing was observed in bulk specimens. PEEK and PEI are expected to have similar entanglement densities. Disentanglement crazing is observed at temperatures up to 100°C below T_g for another amorphous polymer with similar entanglement density (Gensler, Plummer, Kausch and Munstedt, 1997). For this reason, it is assumed that crazing in the PEI/PEEK blends occurred also by chain disentanglement. In the microneck of thin films of PEEK, crystallized arrangements were detected by low angle electron diffraction (LAED). Strain-induced crystallization was thought to be the principal reason for the inhibition of disentanglement crazing.

The inhibition of crazing correlated with an increased tendency to crystallize has also been reported in polystyrene (PS) (Morel and Grubb, 1984; Plummer and Kausch, 1993a). Amorphous thin films of atactic PS and isoatactic PS of the same molecular weight both crazed during tensile elongation at room temperature while only atactic PS crazed at low strain rate and at a temperature of 20°C or less below T_g (Plummer and Kausch, 1993a). In polymers with an entanglement density similar to PS (PES), the transition from scission crazing to disentanglement crazing occurred near T_g (Plummer and Donald, 1989). As for the PEI/PEEK blends, the inhibition of crazing correlated with a higher tendency of the material to crystallize has been observed when chain disentanglement was expected to be the principal mechanism of separation between the macromolecules.

b) Morphology and Growth Mechanism of Low Temperature Crazes

The effect of crystallites on the craze growth mechanism can be evaluated by comparing the morphology of crazes formed in the completely amorphous structure and in a semicrystalline structure of the same polymer. The induction of crystallinity, by heat and chemical treatment or by producing macromolecules of higher regular arrangement of the side groups, has been reported to have little effect on the size and spacing of low temperature craze fibrils in the following polymers:

- atactic and isotactic PS (Brady and Yeh, 1973; Morel and Grubb, 1984; Plummer, Cudre-Mauroux and Kausch, 1994);
- amorphous and solvent crystallized polycarbonate (PC) (Yee, Plummer, Soles, Xiao, Wu and Kausch, 1995; Plummer and Kausch, 1996a).

Based on these results, the models for craze advance and thickening mechanisms well developed for amorphous polymers (c.f. appendix, section 1A.2.4.1) may also apply to low temperature crazes in semicrystalline polymers. For example, Argon and Hanoosh (1977) hypothesized that craze-tip advance in semicrystalline isotactic PS occurs by a meniscus instability mechanism. However, local variations in the thickness of the crazes have been observed in isotactic PS (Morel and Grubb, 1984 and Plummer, Cudre-Mauroux and Kausch, 1994). When compared to amorphous regions, the craze fibril extension ratios were generally higher when the thickness direction of the crystallites was perpendicular to the tensile axis and lower when the thickness direction was parallel to the tensile axis (Morel and Grubb, 1984). Morel and Grubb (1984) demonstrated that crystallites are substantially destroyed during surface drawing in the active zone. It remains to be clarified whether such a destruction affects the time or energy required to promote the alignment along the tensile axis of macromolecular segments. The thickness of the active zone in PS at room temperature (approximately 20 nm, c.f. appendix, section 1A.2.4.1) is not much larger than the typical crystallite thickness (of the order of 10 nm, c.f. section 2.1).

c) Morphology and Mechanism of Formation and Growth of Fibrillated Deformation Zones

When the testing temperature is increased, a transition from low temperature crazes to fibrillated deformation zones is observed in thin films of PS (Plummer, Cudre-Mauroux and Kausch, 1994), PP (Plummer and Kausch, 1996b), PA66 (Plummer and Kausch, 1996a), and solvent crystallized PC (Yee, Plummer, Soles, Xiao, Wu and Kausch, 1995; Plummer and Kausch, 1996a). As shown in Figure 2.9, the approximate conditions for which the transition is observed in several polymers appear to depend on the entanglement density and on the testing temperature relative to T_g. The apparent linear relationship suggests that the molecular weight has no effect on the temperature at which the transition is observed, which could suggest that the transition in the mechanism is really from scission crazing to shear deformation since both of these mechanisms do not depend on molecular weight.

For fibrillated deformation zones in thin films of PP crystallized at low temperature, Plummer and Kausch (1996b) reported an extension ratio independent of the testing temperature in the range from –60 to 120°C. This ratio was almost equal to the maximum extension ratio of the entanglement network (λ_e) calculated from molecular weight between entanglements (M_e) using an equivalent of Equation A.24 by assuming that the entanglement network was maintained during crystallization. This assumption can apply for rapidly crystallized polymers since in this case the formation of crystals involves only local conformational changes which do not affect the entanglement structure present in the melt (c.f. section 2.1.1.3). However, as the crystallization temperature was increased, the extension ratio of the craze-like deformation zones increased but still remained independent of the testing temperature. To explain this result, Plummer and Kausch (1996b) suggested that some disentanglement occurred during crystallization at high temperature. In summary, it appears that the maximum extension of fibrillated deformation zones is, as in the case of amorphous polymers, controlled by the structure of the entanglement network.

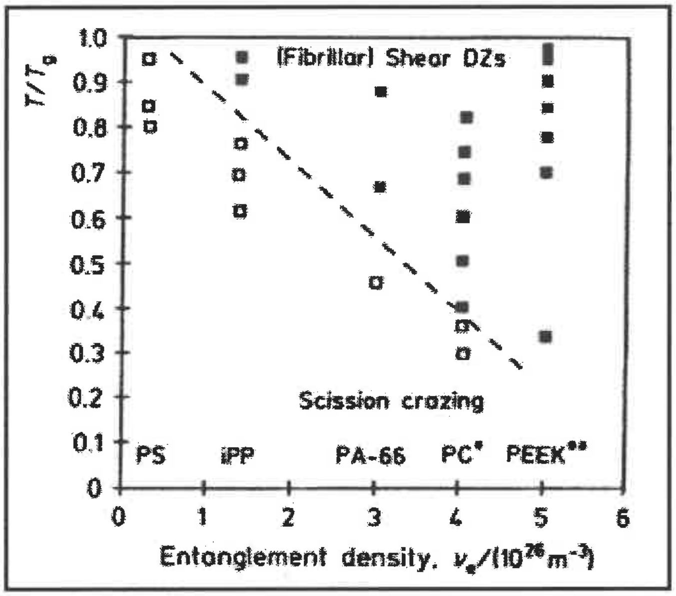

Figure 2.9: Conditions for which deformation of semicrystalline thin films induces either low temperature crazes or fibrillated deformation zones (Plummer and Kausch, 1996a).

Swapan, Bhattacharyn and Brown (1984) studied the evolution of damage during stable crack propagation from a notch in PE. They observed that fibril fracture consisted of a slow process of thinning by shear followed by rapid fracture.

A particular feature of fibrillated deformation zones when compared to crazes in amorphous polymers is that they can contain thin and elongated zones of non-deformed material. Above the glass transition temperature, this feature was reported in thin films of isotactic PS (Plummer, Cudre-Mauroux and Kausch, 1994) and PP (Kausch, Gensler, Grein, Plummer and Scaramuzzino, 1999). In the case of PP, it was reported that further stretching of the films leads to the breakup of the non-deformed regions present in the fibrillated deformation zone. The morphology and preferential orientation of the non-deformed region suggest that they contain crystallites which are oriented perpendicularly to the strain axis. Accordingly, the mechanism of fibrillated deformation zones in the equatorial disks appears to result from interlamellar separation and voiding.

Friedrich (1983) was the first to propose a three stage mechanism of craze initiation in semicrystalline polymers. These stages are as follow:

I. deformation in the amorphous phase: local interlamellar slip in regions of stress concentration (e.g. preexisting voids) or at sites where the angle between the crystallite thickness direction and the local maximum principal tensile stress direction is nearly 45°;

II. segmentation of the crystallites accompanied by the formation of microvoids;

III. complete extension of the stretched fibrils followed by fibril coalescence.

The combination of stages I and II, excluding void formation, is similar to the mechanism of high amplitude deformation, when the direction of the crystallite thickness and the loading direction are at a high angle (c.f. section 2.1.2.5). The mechanism of void initiation has not been observed or proved. In light of the recent observations previously mentioned (difference in the mechanism of growth of low temperature crazes and of fibrillated deformation zones), the details of the model of Friedrich (1983) cannot be considered for all circumstances. Although Friedrich (1983) attempted to describe the formation of low temperature crazes, it is now believed that the description is more appropriate to the formation of fibrillated deformation zones (More and Donald, 1992; Plummer and Kausch, 1996b). Although More and Donald (1992) agreed with the first two stages, they reported that stage III was not observed in thin films of PA6 or PA66.

Fibrillated deformation zones are also reported in bulk specimens and are often called crazes. However, such crazes present similarities with the fibrillated deformation zones observed in thin films. In specimens of PP strained at room temperature, Narisawa and Ishikawa (1990) reported crazes 15 μm thick containing a few non-deformed zones. Similar non-deformed zones have also been observed in a 1 μm thick craze formed in non-notched PP at –60°C (Jang, Uhlmann and Vander Sande, 1985) and in bulk specimens of polyoxymethylene (POM) deformed in creep (Plummer, Scaramuzzino, Kausch and Philippoz, 2000). In the case of non-notched PP, the relative temperature (T/T_g) was 0.85. According to Plummer and Kausch (1996b), fibrillated deformation zones are formed in thin films of PP tested at this temperature (c.f. Figure 2.9). In both studies, cross-tie fibrils oriented randomly were observed. However, since at least Jang, Uhlmann and Vander Sande (1985) employed solvents in order to reveal the internal structure of the crazes, it is possible that artifacts resulted from preferential dissolution of one of the craze components. The most reliable result from the observation of the craze morphology is probably the presence of non-deformed zones within the craze. Narisawa and Ishikawa (1990) proposed that craze thickening occurred by separation of small portions of the non-deformed matrix which are then broken to form fibrils.

d) Effect of the Crystallinity on Crazing

The deformation properties of the crystallites are highly anisotropic (high rigidity along the chain direction and lower rigidity in the other directions). Also, the crystallites present a higher stiffness in average than the amorphous regions. For these reasons, one could expect the presence of crystallites in an amorphous glassy matrix material to favor craze initiation by promoting fluctuations in the stress intensity at the microscopic scale. The role of the spherulite structure on the initiation and growth of low temperature crazes will be first presented.

The effect of the crystallites on this type of crazes is observed experimentally. In isotactic PS, Morel and Grubb (1984) observed local deviations in the craze plane toward the center of the spherulites. Multiple craze initiation from spherulite nuclei has been reported by Olf and Peterlin (1974) for thin films of PP tested at –196°C. In general, the crazes were found to be oriented along the local spherulite radius rather than perpendicular to the principal maximum tensile stress. Also, their length was limited to the spherulite radii. The same crazing behavior was observed up to room temperature. Olf and Peterlin (1974) also studied the crazing behavior of non-spherulitic but crystallized (smectic) PP. The initial crazing stress was similar for both the spherulitic and the non-spherulitic forms but the extension at fracture was higher in the latter case. To compare these results with others studies, Plummer and Kausch (1996a) reported a distribution of small low temperature crazes not correlated with the spherulite structure in thin films of PP deformed at –100°C. However, the difference in the results from both investigations could be attributed to an important difference in the entanglement density resulting from different crystallization kinetics. The specimens of Olf and Peterlin (1974) were compression molded by pressing and turning off the press heater, thus allowing slow cooling from the melt. Those of Plummer and Kausch (1996a) were isothermally crystallized at low temperature. Accordingly, crystallization in this latter case might have resulted in less loss of entanglements.

As Olf and Peterlin (1974), Plummer and Kausch (1993b) reported an effect of the crystalline phase on the location, orientation and length of craze-like features. They employed an identical grade of PEEK to produce thin films in three different forms through proper thermal treatment. The conclusions from the observations were as follows: no craze-like features were present in amorphous films, long and straight fibrillated deformation zones were present in the non-spherulitic films, and fibrillated deformation zones aligned parallel to the local spherulite radii and limited to the spherulite diameter were present in the spherulitic films. Although these tests on thin films of PEEK were performed well below T_g, heterogeneous deformation resulted in fibrillated deformation zones presumably because the entanglement density was too high to promote low temperature crazes (c.f. section 2.1.3.2.c).

Fibrillated deformation zones running preferentially through the radii of the spherulites have also been reported in thin films of POM tested above T_g (Plummer and Kausch, 1996a). From the results described above, it can be stated that, under several but not all conditions, the growth of both low temperature crazes and fibrillated deformation zones in thin films occurs preferentially in the equatorial disks.

The above conclusion can be extended to heterogeneous deformation in bulk specimens. In polyhydroxybutyrate tested at room temperature ($T_g \sim 0^oC$), an increased occurrence of fracture initiation in the spherulite cores after high temperature annealing was observed (Hobbs and Barham, 1999). This fracture initiation was thought to facilitate craze-tip advance. Local deviations of approximately 15^o in the craze plane have been reported in non-notched PP at -60^oC (Jang, Uhlmann and Vander Sande, 1985) under conditions where crazing was not interspherulitic. With notched specimens of PA6, similar deviations were observed with small crazes formed near T_g (Narisawa and Ishikawa, 1990). In this case, etching to reveal the spherulite boundaries clearly indicated preferential growth along the crystallite length.

The results of Snyder, Hiltner and Baer (1994) indicated that the spherulitic structure could be more susceptible to crack tip advance than oriented structures. Using notched tensile specimens of PP, they compared the morphology of the damage zone produced in specimens with different degrees of biaxial orientation introduced by rolling. The specimens with thickness reduced by a ratio of 5 showed an approximately cylindrical damage zone, while this zone was elongated for lower degrees of orientation. For this change in the shape of the volume of the damage zone, the effect of global macromolecular orientation probably needs to be taken into account.

In bulk specimens of PP tested below T_g, Friedrich (1983) studied the effect of the different spherulite structures on the position where the crazes initiate and grow preferentially. In a fine spherulitic structure, the orientation of large crazes was found to be independent of the structure, which can be attributed to the fact that the craze thickness was larger than the spherulite radii. In a partially coarse spherulitic structure, similar large crazes were found to grow preferentially in the fine spherulitic structure and to be stopped in non-equatorial zones of coarse spherulites. In a completely coarse structure, the spherulites did not grow preferentially in the equatorial planes. From the published photomicrographs, the density of the crazes in the latter case appears higher near the spherulite boundaries. Based on these results, the effect of the spherulite structure on crazing depends on the size distribution of the crazes.

For several polymers and testing conditions, it has been observed that crazing in thin films as well as in bulk specimens is favored when crazes can advance along the local radii of the spherulites. By doing so, the advancing crazes avoid crossing thick crystallites which are not oriented in their plane. This result could be correlated with a higher facility to draw portions of crystallites or to promote chain unfolding and/or the presence of a higher level of hydrostatic tension, which can result from prior inhomogeneous inelastic deformation of the spherulites.

e) Effect of Crystallinity on Properties

The effect of crystallinity on the properties is different below and above T_g. Below T_g, ductility and toughness decrease when an amorphous polymer is crystallized. Foot and Ward (1972) compared the notched tensile behavior of amorphous and semicrystalline polyethylene terephthalalte (PET). For high molecular weight specimens, the semicrystalline polymers failed without the development of multiple crazes that formed in the amorphous specimens. Jones, Carriere, Dineen and Balwinski (1997) compared the fracture properties of atactic and syndiotactic PS of similar molecular weights at room temperature. During tensile loading, syndiotactic PS samples failed in the quasi-linear regime at a stress level approximately equal to that where pronounced deviations from linearity were observed in atactic PS samples. The presence of crystals reduced the critical stress intensity factor in the crack opening mode (K_{Ic}) and the critical energy release rate in mode I (G_{Ic}) by 35% and 77%, respectively. This effect was accompanied by an increase in the shear yield stress, which should result in a decrease in the plastic zone size. On the fracture surfaces, a rough correspondence was observed between the spherulite size and the average dimple size. The authors suggested that crazes formed between crystalline lamellae and grew in the equatorial disk until they met in the interspherulitic zones.

Above T_g, no direct comparison between crystallized and amorphous polymers with similar macromolecular structure has been found in the open literature. However, the effect of the crystallization temperature on K_{Ic} of POM was studied by Plummer, Menu, Cudre-Mauroux and Kausch (1995). Generally, an increase in the crystallization temperature increases the crystallite thickness as well as K_{Ic}. The decrease in K_{Ic} with an increase in the crystallization temperature above a critical value was interpreted as caused by a loss of entanglements during crystallization.

2.1.4 Summary

Within the amorphous phase of a semicrystalline polymer, the concepts on the structure and deformation behavior of amorphous polymers are likely to apply. For the crystalline phase, the shear strength depends on the crystal structure but also on the form and density of the defects. In a bulk solidified semicrystalline polymer, the crystalline phase is generally distributed in thin elongated plates called crystallites which are the result of chain association. Crystallites can form microdomains in which a few of them are stacked parallel to each other and are separated by thin amorphous layers. It is suggested that the entanglements present in the melt are concentrated in the amorphous phase during crystallization. Many tie molecules retain the amorphous and crystalline regions together. At the highest structural level, the microstructure is generally an array of spherulites.

Because of its lower stiffness and strength, the deformation is initially localized in the amorphous phase. In such a case, the principal deformation modes are intercrystallite slip, intercrystallite deformation and stack rotation. After 25% of deformation in HDPE, plastic deformation was found to be well characterized by the behavior of the crystalline component alone. In such a case, deformation results from crystallographic slip and twinning/stress induced localized cavitation. The spherulite structure is reported to be maintained in dried PA6 drawn to a ratio of 2. Because of changes in the local stress field and in the orientation of the microstructure with respect to this stress field, the local deformation mechanisms are different in the equatorial disk, the 45° domains and the polar fans of a spherulite.

A possible sequence of events for the early stages of deformation within each spherulite of PA6 involves shear deformation in the 45° domains followed by intercrystallite separation in the equatorial disks and by segmentation of the crystallites in the polar fans. From the deformation mode and stress redistribution expected as well as from the observation of dark spots in dried PA6, the equatorial disk should be a preferential site for the nucleation of voids. In thin films of PA6, heterogeneous deformation by shear banding has been reported.

Upon drawing, the spherulite structure can be transformed into an oriented structure. Depending on the local orientation between the chain direction and the flow direction, such transformation is expected to involve fragmentation of the crystallites and rotation of the fragments or break up of crystallites and re-crystallization. Transformation by drawing in tension produces an array of parallel fibrils that can contains microfibrils. This arrangement is thought to be the result of micro-necking. Compressive deformation can produce structures with similar orientations as those produced in tension. For this reason, micro necking is not a necessary condition for the formation of an oriented structure but it could facilitate and accelerate the process. Further deformation of a fibrillated structure is believed to occur by a relative displacement of the fibrils or microfibrils.

Heterogeneous deformation by shear banding has also been observed in semicrystalline polymers for a limited set of testing conditions. Craze-like features can be classified into two categories. The low temperature crazes are generally similar to the crazes formed in amorphous polymers. The fibril size and spacing in these crazes are found to be independent of the crystalline structure but local variations in the thickness of the crazes have been correlated with the local orientation of the crystallites. In polymers presenting an increasing tendency to crystallize, crazing assisted by chain disentanglement is found to be gradually inhibited. In thin films of several polymers, a transition from low temperature crazing assisted by chain scission to micro necking is observed and found to depend on the entanglement density. These fibrillated deformation zones are the second category of craze-like features. They are expected to result from processes similar to those observed during homogeneous tensile drawing. Their fibril extension ratio was found to be controlled by the maximum extension ratio of the entanglement network and independent of temperature.

Crystallinity has several effects on the crazing behavior and properties. Slow crystallization is likely to result in a loss of entanglement density, which can explain an increase in the extension ratio of the fibrils in fibrillated deformation zones. Under several but not all conditions, the growth of both low temperature crazes and fibrillated deformation zones in thin films and bulk specimens occurs preferentially in the equatorial disks. The effect of crystallinity on properties depends on the ductility. Below T_g, ductility and toughness decrease when an amorphous polymer is crystallized. Above T_g and in conditions where crystallization did not resulted in a lost of entanglements, an increase in the crystallization temperature has been reported to increase the K_{Ic}.

2.2 POLYMER NANOCOMPOSITES

The term polymer nanocomposites refers to a class of polymer composites in which at least one dimension of the dispersed particles is in the nanometer range (Alexandre and Dubois, 2000). Polymer nanocomposites can be classified into three categories according to the number of dimensions of the dispersed particles which are in this dimensional range. For isodimensional polymer nanocomposites, all three dimensions of the filler are in the nanometer range. For nanotubes or whiskers, two dimensions are in the nanometer range. For polymer-layered crystal nanocomposites (PLCNC), only the thickness of the particles is in the nanometer range. Depending on the nature of the two components and on the process employed to associate these two components, a microcomposite, an intercalated nanocomposite or an exfoliated nanocomposite can result. These different types of composites are schematized in Figure 2.10. If no polymer is present between the crystal layers, the product is called a phase separated microcomposite and it has properties in the range of traditional microcomposites. An intercalated structure is characterized by a well ordered build up of alternating polymeric and crystal layers. An exfoliated structure is characterized by a uniform dispersion of the crystal layers in a continuous matrix.

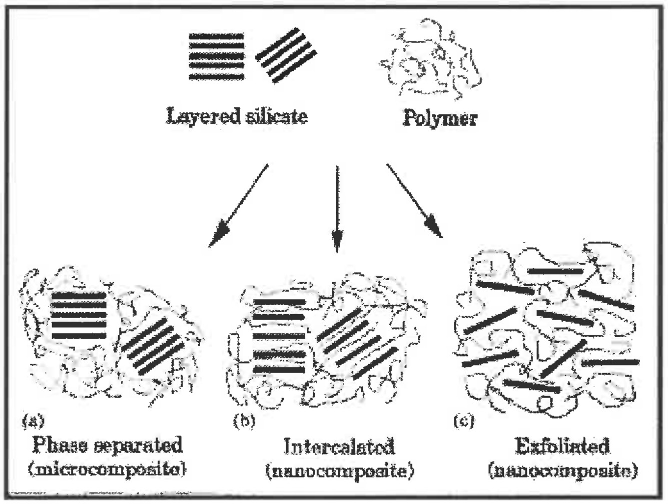

Figure 2.10: Types of composites that can arise from processing of PLCNC (from Alexandre and Dubois, 2000).

In the next subsections, a few important aspects related to the processing and structure of intercalated and exfoliated PLCNC are summarized. Some known features specific to PA6NC are included. Most of the known effects of the addition of nanoparticles on the microstructure and mechanical properties of PLCNC are highlighted. Furthermore, the current knowledge and proposals on the mechanisms of deformation and cracking of this new class of material are described and discussed.

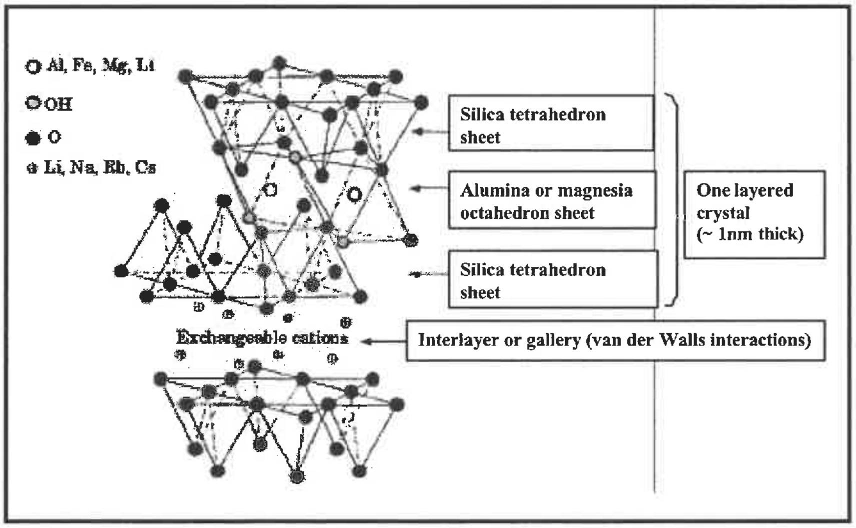

Figure 2.11: Structure of 2:1 phyllosilicates layered crystals (adapted from Giannelis, Krishnamoorti and Manias, 1999).

The raw material commonly employed to produce the filler for PLCNC belongs to the family of the 2:1 phyllosilicates (Alexandre and Dubois, 2000). In their natural form, these phyllosilicates consist of a stacking of layered crystals. As shown in Figure 2.11, the structure of each layered crystal is a stacking of one octahedral sheet of alumina or magnesia between two tetrahedron sheets of silica. These layered crystals, which are approximately 1 nm thick with lateral dimensions from 30 nm to several microns, are stacked parallel to each other and are bonded by van der Walls forces. The gap between layered crystals is called the interlayer or the gallery. The interlayer is an important characteristic of the 2:1 phyllosilicates family allowing intercalation of polymers between the layered crystals and exfoliation of these crystals. During PLCNC processing, the interlayer chemistry can be modified in order to promote chemical bonding between the polymer and the layered crystals, which is responsible of some of the effects of the addition of nanoparticles on the microstructure and mechanical properties.

2.2.1 Preparation of PLCNC

Like their unfilled polymer matrix, thermoplastic PLCNC can be molded using pellets in which the filler is already bended. This subsection intends to briefly describe how those pellets are produced. Although special attention is paid to the PA6 / montmorillonite nanocomposite (PA6NC) of commercial grade 1015C2 produced by Ube Industries, the two others processes currently employed to produce PLCNC are also briefly introduced.

The process employed for the preparation of PA6NC of commercial grade 1015C2 lies in the category of the *in situ* intercalative polymerization processes. The process steps are summarized in Figure 2.12.

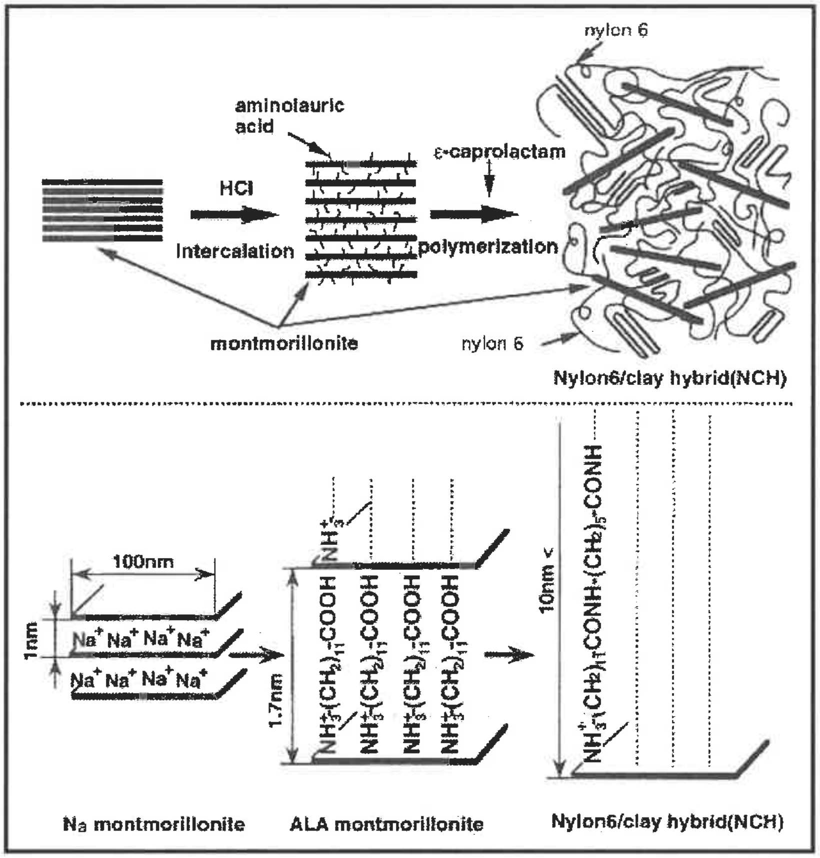

Figure 2.12: Processing steps for preparation of PA6NC (from Yamashita, Takahara and Kajiyama, 1999).

The starting material is a layered crystal member of the 2:1 phyllosilicate family. It is a montmorillonite, which has the chemical composition $M_x(Al_{4-x}Mg_x)Si_8O_{20}(OH)_4$ where x varies between 0.5 and 1.3 and M represents exchangeable cations. The exchangeable cations (M) located in the interlayers are sodium cations. This specific type of montmorillonite is called Na-montmorillonite. This Na-montmorillonite is initially hydrophilic (the antonym of hydrophobic), since it has a good affinity for water. The interlayers of the Na-montmorillonite are modified through a first processing step. Na-montmorillonite is hydrated in the presence of hydrochloric acid (HCl) and aminolauric acid ($+H_3N\text{-}(CH_2)_{11}\text{-}COOH$) (ALA). During this submersion, the cations of sodium located in the interlayers are substituted by the cations of the ALA. The resulting material can be called ALA-montmorillonite when referring to Figure 2.12. As a second processing step, the ALA-montmorillonite is mixed with ε-caprolactam polymer monomers. A small amount of polymerization accelerator is added and the mixture is stirred and heated up. The cooled and solidified product is crushed, washed and dried. For less than 15 wt% of ALA-montmorillonite, an exfoliated structure is obtained as evidenced by XRD and TEM measurements (Usuki, Kojima, Kawasumi, Okada, Fukushima, Kurauchi and Kamigaito, 1993). Using XRD, the proportion of particles that are intercalated but not exfoliated can be estimated by the diffraction peak associated with the regularly spaced crystals.

The two other categories of processes widely employed for the preparation of PLCNC are exfoliation-adsorption and melt intercalation (Alexandre and Dubois, 2000). In the exfoliation-adsorption processes, the layered crystals are exfoliated into single layers using a solvent in which the polymer or the prepolymer is soluble. The polymer added to the solvent is then adsorbed onto the delaminated sheets. In the melt intercalation processes, the layered crystals are mixed with the polymer matrix in the molten state and the polymer extends into the interlayer space if the compatibility between the interlayer treated surfaces and the polymer is sufficient.

2.2.2 Microstructure and Mechanical Properties

In PLCNC, the critical microstructural parameter is the level of exfoliation. The level of exfoliation depends on the processing conditions as well as on the concentration of clay. For the effect of the processing conditions on the exfoliation process, the reader is referred to the review of Alexandre and Dubois (2000). In general terms, the swelling behavior of the treated or un-treated clays with the solvents and/or polymer is an important parameter. As the clay concentration increases above a critical value (generally in the range of 5 to 10 wt%), exfoliation is progressively inhibited. The level of exfoliation appears to have a controlling effect on the improvement in stiffness. A significant increase in E associated with the presence of less than 10 wt% of partially or completely exfoliated nanoparticles has been reported in matrix systems of elastomers, epoxies, PP and PA6 (Alexandre and Dubois, 2000).

PP-based PLCNC have also been studied widely but exfoliation of the nanoclays appears to be more difficult to achieve than in the case of polyamides. Ton-That, Perrin, Lacand, Cole, Denault and Enright (2001) reported an increase in Young's modulus and tensile strength of approximately respectively 24 and 7 % as a result of the addition of 6 wt% of nanoclays and partially optimized melt intercalation conditions. Similarly, Krishna, Bulakh and Jog (2001) reported increases in Young's modulus and tensile strength of approximately 40 and 10%, respectively, as a result of the addition of 5 wt% of nanoclays. These increases are relatively low when taking into consideration that the properties are evaluated above T_g. The low level of exfoliation of the nanoclays, that was deduced from the diffraction peak of the original intercalated structure still observed after bending, could be the main reason for the small increase in properties.

Polyamide-based PLCNC are frequently encountered thermoplastic systems in which both Young's modulus and the UTS are largely increased when compared to the unfilled matrix (Okada and Usuki, 1995; Yang, Ou and Yu, 1998; Liu, Qi and Zhu, 1999; Bureau, Glowacz and Denault, 2001). In these systems, a large proportion of the nanoclays are generally exfoliated. Increases of E in the dry state (T_g above test temperature) and in the conditioned state (T_g slightly below test temperature) of 40 and 125% respectively are reported for injection-molded PA6 filled with 2 wt% of nanoclays (Bureau, Glowacz and Denault, 2001). The increases in the tensile strength were of approximately 25 and 35% for the dry and conditioned states, respectively. These results indicate that the increase in stiffness can be much more pronounced above than below T_g while it appears that the increase in strength can be less dependent on the viscoelastic state. According to Nair, Goettler and Lysek (2001), a modulus increase by a factor of 1.4 is well within the bounds of conventional composite models, such as the Halpin-Tsai model, using an acceptable clay modulus value of 170 MPa. The increase in strength is usually explained by the presence of strong (ionic) interactions between the nanoparticles and the matrix (Alexandre and Dubois, 2000). Few other tensile strength data have been reported for thermoplastic systems in which high levels of exfoliation have been achieved. However, Kalgaonkar and Jog (2001) reported increases in E and tensile strength of 50 and 17% respectively in largely exfoliated polybutylene terephthalalte (PBT)-based PLCNC. The level of exfoliation could also be the main reason for the exceptional increase in strength in the polyamide systems.

Apart from the effect of exfoliation, an effect of the processing conditions needs to be considered. For instance, the increases in Young's modulus and tensile strength of dried PA6 reported above for injection-molded specimens appear to be both diminished to approximately 15% when the same PLCNC pellets are compression molded (Bureau, Denault, Cole and Enright, 2001). Through TEM observations and XRD measurements on molded polyamides-based PLCNC, it has been showed that the nanoclays are preferentially aligned along the shear deformation plane during injection molding (Kojima, Usuki, Kawasumi, Okada, Fukushima, Kurauchi and Kamigaito, 1993; Varlot, Reynaud, Kloppfer, Vigier and Varlet, 2001; Kim, Lee, Hoffmann, Kressler and Stoppelmann, 2001). Factors such as a change in the level of preferential orientation of the nanoclays or in the crystallization conditions could explain this discrepancy.

A fine dispersion of particles in the PA6 matrix could favor the nucleation phase of crystallization and lead to higher level of crystallinity. Reynauld, Jouen, Gauthier, Vigier and Varlet (2001) reported no significant effect of the presence of spherical nanoparticles in the size range from 12 to 50 nm on the overall crystallinity and on the proportion of α and γ phases. In compression-molded samples, Bureau, Denault, Cole and Enright (2001) even reported crystallinity indexes respectively of 31 and 25 % for PA6 and PA6NC compression molded under the same conditions. Contrary to the effect of spherical nanoparticles, the presence of nanoclays appears to affect the proportions of each form of crystals formed. An increase in the proportion of the γ phase is generally observed even in conditions where the samples are compression molded from PA6NC pellets (Bureau, Denault, Cole and Enright, 2001). Medellin-Rodriguez, Burger, Hsiao, Chu, Vaia and Philips (2001) employed PA6NC films and showed that shear deformation in the melt state followed by non-isothermal crystallization further increased the proportion of γ phase. The authors suggested that this behavior could be attributed to crystallization under conditions where the chains are locally extended. As shown by Bureau, Denault, Cole and Enright (2001), the increases in stiffness and strength associated with the addition of nanoclays cannot be attributed to the change in the proportion of each phase since the γ phase has an inherent lower strength.

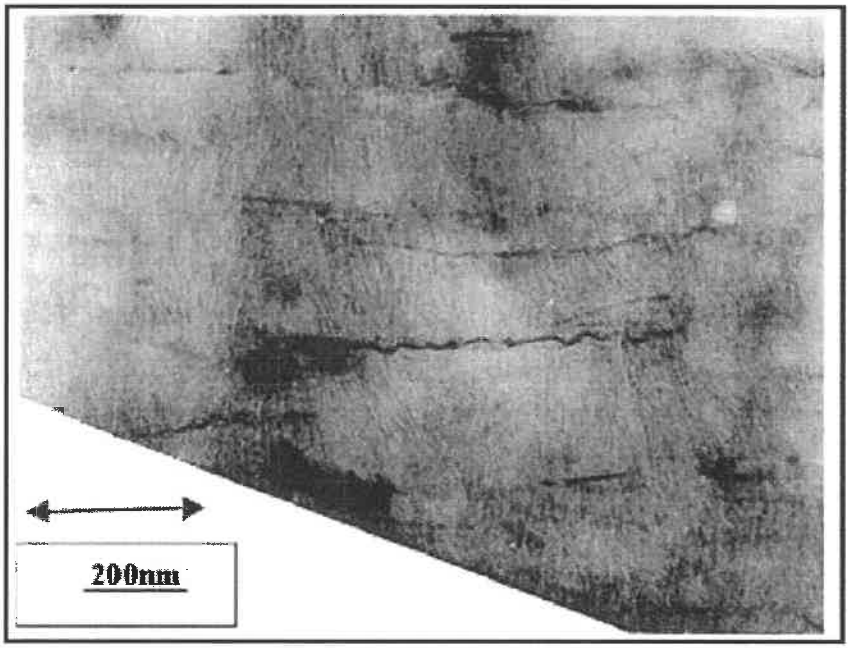

Figure 2.13: TEM micrograph of a PA12-based PLCNC in which the crystallites have their length preferentially oriented perpendicularly to the preferential plane of the nanoparticles (the arrow indicates the injection direction) (Kim, Lee, Hoffmann, Kressler and Stoppelmann, 2001).

Specimens produced by injection molding generally presents three different regions: a skin, a subskin and a core (c.f. appendix, section 1A.1.1). The addition of nanoclay can affect the microstructure differently depending on the region considered. For a specimen thickness range of 0.75 to 3.25 mm, Akkapeddi (1999) measured the crystallinity index in the skin and in the core of specimens of PA6 and melt compounded PA6NC (tensile strength of 98 MPa). In PA6, the crystallinity was always higher in the core than in the skin. PA6NC presented the opposite trend. Also, the difference between the crystallinity in both regions was lower in the case of PA6NC. Finally, for a thickness of 3.25 mm, the crystallinity index in the core and skin of PA6NC was respectively 38 and 44 %, which is significantly higher than the values of 30 and 18 % reported for PA6.

Crystallites with their length preferentially oriented perpendicularly to the preferential plane of the nanoparticles have been reported by Kim, Lee, Hoffmann, Kressler and Stoppelmann (2001) in injected-molded PA12 (Figure 2.13). Also, thermodynamic and kinetic calculations suggested that exfoliated clays in PE induce a bi-dimensional crystallization process (Lee, Gopakumar, Kontopoulou and Parent, 2002). If the microstructure of PA6NC specimens presents locally a similar anisotropic arrangement, one could expect an effect on the mechanism of deformation of the matrix. The increase in the yield stress could be through a direct reinforcing effect and/or an indirect effect originating from the change in the supermolecular structure of the matrix. Also, whether the properties of the interface between exfoliated nanoclays and the matrix play a decisive role in the properties of the composite still remains to be established.

2.2.3 Deformation and Cracking Behavior

Few studies on the effect of the addition of nanoparticles on the deformation and fracture mechanisms in polymer systems have been reported. Their addition to PA6 induces an important dilatational component to the overall inelastic deformation of specimens tested above T_g (Gloaguen and Lefebvre, 2001; Figure A.4). Kim, Lee, Hoffmann, Kressler and Stoppelmann (2001) showed that intercalated layered silicates are preferential sites for the initiation of voids. These authors proposed different mechanisms of deformation of the intercalated clusters depending on the relative orientation between the stacking plane and the tensile direction. In an epoxy/intercalated clay nanocomposite, Zerda and Lesser (2001) reported an important increase in fracture toughness over a limited concentration range of filler. The improved toughness measured was correlated with a higher fracture surface roughness, which suggests a change in cracking mechanism. From these few studies, it is clear that intercalated clusters enhance void nucleation during deformation.

The effect of exfoliated nanoclays have not been directly observed. Below T_g, PA6NC in which a large proportion of the nanoclays are exfoliated presents a highly reduced ductility when compared to the non-filled PA6 (Gloaguen and Lefebvre, 2001; Bureau, Denault, Cole and Enright, 2001; Bureau, Glowacz and Denault, 2001). In all reported cases, fracture occurred before the formation and stabilization of a neck. The reduced ductility measured through tensile testing is probably a consequence of the increase in the yield stress, which favors craze initiation and propagation prior to yielding.

A direct consequence of the increased yield stress and/or reduced ductility is an important decrease in the fracture toughness. This decrease has been reported in dried and conditioned PA6NC (Bureau, Glowacz and Denault, 2001; Nair, Goettler and Lysek, 2001). Nair, Goettler and Lysek (2001) reported a linear relationship between the plastic zone size, which was in the range from 1 to 5 mm, and the value of the J-integral fracture toughness. This behavior infers that the critical plastic zone size is reduced as the yield stress is increased.

In comparing dried PA6 and dried PA6NC, Bureau, Glowacz and Denault (2001) reported a change in the crack propagation mechanism from shear to crazing. Many microstructural factors could have contributed to this change.

2.3 CREEP AND FATIGUE

Both creep and fatigue are treated simultaneously because the response of polymers to these types of loading presents similarities. In the textbook by Hertzberg and Manson (1980), the topic of fatigue in polymers has been reviewed. Although not recent, the reader is directly referred to this textbook for generalities on the testing techniques and for the effect of testing parameters. While a few references will be made to the behavior of amorphous polymers, the main objective here is to present the current knowledge in the case of semicrystalline polymers. Since crack propagation has been more extensively studied and is better understood than changes in the bulk during and prior to crack initiation, this aspect will be treated first.

2.3.1 Crack Propagation

Between crack initiation and final fracture, discontinuous and/or continuous slow crack growth generally occurs over a significant proportion of the lifetime. Crack propagation is easier to characterize and is generally more dependent than crack initiation on parameters which are intrinsic to the material. In this section, a general description of the damage zone ahead of a crack will be first presented. The results and interpretation of recent experiments on fatigue and creep crack propagation in PE will then be presented. Finally, the topic of crack propagation in other semicrystalline polymers will be addressed.

2.3.1.1 Damage Zone ahead of a Crack

In front of the tip of a growing creep or fatigue crack, localized homogeneous shear yielding, shear banding, voiding, fibrillation and/or crazing occur. These deformation processes are confined in a relatively small volume which is referred to as the damage zone. In cases where crazing or fibrillation occurs, the size and morphology of the damage zone can generally be predicted by the Dugdale model. This model considers a flat elliptical hole of length 2c in an infinite plate loaded in tension (Figure 2.14). The boundaries of the plastic zones located at each end of this ellipse are assumed to be under a uniform internal compressive stress (σ_c).

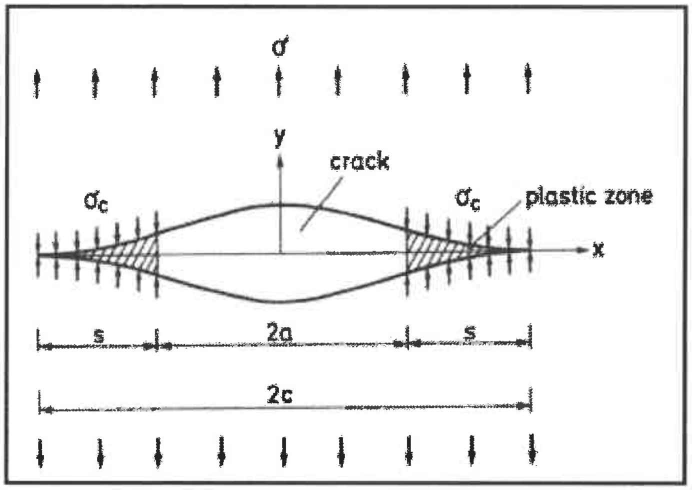

Figure 2.14: Dugdale model for the plastic zone ahead of a crack tip formed by normal yielding.

For small-scale yielding (small plastic zone confined in a large elastic field) and by assuming a flat ellipse (a crack), the length of the plastic zone (s) can be estimated as (Dugdale, 1960; Doll and Konczol, 1990)

Equation 2.1

$$s = \frac{\pi}{8}\left(\frac{\dot{K}_I}{\sigma_c}\right)^2 .$$

A linear dependence with $(K_I/\sigma_c)^2$ is also characteristic of the well-known Irwin equation for the radius of the plastic zone, estimated by the distribution of the stress field at the head of an infinitely sharp crack tip and a yield criteria, in shear yielding materials. The length to thickness ratio of the damage zone is larger in normal yielding than in shear yielding.

Since plastic deformation and damage accumulation by the formation of voids or microcracks absorb energy, the events occurring in the damage zone affect the resistance of a material to crack propagation. The nature and extent of these events can vary widely depending on the material considered. Three different particular situations observed in fatigue will be outlined.

In ductile polymers such as PC, it has been showed that the enthalpy of damage (energy per unit volume of material in the damage zone) is independent of the specimen thickness and stress intensity factor (Sehanobish, Haddaoui and Moet, 1993). These results indicate that the local accumulated strain is constant throughout the damage zone, which clearly suggests that the deformation occurs at the interface between the damaged material and the non-deformed bulk material. Based on this inference, the damage zone in this ductile polymer would grow similarly to a shear band.

During fatigue in the discontinuous crack growth regime, the damage zone can have an epsilon shape formed by three heterogeneous deformation zones emerging from the crack tip: two shear bands and a craze. This phenomenon has been widely reported in PC and has been reviewed by Takemori (1990). More recently, it has been reported in PE (c.f. section 2.3.1.2). The shear bands appear to stabilize the crack front and to promote the formation and growth of a thick membrane that can remain unbroken even after breakdown of the fibrils ahead of the crack tip (c.f. section 2.3.1.2).

During fatigue in PS, multiple crazing can occur in the damage zone. Botsis, Chudnovsky and Moet (1987) studied the effect of the initial stress intensity at the tip of a notch on the fatigue crack growth behavior. The tests were performed under a constant nominal stress. They observed a higher density of crazes at crack initiation for the conditions of lower nominal stress. This higher density was shown to be partially maintained after crack initiation. This observation was employed to explain the difference in the crack growth resistance expressed in terms of the energy release rate between the specimens tested at different nominal stresses. Multiple crazing has also been observed in PP (Chudnovsky, Moet, Bankert and Takemori, 1983). The variations in the crack growth rate were correlated with changes in the shape and size of the damage zone during crack propagation.

For the three cases outlined above, the Dugdale model may not be of particular help. The idea that the damage zone morphology may depend on the previous loading history should be kept in mind when comparing results obtained for conditions where the initial stress intensity factor or its rate of increase are different.

In semicrystalline polymers, the deformation of the spherulitic structure ahead of a crack has been studied for two different fatigue conditions. At high stress intensity or when the ductility of the material is important, the size of the damage zone can be larger than the size of the spherulites. In such a case, elongation of the spherulites in the crack propagation direction was observed on transverse cross-sections (Andrews and Walker, 1971; Bretz, Hertzberg and Manson, 1981a). By observing on the fracture surfaces an elongated ribbon-like structure of width similar to the spherulite diameter, these surfaces also suggested such elongation of the spherulites (Teh and White, 1979; Bretz, Hertzberg and Manson, 1981a). Teh and White proposed that the spherulites were drawn out in the direction of crack growth while Bretz *et al.* suggested that the elongation was a consequence of deformation in compression (even though the loading ratio R was maintained at zero). Bretz *et al.* proposed the following sequence of events in the damage zone when the damage zone size is much larger than the spherulite diameter:

- crazing in the local equatorial disks and in the interspherulitic regions, with the size of these crazes being of the order of the spherulite diameter;
- coalescence of the crazes, with the cyclic tensile deformation being mainly accommodated by the fibrils;
- deformation of the crazed spherulite structure, this deformation is stated as occurring in the region just ahead of the crack tip called the reversed plastic zone;
- the fatigue crack passes through the heavily deformed region which is interpreted as apparently between the reversed plastic zone and the monotonic plastic zone.

The observations employed by Bretz *et al.* to elaborate this model were made on FCP specimens of polyvinylidene fluoride (PVDF, T_g = -35 °C) and PA66 conditioned at 2.2 wt% H_2O (T_g = 37 °C). Whether compression forces are at the origin of the elongation of the structure along the tensile direction remains to be determined.

High local elongation along the crack propagation direction has also been observed below the crack surface during impact fracture toughness tests in rubber-toughened PA6 (Muratoglu, Argon, Cohen and Weinberg, 1995) and in rubber- and calcium carbonate-toughened HDPE (Bartczak, Argon, Cohen and Weinberg, 1999a and 1999b). In these systems, a large increase in the energy to fracture is observed at low temperature and/or high strain rates. In these conditions, the amorphous matrix is in the glassy state. For the filled systems mentioned above, it has been demonstrated that crystallites are aligned with their approximate 0.3 μm length perpendicular to the particle matrix interface. In their preferential shear plane, the local resistance to plastic flow of this layer of anisotropic material is approximately half of that of randomly oriented crystallites (Bartczak, Argon, Cohen and Weinberg, 1999a). When the distance between adjacent particles is of the order of 0.6 μm, cavitation around the particles favors the initiation of plastic flow in the ligaments between the particles. The model of critical matrix ligament thickness initially proposed and demonstrated experimentally by Wu (1988) can be well explained through this mechanism. In order to explain the occurrence of striations parallel to the crack front in rubber particle filled-PA6, a detailed characterization of the microstructure in the damage zone has been performed by Muratoglu, Argon, Cohen and Weinberg (1995). The prime damage parameter employed was the aspect ratio of the internal voids (λ) and the orientation of the long axis of the pores relative to the crack propagation direction (Ψ). These parameters were measured as a function of the distance to the crack plane (Figure 2.15). The authors suggested that aspect ratio of the pores was a direct measure of the local plastic strain. The presence of striations was attributed to buckling of the previous highly strained material upon partial strain recovery behind the crack propagation front. This buckling is believed to be favored by a large compliance in the direction perpendicular to the crack plane of the porous material. The authors expected that this same mechanism could explain the presence of striations uncorrelated with the crack growth rate previously reported for high FCP rate in rubber-toughened PA6 (Hahn, Hertzberg and Manson, 1986). Unfortunately, no suggestion was made on the sequence of deformation leading to a structure highly stretched along the crack propagation direction.

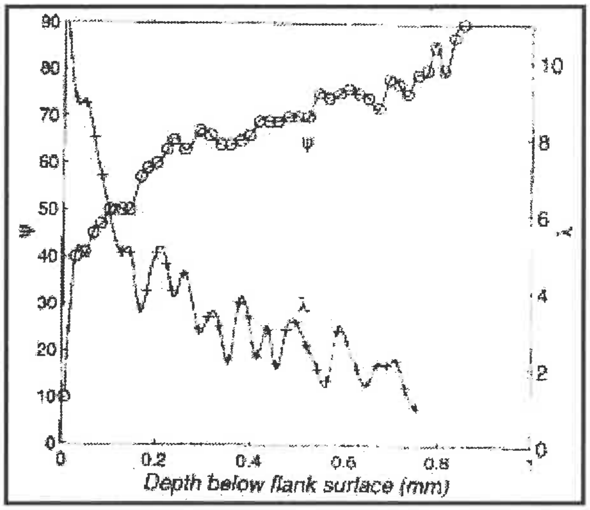

Figure 2.15: Deformation in a damaged zone: Distribution of the aspect ratio λ of the pores (+) and of the angle Ψ between the long axis of the pores and the direction of crack propagation (o) plotted as a function of the depth below fracture surface (Muratoglu, Argon, Cohen and Weinberg, 1995).

Under lower stress intensity or in the case of decreased ductility, the thickness of the damage zone might be smaller than the spherulite diameter. In such a case, the crack propagation path and the morphology of the damage zone are different. Interspherulitic cracking was reported by Andrews and Walker (1971) in PE. Cracking revealing the radial orientation of the crystallites on the fracture surface has also been reported in polyacetal (Hertzberg, Skibo and Manson, 1978; Bretz, Hertzberg and Manson, 1981b).

In an intermediate regime between the two discussed above, the crack can grow through a combination of surface separation by shear deformation and propagation through preexisting voids or crazes. This mode of crack propagation, leading to a distribution of half dimples or craters, has been reported in polybutylene terephthalate (PBT, Tg ~ 50°C) (Morelli and Takemori, 1984), in PEEK (Said, Evans and Isaac, 1993) and in polyamides (Bretz, Hertzberg and Manson, 1979, 1981b and 1982). The presence of half dimples indicates void nucleation and growth occur ahead of the crack. Independently of the mechanism of crack propagation, it is evident that a crack in a semicrystalline polymer may propagate through a structure highly different than the non-deformed spherulitic structure.

2.3.1.2 Mechanisms of Fatigue Crack Propagation in Polyethylene

Particular attention will now be given to the subject of fatigue crack propagation (FCP) in polyethylene. The fractographic features of a fracture surface produced at relatively high range of stress intensity factor (ΔK) can present a transition from discontinuous crack growth through fibrillation to the formation of half dimples (Reynold and Lawrence, 1993). During FCP tests in polyethylene, Andrews and Walker (1971) also observed a transition from a first regime (termed regime 1) where the fracture surface was microscopically brittle to a last regime (termed regime 3) where it was microscopically ductile. In regime 1, the surface was stated to be finely granulated; whereas in regime 3, it was much rougher and presented "parabolic secondary fracture markings". Optical observation of the vicinity of the crack tip on etched transverse cross-sections revealed that the elongation of the spherulites along the crack propagation direction was observed in regime 3 but not in regime 1. On a Paris type of plot (crack propagation rate versus the stress intensity factor on a log-log scale), the transition in the fracture surface morphology corresponded to a plateau called regime 2 between two linear regimes. Similar findings were reported in a subsequent study (Teh, White and Andrews, 1979b). This result suggests that the crack growth kinetics are changed when the mechanism of crack propagation changes from fibrillation to a regime where the separation of the surfaces does not involve microscopic fibrillation by normal yielding.

In experiments where the maximum tensile stress was maintained constant, the rate of crack growth in regime 2 was found to decrease with an increase in the absolute value of the maximum compressive stress, with R varying from -0.7 to -1.9 (Teh, White and Andrews, 1979a). The enhancement of the fatigue resistance while applying a compression load in regime 2 is contrary to the effect expected when fibrillation occurs (c.f. end of this section) and could be possibly related to an increase in the size of the plastic zone.

In the remaining portion of this section, the discussion will be limited to situations where fibrillation occurred. FCP accompanied with fibrillation is frequently reported ahead of a notch in PE specimens. A transition from quasi-continuous to a discontinuous crack propagation mechanism has been observed at 80°C at R = 0.1 when the initial stress intensity factor increased from 0.2 to 0.3 MPa.m$^{1/2}$ (Favier, Giroud, Strijko, Hiver, G'Sell, Hellinckx, and Goldberg, 2002). In the quasi-continuous regime, there was no evidence of voiding ahead of the crack tip. Also, the fibrils appeared to be very thin with a cylindrical morphology. In the discontinuous regime, coarse lamellar microfibrils in the crack and cavitation ahead of the crack tip were observed, as shown in Figure 2.16. It should be noted that the specimens employed in this study were compression molded.

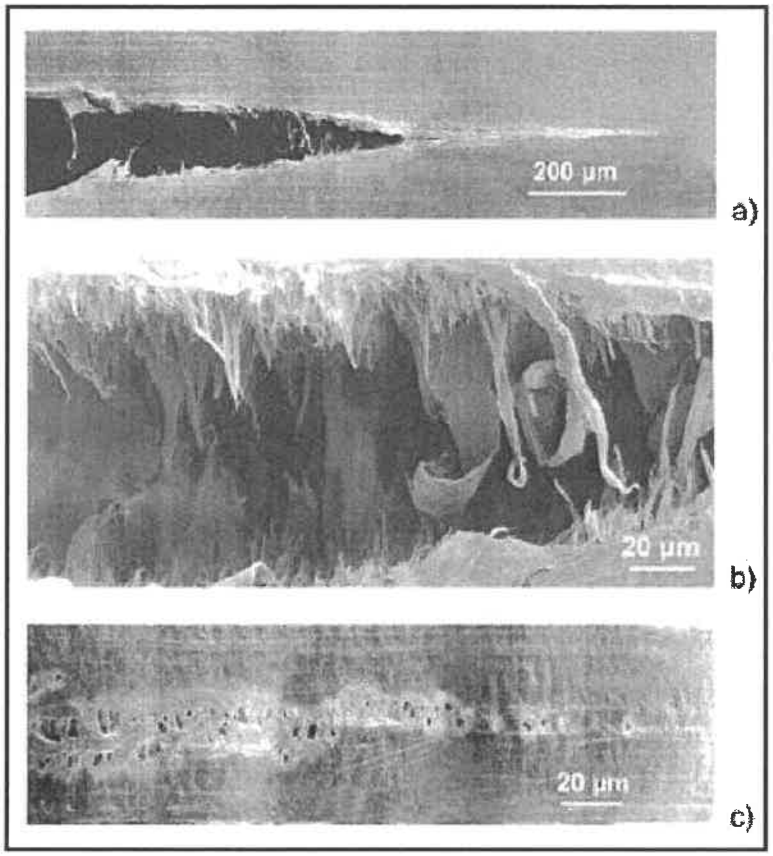

Figure 2.16: Observation of a fatigue crack in PE at 80°C under K_{max} = 0.3 MPa.m$^{1/2}$ and R = 0.1: (a) overall view of the crack and the damage zone, (b) coarse microfibrils within the crack, and (c) cavitation ahead of the crack tip (from Favier, Giroud, Strijko, Hiver, G'Sell, Hellinckx, and Goldberg, 2002).

Discontinuous fatigue crack growth has also been observed at room temperature by Shah, Stepanov, Capaccio, Hiltner and Baer (1998) and by Parsons, Stepanov, Hiltner and Baer (1999, 2000a, 2000b, 2001) in various grades of PE. By observing the evolution of the damage zone before the first jump in a medium density polyethylene (MDPE), Shah *et al.* (1998) showed that fibril breakdown initiated ahead of the crack tip. At the crack tip, a thick continuous ligament called the membrane and a pair of shear-crazes, which are zones of localized plastic deformation oriented at an angle (very approximately 45^o) from the crack plane, were observed. When voids appeared in the membrane, the next membrane was observed employing a video-camera. The last fibrils to break down during a crack advance step appeared to be those formed at the position of the membrane. The thickness of the membrane remained approximately constant during its extension by a factor of two. For this reason, the pair of shear-crazes originating from the crack tip are thought to be a source of material for the extension of the membrane.

As in the Dugdale model, the distance between striations in the discontinuous growth regime is found to be proportional to $(K_{I,Max})^2$ (Shah, Stepanov, Hiltner, Baer and Klein, 1997; Parsons, Stepanov, Hiltner and Baer, 2001), where $K_{I,Max}$ is the maximum cyclic stress intensity factor in mode I. However, this proportionality can also be expected from the stress field in an elastic continuous solid (c.f. 2.3.1.1). Parsons, Stepanov, Hiltner and Baer (2001) compared the damage zone ahead of a notch in HDPE and MDPE. Although in both cases the propagation was discontinuous (Figure 2.17b), shear-crazes were observed only in MDPE (Figure 2.17a). On the fracture surfaces, small approximately cylindrical fibrils were observed in HDPE; whereas, MDPE presented biaxially oriented sheets (Figure 2.17c). Viewed from transverse cross-sections, the structure appeared to be fibrillar in HDPE and cellular in MDPE (Figure 2.17d). The origin of these differences was not discussed. The fractographic and transverse cross-section observations of Parsons, Stepanov, Hiltner and Baer (2001) are very similar to those of Strebel and Moet (1991). These last authors proposed that the voided area in front of the crack tip consists of a large yielded membrane oriented along the crack front followed by a network of randomly oriented membranes.

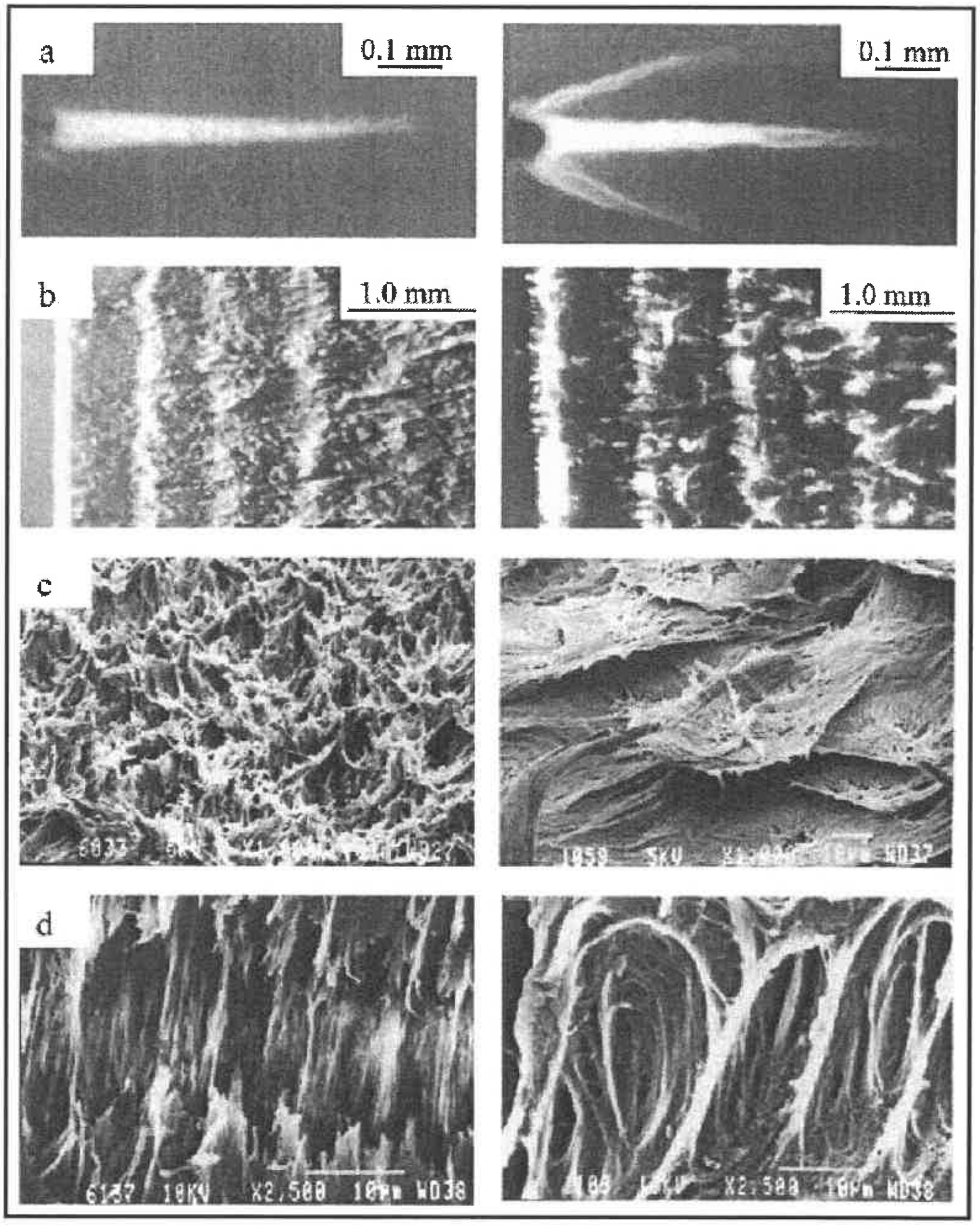

Figure 2.17: **Comparison of the discontinuous crack growth process between HDPE (left) and MDPE (right) during fatigue at room temperature with $K_{I,Max} = 1.3$ MPa.m$^{1/2}$ and $R = 0.1$ (Parsons, Stepanov, Hiltner and Baer, 2001): (a) wedge shaped and epsilon damage zones, (b) striations indicating the discontinuous crack growth mode, (c) details of the fracture surface between the striations and (d) transverse view of extended fibrils.**

At lower $K_{I,Max}$ in MDPE, the shear-crazes disappeared and the number of bading cycles between the first and the second crack jump decreased (Parsons, Stepanov, Hiltner and Baer 2001). However, the length of each jump continued to follow the same proportionality relative to $(K_{I,Max})^2$. Therefore, the shear-crazes absorbed additional deformation energy but do not seem to directly change the length of the zone of fibrillation ahead of the crack tip.

As can be seen from the above discussion, fatigue crack growth accompanied by some type of void formation can occur during continuous or discontinuous crack growth with or without the presence of shear-crazes. Void formation can result in an array of fibrils in a network of interconnected voids or alternatively in an array of voids in a network of interconnected lamellar fibrils. At least in the latter case, the craze tip is unlikely to advance through the meniscus instability mechanism (c.f. appendix, section 1A.2.4.1).

No discussion about the mechanism by which the fibrils extend during fatigue crack growth of PE has been found in the open literature. However, some concepts to determine how the loading parameters affect the craze stability have been proposed. Zhou and Brown (1989, 1992, 1995) suggested two mechanisms responsible for the damage of the fibrils: disentanglement of fibrils near the maximum stress and bending of fibrils near the minimum stress. They observed that fibril breakdown occurs in the midrib for $R<0$ and at the end of the fibrils for $R>0$. This result was interpreted by a difference in the position where the fibrils are locally subjected to the highest bending moment. Bending of the fibrils is proposed to enhance the rate of disentanglement.

Employing a square waveform with a loading frequency of 0.1 Hz and a loading ratio of $R = -1$, Zhou and Brown (1992) studied the effect of varying the time under maximum stress (t_{max}) and the time under minimum stress, $10s - t_{max}$. t_{max} was varied from 0 to 10s. They found a maximum damage rate for a symmetrical waveform (t_{max}=5s). This result indicates that damage occurs under the compression part of the loading cycle. For the same loading ratio of $R = -1$, Harcup, Duckrett, Ward and Capaccio (2000a) found an inversion in the ranking of different PE resins based on the fatigue crack propagation resistance when compared to the resistance to slow crack growth. Based on these results, the mechanism and/or mechanics of damage under minimum and maximum loads can be expected to be different.

As for the tensile-compression loading cycles, an important effect of the unloading time during testing at R = 0 has been reported by Harcup, Duckett, Ward and Capaccio (2000b). It was proposed that the crazes are also compressed under these conditions. By keeping the maximum cyclic stress constant and varying the load ratio R from –1.5 to 1, Zhou and Brown (1989) recorded a maximum in the fatigue life of notched specimens cycled at R = 0.1 when the waveform was sinusoidal and at R = 0.5 when the waveform was trapezoidal. These results were interpreted as supporting their proposed mechanism of fatigue damage through bending.

2.3.1.3 Crack Growth in Polyethylene during Fatigue versus Creep

Because the rate of discontinuous crack growth is higher in fatigue than in creep, efforts have been devoted to correlate the kinetics and mechanisms of damage under these two fundamentally different modes of loading.

Lu, Qian and Brown (1991) observed in a PE copolymer the mechanism of discontinuous crack growth already discussed for MDPE in the previous section. During continuous slow crack propagation, Chan and Williams (1983) showed that the size of the fibrils and of the cavities increased with increasing stress intensity factor. This increase can be interpreted as an effect of the reduced time for void nucleation. As in almost constant stress conditions, Duan and Williams (1998) showed that fibril breakdown does not occur by micronecking in creep-resistant MDPE. Indeed, the fibrils appeared to fracture either near the mid-length or near the interface between the fibrils and the bulk material. Although its cross-section might be larger in the latter case, the material at the latter position contained microvoids and its microstructure could be in a relatively unstable state.

Kasakevich, Moet and Chudnovsky (1990) compared the damage in fatigue and creep loading using the crack layer approach. They found specific enthalpies of damage Γ^* of 2.2 and 1.3 cal/g, respectively. This difference was interpreted as within the limits of the experimental errors and assumptions made during the computation. Zhou, Lu and Brown (1993) studied the fatigue and creep resistance of 17 different commercial grades of ethylene-hexene copolymers. The ratio between the fatigue and creep lifetimes varied widely. A weak correlation was observed between these lifetimes on a log-log scale.

Parsons, Stepanov, Hiltner and Baer (1999, 2000a, 2000b) carried out extensive studies employing both HDPE and MDPE on the effect of the loading ratio on the crack growth rate and fracture surface morphology. For MDPE at five different temperatures in the range from 21 to 80°C, they found the crack growth rate to be proportional to the factor $K_{I,max}^{4}(1+R)^{-6}$. In this study, R was varied from 0.1 to 1. A similar correlation was observed in HDPE with the difference that the proportionality factor employed was $K_{I,max}^{4.5}\ K_{I,mean}^{-0.5}$. This factor is analytically equivalent to $K_{I,max}^{4}(1+R)^{-0.5}$. In both cases, the term $(1+R)^{-n}$ can be viewed as an acceleration factor due to fatigue. The exponent n is then a measure of the sensitivity of the material to fatigue.

In a parallel analysis for HDPE, Parsons, Stepanov, Hiltner and Baer (2000a, 2000b) employed the proportionality factor $B[K_I^4(t)]_T\ \beta$, where $B[K_I^4(t)]_T$ is the creep component calculated by averaging the known dependence of creep crack growth rate on K_I over the period T of a loading cycle and β is the fatigue component which is a function only of the average strain rate. They presented a relatively good fit of data obtained at frequencies ranging from 0.01 to 1 Hz. They suggested that the acceleration due to fatigue could be a consequence of only the average strain rate.

The fractographic observations of Parsons, Stepanov, Hiltner and Baer (1999, 2000a, 2000b) generally indicate very similar broken fibrils produced in creep and in fatigue for R values in the range from 0.4 to 1 (comparisons generally made at the same $K_{I,max}$). However, from the micrographs published, the remnants of the fibrils at $R = 0.1$ were less extended than at higher R values and appeared to be bent.

As in creep, the breakdown of fibrils during fatigue is suggested to be largely controlled by chain disentanglement (Zhou and Brown, 1992#199; Parsons, Stepanov, Hiltner and Baer 2000b). This suggestion could possibly be supported by the effect of the structure on the crack growth resistance in creep (c.f. section 2.3.1.4) and in fatigue (c.f. section 2.3.1.5). Apart from the bending effect proposed by Zhou and Brown (1992#369 and 1995), no discussion on how a variation of the load can promote disentanglement was found in the present literature survey.

When the fibrils are bent under minimum load during fatigue, the mechanism of fibril breakdown could be somewhat different than in creep. Zhou and Brown (1995) observed fibril breakdown by shear thinning in creep and a different fracture mode in fatigue. The latter fracture requires complete separation of the fibrils along a particular plane and might involve both chain disentanglement and scission. As proposed by Zhou and Brown (1995), this difference in the fibril breakdown process could explain the more important influence of molecular weight in fatigue.

2.3.1.4 Structure and Slow Crack Growth under Constant Load in PE

Little work has been devoted to the effect of the spherulitic arrangement on the resistance to slow crack growth under constant load. Plummer, Goldberg and Ghanem (2001) reported interlamellar cavitation ahead of the crack tip in highly crack resistant PE pipe material when the tests were performed in a solvent (solution of Igepal). However, this behavior was not observed in air and in less resistant PE. As in the case of uniaxial extension (c.f. section 2.1.3.2), the effect of the spherulite structure may depend on the material and testing conditions.

It is difficult to differentiate between the effect of the microstructure on the yield stress, which affects the size of the plastic zone at the crack tip (c.f. section 2.3.1.1), and the resistance to disentanglement of the material, which should affect the stability of the fibrils (Lu and Brown, 1987; Zhou and Brown, 1994; Zhou, Brown and Crist, 1995;

Plummer, Goldberg and Ghanem, 2001). Plummer, Scaramuzzino and Kausch (2000) also proposed that chain disentanglement was a controlling factor during creep in POM.

It is reported that annealing of quenched PE specimens in the temperature regime where lamellae thickening is observed reduces the resistance to slow crack growth (Lu, Mcghie and Brown, 1992). In this study, the resistance was characterized only in terms of lifetime. Whether this effect originates from a change in the yield stress or in the resistance to disentanglement is not clear. Barry and Delatycki (1987) proposed that the size of the amorphous regions could be an important factor in determining the resistance to voiding. However, the size of the amorphous regions varied simultaneously with the total crystallinity and hence with the yield stress and with other parameters. Accordingly, their proposal is not unambiguously supported by their results.

In a study in which eleven different microstructures were prepared from the same material by employing a variety of thermal treatments, a linear correlation was observed between the yield stress and the initial rate of notch opening (Lu and Brown, 1987). As the yield stress increased, the initial rate of notch opening under the same stress and at the same temperature increased. Since in these experiments the molecular parameters were maintained constant, the variations in resistance were probably a consequence of changes in the plastic zone size rather than a change in the resistance to disentanglement.

An increase in the branch density is reported to increase the resistance to slow crack growth (Kadota, Chum and Chudnovsky, 1993; Zhou, Brown and Crist, 1995; Egan and Delatycki, 1995). However, it should be noted that the increase in the branch density can be accompanied by a small decrease in the yield stress, Young's modulus and temperature of crystallization. When this is the case, branching could have a double effect in lowering the yield stress and in enhancing the resistance to disentanglement.

Zhou and Brown (1994) studied the effect of blending a high density PE (HDPE) and a linear LDPE on the low crack growth resistance. The molecular weight of HDPE and linear LDPE were 66800 and 192000, respectively, and the linear LDPE was branched. This linear LDPE presented a much higher resistance to slow crack growth than the HDPE. For a given composition, the crystal thickness was also estimated by comparing the resistance of slowly cooled and quenched samples. The effect was relatively small when compared to the effect of composition. The authors proposed a model in which the density of tie molecules would have an important effect on the resistance to slow crack growth. Strebel and Moet (1995) also proposed an important effect of the tie molecules. In both cases, the effect of molecular structure and thermal treatments on the yield stress appeared to have been neglected. Furthermore, an effect of molecular weight could originate from an increase in the resistance to disentanglement rather than to an effect on the tie molecule density.

Yeh, Chen and Hong (1994) produced specimens of PE with different branch lengths but which were expected to have the same supermolecular structure (degree of crystallinity, spherulite structure, tie molecule density and lamellar thickness), molecular weight and branch frequency. With increasing branch length, an improvement in creep crack propagation resistance was noted and attributed to the increased sliding resistance of the polymer chains through the crystal and through entanglements in the amorphous region. The yield stress of the three different materials studied was approximately the same and was not correlated with the increase in the creep resistance.

From the knowledge on the development of crazes during static loading in thin films of semicrystalline polymers (c.f. section 2.1.3.2), the belief that chain disentanglement controls the craze stability during slow crack growth seems reasonable. However, this effect appears to have been demonstrated in only one study.

2.3.1.5 Effects of Structure on Fatigue Crack Propagation in PE and POM

As for creep loading, Zok and Shinozaki (1994) showed that environmental fatigue cracking in PE can be accompanied by intercrystallite voiding ahead of the crack tip. Also as in the case of creep, such voiding has not been reported for fatigue cracking in air.

For a given polymer, variations in the crystallization conditions or heat treatment can affect the resistance to FCP. In the discontinuous regime, Shah *et al.* (1998) showed a decreased resistance as the material conditions varied from slowly cooled to rapidly cooled to quenched. A decreased resistance has also been reported by Strebel and Moet (1995) when comparing slowly cooled and annealed with quenched specimens.

Employing quenched specimens, Runt and Jacq (1989) studied the effect of the annealing temperature on the resistance to FCP. As the annealing temperature increased, the FCP resistance increased even though no noticeable change was noticed in tensile elongation. Differential scanning calorimetry (DSC) measurements also indicated an increase in crystallinity, which was suggested to be the cause of the increase in resistance. A similar effect was later reported for POM (Runt and Gallagher. 1991). Runt and Jacq (1989) also studied the effect of the isothermal crystallization treatment temperature on the resistance of PE to FCP. They found that an increase in the crystallization treatment temperature from 120 to 126°C increases the FCP resistance. This increase was associated with an increase in yield stress, which should have caused a deleterious effect on the crack propagation resistance. The authors concluded that the origin of the change was unknown. From the above results, it appears that increased crystallinity and increased crystallite thickness can induce an increased resistance to crack propagation in semicrystalline polymers tested above T_g.

As in slow crack growth, an increase in the branch density increases the FCP resistance (Shah *et al.*, 1998). This result is interpreted in terms of an increase in the resistance to disentanglement and as an increase in the density of tie molecules. However, the effect on the yield stress should also be considered.

By employing nucleating agents and thermal treatments, Runt and Gallagher (1991) produced different structures with similar crystallinity levels but different spherulite diameters. They concluded that the spherulite diameter had no effect on the crack propagation resistance. Experimental results were however not included in their publication. In some cases, the heterogeneous nature of the fracture surfaces suggest an effect of the supermolecular structure. As an example, Figure 2.18 presents irregularities in the morphology of the fibrils that could be related to the spherulite structure. Unfortunately, no studies in which the fractographic features were compared to the deformation of the spherulites ahead of the crack appear to be present in the open literature. Such a comparison could allow to determine if craze thickening in the different fractographic regimes consumes deformed or non-deformed material.

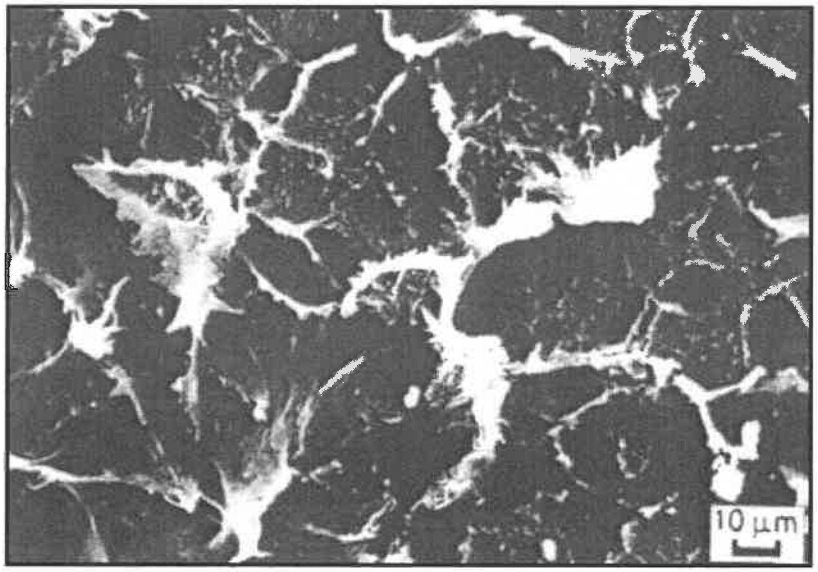

Figure 2.18: Fracture surface produced during fatigue crack propagation in HDPE (Strebel and Moet, 1991).

2.3.1.6 Fatigue Crack Propagation in Polyamides

A few studies have been reported on fatigue crack propagation in polyamides. The glass transition temperature of these semicrystalline polymers typically varies from 60°C to −10°C, depending on the moisture content. The changes observed on the fracture surface by increasing the water content were found to correlate with an increase in the level of plastic deformation in the damage zone (Bretz, Hertzberg and Manson, 1981b). At a given stress intensity factor, the variations in the crack propagation resistance measured by Bretz, Hertzberg and Manson (1981c) have been interpreted as a competitive effect between lowering the elastic modulus and enhancing crack tip blunting. In a subsequent study (Hahn, Hertzberg, Manson and Sperling, 1986), the crack growth rates at a ΔK value of 2.5 $MPa.m^{1/2}$ were measured for different temperatures and water contents. The data suggested the presence of an optimum in the viscoelastic state that minimized the crack propagation rate. This optimum was observed at a temperature of approximately 50°C below the glass transition temperature. Interestingly, the mobility of the chains is highly reduced around this temperature (c.f. appendix, section 1A.1.2.2).

An increase in molecular weight was found to increase significantly the resistance to crack propagation (Bretz, Hertzberg and Manson, 1982). Under conditions in which temperature increases at the crack tip were avoided, Wyzgoski, Novak and Simon (1990) showed a decrease in crack growth rate with decreasing test frequency from 5 to 0.1 Hz. This result was related to a time-under-load effect.

2.3.1.7 Surface Separation Mechanism during Fatigue

In amorphous polymers, molecular weight and molecular weight distribution are well known to have an important effect on the resistance to crack propagation in PS and polymethylmethacrylate (PMMA). This effect has been reviewed by Hertzberg and Manson (1980) and by Sauer and Hara (1990). Craze fibril breakdown is believed to be caused by a viscoelastic process involving cyclic stress-induced disentanglement of the molecules in each fibril. This disentanglement is believed to become easier as the molecular weight is decreased. Also, an increase in the molecular weight could have a positive effect on the strain orientation hardening.

As previously discussed, several authors believe that the crack propagation resistance of PE is largely controlled by the resistance of the material to chain disentanglement. However, only the results in creep of Yeh, Chen and Hong (1994) support this belief. An important effect of molecular weight has been reported in PE, in polyamides and in PEEK (Said, Evans and Isaac, 1993). However, the molecular weight also influences the supermolecular structure. For this reason, the origin of the improvement cannot be clearly isolated. In PBT (T_g = 50°C), Yeh and Runt (1989) varied the molecular weight and tie molecule density through a thermal treatment in which oxydative degradation leading to a decrease of M_w occurred without significant variation in the supermolecular structure. They observed a significant decrease in the fatigue crack propagation resistance with a decrease in the M_w. From the results of Yeh, Chen and Hong (1994) and of Yeh and Runt (1989), it can be concluded that the M_w and the tie molecule density are important parameters determining the resistance to crack propagation of semicrystalline polymers tested below as well as above T_g. This suggests that the concepts of craze fibril stability originally developed for amorphous polymers might also be applicable to semicrystalline polymers.

2.3.1.8 Effect of Crystallinity

As discussed in section 2.3.1.5, an increase in crystallinity or crystal thickness through thermal treatments is not found to have a deleterious effect on the crack propagation resistance above T_g for the annealing temperature range studied. Below T_g, the effect of crystallinity appears to vary with the crystallization conditions. Pecorini and Hertzberg (1993) studied this effect in PET (T_g~70°C). To avoid an effect of the spherulitic structure, all specimens were initially quenched to produce an amorphous structure and subsequently annealed under vacuum at different temperatures. In the low crystallization temperature regime, a specimen with a final crystallinity of 37% was found to have similar fatigue resistance and fracture toughness as an amorphous specimen. Even if the properties were similar, the mechanism of crack tip blunting during fracture toughness tests changed from shear yielding in the amorphous specimens to multiple crazing in the specimens with 37% crystallinity. Crystallization at higher temperature was found to progressively decrease the resistance to crack propagation. This decrease was explained by a decrease in the tie molecule density resulting from the formation of crystallites having a regularly folded conformation (secondary crystallization). Based on these results, the presence of crystallites below T_g may not have a deleterious effect on the resistance to FCP, if the strength of the interface between the two components is sufficient to promote craze stability. Also, the tests reported by Pecorini and Hertzberg (1993) were performed at relatively high stress intensity factors. The results may not be applicable to situations were the size of the plastic zone is in the range of the crystallite arrangement.

2.3.2 Creep and Fatigue of Non-Notched Specimens

Even if it is recognized that fatigue fracture is controlled by initiation in most homopolymers (Rabinowitz and Beardmore, 1974; Lesser, 1995), a limited amount of research has been carried out on the mechanisms of fitigue crack initiation. Before crack initiation, several microstructural changes can occur in the volume of a polymeric specimen subjected to constant or cyclic loading. It is generally not possible to observe directly the nature of these microstructural changes. For this reason, several investigators have relied on the macroscopic mechanical response of non-notched specimens to characterize these changes.

2.3.2.1 Types of Macroscopic Mechanical Responses in Fatigue

Using non-notched specimens and depending on the fatigue testing parameters, two completely different types of behavior can be observed. At high cyclic load or frequency, an unstable increase in the specimen temperature resulting from adiabatic heating induces what is often called a thermally dominated fatigue fracture (not to be confounded with thermal fatigue in metals). When compared to metals, polymers have a high damping capacity and a low thermal conductivity. A small increase in temperature above room temperature generally increases the damping capacity and reduces the stiffness. It is for these reasons that non-notched polymeric specimens are more likely to fail as a result of an unstable temperature increase than their metallic counterparts. The heat generated during cycling is not completely dissipated so the temperature increases. Due to this increase, the dynamic properties of the polymer change and the heat generation rate increases. As a result, the temperature continues to increase until fracture.

In real components, small zones of stress concentration generally exist and microstructural changes leading eventually to crack initiation are likely to occur only in these zones. In such a case, thermal fracture is less likely to occur because the heat generated in the small zones of stress concentration can be dissipated to the surrounding material. Thermally dominated fatigue fracture can thus be considered as a consequence of the accelerated nature of the tests carried out on laboratory specimens and of the large volume of material subjected to high cyclic stresses.

For these reasons, many investigators try to avoid thermal effects. In order to characterize the mechanically dominated fatigue fracture regime, it is often necessary to carry out the tests at low cycling frequencies. For a given polymeric specimen, Crawford and Benham (1974a, 1975) have shown that the stress amplitude for which a transition from thermally dominated fatigue fracture to mechanically dominated fatigue fracture varies linearly with the logarithm of the testing frequency. Employing a low frequency is even more critical in axial loading than in bending (Crawford and Benham, 1974b) since in the axially loaded case, the complete gauge length is subjected to the same maximum stress, which is a disadvantage in terms of heat dissipation but an advantage in characterizing the stress-strain response. Most of the results reported here were obtained through axial fatigue testing.

2.3.2.2 Macroscopic Mechanical Response

Rabinowitz and Beardmore (1974) carried out fully reversed strain controlled axial fatigue tests at different strain amplitudes to study the stress-strain response of PC and polyamide at room temperature. Strain rates were selected to avoid any temperature rise of more than 2°C. The stress response of PC included: an initial incubation period, a transition period in which the stress decreased rapidly, a zone of cyclic stability, and a final zone in which the stress further decreased presumably as a result of crack propagation. In contrast, there was no incubation period in polyamide and in other PC specimens tested above a threshold value of strain amplitude. The presence of a threshold value in PC was interpreted as a level where the production of mobile defects occurred during the first tensile cycle. The absence of an incubation period in polyamide was interpreted as a consequence of the heterogeneity of the semicrystalline structure. However, the range between the test temperature and T_g was smaller in the case of polyamide. In all cases, softening in the transition period was observed in both the tensile and compressive portions of the cycles. The transition periods were followed by regions of cyclic stability.

Rabinowitz and Beardmore (1974) also carried out a test on a cold drawn PC. In this case, cyclic softening was observed mainly in the tensile response. After 200 cycles, the stress levels in both tension and compression were near the values for an initially isotropic material. This reduction in the difference between the tensile and compressive maximum stresses occurred without significant changes in the level of macromolecular orientation (measured by birefringence). These results suggest that any increase in stiffness resulting from cold drawing can be lost during the fatigue process. This also indicates that initial anisotropy of the material can have a profound effect on the stress-strain response.

In tension-tension load controlled testing with a trapezoidal waveform, Remmerswaal (1992) studied the effect of the loading parameters on the time for PC specimens to reach an accumulated strain of 7% ($t_{7\%}$). Figure 2.19a presents data on $t_{7\%}$ as a function of the maximum cyclic stress for different loading rates. Above a value of 10 MPa/s, the loading rate appears to have little effect on $t_{7\%}$. Figure 2.19b shows that $t_{7\%}$ is progressively decreased when the time at maximum and minimum loads is increased. For non-notched specimens, the creep deformation process and the fatigue deformation process might be related.

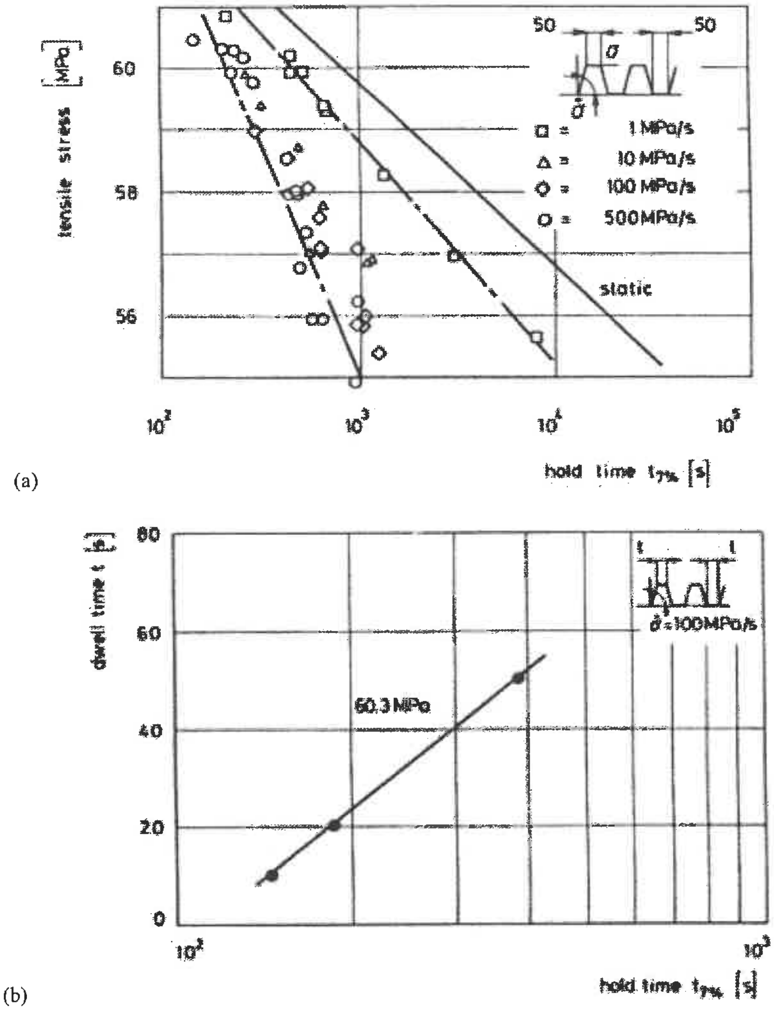

Figure 2.19: Creep-fatigue interaction in PC: effect of (a) the loading rate and maximum stress and of (b) the time under maximum and minimum stresses (Remmerswaal, 1992).

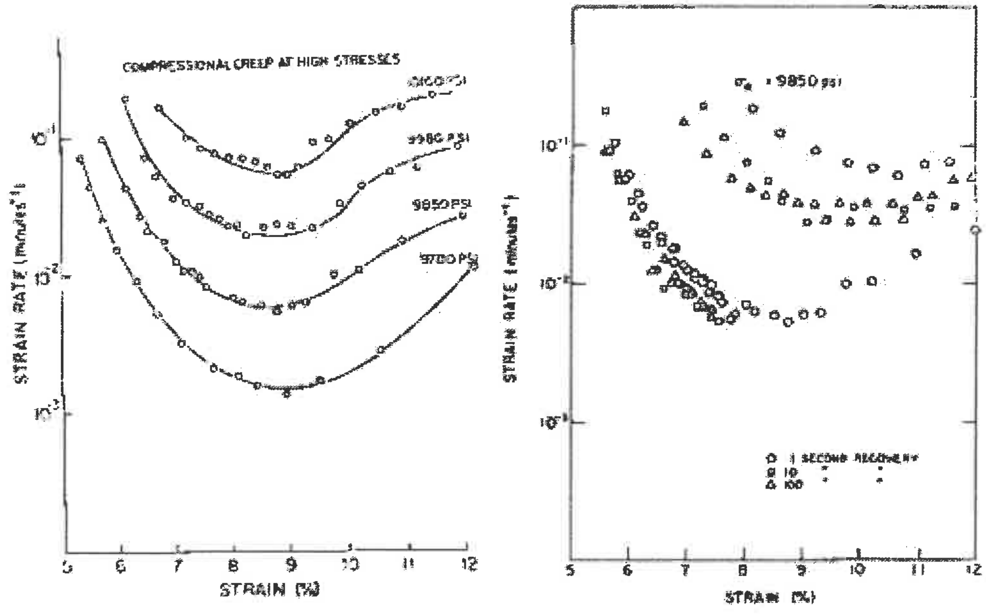

(a)

(b)

Figure 2.20: Relationship between the accumulated strain and the strain rate in creep compression: (a) uninterrupted creep tests at different stresses and (b) creep tests interrupted (1, 10 and 100 seconds) at approximately 7.5% of strain and restarted compared to an uninterrupted creep test at the same stress (Mindel and Brown, 1974).

The relationship between these two different processes in PC has been studied by Mindel and Brown (1973, 1974) at very high stresses and low frequencies. Before discussing the effect of cyclic loading, it is appropriate to describe the behavior under a static load. During creep tests performed in compression at different loading rates, Mindel and Brown (1974) observed an initial decrease in the strain rate followed by an increase. The transition between these two regimes occurred at a critical value of accumulated strain, which value was almost independent of the nominal stress (Figure 2.20a). A very similar behavior was observed in tension (Mindel and Brown, 1973), with the differences being that the critical value of accumulated strain slightly decreased with nominal stress and that the strain rates for a given nominal stress were generally higher than in compression These differences could be explained by an effect of hydrostatic component of stress on the shear deformation.

To explain the transition from a decreasing strain regime to an increasing strain regime, Mindel and Brown (1973, 1974) introduced the concepts of recoverable and persistent strains. The recoverable and persistent strains were experimentally measured by carrying out creep and recovery experiments for different creep times. The recoverable strain was measured as the difference in strain after linear recovery upon unloading. The persistent strain was that non-recovered after a long recovery time. The persistent strain started to be significant when the total accumulated strain during the creep test was slightly lower than the value leading to the minimal strain rate. The recoverable strain is suggested to be associated with the decrease in creep rate and to be proportional to the internal stress. The persistent strain is suggested to be involved with a softening process. The rate of softening should increase with accumulated strain. By employing an equation similar to the Eyring equation for non-linear viscoelasticity (Equation 2.4), a good superposition of all data shown in Figure 2.20a was obtained. The only conclusion from the applicability of this equation was that the creep process was thermally activated and that the activation energy or volume was independent of the accumulated strain.

The strain response obtained by loading programs of two cycles are shown in Figure 2.20b for different unloading times between the two creep loading cycles. Just after reloading, the strain rate during the second cycle was similar to the strain rate immediately after the first loading (Figure 2.20b). A similar effect was observed in a succession of four loading and unloading cycles (Mindel and Brown, 1974) that led to fracture. Measurements of the instantaneous strain indicated that most of the strain recovery occurred during the first second of unloading. Therefore, the internal stress when the specimen is reloaded can be expected to be near zero when the unloading time exceeds one second as was the case. Accordingly, a strain rate just after reloading similar to the strain rate immediately after the first loading cycle can be interpreted by the quasi-absence of internal stresses in both cases.

The fatigue studies of Mindel and Brown (1974) were performed for conditions of high creep stresses and very low number of loading cycles. Jinen (1986, 1987) studied the strain response of short fiber reinforced PA66 subjected to creep loading and to tension-tension stress controlled fatigue. At different nominal stresses in both creep and fatigue, linear relationships were reported on a log-log scale between the accumulated strain and the time or number of loading cycles. This type of empirical relationships have been reported previously in creep (c.f. appendix, section 1A.1.2.5) but not in fatigue. As a difference between the two responses, the strain at creep fracture was almost independent of the nominal cyclic stress; whereas, the maximum or accumulated strain at fatigue fracture decreased linearly as the cyclic stress amplitude decreased.

Apart from inducing the accumulation of strain, axial fatigue can also induce changes in the apparent viscoelastic properties of the polymer. Employing a sinusoidal cyclic load and a loading ratio R of 0.05, Lesser (1995) studied the dynamic response of two semicrystalline polymers: polyacetal (T_g~70°C) and PA66 conditioned at 50% humidity (in air at room temperature for 8 weeks). In all cases, a gradual decrease in the loss modulus (E'', c.f. appendix, section 1A.1.2.2) was observed throughout the fatigue life. However, whereas the storage modulus, E', of polyacetal was found to decrease throughout the fatigue life, that of PA66 showed an initial decrease followed by an increase. The transition between a decreasing E' and an increasing E' corresponded to a time at which a rapid increase in the accumulated strain was noted. During that transition, the irreversible work (area of the hysteresis loop) reached a maximum value. Under the conditions tested, the T_g of PA66 was probably just below the testing temperature, which could have resulted in particular deformation events.

A loss in E' as a result of mechanical fatigue of polyacetal has also been reported by Mizuno, Kawagoe, Qui and Morita (1997) and by Lazzeri, Marchetti and Levita (1997). The latter authors also reported a slight decrease in the irreversible work throughout the fatigue life. In the case of drawn HDPE, Jo, Takahara and Kajiyama (1994) found an increase in E' and a decrease in E'' during tension-tension strain-controlled tests performed in the temperature range from 27 to 77°C. Bouda, Zivlar and

Staverman (1976) also reported a decrease in E'' in PMMA and PA66. Jones and Lesser (1998) reported a gradual decrease in both E' and E'' during tension-tension load control fatigue in PP. In general, cyclic loading in tension-tension induces a reduction in E'', whereas, E' can decrease, increase or do both.

Paradopoulos and Korovesis (1996) studied the stress-strain response of PA6 in tension-tension (mean stress of 14 MPa and stress amplitude of 3 MPa) and compression-compression loading. The moisture conditioning was not specified but, with a Young's modulus of 3300 MPa and a yield stress of 78 MPa, one can expect a condition near dry-as-molded. In the compression experiments, a decrease in area of the hysteresis loop was observed as a result of cycling. In both tension-tension and compression-compression experiments, fatigue resulted in an increase in the post-fatigue tensile Young's modulus. However, the increase was more pronounced in the case of tension-tension loading. This difference was employed to suggest that cyclic loading in tension induces more internal damage than cyclic loading in compression.

Care must be taken when comparing the effect of cyclic loading on the dynamic storage modulus E' measured *in-situ* and on the post-fatigue tensile Young's modulus. By assuming that strain recovery is not completed in the time period between unloading and tensile testing, the increase in the tensile Young's modulus may originate from stored internal stresses or energy.

2.3.2.3 Microstructural Changes and Damage Accumulation

At the same time that amorphous or semicrystalline polymers deform by processes involving the relative movement between chains (potential mechanisms outlined in section 0), more apparent microstructural changes such as chain scission, destruction of crystals, crystallization, voiding and/or crazing can also occur. The extent to which these changes affect the stress-strain response is not clearly established; however, these more apparent changes can be directly quantified through measurements of molecular weight, degree of crystallinity, specimen volume variation, TEM observations, and/or mechanical properties (e.g. effect on E', E'' or on the post-fatigue tensile Young's modulus described in the previous section).

Post-fatigue measurements of the melt viscosity of three different polyacetal resins enabled Lazzeri, Marchetti and Levita (1997) to conclude that fatigue induced a large decrease in the molecular weight. In contrast, Li, Hristov, Yee and Gidley (1995) reported no significant effect of fatigue damage on the molecular weight of PC. No other information regarding such a possible change in molecular weight was found in the open literature. It cannot be established whether the reduction in molecular weight reported by Lazzeri, Marchetti and Levita (1997) was a particularity of the material employed.

Trotignon and Verdu (1987a, 1987b) reported small but significant increases in the crystallinity indexes (measured by DSC) resulting from flexural fatigue of PP. In the sub-skin of their injection-molded specimens, they also found a decrease in the crystallite orientation index (determined by wide angle X-Ray spectroscopy). Lesser (1995) also reported DSC results suggesting fatigue-induced crystallization in polyacetal and PA66. However, the differences were not necessarily significant in this study.

Crystallization during fatigue is not necessarily a deleterious process; however, its occurrence may affect the mechanical response of the polymer previously discussed. Also, the presence of crystals in an amorphous matrix may favor void nucleation in regions of stress concentration. For instance, Jo, Takahara and Kajiyara (1994) explained the increase in the fatigue resistance of HDPE when the temperature increased from 50°C (α transition temperature of the crystals) to 77°C (β transition temperature of the crystals) by a decrease in the difference between the deformability of the phases.

Contrary to crystallization, the formation and growth of voids or crazes is a microstructural change that is most likely to reduce the resistance of the material to crack initiation. Yee, Gidley and coworkers (see specific references below) carried out experiments in an attempt to characterize the microstructural changes which act as the precursor to craze initiation in PC. By employing positron annihilation lifetime spectroscopy (Liu, Gidley and Yee, 1992), they compared the effect of physical aging followed by fatigue to the effect of physical aging alone. They showed that fatigue in well-aged PC specimens induces an increase in the size of the voids as well as a decrease in the number density of voids. On the opposite side, physical aging alone was found to decrease the size of the voids. As measured by fracture toughness tests, both fatigue loading and physical aging (thermal treatment below T_g that promotes a reduction in the portion of free volume) can induce embrittlement (Li, Hristov, Yee and Gidley, 1995). Whereas the density of the material and the yield stress increased as a result of physical aging, fatigue at different stress amplitudes generated a small but significant decrease in density and a marginal increase in the yield stress. The authors concluded that the embrittlement resulting from fatigue loading is likely to result from the formation of "procrazes", which are the primary forms of crazes.

In the study of the formation and growth of procrazes by TEM (Hristov, Yee and Gidley, 1994), the observations suggested that the critical size for a stable void or "procraze" is approximately 50-60 nm. Also, inclusion particles with diameters in the range from 50 to 100 nm were found to be effective craze nucleation sites. The similarity between fatigue induced crazes and high temperature crazes in PC, suggested that chain disentanglement should play an important role in the formation and growth of a procraze. Cyclic loading is likely to generate regions of reduced entanglement density that could be preferential sites for procraze nucleation.

Bouda, Zivlar and Staverman (1976) previously proposed a slightly different sequence of events as the precursor to void nucleation in glassy polymers. They employed the decrease in E'' as experimental evidence for a process of localized volume contraction during fatigue. They proposed that a non-uniform volume contraction creates local internal tensions which are relaxed gradually by yielding and formation of voids. Their argument of local volume contraction based on the decrease in E'' would be seriously undermined if one could prove that the accumulation of internal energy or stress can also reduce the damping capacity.

Voids are also formed during fatigue of semicrystalline polymers. Lesser (1996) measured a significant dilatational volume variation in tension-tension axial fatigue on a polyacetal copolymer ($T_g \sim 70°C$). Void formation was also suggested by Lazzeri, Marchetti and Levita (1997) as the origin for the strong dependence for the post-fatigue fracture toughness on the stress amplitude in several other polyacetal resins. In these experiments, a decrease in the post-fatigue tensile yield stress was measured. For this reason, the decreased fracture toughness cannot be attributed to a yield stress effect on the plastic zone size.

During tension-compression fatigue in PP, a significant dilatational volume variation was measured by Zok and Shinozaki (1987). This dilatation was also attributed to the formation of voids and crazes. Theses crazes were observed by TEM. They were relatively uniformly spaced and more sharply defined than other crazes formed by a single uniaxial extension at larger strain. At high magnification, each craze appeared segmented. This apparent segmentation can be interpreted in light of a recent study of Jones and Lesser (1998) on the evolution of the crazes with time during fatigue. These authors showed a progressive decrease in the craze number density and an increase in the size of the crazes with the number of tension-tension load controlled fatigue cycles. These observations suggest that crazes can grow by coalescence of previously formed procrazes or small crazes.

Relationships between the macroscopic response and the microstructural changes have not been clearly established in the open literature. With the exception of the variation in volume, most of the other variations in the mechanical response are probably a consequence of the relative movement between the chains and of the variations in the internal energy or stresses. These events are more difficult to characterize but they can have an effect on the mechanism of void nucleation.

A way to characterize the overall resistance to crack initiation of a material is to consider its endurance limit. This value determines the critical stress level below which no crack initiation occurs, independently of the number of loading cycles. Trotignon, Verdu, Martin and Morel (1993) measured an important increase in the endurance limit of polyetherimide (PEI) and polysulphone (PSU) when the molding process was changed from compression molding to injection molding. The authors interpreted this result by an increase in the resistance to craze initiation due to an initial molecular orientation. However, a skin/core effect (c.f. appendix, section 1A.1.1.2) might have resulted in a change in the position of the crack initiation site from the external surface to the bulk. For this reason, the resistance of the entanglement network to the initiation, growth and coalescence of microscopic voids to form cracks cannot necessarily be obtained from the endurance limit.

The multiple changes that occur during fatigue testing can be different depending on the region within the bulk specimens. This can be particularly true if the specimens are injection molded due to their skin, sub-skin and core regions. By carrying out tensile tests on thin foils (approximately 85 μm thick) microtomed from fatigued and non-fatigued 33 wt% short glass fiber reinforced PA6 specimens, Horst and Spoormaker (1996) found a more important effect of fatigue on the tensile strength for the material located in the subskin (or shell region). However, this difference in the level of damage might have been accentuated by the presence of fibers. As will be described in the next subsection, reinforcement particles or fibers can have an effect on the micromechanisms of damage associated with fatigue.

2.3.3 Effect of Inorganic Fillers

Inorganic particles added to semicrystalline polymers increase the stiffness and, when the bonding is strong, the strength. The effect of these particles on the fatigue properties have been characterized by several investigators.

2.3.3.1 Fibers

Fibers can have several effects on the fatigue life and the mechanisms of fracture of non-notched specimens. Horst and Spoormaker (1997) classified these mechanisms in two categories. In some cases, general degradation of the material occurs without the presence of cracks. During this degradation, there is decohesion of the interface due to its poor strength or due to a large difference in the deformability of the materials. The post-fatigue tensile strength is largely decreased. This behavior has been observed in a PE filled with glass fibers and in an equilibrium water conditioned PA66 filled with carbon fibers (references in Horst and Spoormaker, 1997).

The second class of mechanisms of fatigue fracture involve crack initiation and FCP. The following discussion will concentrate on the effect of well-bonded glass-fibers on the fatigue behavior of PA66 or PA6. In this system, the micromechanisms of FCP varies depending on the orientation of the long axis of the fibers and the crack propagation direction and on the ductility of the matrix. Void initiation is reported at the fiber end when the long axis of the fiber is parallel to the tensile direction (Horst and Spoormaker, 1997). For the orientation perpendicular to the long axis, the initiation is likely to occur in micro-locations where the adhesion is relatively poor, regions that invariably exist even in well-bonded composites (Lang, Manson and Hertzberg, 1987).

After crack propagation with the long axis of the fibers in the crack plane, the fracture surface presents three types of regions: small regions where the fiber surfaces are free from polymer, other small regions where the fiber surfaces are covered with remnants of stretched polymer and regions free from fibers where the matrix has been highly stretched to form ligaments. These observations support the following sequence of events involved in fatigue crack propagation (Lang, Manson and Hertzberg, 1987): localized decohesion of the interface to form microvoids, partial coalescence and growth of these microvoids, shear deformation and final fracture of the matrix under plane stress conditions.

When the long axis of the fibers is perpendicular to the crack propagation plane, fractographic observations by Lang, Manson and Hertzberg (1987) revealed that crack propagation in the matrix, pull out of the fibers, and fracture of the fibers upon unloading was the dominant sequence of events during crack propagation. However, most of the observations reported were carried out in the dry state. In the conditioned state, fractographic and post-fatigue morphological observations of the damage zone by Horst and Spoormaker (1996, 1997) revealed that the fibers can act as bridges and prevent or retard crack growth. However, they stated that the effect was not observed in the dry state. It can be concluded that the bridging effect is limited to cases where the ductility of the PA66 matrix is sufficient.

Karbhari and Dolgopolsky (1990) reported a transition in the mode of fatigue fracture of the PA6 matrix as the cyclic stress intensity factor increased during the test. The fracture of the matrix was microscopically brittle in the initial regime; whereas, drawn ligaments were observed in what was called the microscopically ductile regime. The transition between the two regimes was correlated with an increase in the resistance to crack propagation as measured employing the crack layer approach.

In quantitative terms, the effect of reinforcement by glass fibers appeared correlated with the changes in Young's modulus and in tensile strength. Wyzgoski and Novak (1991) expressed the resistance to FCP in terms of the range of strain energy release rate ($\Delta G = \Delta K^2/E$). With dry-as-molded specimens, they observed a similar resistance of a non-filled PA66 and of a 33 wt% fiber reinforced PA66 tested under conditions where the long axis of the fibers was respectively parallel or perpendicular to the tensile axis. Horst and Spoormaker (1996, 1997) reported that the S-N curves of a 33 wt% fiber reinforced PA6 tested with three different fiber orientation were quite similar when the maximum cyclic stress was normalized by the tensile strength. However, the normalized resistance of the non-filled PA6 was higher.

2.3.3.2 Other Mineral Particles

Trotignon, Demdoum and Verdu (1992a, 1992b, 1993) carried out flexural strain-controlled fatigue testing on mineral particle-filled PP and dried PA6. At a given strain amplitude, the fatigue lifetime was always lower for particle-filled polymers than for the non-filled matrix. For the tests carried out on PP (Trotignon, Demdoum and Verdu, 1992 and 1992b), small changes in the flexural modulus were noted between the different specimens but the small amount of fatigue data and the fact that other parameters varied between the specimens (e.g., the nucleating effect of the particles) did not enable quantitative conclusions to be drawn. For the tests carried out on dried PA6 (Trotignon, Demdoum and Verdu, 1993), the type of filler appeared to have a more profound effect on the fatigue lifetime than its concentration (in the range from 1 to 5 wt%; c.f. table 2 in Trotignon, Demdoum and Verdu, 1993). As a result of filler addition, a small change was observed in the stiffness of the specimens (inferred from the stress response). Due to the scatter in the data, it is not clear that further conclusions can be drawn.

Finally, Yamashita and coworkers (Yamashita, Takahara and Kajiyama, 1999; Yamashita, Higashi, Komatsu, Takahara and Kajiyama, 1998) studied the fatigue resistance of dried PA6NC and non-filled PA6, but the regime investigated was the thermal regime with possibly one point in the mechanical regime (Figure 2.21). It is the only study on fatigue of PA6NC found in the open literature.

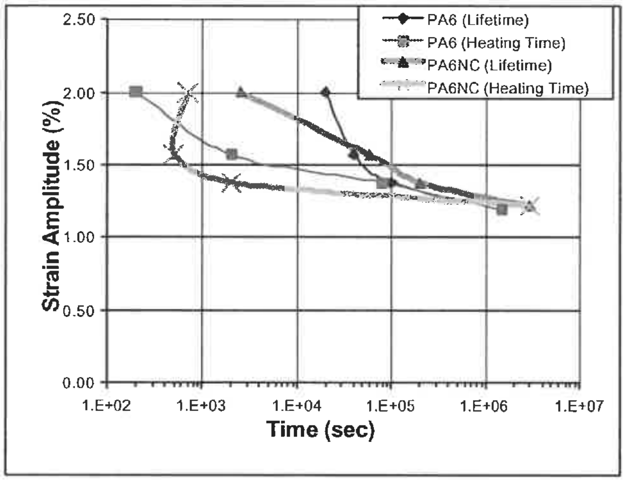

Figure 2.21: Stress versus number of loading cycles to fracture (S-N) curves of PA6 and PA6NC (dried under vacuum at 110^{0}C for 8h) in tension-compression strain controlled axial fatigue at 6.71Hz (Data: Yamashita, Takahara and Kajiyama (1999) for PA6NC and Yamashita, Higashi, Komatsu, Takahara and Kajiyama (1998) for PA6).

3 MATERIALS AND FATIGUE EXPERIMENT METHODOLOGY

The main objective of the literature review presented in the previous section was to support the interpretation of the experimental results. In this section, the characteristics of the materials employed for the fatigue experiments and the fatigue testing methodologies are described.

3.1 MATERIALS

The two materials employed were a PA6 containing 2-wt% of montmorillonite (commercial grade 1015C2), here referred to as PNC, and a non-filled PA6 (commercial grade 1015B), here referred to as PA6. Both materials were supplied by UBE Industries in the form of pellets. UBE Industries employed an *in situ* intercalative polymerization process (c.f. section 2.2.2) to prepare the PNC. The molecular weight and molecular weight distribution of PNC and PA6 are expected to be the same.

Small specimens (approximately 1 mm thick) of both materials were prepared by compression molding (Carter Laboratory Press model M, mold temperature of 230°C, preheating of pellets for 6 minutes in the mold, two pressing cycles at 2000 psi, a last pressing cycle at 2500 psi, fast cooling through water circulation) in order to characterize the dynamic properties as a function of temperature and moisture content. The tests were carried out employing a rheometric mechanical spectrometer at a frequency of 1 or 10 Hz and at a constant rate of temperature increase of 2°C/min. The moisture content, dried or equilibrated at 50% humidity and room temperature, was controlled through two different conditioning procedures: drying four days under vacuum at 80°C or immersion in a solution of potassium acetate for 4 days at approximately 80-90°C (ISO 1110-1975).

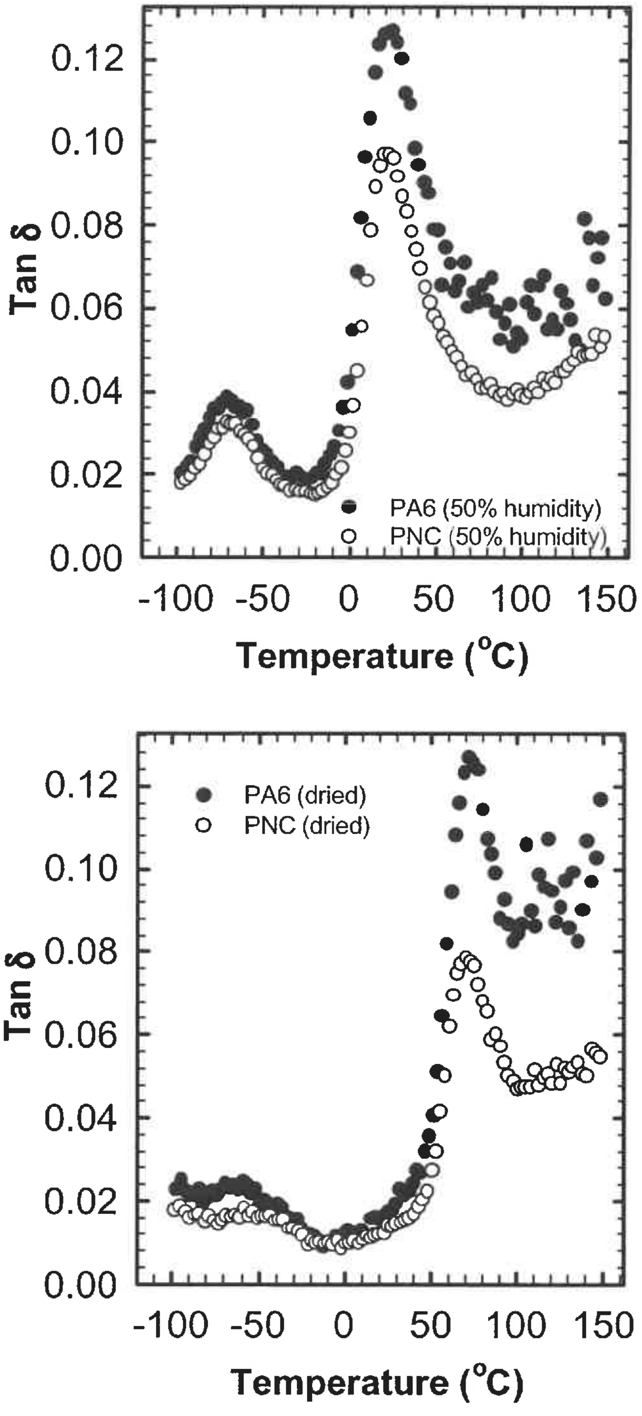

Figure 3.1: Tan δ as a function of temperature for PNC and PA6, conditioned at a) 50% humidity or b) dried, tested at a frequency of 1 Hz.

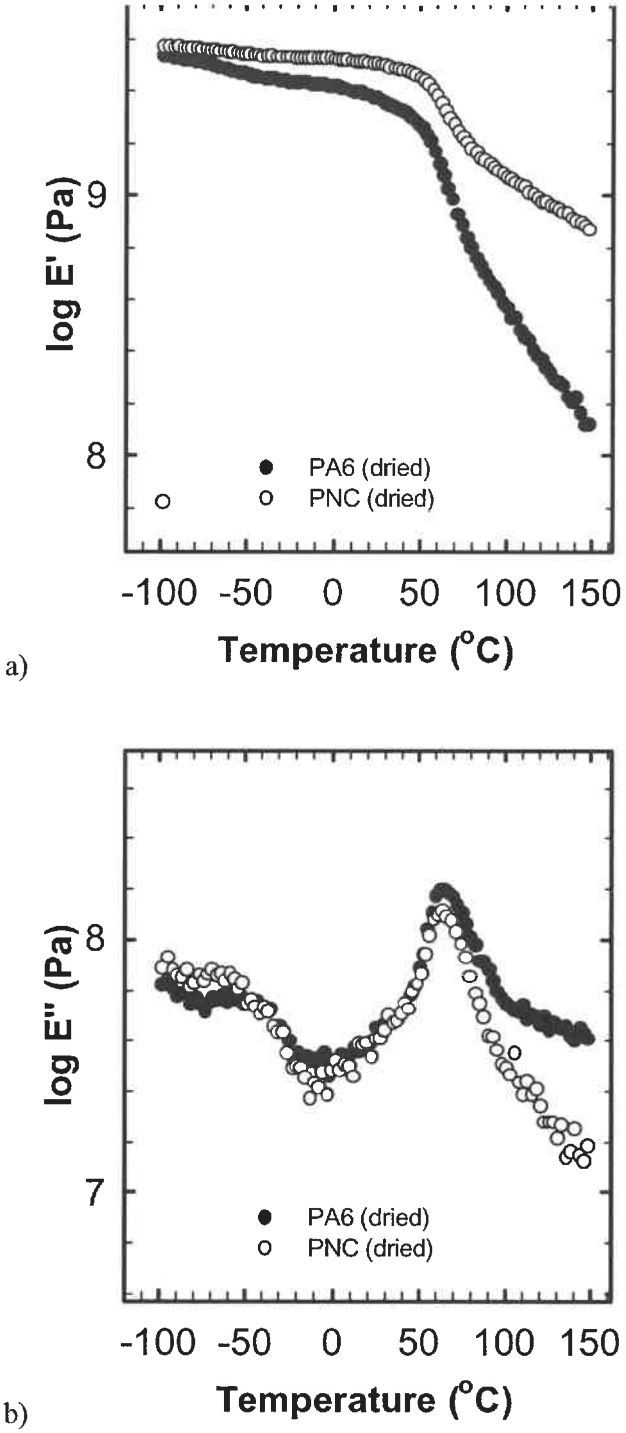

Figure 3.2: Variations of a) E' and b) E'' as a function of temperature for dried PA6 and PNC tested at a frequency of 1 Hz.

The definition of the viscoelastic parameters and a brief summary on the relationships between the molecular mobility and the transition temperatures can be found in appendix (section 1A.1.2.2). Figure 3.1 presents the evolution of tan δ with temperature for PNC and PA6 tested at a frequency of 1 Hz. Even though the value of T_g was estimated from the peak value of E'' (see following paragraph), it also approximately corresponds to the peaks of the tan δ curves. The effect of nanoparticles on the damping capacity is less pronounced below than above T_g. Humidity decreases the T_g from above to below room temperature.

Figure 3.2 presents the evolution of the storage modulus E' and of the loss modulus E'' as a function of temperature for dried PNC and dried PA6 tested at a frequency of 1 Hz. Even at low temperatures, some reinforcing effect of the particles on E' can be noted. The effect of the nanoparticles to reduce the parameter E'' is important above but not below T_g. At a frequency of 1 Hz, T_g was 66°C for dried PNC, 64°C for dried PA6, 10°C for conditioned PA6 and 15°C for conditioned PNC. Employing a frequency of 10 Hz increased these values by typically 2°C.

3.2 TEST SPECIMENS

For the tensile and fatigue tests, the specimens were injection molded. The pellets of PNC and of PA6 were dried for 2 days at 80°C under vacuum prior to injection molding. Injection molding was carried out at two different melt profile temperatures and at a constant mold temperature of 80°C. In the first and second molding batches (batches 1 and 2), the final melt temperature was set at 250°C. At that melt temperature, impurities were either detached from the inner walls of the injection system or formed by degradation of the material. Some of these impurities were so large that it was possible to detect them by careful visual inspection. Because of their higher transparency, the detection was easier with the PA6 specimens. During the third and last molding batch (batch 3), a decrease in the final melt temperature to 225°C reduced considerably the presence of impurities. Unless otherwise specified, the axial fatigue test results reported in this thesis were obtained from batch 3.

Because of the hygroscopic nature of PA6, efforts were made to control the humidity content of the specimens. The as-molded specimens were kept in plastic bags (under vacuum or not) in order to prevent humidity pick-up. After a variable period of time, they were dried for two weeks at 80°C under vacuum in order to remove any trace of humidity resulting from processing and storing. In most cases, the weight of the specimens was monitored daily during drying. The weight loss during the first week varied widely, depending on the way that the as-molded specimens were stored. After a week of drying, the weight lost varied almost linearly with time and was very small. After drying, the specimens were kept under vacuum at room temperature for a variable period of time prior to testing. All the specimens were directly molded to their final geometry.

Axial fatigue specimens had a nominal thickness of 3.1 mm and their gauge section width and length were respectively 10 mm and 14 mm. All the specimen dimensions are shown in Figure 3.3. The design was based on the standard practice ASTM E 606, which is intended to the determination of the fatigue properties of nominally homogeneous materials by the use of uniaxially loaded test specimens (ASTM, 1998), but the radius of curvature has been increased to the one specified by the standard test method D 638, which is intended to the evaluation of tensile properties of plastics (ASTM, 2002). Fatigue crack propagation specimens were machined from 5 mm thick plates, which were injection molded according to the molding parameters of batch 1 and 2. Two sets of similar specimens were machined from the plates. The dimensions of the second set of specimens, shown in Figure 3.4, followed the ASTM E-647 standard test method. The dimensions of the first set of specimens were the same as for the second set except for the position of the holes. The distance between the center of the holes and the top of the specimen was 11 mm instead of 15 mm.

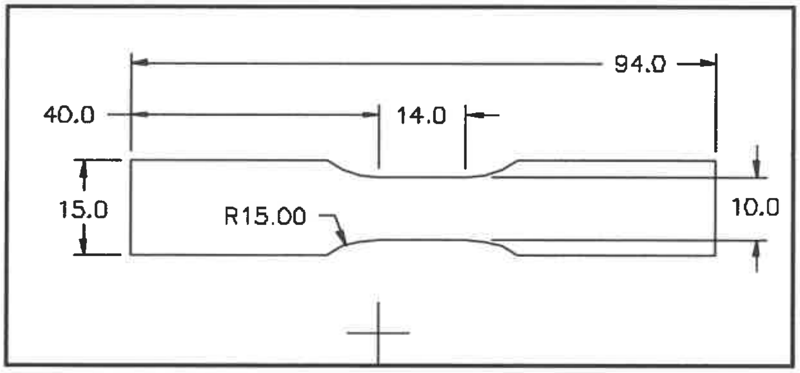

Figure 3.3: Geometry of the axial fatigue specimens (all dimensions in millimeters).

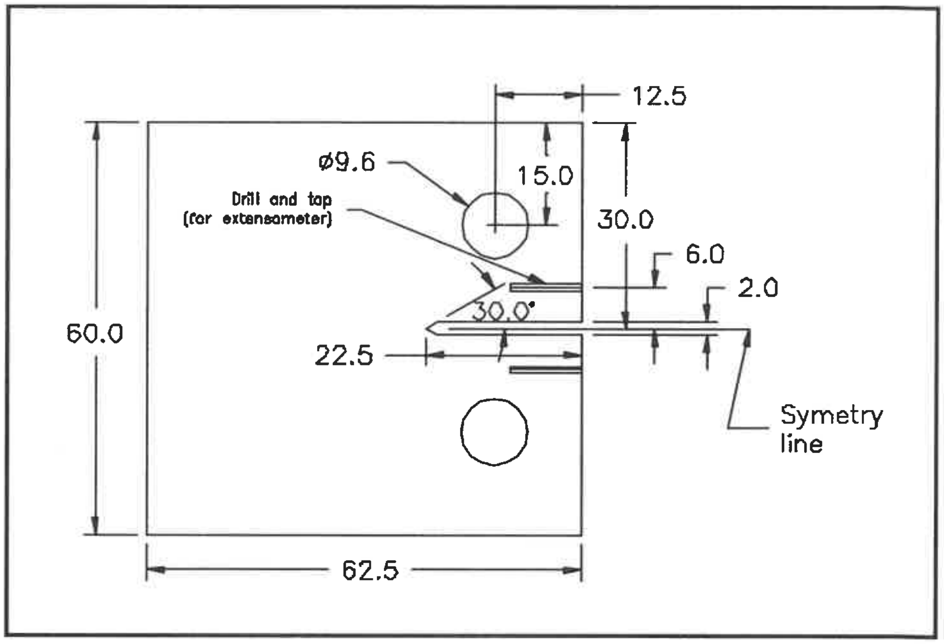

Figure 3.4: Geometry of the fatigue crack propagation specimens (all dimensions are in millimeters).

3.3 MORPHOLOGY AND TENSILE PROPERTIES OF THE SPECIMENS

It is difficult to reveal the spherulite structure of bulk PA6 samples by etching polished surfaces. Perrin (2002) made several attempts. In the best cases, the boundaries of the spherulites were resolved but it was not possible to obtain details on the crystallite arrangement within these spherulites. During scanning electron microscopy (SEM) observations on polished and gold-palladium coated specimens, the damage generated by a relatively high current or a long exposure time enabled to obtain a contrasted image of the inner structure of the spherulites. The images obtained (Figure 3.5a) clearly suggest a radial alignment of crystallite domains in PA6. By employing this same electron beam damage procedure with very similar parameters on PNC samples, the images obtained (Figure 3.5b) did not provide any indication of spherulites with diameter of the same order of magnitude. The observations were made near the middle of the specimens and the observation planes were nearly perpendicular to the width direction. The electron beam etching procedure might have induced some artifacts. However, it appears that that the polymer structure at the supermolecular level is different in PNC than in the non-filled PA6. The structure of PNC could be similar to the structure of PA12-based nanocomposite, for which a preferential alignment of the crystallites perpendicular to the preferential orientation plane of the montmorillonites has been reported (c.f. section 2.2.3). This possibility will be recalled in the discussion.

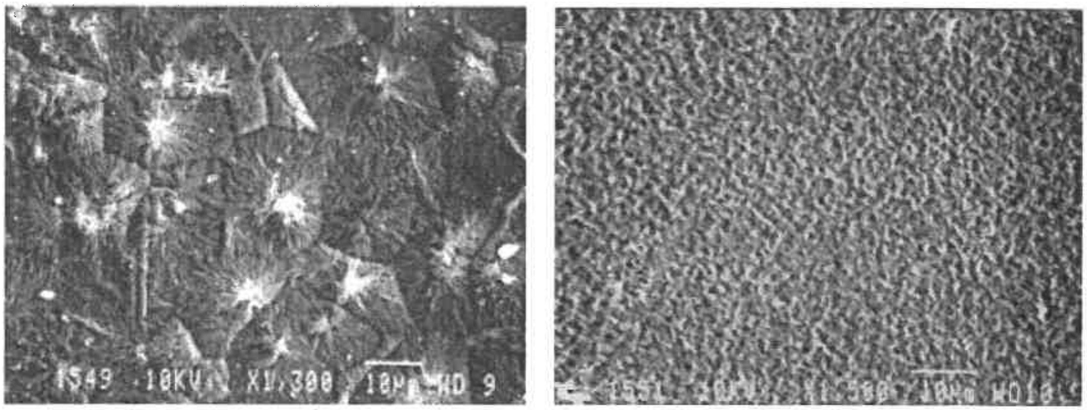

a) b)

Figure 3.5: Bulk microstructure of a) PA6 and b) PNC observed on polished and beam damaged surfaces (observations near the middle of the specimens; observation planes perpendicular to the width direction)

For the same materials (processed at the same time as the specimens from batch 1) and conditioned following the same procedure, tensile test results indicated values of Young's modulus, UTS, strain at UTS and strain at fracture respectively of 4.1 GPa, 100 MPa, 4% and less then 10% for PNC and respectively of 2.7 GPa, 74 MPa, 5% and 175% for PA6. These results are also reported in Table 3.1.

Table 3.1: Tensile properties of PNC and PA6 specimens from batch 1 (Bureau, Denault and Glowacz, 2001).

	PNC	PA6
Young's modulus	4.1 GPa	2.7 GPa
Ultimate Tensile Strength (UTS)	100 MPa	74 MPa
Strain at UTS	4%	5%
Strain at fracture	< 10%	175%

3.4 TESTING METHODOLOGY FOR AXIAL FATIGUE

Axial load-controlled fatigue tests were carried out employing an Instron 8511 or an MTS 415 servo-hydraulic mechanical testing machine. Axial loading was preferred to loading in bending since the former provides the possibility of employing extensometers to measure the strain in both the longitudinal and the long transverse directions. It has the disadvantage of increasing the susceptibility of the specimen to macroscopically ductile fracture (c.f. section 1.3.2). The extensometer for strain measurement in the long transverse direction (Instron model 2640-007) was employed only for the tests on the Instron 8511 machine. On this machine, the gauge length of the longitudinal extensometer (Instron model 2620-827) was set at 12.6 mm for the tests employing specimens from batch 2 and at 8 mm for the tests employing specimens from batch 3.

Except for one particular test where a reversed loading mode was applied, the load or R-ratio ($R = \sigma_{min}/\sigma_{max}$) was maintained constant at 0.1. Unless otherwise specified, a sinusoidal cyclic waveform and a cycling frequency of 5 Hz were employed. In an attempt to minimize the duration of the test program, other types of waveforms were tried. For all the tests carried out on the Instron 8511 machine, a linear ramp was employed to increase the load from zero to the minimum cyclic stress within 1 to 5 seconds. Cycling started when the minimum load was reached. The load thus increased during the first half of every loading cycle while the load decreased during the second half.

During most of the tests carried out with specimens from batch 2, a K-type thermocouple was employed to monitor variations in the specimen surface temperature during cycling. Subsequently, the macroscopic mode of fracture was employed to discriminate between the fatigue regimes. For the first few tests, glue ("crazy glue") was employed to attach the junction of the thermocouple to the specimen surface. Subsequently, the junction was retained on the surface by a rubber band. Also, for the first few tests, the extensometer knifes and the grips were directly in contact with the specimen. Subsequently, a thin rubbery plastic band (approximately 0.25 mm thick) was installed between the extensometer knifes and the grips as protection to avoid surface crack initiation at these locations.

A data acquisition rate of approximately 50 Hz was employed for the tests carried out on the MTS 415 machine. This rate was not sufficient to enable the calculation of the dynamic properties parameters (c.f. section 3.5). For these tests, only the fatigue lifetime results are reported here. For the tests on the Instron 8511, the signals from the load cell and from the extensometers were collected by the controller and transferred to a computerized data acquisition system at a frequency of 500 Hz during preprogrammed loading cycles. Wavemaker software (Series IX Software Suite, v1004, Instron, 1996) was employed to control the test. For each preprogrammed loading cycle, the software stored a set of approximately 100 data points. Before typically 2 million cycles of loading, the first data points of each set corresponded approximately to the beginning of the third quadrant of the waveform (point of minimum stress). After typically 2 millions cycles, the first data point of each set corresponded to other positions on the waveform (often at the beginning of the fourth or even the first quadrant). The capacity of the computer or an error in the software are proposed as potential origins. In order to carry out regressions on the data at given positions on the hysteresis loops, it was at time necessary to join the data points from the beginning and the end of a set. This procedure did not appear to have any consequence on the variability in the values of the strain response parameters and of the dynamic properties parameters (see section 3.5) calculated employing a home designed Microsoft Excel "macro" program, which has been written in Microsoft Visual Basic.

3.5 STRAIN RESPONSE AND DYNAMIC PROPERTIES PARAMETERS

The four prime parameters employed to characterize the strain response were the longitudinal strain amplitude (ε_{Amp}), the longitudinal accumulated strain (ε_{Acc}), the rate of strain accumulation ($\dot{\varepsilon}_t$) and the accumulated volume strain ($\Delta V/V_{0,\ Acc}$). These parameters were calculated from the following relationships:

Equation 3.1:
$$\varepsilon_{Amp} = \frac{1}{2}(\varepsilon_{Max} - \varepsilon_{Min}) \quad ,$$

Equation 3.2
$$\varepsilon_{Acc} = \varepsilon_{Min} - \varepsilon^{1}_{Min} \quad ,$$

Equation 3.3
$$\dot{\varepsilon}_t = \frac{\varepsilon_{t+1} - \varepsilon_{t-1}}{N_{t+1} - N_{t-1}} \quad ,$$

Equation 3.4
$$\frac{\Delta V}{V_0} = (1+\varepsilon_L)(1-\varepsilon_W)^2 - 1 \quad ,$$

Equation 3.5
$$\left(\frac{\Delta V}{V_0}\right)_{Acc} = \left(\frac{\Delta V}{V_0}\right)_{Min} - \left(\frac{\Delta V}{V_0}\right)^{1}_{Min} \quad ;$$

where ε_{Max} is the maximum longitudinal strain in a single cycle, ε_{Min} is the minimum longitudinal strain in a single cycle, the superscript "1" indicates the values measured during the first loading cycle, $\Delta V/V_0$ is the instantaneous volume strain, ε_L is the instantaneous longitudinal strain, ε_W is the instantaneous transverse strain (i.e. strain in the width or long-transverse direction), and $\Delta V/V_{0,\ Min}$ is the minimum volume strain in a single cycle. When the tests were carried out employing the option "amplitude control" on the Instron controller, a decrease in the minimum cyclic stress of the order of 1 MPa was noted during the first 100 cycles. For this reason, a correction on the accumulated strain has been applied in most cases by employing, instead of Equation 3.2, the following equation:

Equation 3.6

$$\varepsilon_{Acc} = \varepsilon_{Min} - \varepsilon^{1}_{Min}\frac{\sigma_{Min}}{\sigma^{1}_{Min}} \quad ;$$

where ε_{Min} is the minimum longitudinal strain in a single cycle, the superscript "1" indicates the values measured during the first loading cycle and σ_{Min} is the minimum cyclic stress. Finally, for the few tests carried out in tension-compression, the accumulated strain was calculated from the above equations but also from the following equation:

Equation 3.7

$$\varepsilon_{Acc} = \varepsilon_{Max} - \varepsilon^{1}_{Max}\frac{\sigma_{Max}}{\sigma^{1}_{Max}} \quad ;$$

From the time-stress-strain response, numerous calculations have been made to characterize the evolution of several parameters of the dynamic properties. The three prime parameters considered were the average width of the hysteresis loops (w_{Hyst}), the loss tangent ($tan\ \delta$) and the storage modulus (E'). These parameters were calculated from the following relationships:

Equation 3.8:

$$w_{Hyst} = \frac{1}{3}\sum_{i=20,50,80}\left(\frac{(\sigma_{Min} + i\% * 2\sigma_{Amp}) - b_{i,increase}}{m_{i,increase}} - \frac{(\sigma_{Min} + i\% * 2\sigma_{Amp}) - b_{i,decrease}}{m_{i,decrease}}\right),$$

Equation 3.9: $$\Delta t = \frac{(\sigma_{Min} + 50\% * 2\sigma_{Amp}) - b_{t,increase}}{m_{t,increase}} - \frac{(\sigma_{Min} + 50\% * 2\sigma_{Amp}) - b_{t,decrease}}{m_{t,decrease}} ,$$

Equation 3.10:

$$\delta = \Delta t * 2\pi * f \quad ,$$

Equation 3.11:

$$E' = \frac{\sigma_{Amp}}{\varepsilon_{Amp}}\cos\delta \quad ;$$

where σ_{Min} is the minimum cyclic stress, σ_{Amp} is the stress amplitude, $m_{i,\ increase}$ and $b_{i,increase}$ are respectively the slope and the ordinate at zero strain of the linear regression between stress and strain employing the seven data points from the increasing part of the cycle that were the nearest to the stress target (of σ_{Min} + $i\%*2\sigma_{Amp}$), $m_{i,\ decrease}$ and $b_{i,decrease}$ are the equivalent from the decreasing part of the cycle, Δt is the time delay of the strain relative to the stress calculated from the symmetry points for the curves (symmetry points estimated at σ_{Min} + σ_{Amp} and ε_{Min} + ε_{Amp}), $m_{t,increase}$ and $b_{t,increase}$ are respectively the slope and the ordinate at zero time of the linear regression between stress and time employing the seven data points from the increasing part of the cycle that were the nearest to the stress target (of σ_{Min} + $50\%*2\sigma_{Amp}$), $m_{t,decrease}$ and $b_{t,decrease}$ are the equivalent from the decreasing part of the cycle, f is the frequency, and ε_{Amp} is the strain amplitude.

The apparent plastic strain ($\varepsilon_{Pl}MaxInc$) was one of the other parameters calculated by the "Excel Macro" program. The calculation was based on the relationship

Equation 3.12: $$\varepsilon_{Pl}MaxInc = \varepsilon_{Max} - \frac{\sigma_{Max} - b_{50\%,increase}}{m_{50\%,increase}} \ ;$$

where ε_{Max} is the maximum cyclic strain, σ_{Max} is the maximum cyclic stress, and $m_{50\%,increase}$ and $b_{50\%,increase}$ are respectively the slope and the ordinate at zero strain of the linear regression between stress and strain employing the seven data points from the increasing part of the cycle that were the nearest to σ_{Min} + $50\%*2\sigma_{Amp}$. Some results from tests carried with specimens from batch 2 were presented in a previous report (Bellemare, PFE1, Ecole Polytechnique, 2001). These results as well as the subsequent results obtained on specimens from batch 3 presented a considerable amount of scatter. This scatter is likely to originate from the imprecision in the values of ε_{Max} and σ_{Max} associated with the data acquisition rate. For this reason, the results are neither presented nor discussed here. With the current data, the deviation from linearity could probably be best described by the difference between $m_{20\%,increase}$ and $m_{80\%,increase}$ (the slope from a linear regression between the stress and strain at stress targets of respectively σ_{Min} + $20\%*2\sigma_{Amp}$ and σ_{Min} + $80\%*2\sigma_{Amp}$).

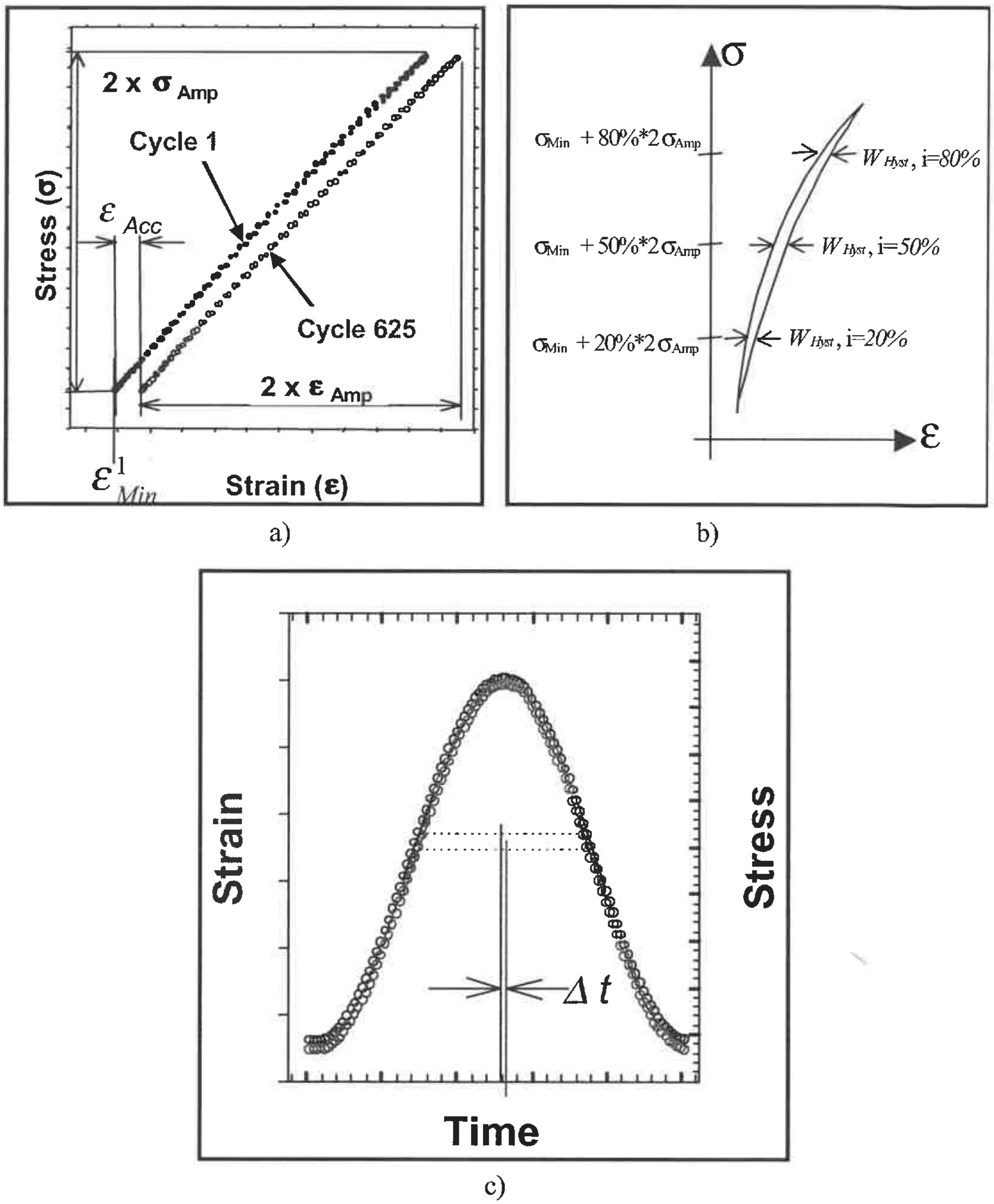

a)

b)

c)

Figure 3.6: **Visual representation of some of the parameters employed to characterize the macroscopic response: a) hysteresis loops from experimental data, b) schematic view of an hysteresis loop and c) real stress-time and strain-time response over a single loading cycle (beginning at the third quadrant).**

3.6 TESTING METHODOLOGY FOR FATIGUE CRACK PROPAGATION

The fatigue crack propagation tests were conducted on the Instron 8511 servo-hydraulic machine at a frequency in the range from 10 to 20 Hz and at a loading ratio R of 0.1. Except for one test, a razor blade cut was introduced at the tip of the notch just prior to testing. An extensometer was employed to measure the crack opening displacement. During testing, the crack advance was automatically calculated by the software from the cyclic compliance response of the specimen. The initial ΔK value was in the range from 0.4 to 0.9 MPa $m^{1/2}$ and the constant ΔK gradient was in the range from 0.04 mm^{-1} to 0.14 mm^{-1}. In the results section, the actual values of the parameters for which a range is given here are specified for each test. The testing procedure corresponded to the standard practices in the laboratory in which the tests were carried out (Bureau, 2001).

3.7 FRACTOGRAPHIC AND MORPHOLOGICAL OBSERVATIONS

After the tests, the fractured specimens were put in individual plastic bags and stored in a desiccator. Fractographic observations were later carried out on many of these specimens. The fracture surfaces were coated with a palladium-gold alloy and the observations were made with a JEOL JSM-6100 SEM. Also, morphological observations on transverse cross-section and near the crack plane have been carried out on one specimen. These latter observations were made on a sample prepared by microtomy at low temperature. The microtomed surface was coated with palladium and the observations were made with a Hitachi S 4700 field emission gun SEM (FEGSEM). The loading conditions and the positions where the observations were made will be indicated in describing the results.

4 FATIGUE AND POST-FATIGUE RESULTS

A few experimental results that are not directly related to fatigue testing have already been presented in the previous section. In this section, the results directly related to fatigue testing are presented. These include results on the stress-strain response and on the fatigue life of non-notched axial fatigue specimens, the crack propagation rates in pre-creaked specimens and the fractographic and morphological observations.

4.1 AXIAL FATIGUE

From the literature review (c.f. section 2.3), it appears that the exfoliated nanoparticles are small and their hypothetical ability to prevent void coalescence, to increase the volume of a damage zone and/or to bridge the fractured surfaces of a small crack could be limited to the initiation regime of fatigue. Also, it is established that the initiation of a macroscopic crack in a non-notched specimen absorbs most of the fatigue lifetime (c.f. section 2.3.2). It is principally for these reasons that several axial fatigue tests have been carried out on non-notched specimens. The methodology described in section 3.4 has been followed and further details regarding the specific test parameters are given in the following subsections.

4.1.1 Types of Fracture

Depending on the testing parameters, different types of fracture were observed. The types of fracture observed experimentally can be classified as follows:

- Macroscopically ductile fracture: an unstable temperature increase is noted before fracture and the specimen fails through necking;
- Macroscopically brittle fracture: the temperature initially increases (by less than 3°C for PNC of batch 2 cycled at 78 MPa, which corresponds approximately to the stress at the onset of non-linearity during tensile tests) but then stabilizes and the specimen fails in a macroscopically brittle manner before any further temperature increase.

For the reasons outlined in section 2.3.2.1, efforts have been made to avoid thermal effects as well as necking. The term thermally dominated fracture employed in section 2.3.2.1 has been changed to macroscopically ductile fracture in light of the possibility that the temperature increase, in some cases, could originate from a mechanical instability (c.f. section 4.1.2). For the tests with PNC specimens from batch 2, the transition between the two regimes was found between 78 and 80 MPa for the regular sinusoidal waveform. Unless otherwise specified, the results reported here were obtained in the macroscopically brittle fracture regime.

4.1.2 Effect of Testing Parameters for PNC

When crack initiation occurred in the bulk rather than at a free surface, the lifetime was increased significantly (graphical comparison in Figure 4.1, single test data are in the legend of Figure 4.2). Although promoting surface initiation through non-controlled defects has the advantageous effect of reducing the duration of the tests, the fatigue lifetime then depends on extrinsic parameters such as the severity of the defect at which crack initiation occurred. For this reason, efforts were made to prevent surface initiation (c.f. section 3.4). Unless otherwise specified, crack initiation occurred in the bulk of the PNC specimens.

In an initial attempt to minimize the duration of each test, the effect of the loading waveform on the fatigue lifetime was studied. As shown in Figure 4.1, the introduction of rest periods does not have a significant effect on the fatigue lifetime. Employing a trapezoidal waveform may reduce slightly the number of cycles to fracture. However, the stress at the transition between the macroscopically ductile and the macroscopically brittle regime was found to decrease from 78 MPa for the continuous sinusoidal waveform to approximately 72 MPa for the trapezoidal waveform (TRA2), thus eliminating the potential reduction in the duration of the tests. Even though the initial objective was not achieved, an analysis of the effect of the waveform on the strain response is of interest in determining the origin of the fatigue damage processes. The effect of the fracture initiation site on the strain response is also of interest. These results are presented here.

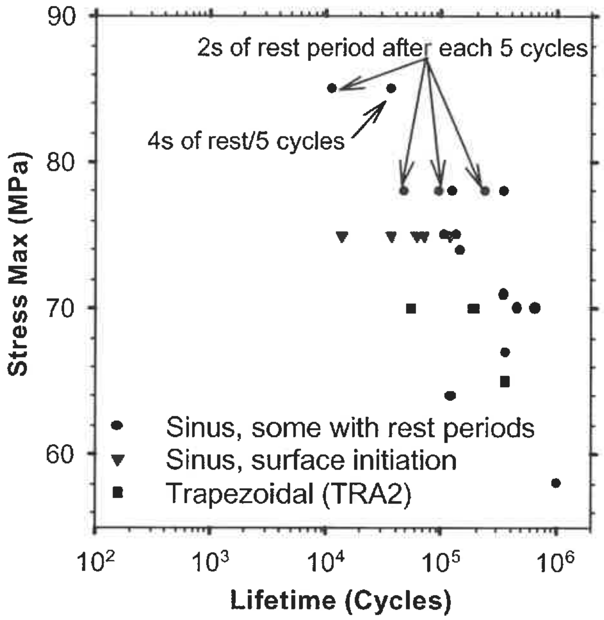

Figure 4.1: Effect of the fracture initiation site and of the waveform on the fatigue lifetime (TRA2: trapezoidal loading with a loading rate of approximately 1600 MPa/s, a hold time of 0.3 s at maximum stress and a hold time of 0.1 s at minimum stress).

The accumulated strain response for different PNC specimens that experienced continuous cycling at the same maximum cyclic stress of approximately 75 MPa is shown in Figure 4.2 as a function of the number of cycles. The legend (in the box to the right of the figure) indicates the crack initiation site, the waveform, the maximum cyclic stress and the lifetime for each test. On a semi-log scale (Figure 4.2a), a comparison of the results from tests PNC 12, 14, 39 and 41 reveals the absence of a correlation between the position of the crack initiation (or the fatigue lifetime) and the accumulated strain response. On a log-log scale (Figure 4.2b), the slopes for the curves near the end of each test are approximately the same for all tests in which the waveform was sinusoidal. However, the slopes appeared slightly reduced when the waveform was triangular (Triang).

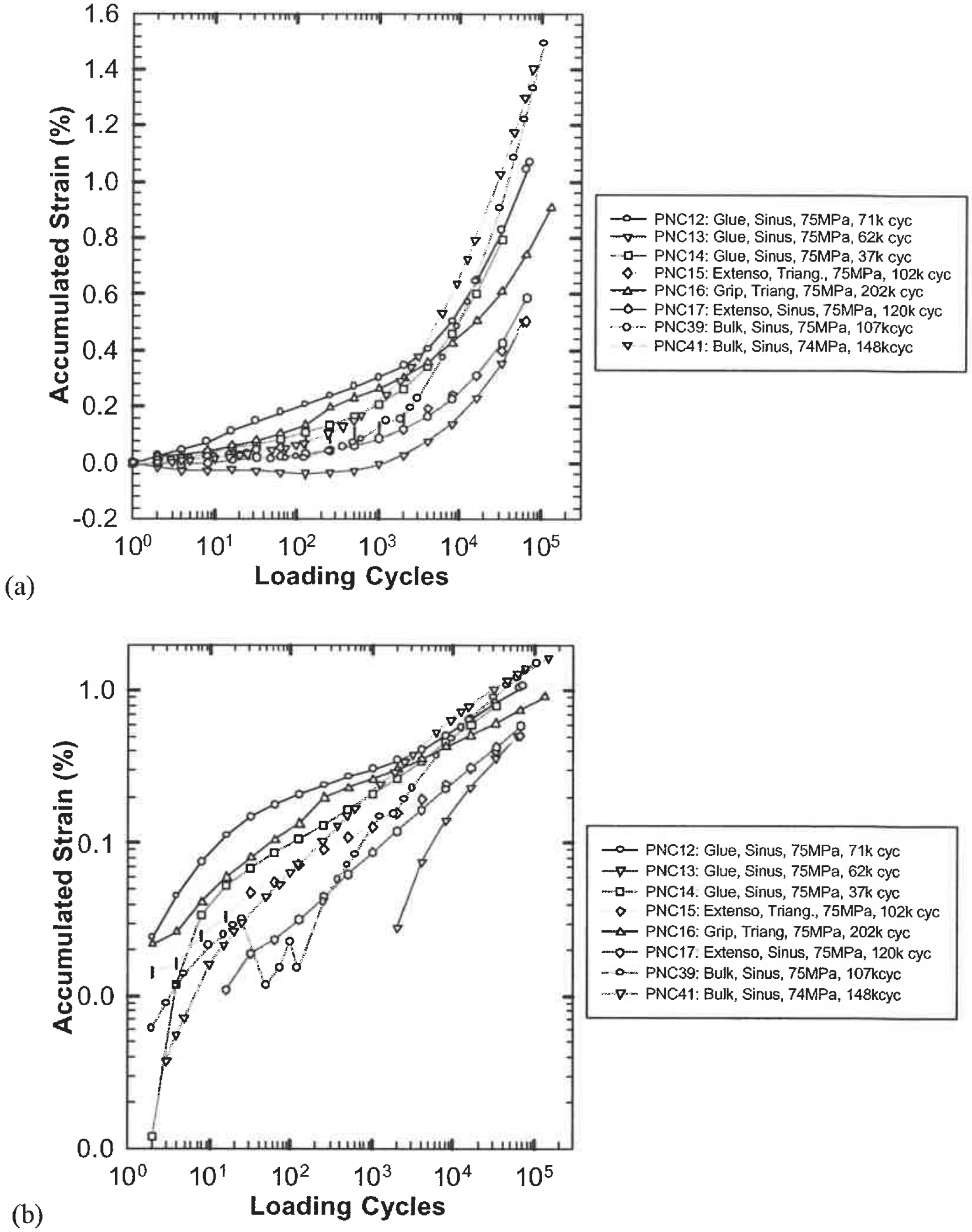

Figure 4.2: **Accumulated strain response of PNC (batch 2) tested at a maximum cyclic stress of approximately 75 MPa with a triangular or sinusoidal waveform. Whether the crack initiated near the glue, near the extensometer knife, out of the gauge section, i.e. in the grip, or in the bulk is specified.**

The strain amplitude response measured during the same tests is shown in Figure 4.3. The initial strain amplitude varies by less than 5% between the tests. This initial difference is maintained throughout the test. Independently of its origin, this variability has no effect on the interpretation of the results. When the waveform is triangular instead of sinusoidal, the increase in the stress amplitude during the test is lower, which is a consequence of a decrease on the time near the maximum and minimum loads. As for the accumulated strain, there is no correlation between the crack initiation location (or the fatigue lifetime) and the measured strain response. Based on these measurements, it can be concluded that the occurrence of microstructural damage by crack initiation and propagation cannot be detected from the accumulated strain or from the strain amplitude responses.

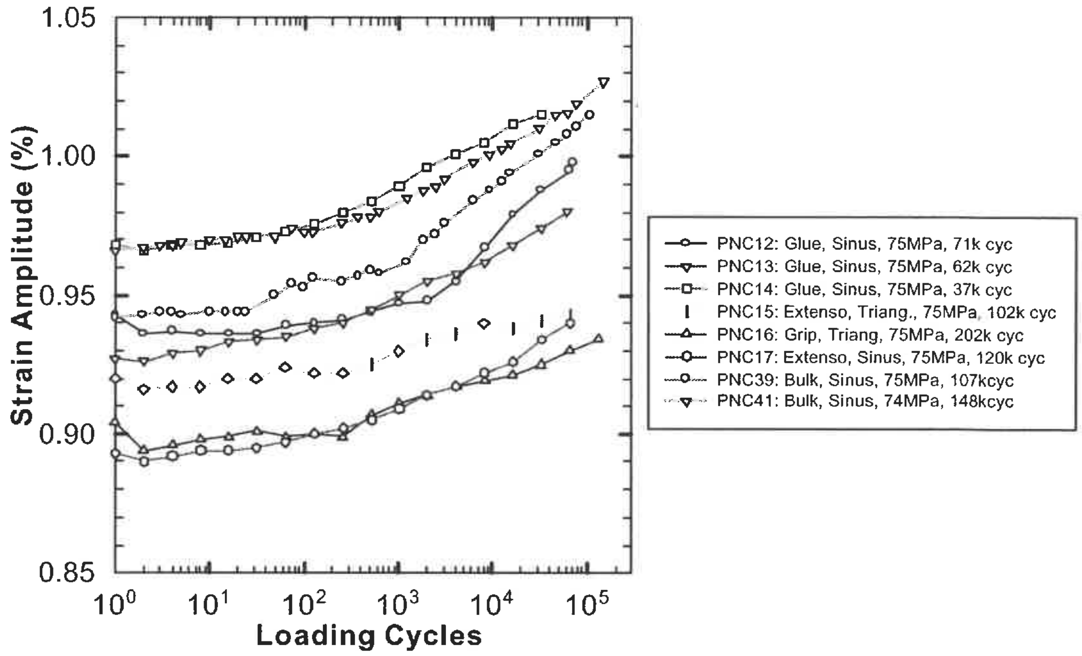

Figure 4.3: Strain amplitude response of PNC from batch 2. Whether the crack initiated near the glue, near the extensometer knife, out of the gauge section, i.e. in the grip, or in the bulk is specified.

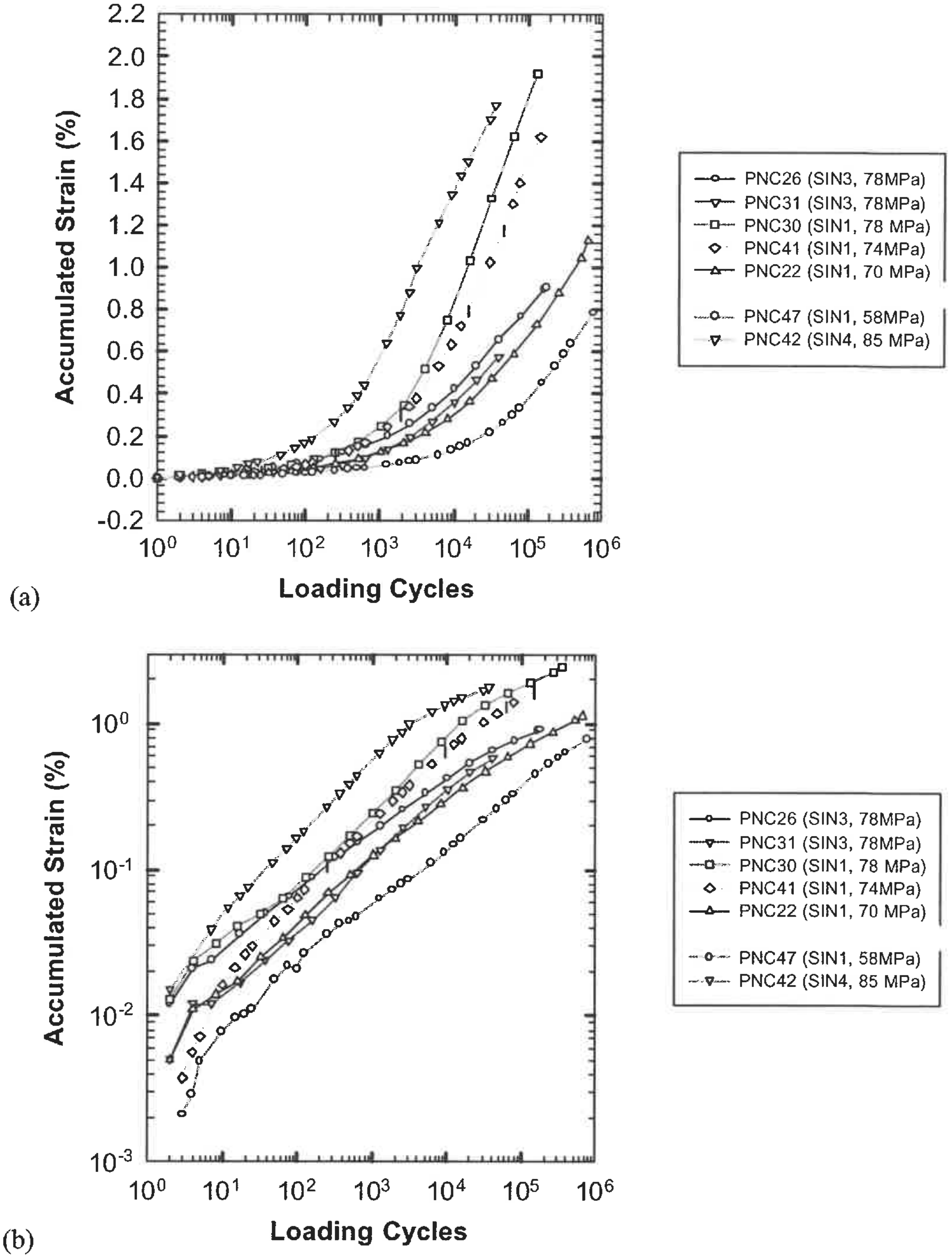

Figure 4.4: Effect of rest periods on the accumulated strain response: PNC (batch 2) cycled continuously (SIN1) or with a rest period of 2 (SIN3) or 4 (SIN4) seconds between blocks of five loading cycles.

The effect of introducing rest periods on the accumulated strain can be determined by comparing the results shown in Figure 4.4a for tests PNC26, PNC30 and PNC31. Rest periods at minimum load appear to reduce the accumulated strain after a given number of loading cycles as well as the slope in the log-log linear regime (Figure 4.4b).

The effect of the time at minimum load and of the loading rate can be examined from the accumulated strain response to different trapezoidal waveforms shown in Figure 4.5. Only the tests at a maximum cyclic stress of 75 MPa are considered here (tests PNC50 to PNC53). Assuming that an increase in the time at maximum load from 0.8 to 0.9 s should have a small effect on the resistance, the difference in the response between test PNC51 and PNC 52 should originate from the increase from 0.1 to 0.9 s in the time at minimum load. This effect has previously been reported during fatigue of PE at R = -1 (c.f. section 2.4.1.2). Since the response during tests PNC52 and PNC53 was similar even if the loading rate was decreased from approximately 2000 to 1000 MPa/s while the other parameters were kept constant, it appears that the strain rate has no important effect on the accumulated strain within the limited range tested.

Also shown in Figure 4.5 is the relationship between the strain response and the occurrence or non-occurrence of necking prior to specimen fracture. For the four tests that failed by necking (PNC50 to PNC 53), the evolution of the curves was approximately the same up to 3% of accumulated strain, which suggests the absence of thermal instability up to that strain. With an accumulated strain of more than 3%, mechanical instability due to a competitive effect between geometrical softening and strain hardening, which results necking, might have been a precursor to the final temperature rise. In practical terms, it appears difficult to increase the total accumulated strain above a certain critical value without inducing necking.

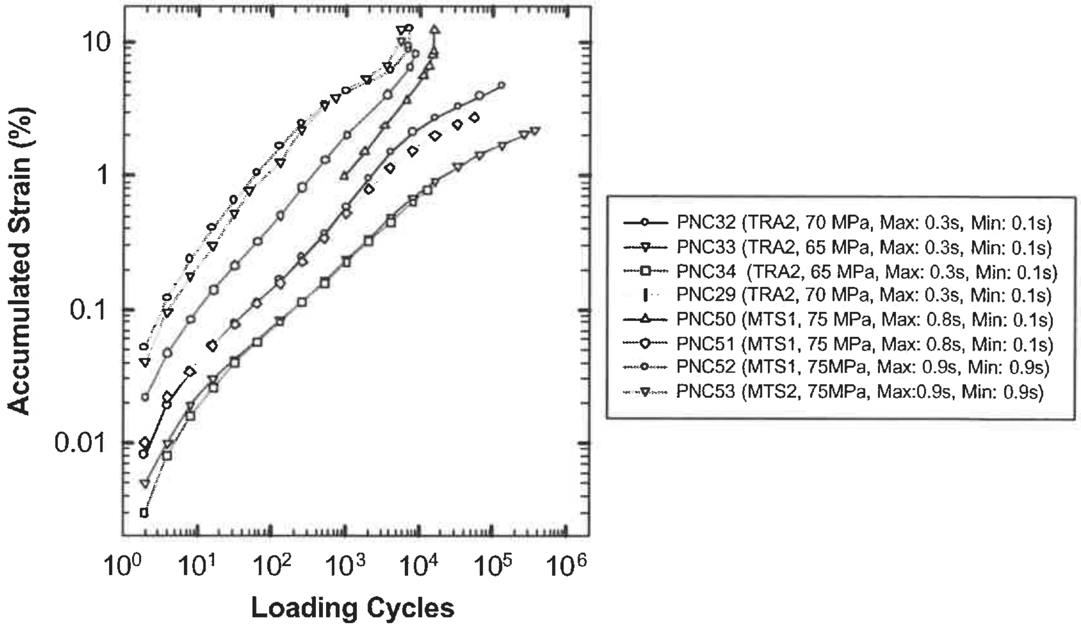

Figure 4.5: Accumulated strain response of PNC (batch 2) loaded employing a trapezoidal waveform with loading rates of approximately 1600 MPa/s (TRA2), 2000 MPa/s (MTS1) or 1000 MPa/s (MTS2) and variable hold times at maximum (Max) and minimum (Min) loads. Note: specimens PNC50 to PNC53 failed by necking.

4.1.3 Effect of the Size of the Heterogeneities in the Bulk

After the axial fatigue tests, the fracture surfaces were observed using SEM. From the divergence of the crack propagation (or ridge) lines on these surfaces, it was possible to determine the crack initiation site (fractographic details are provided in section 4.3). An heterogeneity in the form of an inclusion was found at the crack initiation site in each specimen of PNC. Two of these inclusions found in specimens from batch 2 are shown in Figure 4.6 and Figure 4.7. The X-Ray scattering data collected with an energy dispersive spectrometer (EDS) at the position of these inclusions did not reveal the presence of inorganic compounds, thus suggesting that they corresponded to organic impurities. Two inclusions found in specimens from batch 3 are shown in Figure 4.8 and Figure 4.9. The X-Ray scattering data collected with an EDS at the position of these inclusions (Figure

4.10 and Figure 4.11) revealed the presence of either Mg and Si or Mg and Ca, indicating the presence of inorganic compounds. An increase in the specimen fatigue lifetime was noted between the specimens from batch 2 and 3 and this increase can be correlated with a decrease in size of the particles observed at the crack initiation site (Table 4.1) as well as to a change the nature of the inclusions from organic to inorganic. By changing slightly the processing parameters (c.f. section 3.2) between batch 2 and batch 3, less contaminated specimens were produced. Therefore, the inclusions found in specimens from batch 2 were most probably introduced in the material during injection molding.

The length of the inclusions along their long axis was found to have a determinant effect on the fatigue lifetime (Table 4.1). Efforts made to establish a relationship between the exact size of the inclusion and the lifetime did not give satisfactory results. The stress concentration factor associated with the shape of the particle, the strength of the interface and the site of crack initiation (e.g. distance from the nearest external surface) probably affects the fatigue life results. The presence of inclusions of variable dimensions can shadow the intrinsic properties of the material by affecting the fatigue life of the specimens.

Table 4.1: Relationship between fatigue lifetime, the measured length in the long axis ($D1_{Max}$) and in the short axis ($D2_{Max}$) of the inclusions observed at the crack initiation site for PNC loaded at a maximum cyclic stress of 75-78 MPa (PNC 21 to 26 from batch 2; PNC 57 to 87 from batch 3).

Specimens	Lifetimes (kcyc)	$D1_{Max}$ (μm)	$D2_{Max}$ (μm)
PNC 21	125	180	130
PNC 24	240	60	30
PNC 26	350	50	40
PNC 81	466	50	30
PNC 80	700	20	10
PNC 57	863	Not determined	

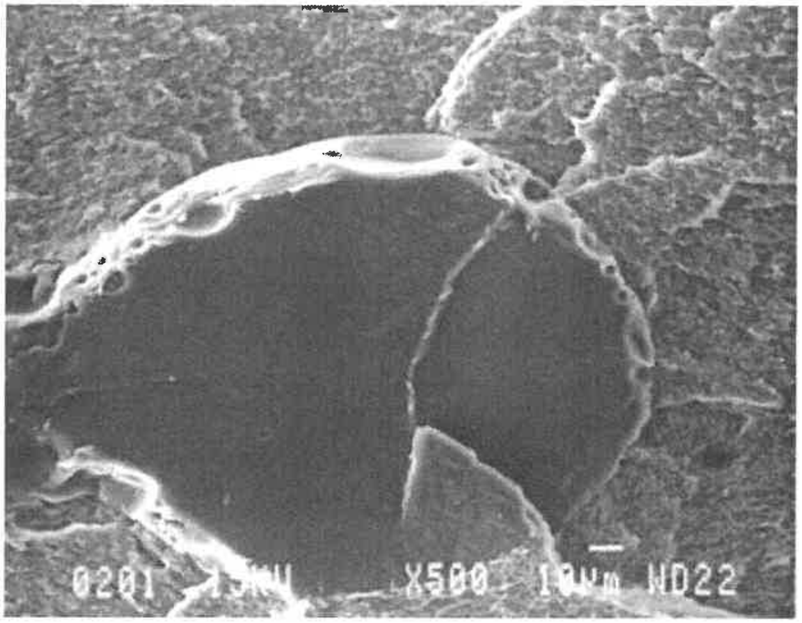

Figure 4.6: Large inclusion at the crack initiation site for test PNC 21 (78 MPa, 125 kilocycles to fracture).

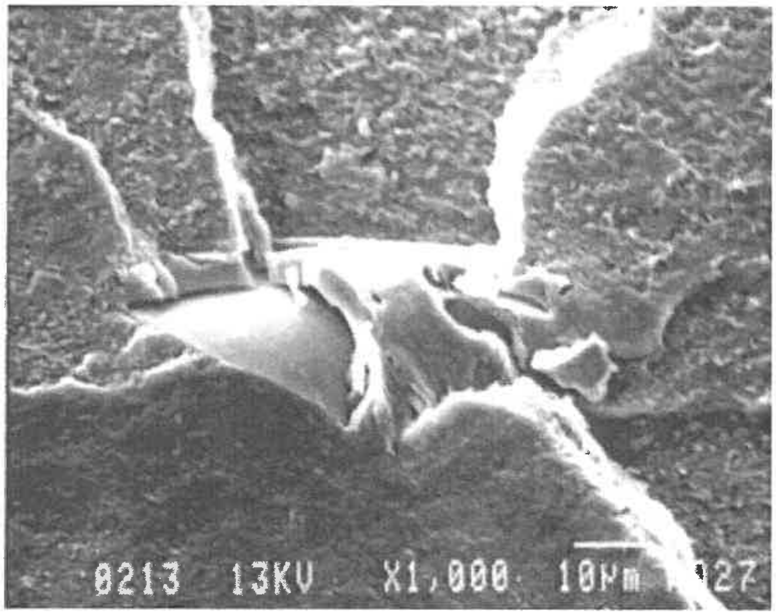

Figure 4.7: Inclusion of intermediate size at the crack initiation site for test PNC 26 (78 MPa, 350 kilocycles to fracture).

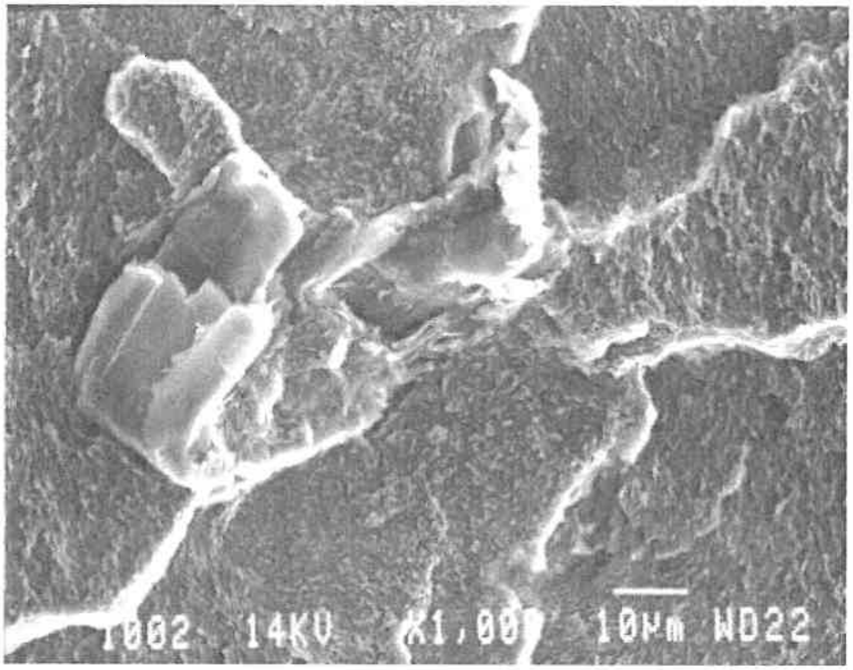

Figure 4.8: Inclusion of intermediate size at the crack initiation site of test PNC 81 (75 MPa, 466 kilocycles to fracture).

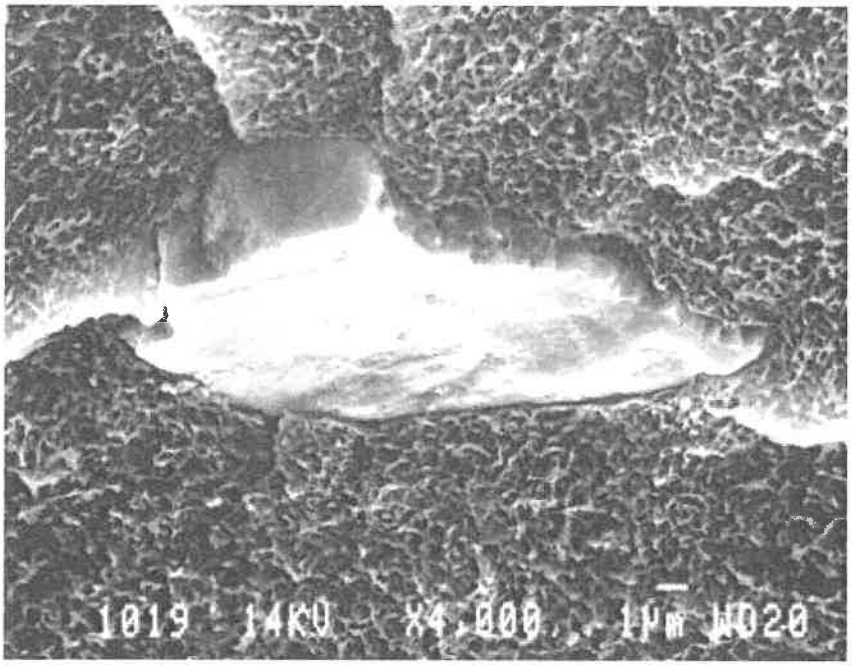

Figure 4.9: Small inclusion at the crack initiation site for test PNC 80 (75 MPa, 700 kilocycles to fracture).

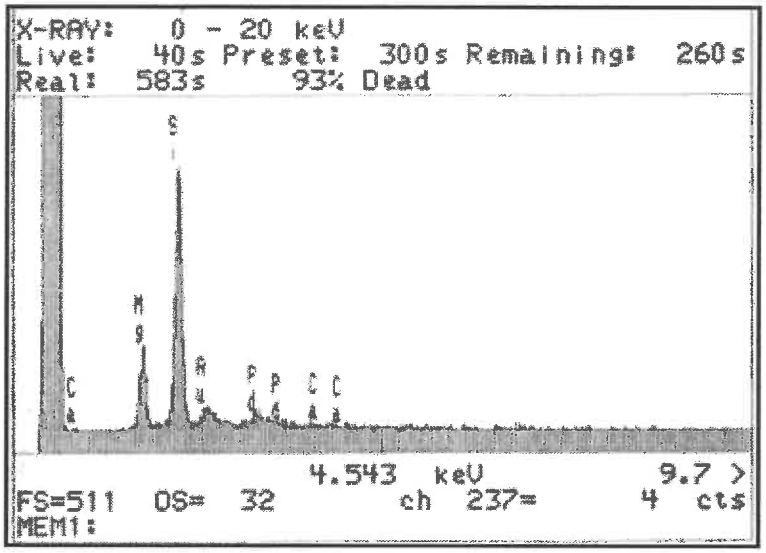

```
X-RAY:    0 - 20 keV
Live:    40s Preset:   300s Remaining:   260s
Real:   583s       93% Dead

              4.543  keV          9.7 >
FS=511   OS=  32       ch  237=      4  cts
MEM1:
```

Figure 4.10: EDS results collected during scanning of a region of the inclusion of intermediate size shown in Figure 4.8.

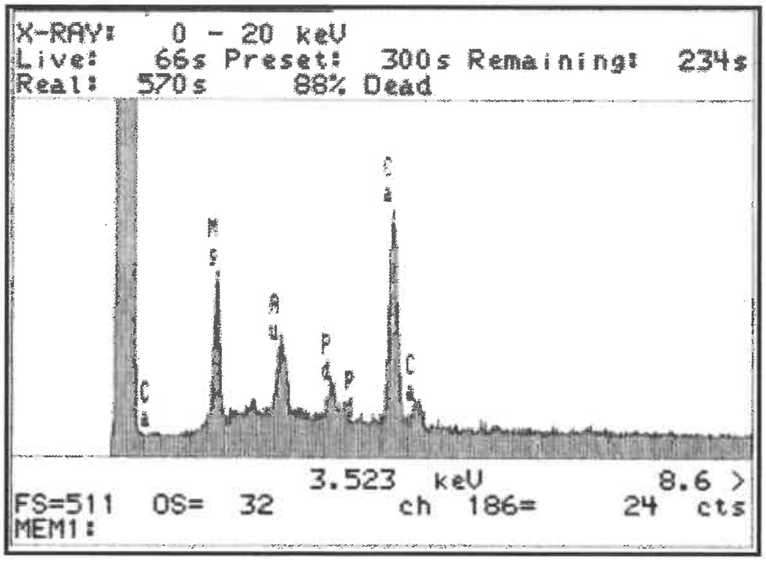

```
X-RAY:    0 - 20 keV
Live:    66s Preset:   300s Remaining:   234s
Real:   570s       88% Dead

              3.523  keV          8.6 >
FS=511   OS=  32       ch  186=     24  cts
MEM1:
```

Figure 4.11: EDS results collected during scanning of the inclusion shown in Figure 4.9.

4.1.4 Stress-Strain-Time Response of PNC versus PA6

All the results presented in this section were obtained by employing specimens from batch 3. The tests on PNC specimens were carried out at maximum cyclic stresses of approximately 75 and 57 MPa. The tests on PA6 specimens were all carried out at a maximum cyclic stress of approximately 57 MPa. The initial strain amplitude during tests on PNC at 75 MPa was approximately 0.98%,while the initial strain amplitude during the tests on PA6 (at 57 MPa) was approximately 0.93%. For this reason, the test parameters employed enable a comparison of the behavior of both materials at similar stress amplitudes as well as at similar initial strain amplitudes. The general parameters and particularities of each test are indicated in Table 4.2.

Table 4.2: General parameters and particularities of each test employing specimens from batch 3.

Test	Maximum stress (MPa)	Lifetime (kcyc)	Particularity (if any)
PNC80	75	700	None
PNC81	75	466	None
PNC82	75	565	None
PNC83	75	241	Fracture out of gauge section (excluded for fatigue life)
PNC57	75	863	No strain data (included only for fatigue life)
PA22	57	1980	None
PA23	57	3321	Stopped for 15 min. at 2541 kcyc and restarted
PA26	57	2230	None
PA27	57	2057	Rubber band holding the extensometer failed at 1560 kilocycles
PNC90	57	4905	None
PNC92	57	10470	None
PNC93	57	4866	Stopped for 4 hours at 2100 kcyc and restarted
PNC66	57	3197	No strain data (included only for fatigue life)

The behavior has been characterized employing the strain response parameters as well as the dynamic properties parameters defined in section 3.5. The figures and tables referred to herein are grouped at the end of this subsection. For the discussion, the macroscopic response of the materials will be divided in three different regimes based upon the accumulated strain response:

- Regime I: regime during which a power law relationship is noted between the accumulated strain and the number of loading cycles,
- Regime II: regime during which the slope decreases on a log-log scale,
- Regime III: final regime during which the slope increases on a log-log scale.

This definition of the regimes based on the accumulated strain response will be employed throughout this section. Figure 4.12 presents the accumulated strain as a function of the number of loading cycles on a log-log scale. The curves are approximately linear from approximately 10 to 10^5 loading cycles. This linearity indicates a power law relationship between the variables. Based upon the variability in the results and on the limited precision on the measurement of the strain, the deviation from the linearity during the first 10 to 100 cycles of the tests are considered within the expected experimental error. Power law relationships have previously been reported in fatigue (c.f. section 2.3.2) and in creep (c.f. appendix, section A.1.2.5). After approximately 10^4-10^5 cycles, a transition to regime II occurred, where the slope of the curves was found to decrease for all PA6 specimens and for PNC specimens tested at 57 MPa (Figure 4.12b). For PNC specimens at 75 MPa, the deviation from the power law regime I is less pronounced than for the other tests. A regime II where the slope decreases is nevertheless clearly observed for at least one test (PNC81). For PNC specimens, a regime III where the slope increases was observed, except for one test at 57 MPa. Whether PA6 presents a regime III is more difficult to establish. For test PA22, a final regime III appears to be present. For the three other tests (PA23, PA26 and PA27), regime II prevailed up to the end of the curves. However, the curves of tests PA23 and PA27 are incomplete. In test PA27, the rubber band holding the extensometer failed at 1560 kilocycles while the specimen failed after 2057 kilocycles. Test PA23 was stopped (electrical shutdown) for 15 minutes at 2541 kilocycles and then restarted. The total lifetime of this specimen was 3321 kilocycles. By adding the data for the second part of this test (PA23B), the presence of a final increasing regime III is plausible. To summarize, regime I was observed in all cases. Regime II was clearly observed at 57 MPa but was less evident for three of the four tests on PNC at 75 MPa. For non-interrupted tests, regime III was observed except for one test on PA6 and one on PNC at 57 MPa.

The accumulated strain response can also be presented on a plot of the logarithm of the rate of strain accumulation versus the accumulated strain, as originally proposed by Sherby and Dorn (c.f. section 2.3.2.2). Sherby-Dorn plots are presented in Figure 4.13. For at least three of the four tests on PNC at 75 MPa, the absolute value of the slope of the curves decreases approximately continuously throughout the test. Near the end of the test, the rate of accumulation of the strain becomes approximately constant. Under these test conditions, there is no clear evidence of a transition between the accumulated strain regimes previously defined. However, the regimes previously defined can be correlated with variations in the shape of the curves of the others tests. Detailed analysis of the data at 57 MPa with PA6 and PNC (c.f. Figure 4.12, Figure 4.13, Table 4.3 and Table 4.4) indicates the following:

- the transition from regime I to regime II is correlated with a change from a positive to a negative inflection on a Sherby-Dorn plot (observed for PNC81 and for all tests at 57 MPa);
- regime III corresponds to the portion of the curves where the slope is approximately zero on a Sherby-Dorn plot (observed for PNC80, PNC81, PNC82, PNC90, PNC92, PA22 and PA23B).

The regimes previously defined based on the accumulated strain versus number of loading cycles appear to correlate with the transitions in the curves of the Sherby-Dorn plots. The Sherby-Dorn plots indicate that the rate of strain accumulation is approximately constant in regime III. For PNC, this plateau value of the rate of strain accumulation appears to be highly sensitive to the maximum stress. An increase in the maximum stress from 57 to 75 MPa led to an increase in the plateau values from approximately 1x10^{-7} to 2x10^{-6} %/cycle. It cannot be clearly established whether, if heterogeneous crack initiation was retarded, PA6 would present a plateau value of accumulated strain at a level similar to that for PNC at 57 MPa. However, the data of Table 4.3 and Table 4.4 from the non-interrupted test PA22 and the interrupted test PA23 suggest the existence of such a plateau. What can be clearly established is that the rate of strain accumulation near the end of the tests is approximately the same for all tests carried out at a maximum cyclic stress of 57 MPa.

In their studies on PC, Mindel and Brown (1973, 1974) found that the component of persistent strain started to be significant just before the minimum value of the strain rate. Accelerated fracture was observed after a minimum in the curve of the Sherby-Dorn plots. This acceleration was probably a consequence of strain localization (necking). In the current experiments, the accelerating regime was not observed. The strain rates during tests PNC90 and PNC92 were clearly found to reach a plateau value, and not a minimum point as previously observed by Mindel and Brown (1973, 1974) (c.f. section 2.3.2.2). This difference could be attributed to the lower accumulated strain at which the minimum strain rate is reached (total strain of approximately 8% for PC at high stress and to less than 5% in the present tests) and/or to the differences in strain hardening behavior between amorphous and semicrystalline polymers.

The evolution of the measured accumulated volume variation during cycling is shown in Figure 4.14a. Up to approximately 10^3-10^4 loading cycles, the volume of the specimens appears to increase slightly, which may be related to an increase in the fraction of free volume in the polymer. After approximately 10^3-10^4 cycles, a decrease in volume was measured. It is not known if the density of the material really increased or if the volume decrease was an artifact of the measurement technique. In the calculation, the contraction in the thickness or short-transverse direction was assumed to be equal to that in the width or long-transverse direction. Assuming that local plane stress conditions would favor lateral contraction, the contraction in the thickness direction should be at least as large as and more probably larger than that in the width direction. Accordingly, the assumption made that the strain in the thickness direction was equal to that measured in the width direction can be expected to underestimate any eventual volume contraction. As alternative to this explanation, the thin plastic band employed to protect the specimen from the grips of the long-transverse extensometer could have contracted during the test. Finally, there could be a systematic experimental error on the measurement of the relative value of the strain in any of the two directions. Even through these experimental errors could have resulted in errors on the measured volume variation, any transition in the shape of the curve nevertheless suggests a transition in the response of the material.

As shown in Figure 4.14b, a transition from a negative inflection to a positive inflection can be noted near the end of the curves in approximately 50% of the cases. In the paper for the conference ANTEC 2002 (Bellemare, Bureau, Denault and Dickson, 2002), this transition (noted for PNC80, PNC82 and PNC83) was suggested to indicate the onset of localized deformation within the gauge length of the longitudinal extensometer but not at the position where the transverse extensometer was installed. However, this suggestion fails to describe the behavior of specimen PNC92. For this specimen which did not fail (the test was intentionally stopped after 24 days), an increase in the volume was noted despite an approximately constant rate of strain accumulation over the last 10 million cycles. Because of the absence of strain acceleration, it is unlikely that macroscopic strain localization measurable by the extensometers would have initiated in this test approximately after 1 million cycles. Based upon Figure 4.12 and Figure 4.14, a fair correspondence could be found between the number of loading cycles at which regime III begins and the number of loading cycles at which the last transition is observed in the curves of tests PNC80, PNC82, PA22, PNC90 and PNC92. This suggests that the proportion of the accumulated strain that is dilatational is larger in regime III than in regimes I and II.

From the evolution of the strain response parameters during the tests, three fatigue regimes have been identified. The definition of these regimes will also be employed to discuss transitions in the evolution of the dynamic properties parameters during fatigue testing. The first dynamic parameter considered is the storage modulus. As shown in Figure 4.15, the curve of the storage modulus versus the logarithm of the number of loading cycles is negative in regime I. In that regime, the storage modulus generally decreases although a small initial increase followed by a decrease was noted for two tests at 57 MPa (PNC93 and PA23). The negative inflection of all the curves suggests a competitive effect between processes of hardening and softening.

At 57 MPa, the transition from regime I to regime II approximately corresponds to the transition from a negative inflection to a positive inflection. In PNC at 75 MPa, the inflection decreased but appeared to remain negative. In all cases, it can be stated that the transition from regime I to regime II corresponds to a condition where the resistance of the material to cyclic softening starts to increase. A decrease in E' followed by an increase has already been reported in tension-tension axial fatigue on PA66 conditioned at 50% humidity by Lesser (1995). Finally, a regime III in the E' response (Figure 4.15) was observed for the same tests as for the accumulated strain (Figure 4.12).

Figure 4.16 presents the measured evolution of the loss tangent (tan δ) during the tests. For a given test, the variability in the results is small when considering that data were stored every 0.02 s and that the time delay of the strain relative to the stress was typically approximately 0.0004 s. This low variability supports the validity of the developed calculation from the raw data. When comparing the tests carried out at 75 MPa with PNC, the variability between the tests also appears acceptable. However, a large discrepancy is found in the results at 57 MPa. For test PNC92, the parameter tan δ even reached a negative value. In order to evaluate the validity of the calculation technique employed for the calculation of tan δ, the results from the calculation of the average hysteresis width are shown in Figure 4.17. For test PNC92, the average hysteresis width is also negative. Figure 4.18 (a and b) presents the raw data for the hysteresis loop stored during the 100th cycle. From Figure 4.18a, the negative value of the width is not due to an improper calculation technique as the loop is completely closed. When a positive width is measured, such as at the $10^{7\text{th}}$ cycle of the same test, a positive width of the hysteresis loop can be resolved easily (Figure 4.18b). Apart from the fact that tan δ and the average width of the hysteresis loop both present the same anomaly, the evolution of these parameters for each test are highly comparable. For this reason, it can be stated that the evolution in the hysteresis energy dissipated during the tests is primarily a consequence of changes in the damping capacity of the material. Therefore, only the evolution parameter tan $\cdot\delta$ will be considered further in this section and in the general discussion (c.f. section 5.1).

To explain the discrepancy between the tests at 57 MPa, it is proposed that the stress and strain were not acquired and stored properly by the acquisition system. Based on this assumption, small corrections have been made on the time scale of the strain for three of the 11 tests carried out. For at least two of these three tests, the pre-loading parameters were slightly different than for the other eight tests, which supports the hypothesis of an absolute error on the time scale of the strain relative to the stress caused by the acquisition system. As shown in Figure 4.19, corrections of less than 0.0003s allowed to conciliate the data.

The data in Figure 4.19 are thought to be more representative of the actual behavior of the materials. In regime I, the damping capacity of all specimens is found to initially decrease and then to increase, but the inflexion of the curves remained positive throughout that regime. The transition between regimes I and II corresponds approximately to an inflexion point. As for the other parameters, the transition is better resolved for PA6 than for PNC. For the tests where a regime III is observed, this regime is associated with a change to a positive inflexion as well as a significant increase in tan δ.

All transitions observed in the evolution of the dynamic parameters correlate with the regimes previously defined based on the evolution of the strain response. The results of this section are summarized in Table 4.5.

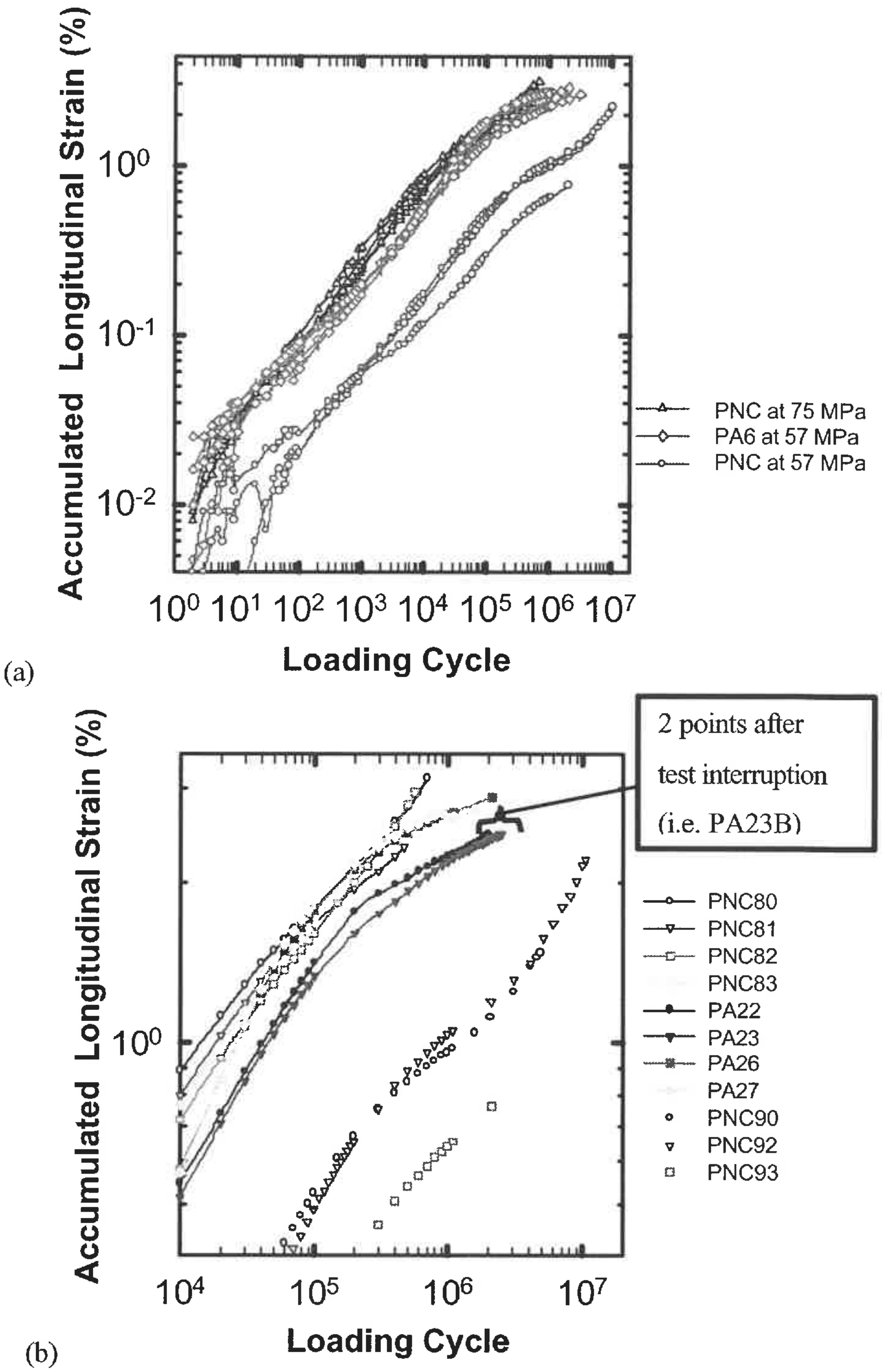

Figure 4.12: The accumulated longitudinal strain versus number of loading cycles for all specimens from batch 3 (For additional details, see Table 4.2).

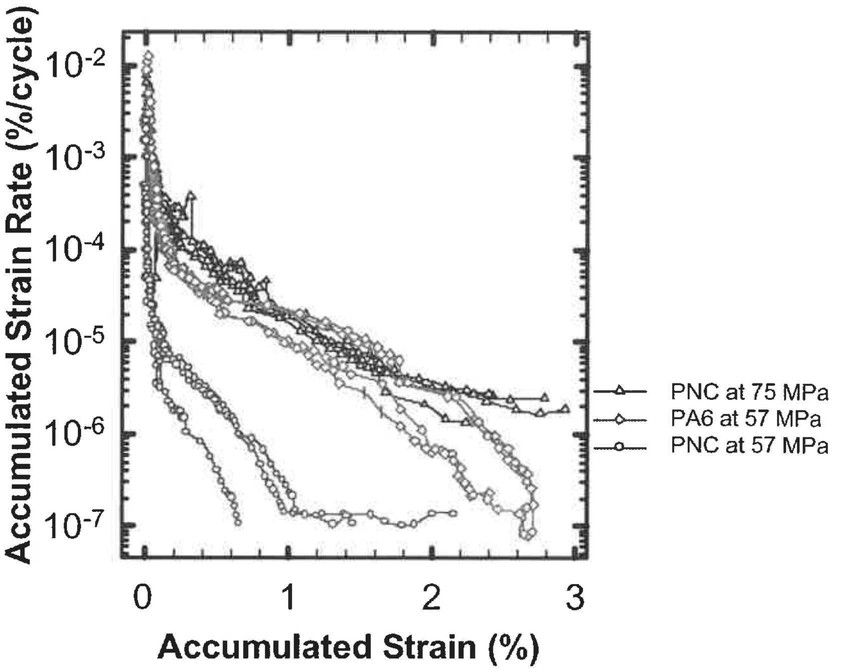

(a)

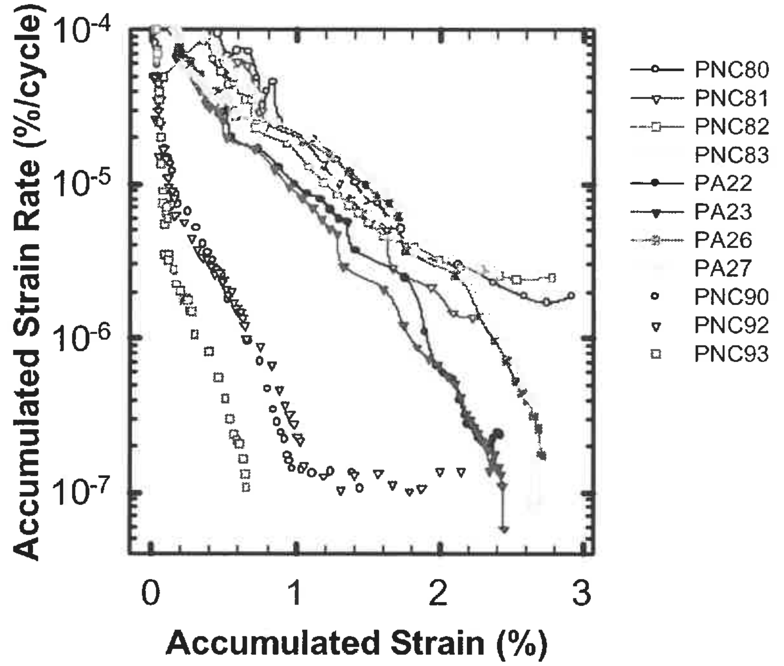

(b)

Figure 4.13: Sherby-Dorn plot of the accumulated strain (For additional details, see Table 4.2).

Table 4.3: The rate of strain accumulated versus number of loading cycles near the end of the non-interrupted test PA22 (For additional details, see Table 4.2).

Cycles	Acc Strain	Acc Strain Rate
	%	%/cycle
1000000	2.2306	
1100000	2.2565	2.48E-07
1200000	2.2801	2.25E-07
1300000	2.3015	2.10E-07
1400000	2.3220	2.06E-07
1500000	2.3427	2.04E-07
1600000	2.3629	1.91E-07
1700000	2.3809	2.22E-07
1800000	2.4073	2.44E-07
1900000	2.4297	2.34E-07
1975000	2.4483	

Table 4.4: The rate of strain accumulation versus number of loading cycles: (a) before test interruption (end of test PA23A) and (b) after interruption (test PA23B) (For additional details, see Table 4.2)

Cycles	Acc Strain	Acc Strain Rate
	%	%/cycle
1000000	2.1887	
1100000	2.2198	2.97E-07
1200000	2.2481	2.67E-07
1300000	2.2732	2.41E-07
1400000	2.2963	2.18E-07
1500000	2.3168	2.09E-07
1600000	2.3380	1.87E-07
1700000	2.3543	1.39E-07
1800000	2.3659	1.60E-07
1900000	2.3862	1.76E-07
2000000	2.4011	1.40E-07
2100000	2.4141	1.44E-07
2200000	2.4299	1.29E-07
2300000	2.4400	1.10E-07
2400000	2.4520	5.79E-08
2500000	2.4516	

(a)

	Acc Strain	Acc Strain Rate
Cycles	%	% / cycle
100000	2.450	
200000	2.460	8.78331E-08
300000	2.468	4.71699E-08
400000	2.469	4.06637E-08
500000	2.476	1.48015E-07
600000	2.499	1.91932E-07
700000	2.514	1.21087E-07
780000	2.521	

(b)

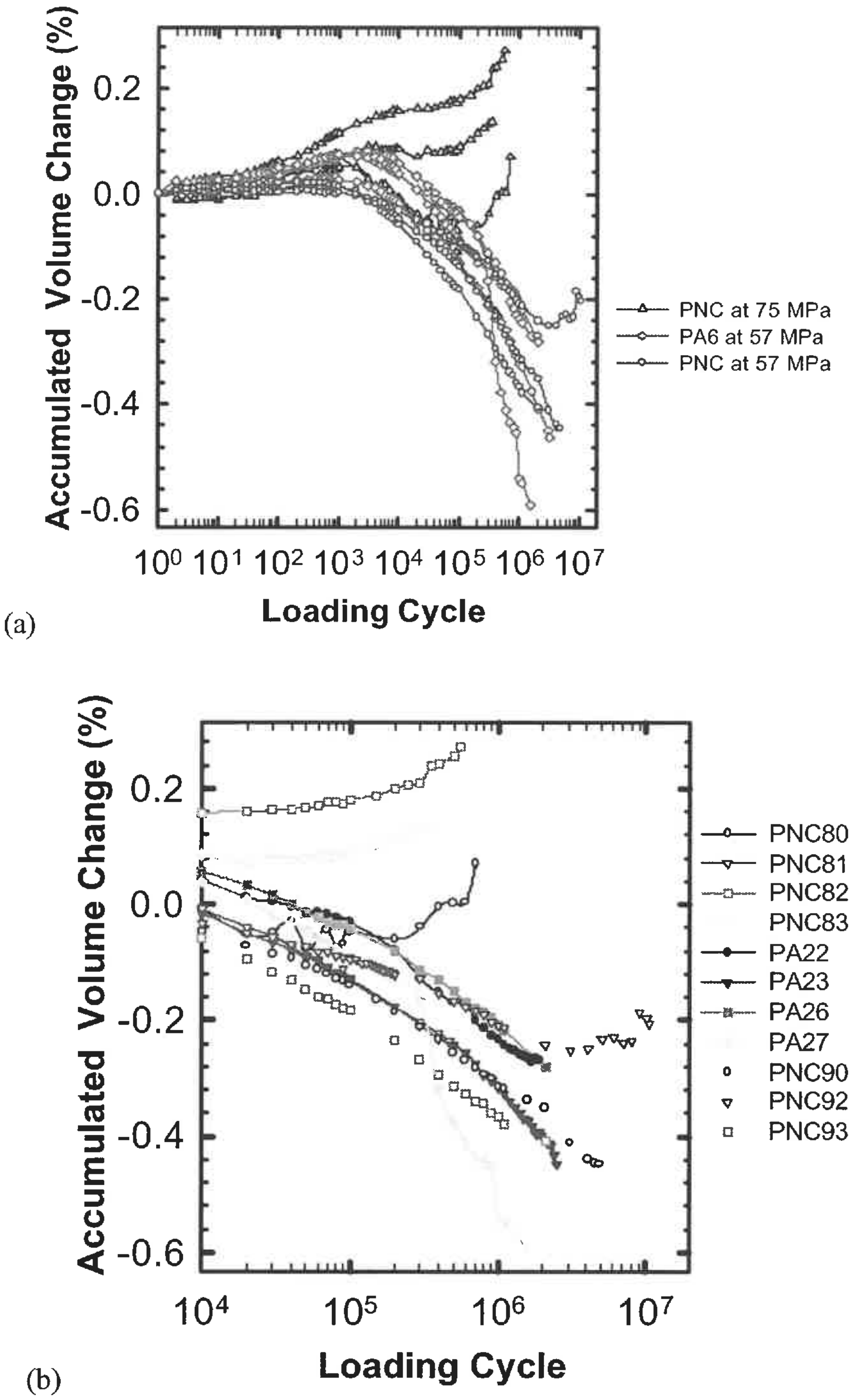

Figure 4.14:The accumulated volume variation versus number of loading cycles for all specimens from batch 3 (For additional details, see Table 4.2).

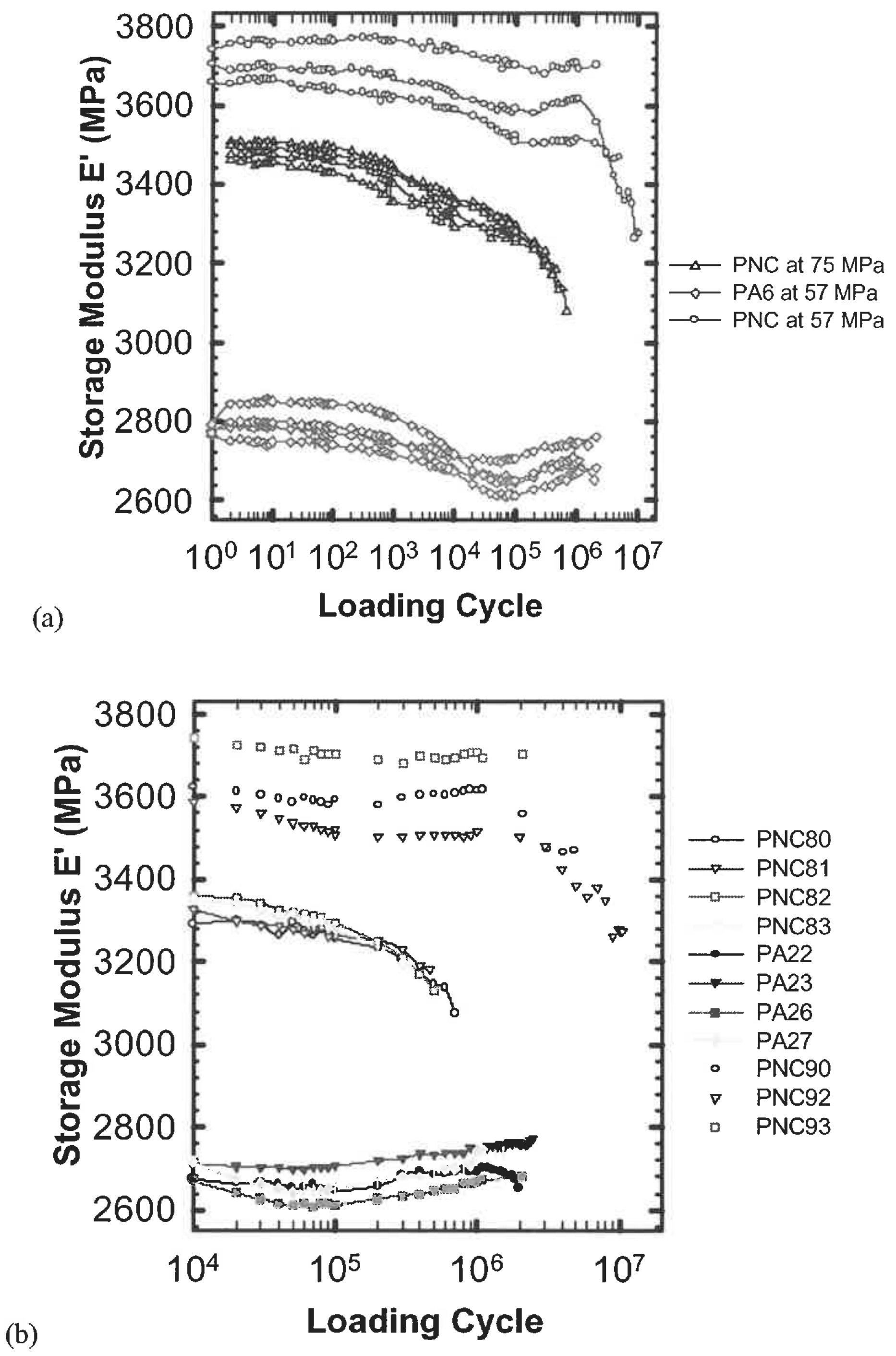

Figure 4.15: The storage modulus E' versus number of loading cycles for all the specimens from batch 3 (For additional details, see Table 4.2).

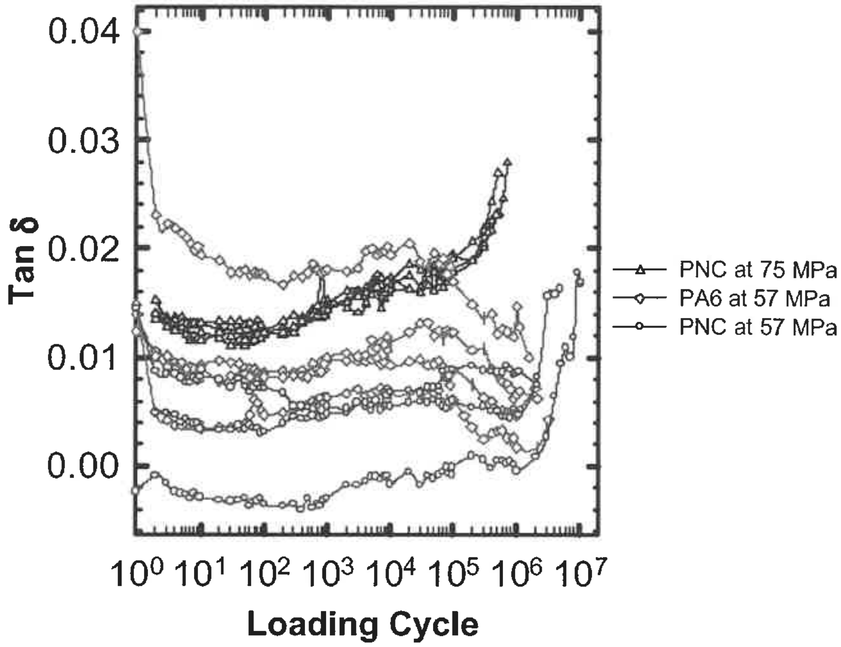

(a)

Figure 4.16: The loss tangent versus number of loading cycles for all specimens from batch 3 (For additional details, see Table 4.2).

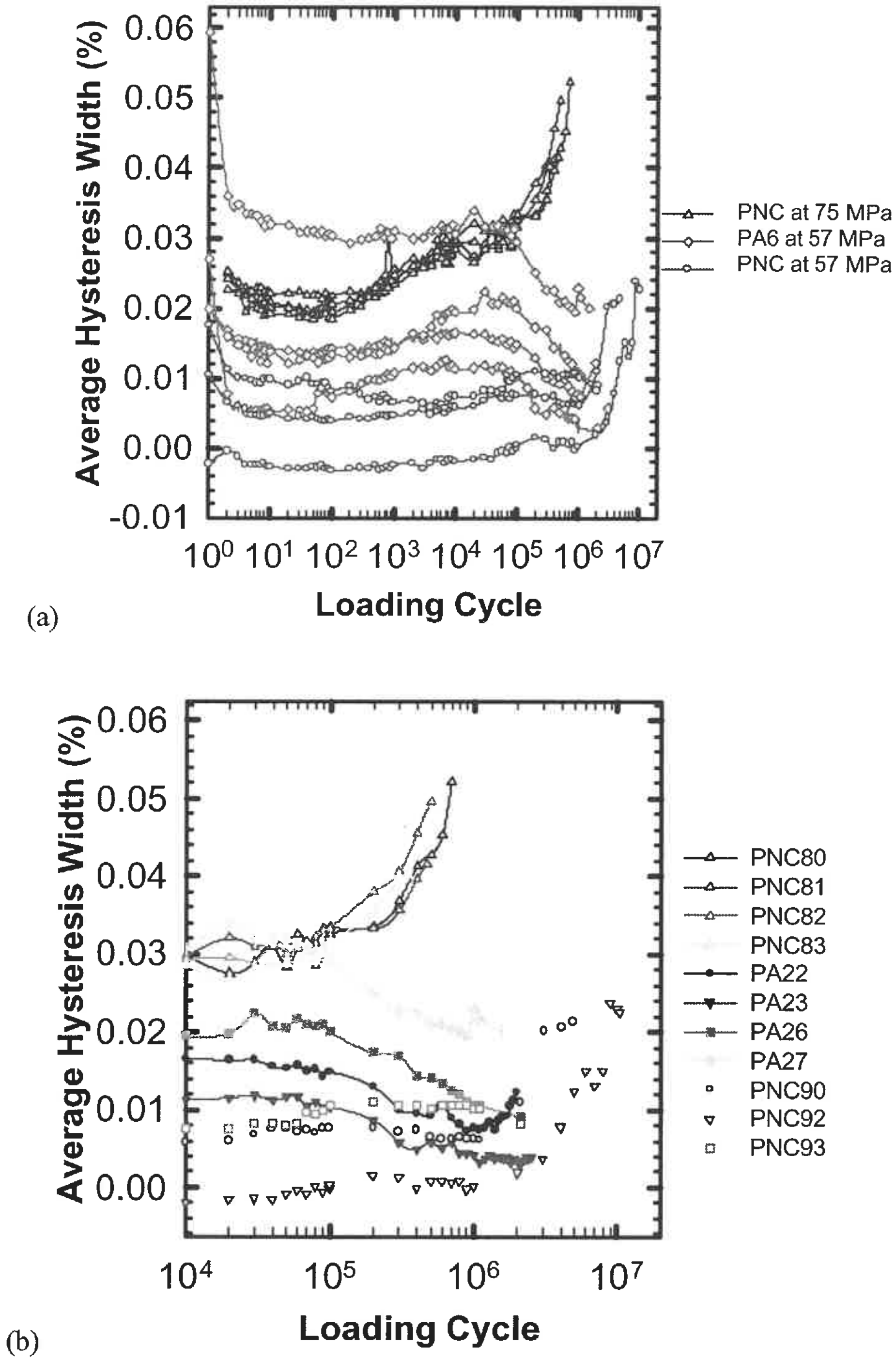

Figure 4.17: The average hysteresis width versus number of loading cycles for all specimens from batch 3 (For additional details, see Table 4.2).

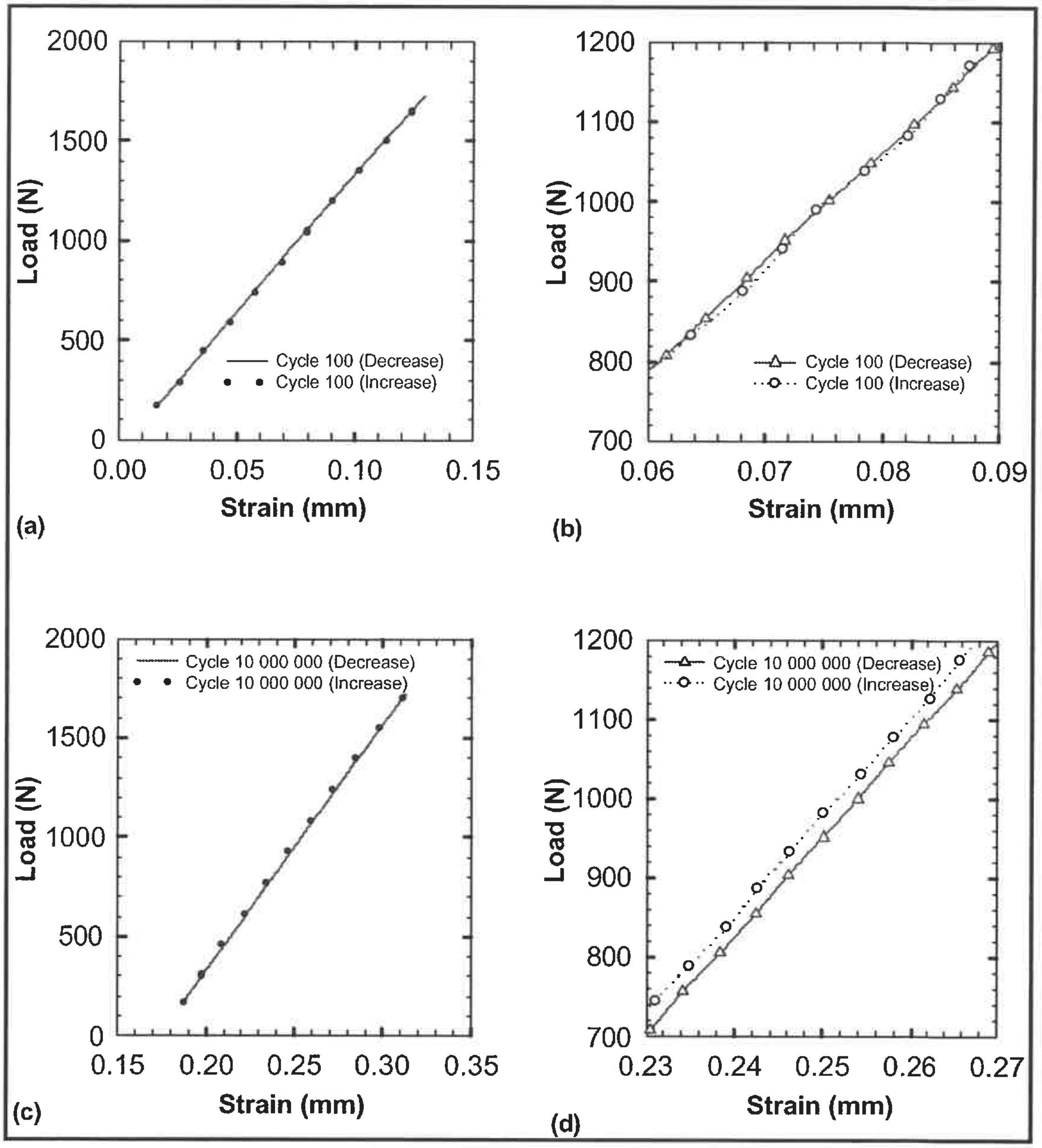

Figure 4.18: The (a, c) general shape and (b, d) width of the hysteresis loops as seen after (a, b) 100 cycles and (c, d) 10 000 000 cycles, respectively. Note the anomaly in the response after 100 cycles (data: PNC 92).

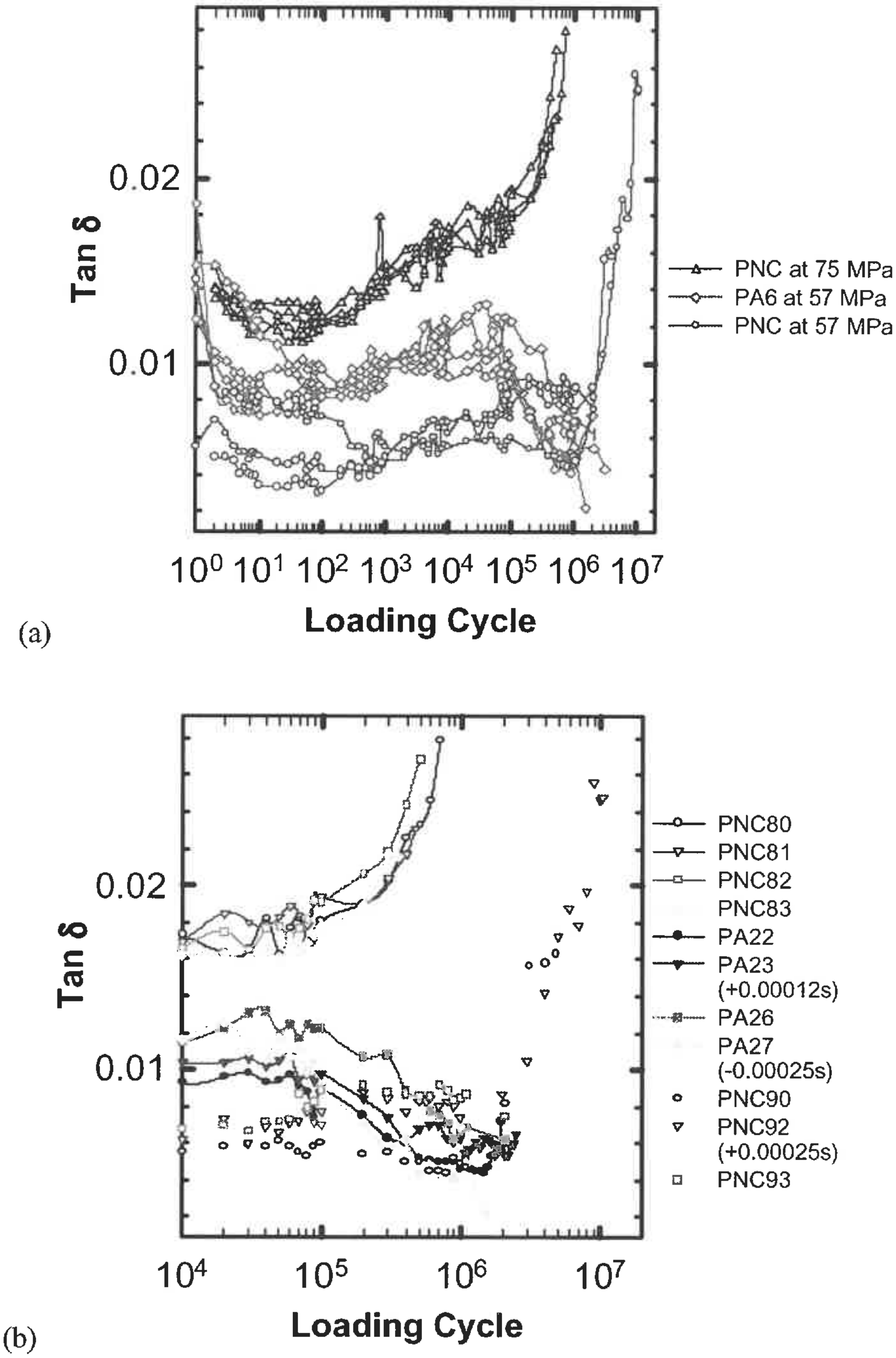

Figure 4.19: The loss tangent versus number of loading cycles for all the specimens from batch 3 after correction of the three curves indicated (For additional details, see Table 4.2).

Table 4.5: Summary of the evolution of the strain response and of the dynamic properties (in the three regimes defined from the strain response).

Parameters	**Regimes**		
	I	**II**	**III**
Accumulated strain versus cycles (log-log scale)	Linear	Negative inflection	Positive inflection
Accumulated strain rate (log scale) versus accumulated strain	Positive inflection	Negative inflection (or positive but smaller inflection)	Value approximately constant
Accumulated volume variation versus cycles (semi-log scale)	Not clearly resolved		Positive inflection (significance ⇑ in several cases)
Storage modulus versus cycles (semi-log scale)	Negative inflection	Positive inflection (or inflection ⇑)	Important ⇓
Tan δ versus cycles (semi-log scale)	Positive inflection	Negative inflection	Important ⇑
Hysteresis width versus cycles (semi-log scale)	Same as for tan δ		

4.1.5 Effect of Test Interruption on the Stress-Strain-Time Response

Test PNC93 was interrupted in regime II after 2100 kilocycles for approximately 4 hours, because of an electrical shutdown, and then restarted. The effects of this interruption on the evolution of the strain response and on the dynamic properties are presented and discussed in this section. The results obtained after the test interruption in PNC93 are presented in test PNC94. Figure 4.20 suggests little history effect on the evolution of the dynamic property tan δ at the beginning of regime I. Assuming that the initial reduction in tan δ is produced by the accumulation of strain energy, this result suggests that an important proportion of that strain energy has been released during the test interruption. Except for the response after 650 kilocycles, the average value of tan δ appears to be approximately the same in the pre-fatigued specimen as in the virgin one. Finally, a sharp peak in tan δ is observed after 650 kilocycles. As will be discussed later, this peak value corresponds to a transition in the accumulated strain response.

As shown in Figure 4.21a, employing a pre-fatigued specimen instead of a virgin specimen has little effect on the overall accumulated strain obtained at 10 kilocycles. However, the shape of the curve has a negative inflection instead of being approximately linear. The accumulated strain at the 100th cycle is higher in the pre-fatigued specimen than in the virgin one. Recoverable strain energy is likely to accumulate during cyclic loading and to induce strain hardening. During the test interruption of 4 hours, most of this strain energy has been released (c.f. tan δ response above). For this reason, the accumulated strain response after test interruption should be similar to the response of the virgin specimen. Finally, some microstructural changes that led to softening might still be present in the microstructure, which could account for the initial higher value.

After 10 kilocycles, the elongation in the pre-fatigued specimen started to be lower than in the virgin one. During test interruption, strain energy stored in a larger activation volume or some microstructural changes might not have been released, which could explain the increased resistance to the accumulation of strain. In the regime II of the pre-fatigued specimen, a rapid increase in the accumulated strain occurred within 10 kilocycles. This rapid increase correlates with a peak value of tan δ (Figure 4.20). Lesser (1995) also reported that a stepwise increase in the accumulated strain correlated with a peak in tan δ.

As shown in Figure 4.21b, the initial storage modulus of the pre-fatigued specimen is approximately the same as the storage modulus at the end of the previous cyclic loading program (curve for PNC94 is the continuation of that for PNC93). Also, the evolution of the storage modulus is different for the pre-fatigued than for the virgin specimen. Strain-induced softening is not observed in the pre-fatigued specimen. Rather, the material appears to harden as if the entire test was in regime II. Based on these observations, it can be concluded that the history effect on the storage modulus is particularly important.

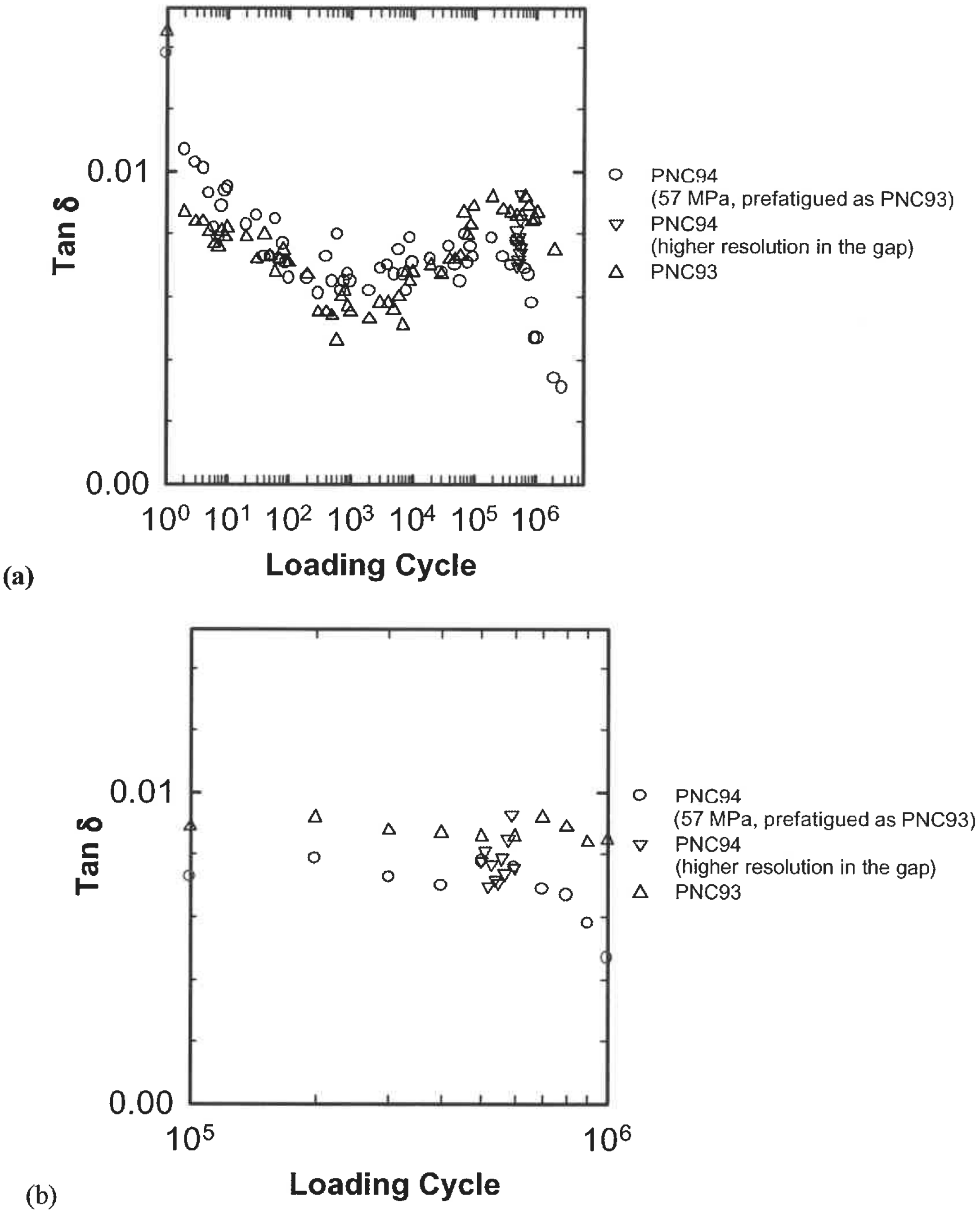

Figure 4.20: Effect of a test interruption of 4 hours on the loss tangent (For additional details, see Table 4.2).

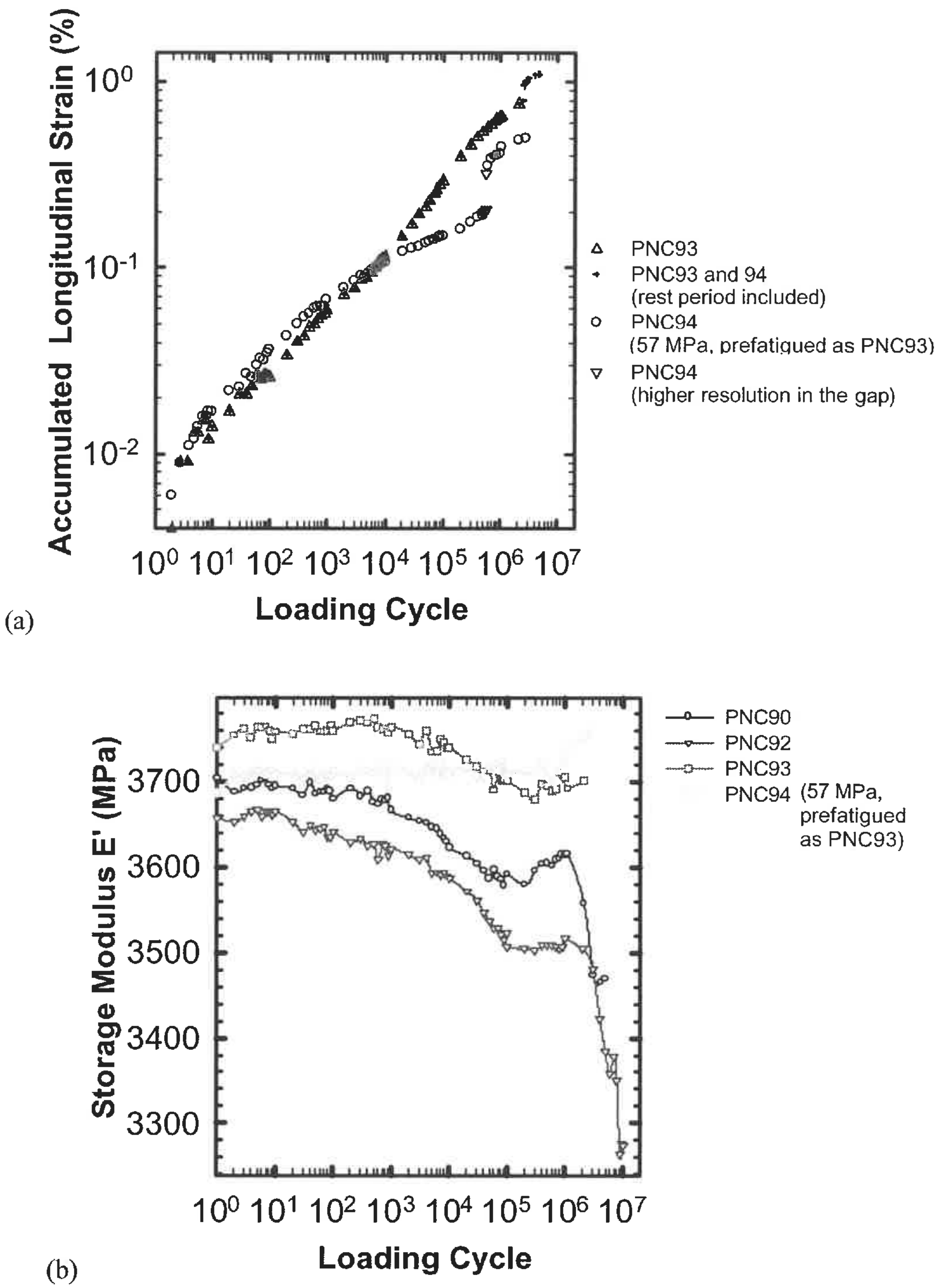

Figure 4.21: Effect of a halt of 4 hours on: (a) accumulated strain; (b) E' (For additional details, see Table 4.2).

4.1.6 Effect of Loading Ratio on the Stress-Strain-Time Response

As mentioned in the methodology (c.f. section 3.4), R was maintained at 0.1 for all tests except for a few tests. These latter tests (PNC43, PNC44 and PNC45) were carried out on PNC specimens at R=-1 (tension-compression), σ_{Amp} = 40 MPa and $\varepsilon_{Amp} \approx$ 1.08%. Under these testing conditions, ε_{Amp} was similar to that in the PNC specimens tested at R=0.1 and at a maximum cyclic stress of 57 MPa (results presented in sections 4.1.4 and 4.1.5).

The accumulated strain response calculated for the minimum strain by employing Equation 3.6 (as for tests carried out at R = 0.1) is shown in Figure 4.22a. Up to approximately 10^5 cycles, there is no significant increase in the accumulated strain calculated from the minimum strain. The variability between the two tests can be partially attributed to the low value of accumulated strain. For test PNC44, the step variation at 2 x 10^5 cycles is probably due to a displacement of the extensometer. Based upon the results from both tests, the accumulated strain appears to increase after 10^5 cycles. Because of the high variability obtained while employing the conventional calculation technique (Equation 3.6), the accumulated strain response has also been characterized employing the maximum strain (Equation 3.7). As shown in Figure 4.22b, the accumulated strain calculated from the maximum strain initially decreases in a similar way during both tests. As for the case where the accumulated strain was calculated from the minimum strain, this strain appears to increase after approximately 10^5 cycles.

Reducing the loading ratio from 0.1 to –1 appeared to eliminate any large strain accumulation up to 10^5 cycles. On a log-log scale, a negative inflection typical of regime II is observed after 10^5 cycles (Figure 4.23). In the PNC specimens tested at R = 0.1 and at a maximum cyclic stress of 57 MPa, the transition between regimes I and II was also at approximately 10^5 cycles. These results suggest that the previously defined regimes are also applicable to the behavior in tension-compression and that strain accumulation is more dependent on the average stress in regime I than in regime II.

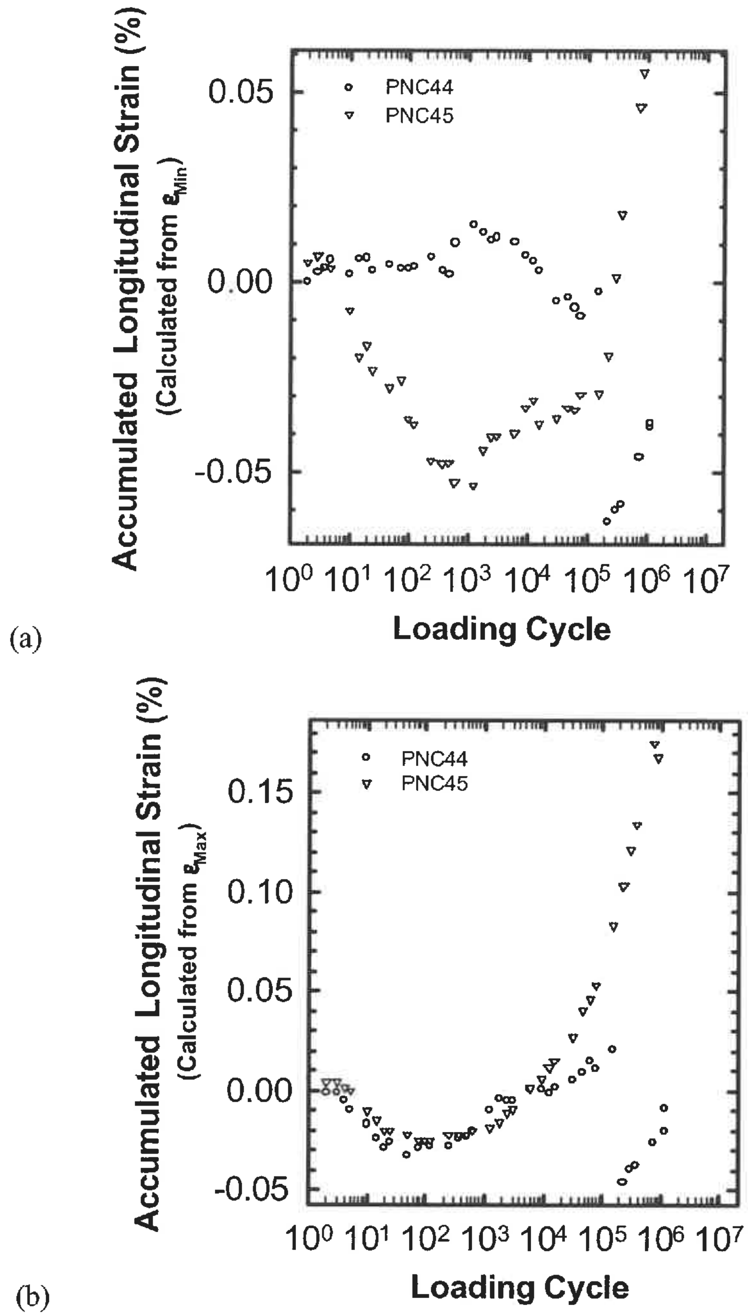

Figure 4.22: Accumulated strain response for PNC specimens tested at R=-1, σ_{Amp} = 40 MPa and $\varepsilon_{Amp} \approx$ 1.08%: (a) Accumulated strain calculated employing Equation 3.6; (b) Accumulated strain calculated employing Equation 3.7. Step variation at ~ 10^5 cycle for PNC44 probably due to measurement error.

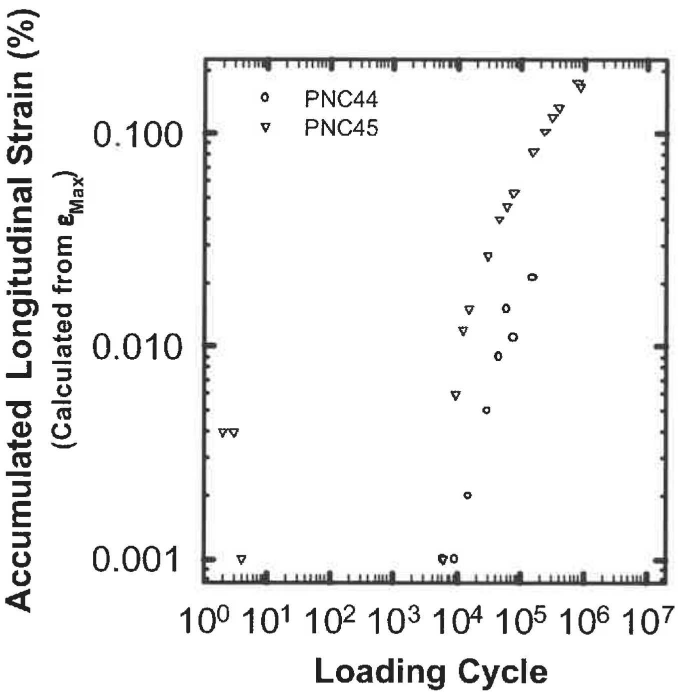

Figure 4.23: Same results as in Figure 4.22 but presented on a log-log scale.

For these tests at R = -1, the parameters for the dynamic properties have also been calculated. As shown in Figure 4.24a, the curves of tan δ present a positive inflection up to approximately 10^5 cycles where a transition to a negative inflection is observed. As shown in Figure 4.24b, the curves of E' present a negative inflection up to approximately 10^5 cycles. At approximately 10^5 cycles, a change to a positive inflection is observed. The evolution of the parameters tan δ and E' as well as the number of cycles at which the transition between regimes I and II is observed are very similar to the those during tension-tension tests at the same strain amplitude. However, E' could possibly stabilize in regime II rather than increase. Varying the loading ratio R from –1 to 0.1 while maintaining the strain amplitude has little effect on the evolution of the dynamic properties. This result strongly suggests that the deformation events leading to the evolution of the dynamic properties are stress (or strain) amplitude controlled. All the stress-strain-time results will be further discussed in section 5.2.

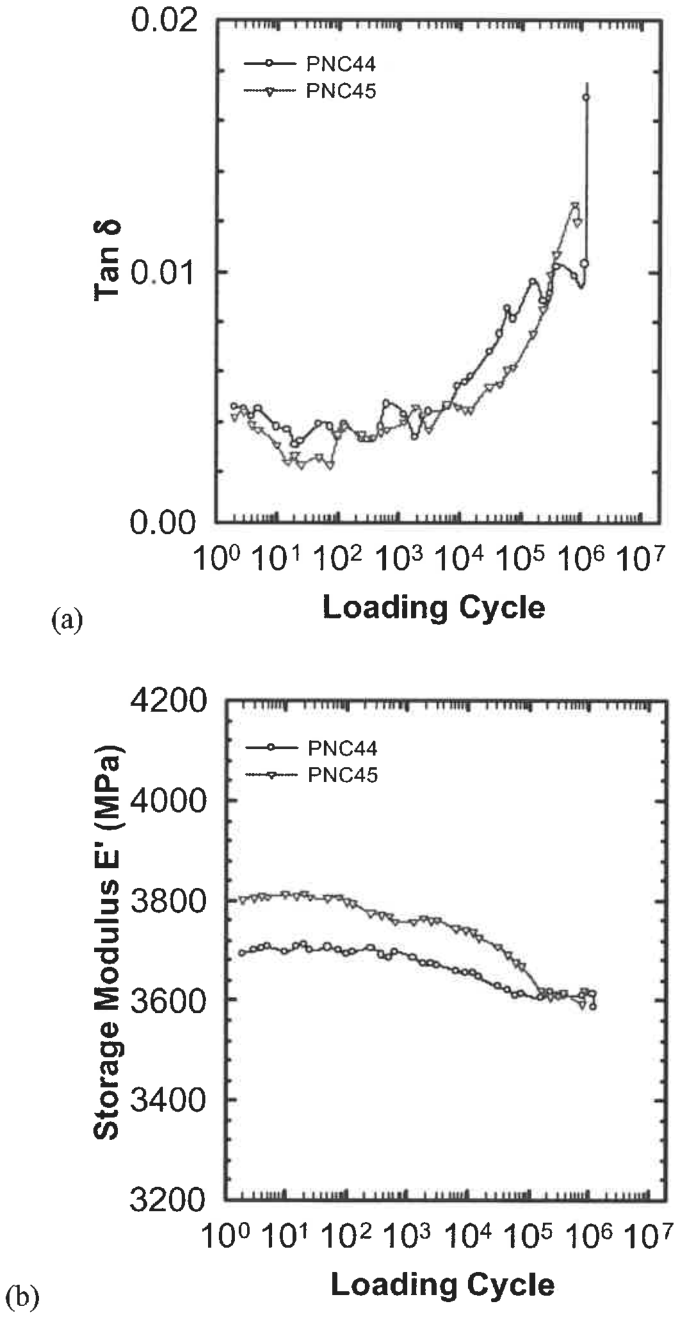

Figure 4.24: Dynamic response for PNC specimens tested at R=-1, σ_{Amp} = 40 MPa and $\varepsilon_{Amp} \approx$ 1.08%: (a) Tan δ; (b) Storage modulus E'.

4.1.7 Fatigue Lifetimes

As a result of cyclic loading, the axial fatigue specimens finally fractured. Above a critical maximum cyclic stress of approximately 78 MPa for PA6/clay and 60 MPa for PA6, fracture occurred in a macroscopically ductile manner (modes of fracture defined in section 4.1.1). Below these critical maximum cyclic stresses, the fracture was macroscopically brittle. It should be noted that the transition between these types of fracture was observed in both materials at a similar initial strain amplitude.

In Figure 4.25, the fatigue life is plotted as a function of the maximum cyclic stress for PA6 and PNC specimens from batch 3 (S-N curves). For PNC, the transition from a macroscopically ductile to a macroscopically brittle fracture corresponded to a change in the relationship between maximum stress and lifetime. For PA6, a similar change is expected even though the amount of data collected in the mechanically dominated regime is not sufficient to conclude. From the results found in the literature (Crawford and Benham, 1974a; Lesser, 1995), the curves in the thermally dominated regime (for the origin of fracture in that regime, c.f. section 2.3.2.1) should have a positive inflection. However, the inflections in the curves in Figure 4.25 are negative in the macroscopically ductile regime. To explain this discrepancy, it is proposed that mechanical instability (necking) was a precursor of the temperature increase for the fractures at maximum cyclic stresses of 78 MPa in PNC and of 62 MPa in PA6. This idea was first introduced at the end of section 4.1.2 based on the apparent threshold value, of the accumulated strain, above which macroscopically ductile fracture occurred. There could be a fatigue regime between the thermally dominated regime and the macroscopically brittle regime in which macroscopic mechanical instability would be a precursor which activates the temperature increase and the macroscopically ductile fracture.

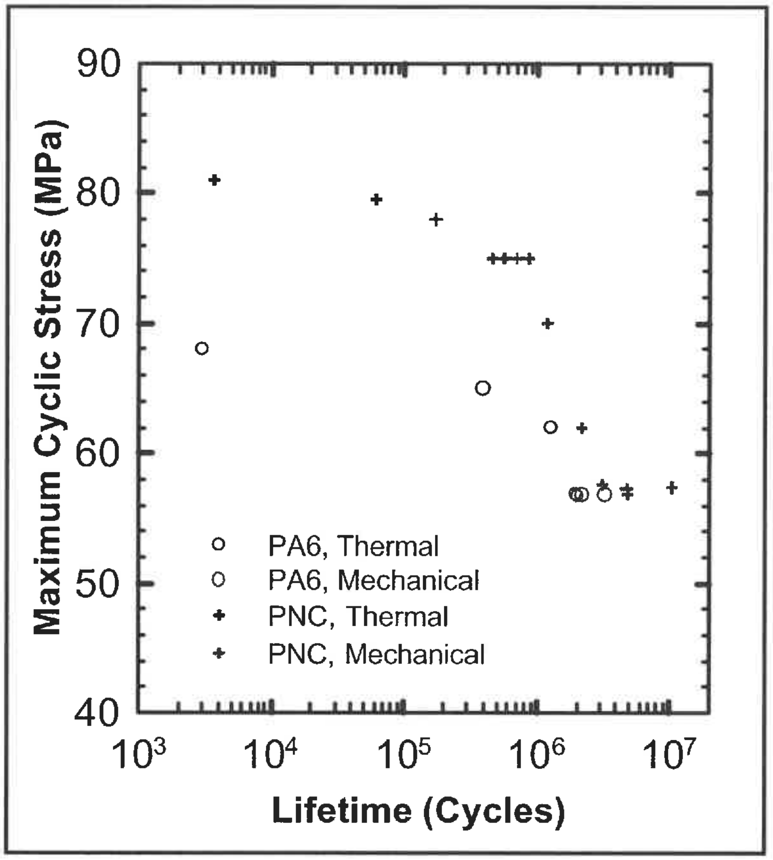

Figure 4.25: S-N curves for PNC and PA6 tested under the same conditions in the thermally and in the mechanically dominated regime.

In the macroscopically brittle regime, the test parameters have been selected to compare the resistance of PNC and PA6 at the same maximum stress of 57 MPa and at similar initial strain amplitude of approximately 0.95% (PNC at 75 MPa and PA6 at 57 MPa). The numerical data for the lifetime of each test specimen are presented in Table 4.2 (page 106) while the average lifetimes calculated from 4 data points for each test condition are presented in Table 4.6 (averages made on the logarithm of the lifetimes). At a same maximum cyclic stress, the average fatigue life was slightly more than 2 times higher for PNC than for PA6. However, at a similar initial strain amplitude the average life was more than 3 times lower for PNC than for PA6.

Table 4.6: Average fatigue lifetime for PNC and PA6 tested at a same maximum stress of 57 MPa or at similar initial strain amplitude of approximately 0.95% (averages made on the logarithm of the lifetimes).

	Same maximum stress (57 MPa)		**Similar initial strain amplitude**	
	PNC	PA6	PNC (75MPa; 0.98%)	PA6 (57MPa;0.93%)
Average lifetime (kcyc)	5289	2344	632	2344
Ratio	More than 2 fold higher for PNC		More than three fold lower for PNC	

4.2 FATIGUE CRACK PROPAGATION

Employing pre-cracked specimens, the macroscopic fatigue crack propagation rate (da/dN) has been monitored as a function of the range of stress intensity factor (ΔK). The results from these tests are presented on Paris type of plots in Figure 4.26 and Figure 4.27. As shown in Figure 4.26, the scatter in the test results for PNC is relatively high. For tests tpacd1 and tpacd2, the constant ΔK gradient employed was probably too high to enable the software to accurately control and monitor the growth of the cracks. As will be shown in the fractographic observations section (section 4.3.2), the step in the crack propagation rate that occurred during test ncd2 corresponded to a point where the local crack propagation direction and the macroscopic crack propagation direction were nearly perpendicular. This difference in the crack propagation directions appears to explain the apparent higher FCP resistance of that specimen. Since the curve for test ncd3 also presents a step at approximately the same position, the FCP resistance might also have been overestimated during that test. In comparison to the curves for tests ncd2 and ncd3, the curve for test ncd5 is very linear. For these reasons, the FCP rate results primarily considered will be those for test ncd5.

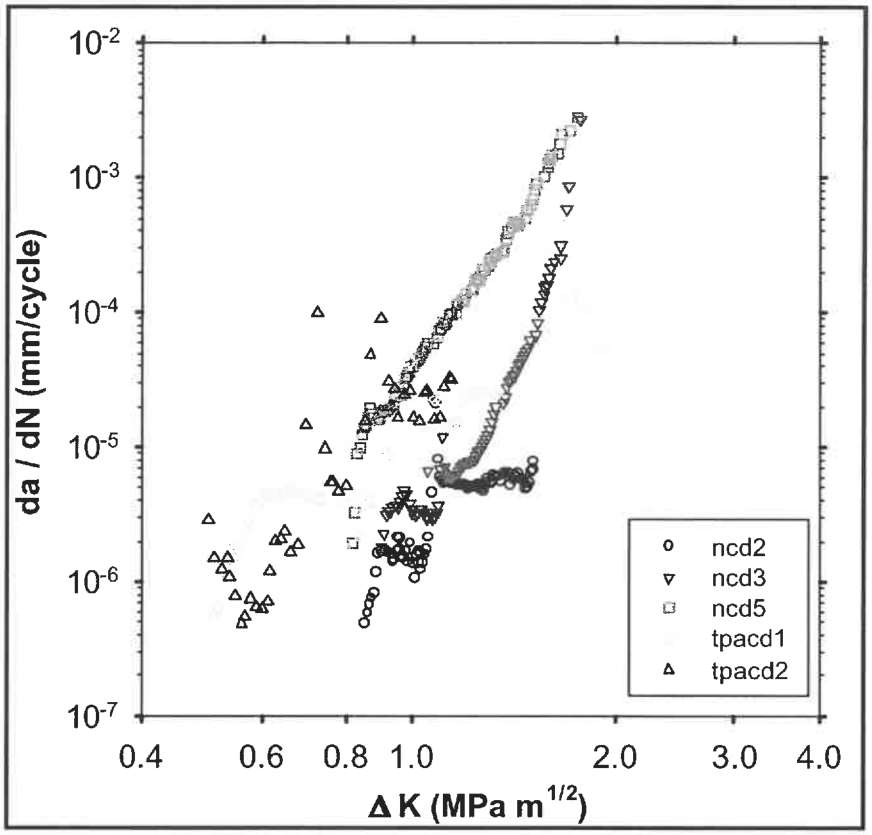

Figure 4.26: Macroscopic fatigue crack propagation rate versus range of stress intensity factor for PNC specimens (initial stress intensity varied; constant ΔK gradient of 0.14 for tpacd1, 0.11 for tpacd2 and 0.04 for the others; razor blade cut introduced before the tests except for test ncd3; results for tests tpacd1 and tpacd2 are from Bureau, 2002).

Three tests were carried out with specimens of PA6 and the results are shown in Figure 4.27. For two of these tests the initial ΔK was 0.9 $MPa.m^{1/2}$, the curves obtained were linear, and the results were highly reproducible. For the third and last test on PA6, the initial ΔK was 0.6 $MPa.m^{1/2}$, the curve was linear (except possibly near the end) and the crack propagation rate was slightly higher than during the two other tests. This small difference in the results could be related to a difference in the initial ΔK. The results shown in Figure 4.27 suggest that the FCP resistance of PA6 is decreased as a result of the addition of nanoparticles.

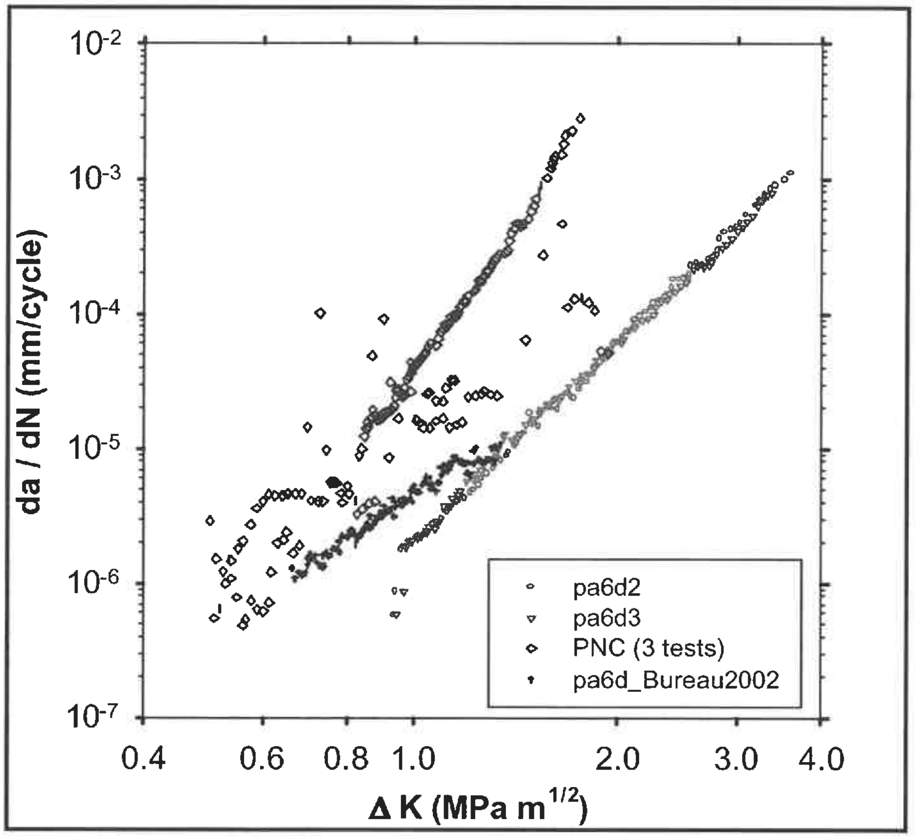

Figure 4.27: **Macroscopic fatigue crack propagation rate versus range of stress intensity for PA6 (one test starting at a ΔK of 0.6 MPa.m$^{1/2}$, 2002, and the two others at 0.9 MPa.m$^{1/2}$; constant ΔK gradient of 0.04; razor blade cut introduced before the tests) and PNC (same data as in Figure 4.26 except that tests ncd2 and ncd3 have been removed).**

4.3 FRACTOGRAPHY

After any axial fatigue tests in the macroscopically brittle fatigue regime, the fracture surface obtained presented two types of regions (c.f. Figure 4.28): a relatively small flat region perpendicular to the loading direction and a surrounding region inclined at very approximately 45° to the stress axis. As will become evident from the results to be presented shortly, the small and flat region corresponded to FCP while the surrounding region corresponded to final fracture. The FCP region is of principal interest here.

4.3.1 Fatigue Cracking in Non-Notched Specimens of PNC

In PNC, the general characteristics of the FCP region were the same for specimens from batches 2 and 3 at all maximum cyclic stresses. These characteristics will be exemplified employing observations made on a specimen from batch 2 loaded at a maximum cyclic stress of 70 MPa. When observed at low magnification (Figure 4.28), the majority of the FCP region appeared brighter on average than the surrounding final fracture region. This observation can be interpreted by a higher average local inclination in the FCP zone resulting from the presence of fibrillated matter, as will be described in detail later. Near the boundaries of the FCP zone, the brightness decreased and became even less than that in the final fracture region. This decrease in brightness corresponded to a transition in the mode of separation of the surfaces. Nearer to the middle of the FCP zone, crack propagation (or ridge) lines were found to emerge from a single point, which was the crack initiation site. A high magnification view taken near that site (Figure 4.29) revealed smaller crack propagation lines as well as the morphology and size of the inclusion from which these lines radiated.

Near the crack initiation site (Figure 4.30), the fracture surface presented small cavities in a network of interconnected lamellar broken fibrils. At a greater distance from the initiation site (Figure 4.31), the voids and fibrils increased in size. Also, the largest fibrils appeared preferentially oriented perpendicularly to the local direction of crack propagation. At the position where the average brightness decreased on the low magnification image (c.f. previous paragraph), transitions in the size and morphology of the fibrils were observed (Figure 4.32). In an intermediate morphology (middle of Figure 4.32), the fracture surface presented an “island type” structure, which probably resulted from fracture at the interface between the fibrillated deformation zone and the non-fibrillated material. Just before this type of structure (Figure 4.33), the fibrils still appeared preferentially oriented perpendicularly to the direction of crack propagation. After the “island type” structure (Figure 4.34), the size of the voids and of the fibrils markedly decreased. The fibrillated structure gradually disappeared and no cavitation was observed to contribute to the mechanism of surface separation in the area located between the end of the partially fibrillated structure and the final fracture line (Figure 4.35).

Returning to Figure 4.28, this area corresponds to the dark regions near the perimeter of the FCP region.

In specimens from batch 3, many inclusions were found to contain Mg, Ca and/or Si; whereas, the inclusions in specimens from batch 2 appeared organic in nature (section 4.1.3 and Figure 4.29). This difference in the nature of the inclusions did not change markedly the general characteristics of the FCP region. Figure 4.36 presents the complete FCP region in a PNC specimen from batch 3 loaded under a trapezoidal waveform with 0.8 s at a minimum stress of 7.5 MPa, 0.1 s at a maximum stress of 75 MPa and at a loading rate of approximately 2000 MPa/s. This region again presents a higher average brightness than the final region except near its perimeter. At a higher magnification in the middle of this FCP region (Figure 4.37), the divergence of crack propagation lines radiated from the crack initiation site. As shown in Figure 4.38, this site was found to contain an inclusion. Observations at the same site of the opposite fracture surface revealed a mirror image of this inclusion (Figure 4.39), indicating that it fractured into two pieces. The presence of very small fibrils on the surfaces of the inclusions (top left corner in Figure 4.38 and top right corner in Figure 4.39) can be noted. X-ray analysis (using an EDS) revealed the presence of Al, Mg and Si in the inclusion of Figure 4.38. For that specimen, crack initiation appears to have occurred at a large intercalated cluster of clay. Apart from this difference between this specimen and the specimen from batch 2 previously presented as an example, the fractographic details were similar. For example, the surface morphology in Figure 4.40, which was taken at half the distance between the crack initiation site and the final fracture blunting line in the specimen from batch 3, is very similar to that observed in the specimen from batch 2 loaded employing the conventional sinusoidal waveform (Figure 4.31).

The effect of the size of the inclusions on the fatigue life at a maximum cyclic stress of 75-78 MPa has already been demonstrated in section 4.1.3. At a maximum cyclic stress of 57-60 MPa, one test was carried out with a specimen from batch 2 and fracture occurred after 1047 kilocycles. As shown in Figure 4.41, a large cavity was found at the crack initiation site. This cavity was probably the trace of an inclusion more than 150 μm in length. During a typical test (PNC66) with a specimen from batch 3 tested at approximately the same maximum cyclic stress, fracture occurred after 3197 kilocycles. In this case, the inclusion at the crack initiation site was approximately 30 μm in length (Figure 4.42). From it morphology, this inclusion is expected to be an aggregate of clay related products.

4.3.2 Fatigue Cracking in Pre-Cracked Specimens of PNC

Fractographic observations have also been carried out on the fracture surfaces obtained from the FCP tests. Under a macroscopic ΔK of approximately 1.5 $MPa.m^{1/2}$ and a da/dN of approximately 10^{-4} mm/cycle (test ncd2), the fracture surface morphology at 1.5 mm from the lateral surface of the specimen (Figure 4.43) was very similar to that observed in the non-notched specimens (Figure 4.31 and Figure 4.40). This similarity and the fact that the size of the fibrils initially increased as the distance from the crack initiation site increased clearly suggests that stable fatigue crack propagation occurred in the FCP region.

For the interpretation of the fatigue crack growth rate data (section 4.2), it is of interest to characterize the manner by which the crack grew in the FCP specimens. Crack propagation (or ridge) lines oriented perpendicularly to the macroscopic crack propagation direction were observed in specimen ncd2 at 5 mm from the razor blade cut (Figure 4.44), thus suggesting an important difference between the macroscopic and the microscopic crack propagation directions. This position approximately corresponds to the step in the crack growth rate, which occurred slightly above a macroscopic ΔK of 1 $MPa.m^{1/2}$ (c.f. Figure 4.26 in section 4.2). As shown in Figure 4.45, crack propagation lines oriented at an angle from the macroscopic crack propagation direction were also observed at high ΔK. The final fracture blunting line in all FCP specimens of PNC presented a pronounced curvature at the specimen mid-thickness. The crack length was approximately 2 mm longer in the middle of the specimen than near the lateral surfaces. The curvature of the final fracture blunting line was much less pronounced in the case of PA6.

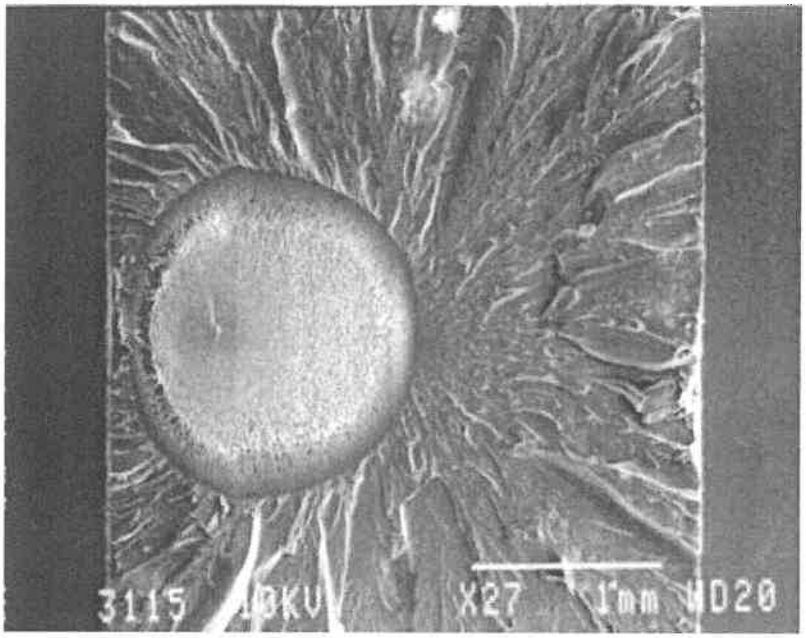

Figure 4.28: Complete region of fatigue crack propagation in a PNC specimen from batch 2 (maximum stress of 70 MPa, 663 kilocycles to fracture).

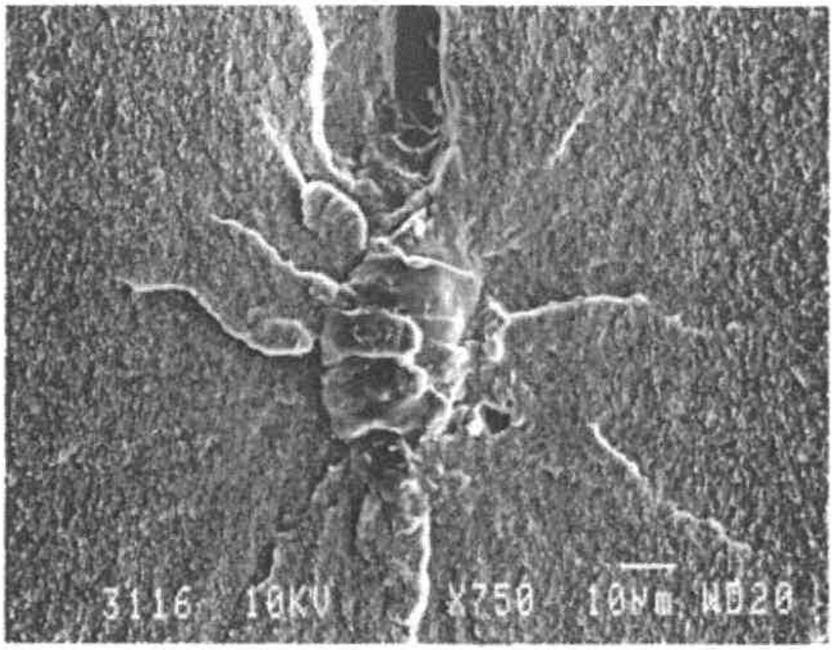

Figure 4.29: Inclusion at the initiation site in the specimen shown in Figure 4.28.

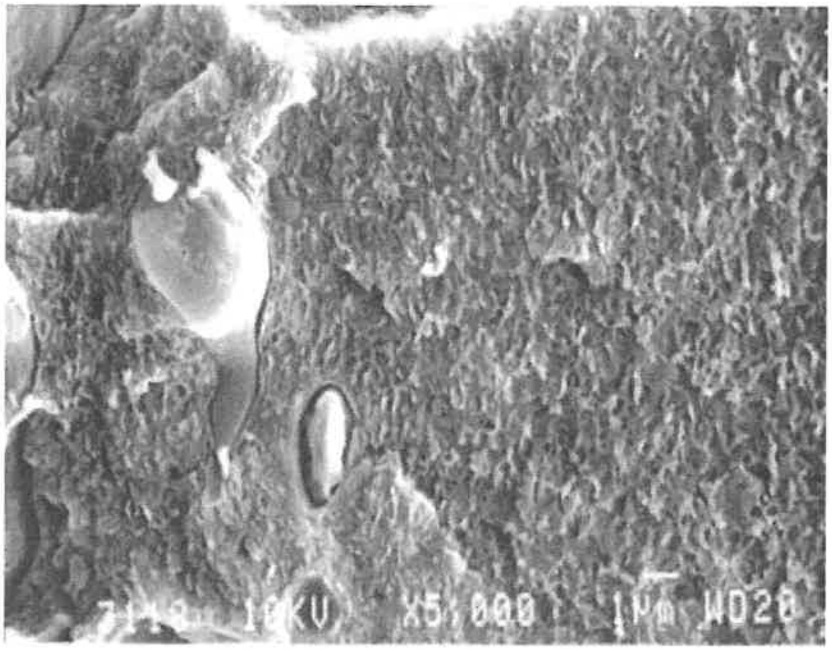

Figure 4.30: **Fractographic features near the fatigue initiation site in the specimen shown in Figure 4.28 (crack propagation direction from left to right).**

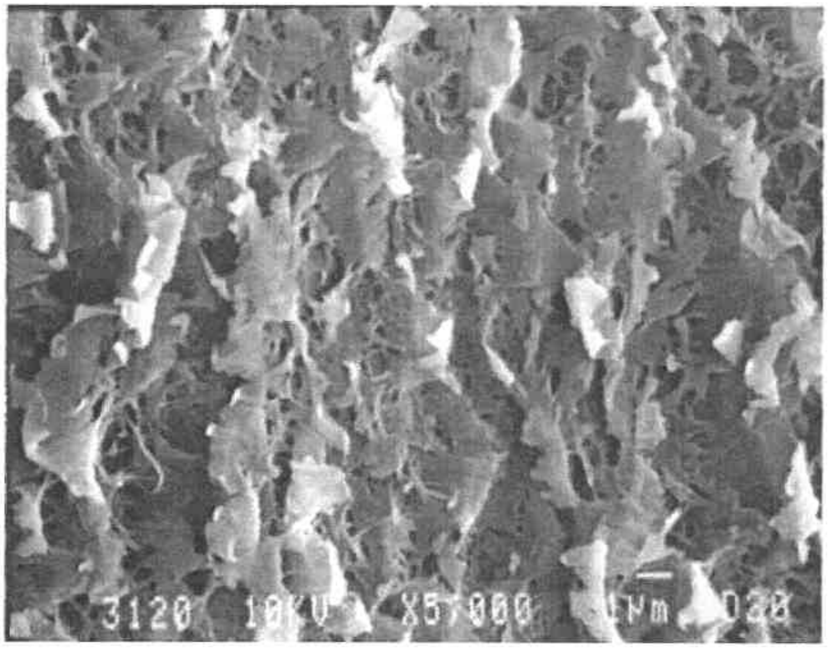

Figure 4.31: **Fatigue crack propagation at approximately 150 µm from the initiation site in the specimen shown in Figure 4.28 (crack propagation direction from left to right).**

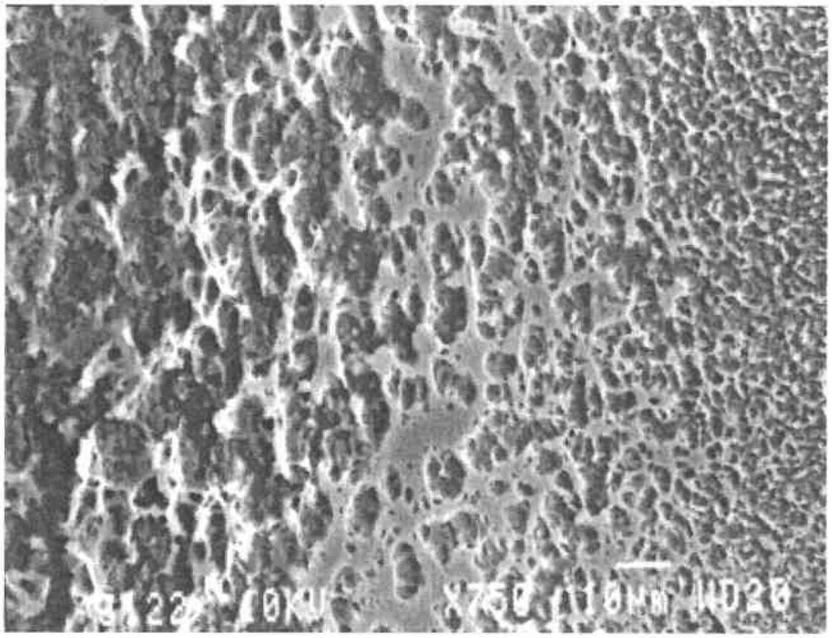

Figure 4.32: Transitions in the fractographic features near the end of the zone of the fatigue crack propagation in the specimen shown in Figure 4.28 (crack propagation direction from left to right).

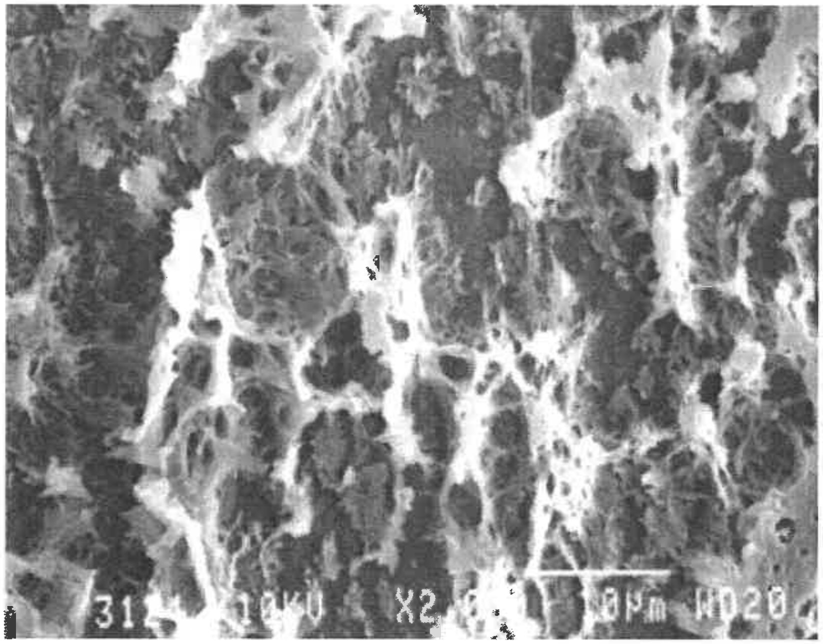

Figure 4.33: Higher magnification view of a region located on the left side of Figure 4.32 (crack propagation direction from left to right).

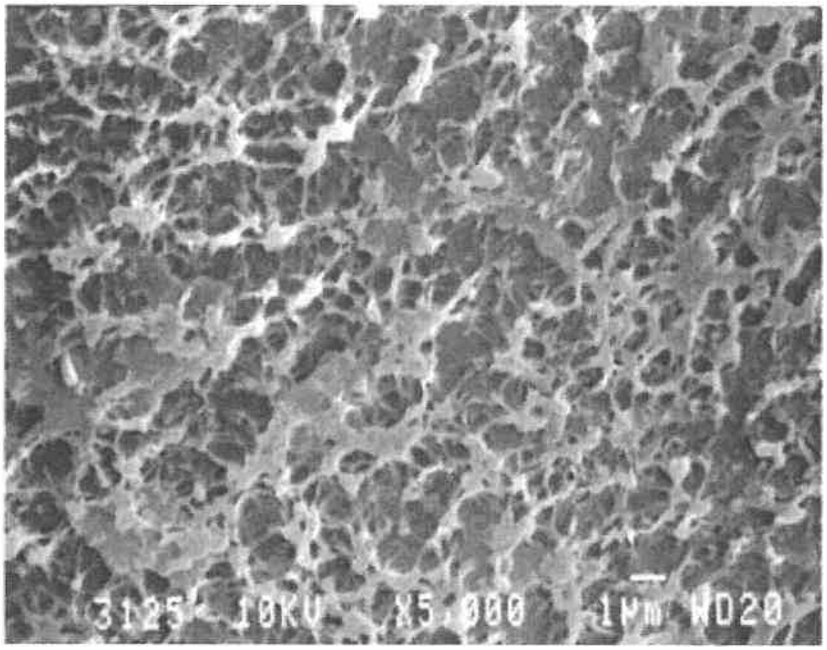

Figure 4.34: Higher magnification view of a region located on the right side of Figure 4.32 (crack propagation approximately from left to right).

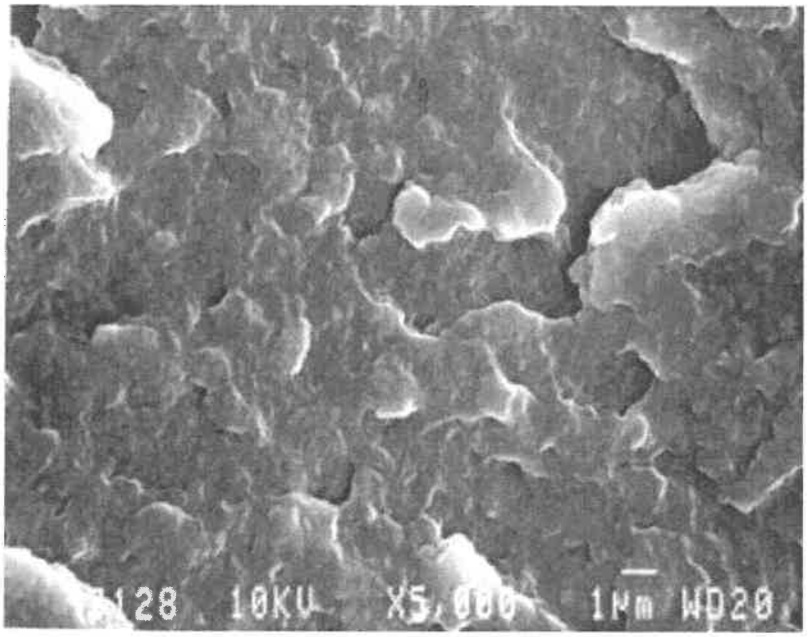

Figure 4.35: Surface separation without apparent cavitation in an area of the fracture surface located between the end of the partially fibrillated structure and the final fracture line (specimen shown in Figure 4.28).

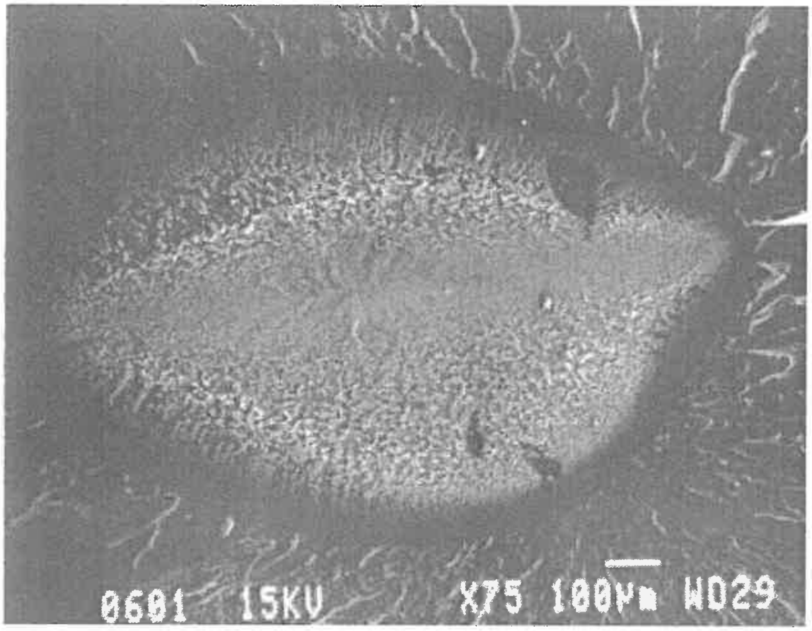

Figure 4.36: Complete region of fatigue crack propagation in a PNC specimen from batch 3 (trapezoidal waveform, 0.8 s at minimum stress of 7.5 MPa, 0.1 s at maximum stress of 75 MPa, loading rate of approximately 2000 MPa/s, 132 kilocycles to fracture).

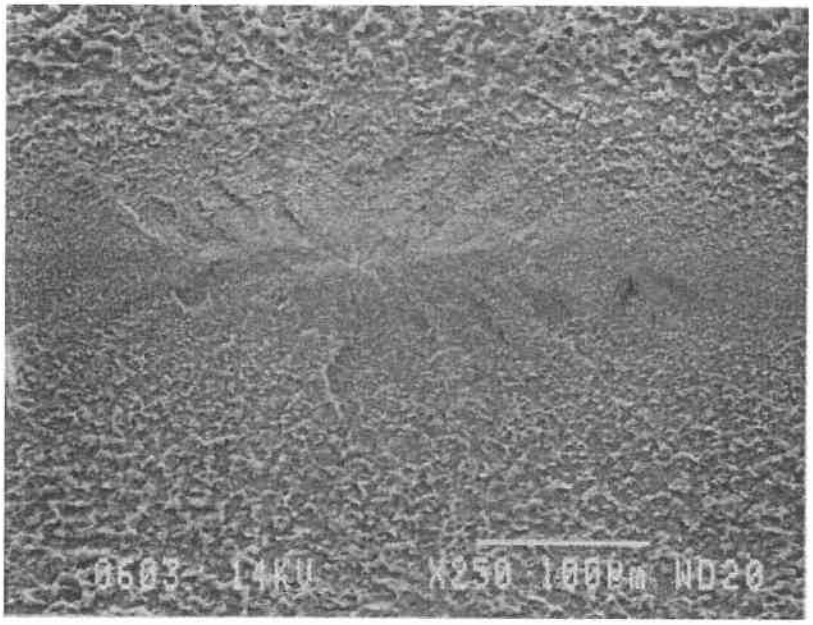

Figure 4.37: Divergence of crack propagation lines from the approximate position of the crack initiation site in the specimen shown in Figure 4.36.

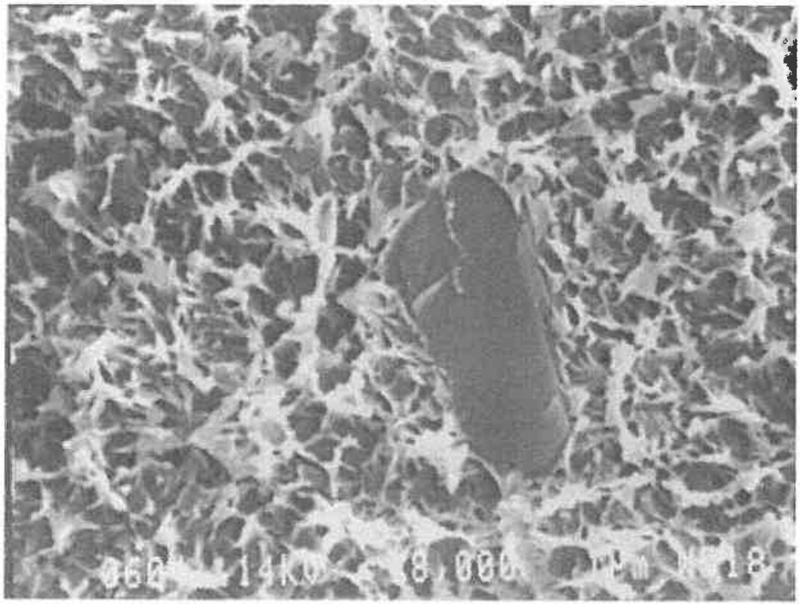

Figure 4.38: Inclusion at the apparent crack initiation site in the specimen shown in Figure 4.36.

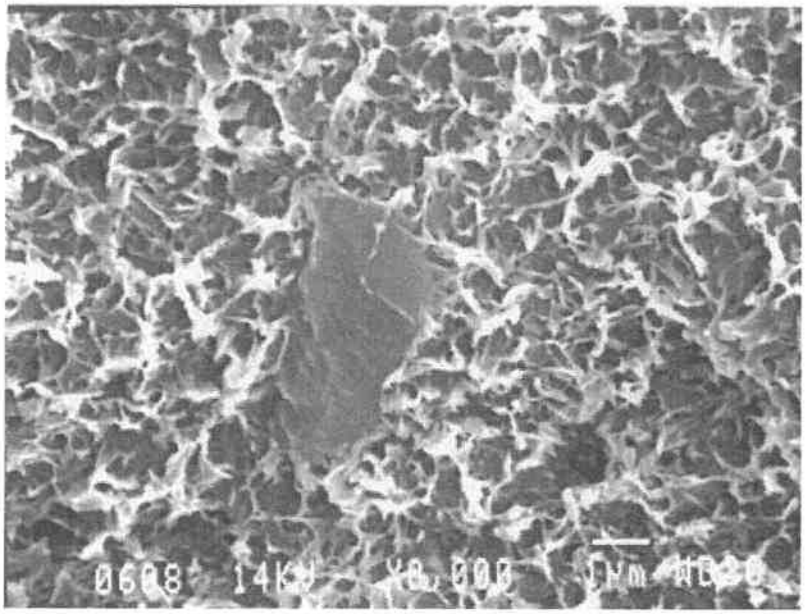

Figure 4.39: View of the opposite surface at the same position as in Figure 4.38 (Note: The lines at matching sites indicate that this inclusion fractured into two.).

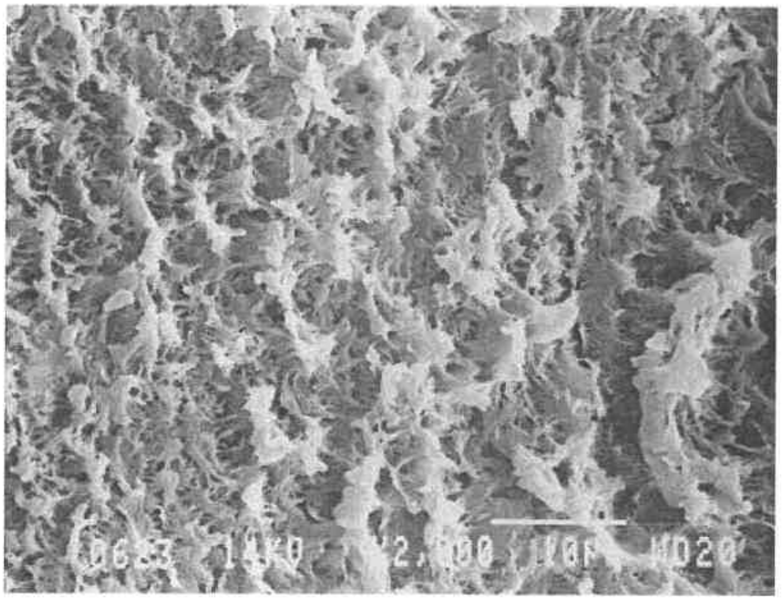

Figure 4.40: Fatigue crack propagation at approximately half the distance between the crack initiation site and the final fracture blunting line in the specimen shown in Figure 4.36 (crack propagation direction approximately from left to right).

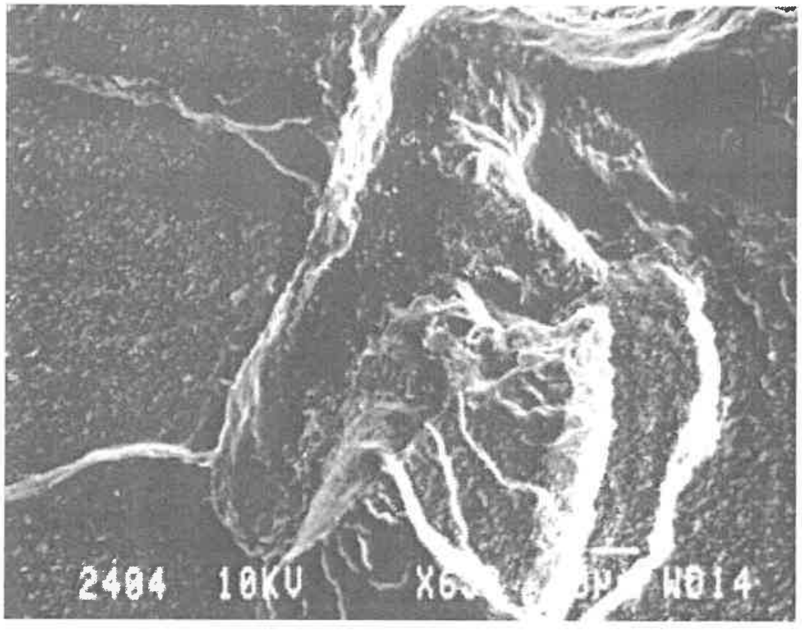

Figure 4.41: Trace of the inclusion at the crack initiation site of a PNC specimen from batch 2 (test PNC47): maximum cyclic stress of 58 MPa, 1047 kilocycles to fracture.

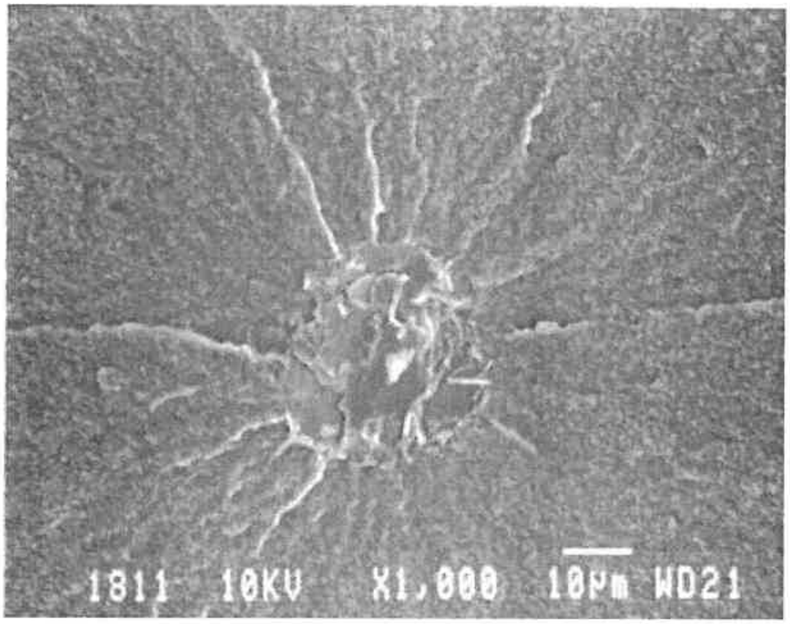

Figure 4.42: Small inclusion at the crack initiation site of a PNC specimen from batch 3 (test PNC66): maximum cyclic stress of 57 MPa, 3197 kilocycles to fracture.

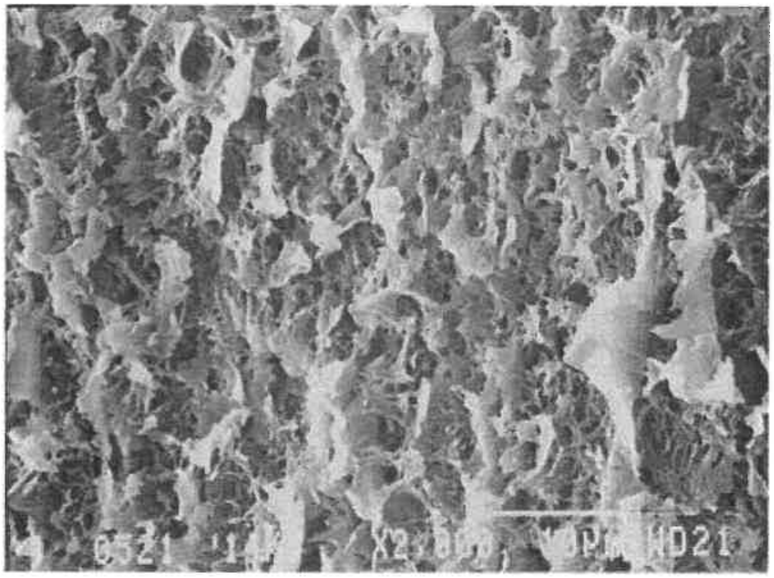

Figure 4.43: Fatigue crack propagation surface obtained during FCP tests on PNC (test ncd3; macroscopic $\Delta K \approx 1.5$ MPa.m$^{1/2}$ and da/dN ≈ 10^{-4} mm/cycle; local crack propagation direction approximately from left to right; observations at 1.5 mm from lateral surface of specimen).

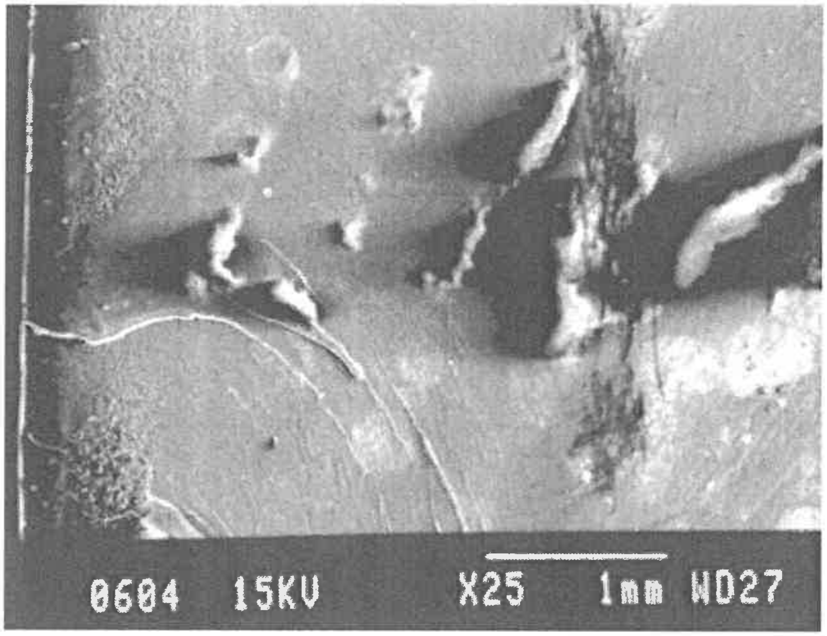

Figure 4.44: Fracture surface at 5 mm from the razor blade cut for the FCP test ncd2: the specimen thickness direction is horizontal. Macroscopic cracking direction is from bottom to top.

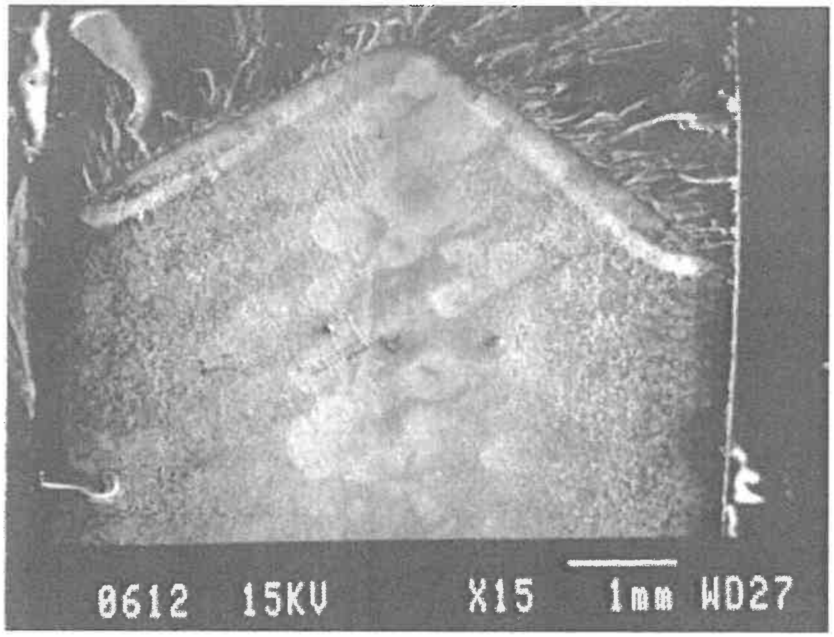

Figure 4.45: Fracture surface just before and after final fracture for the FCP test ncd2: specimen thickness direction is horizontal and the macroscopic cracking direction is from bottom to top.

4.3.3 Fatigue Cracking in PA6

Many characteristics of the FCP region on the fracture surface of specimens of PA6 were different than those already presented for PNC. The observations from a test on a PA6 specimen from batch 2, which failed after 1100 kilocycles of cycling at a maximum stress of 60 MPa, will be first presented. At low magnification (Figure 4.46), a large proportion of the FCP region did not appear brighter in average than the final fracture region. As with PNC, the divergence of the crack propagation lines allowed to determine the crack initiation site. Crack initiation occurred near an inclusion more than 80 μm in length (Figure 4.47). Near the crack initiation site (Figure 4.48), fatigue crack propagation occurred preferentially along the local radii of the spherulites. A few small cavities were observed but most of the surface separation process appears to have occurred by shear. At a larger distance from the crack initiation site (Figure 4.49), large half dimples were observed and these dimples were found to contain smaller half dimples. From the orientation of the half dimples, it is expected that several major crack reinitiation events occurred in front of the crack tip and that the resulting cracks grew in all direction up to a point where they coalesced, which resulted in complete separation of the fracture surfaces. The transition from crack propagation occurring preferentially along the local radii of the spherulites to crack propagation by coalescence of large dimples occurred gradually.

On the fracture surfaces obtained from a FCP test (pa6d3), Bureau (2002) also observed a similar transition. Since the power law relationship between the crack propagation rate and the stress intensity range did not change as a result of that transition (see results for test pa6d3 in section 4.2), it appears that that transition in the fractographic features does not correspond to a fundamentally different mechanism of fatigue crack propagation.

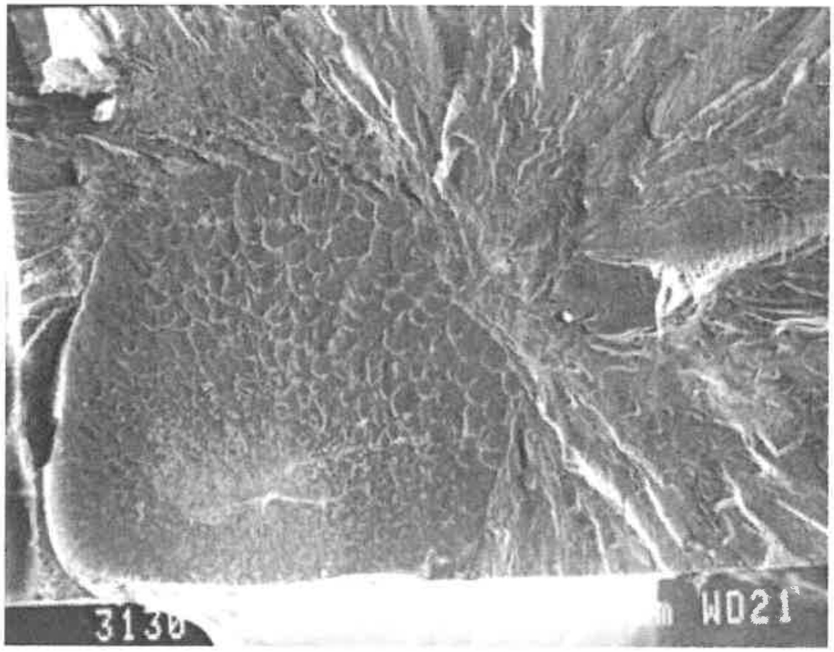

Figure 4.46: Complete region of fatigue crack propagation in a PA6 specimen from batch 2: maximum stress of 60 MPa, 1100 kilocycles to fracture.

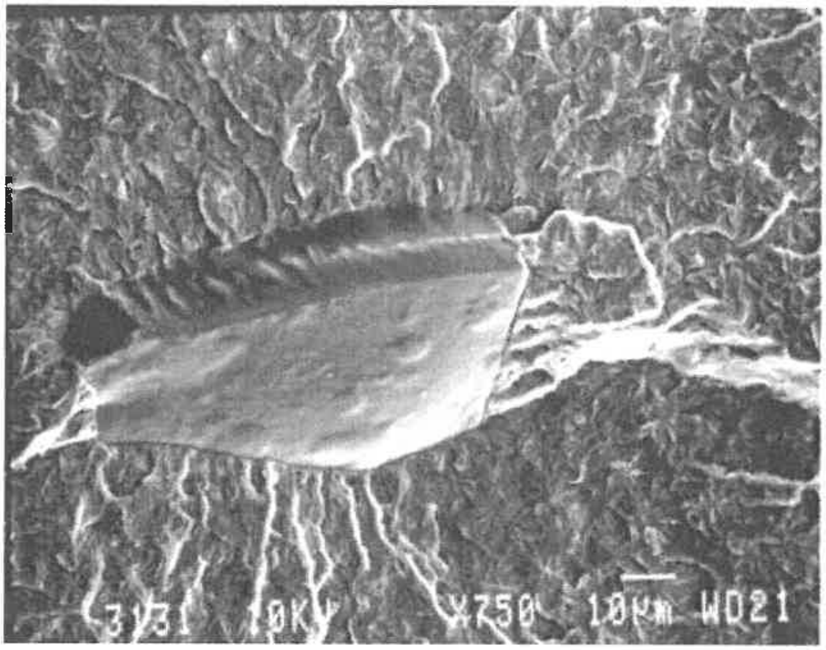

Figure 4.47: Inclusion at the initiation site in specimen shown in Figure 4.46.

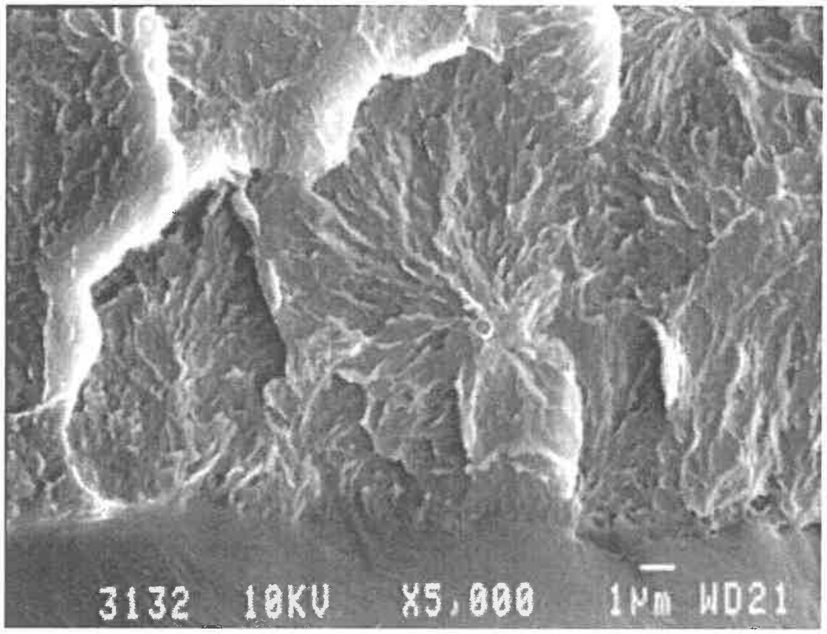

Figure 4.48: Fatigue crack propagation near the initiation site in the specimen shown in Figure 4.46 (crack propagation from bottom to top).

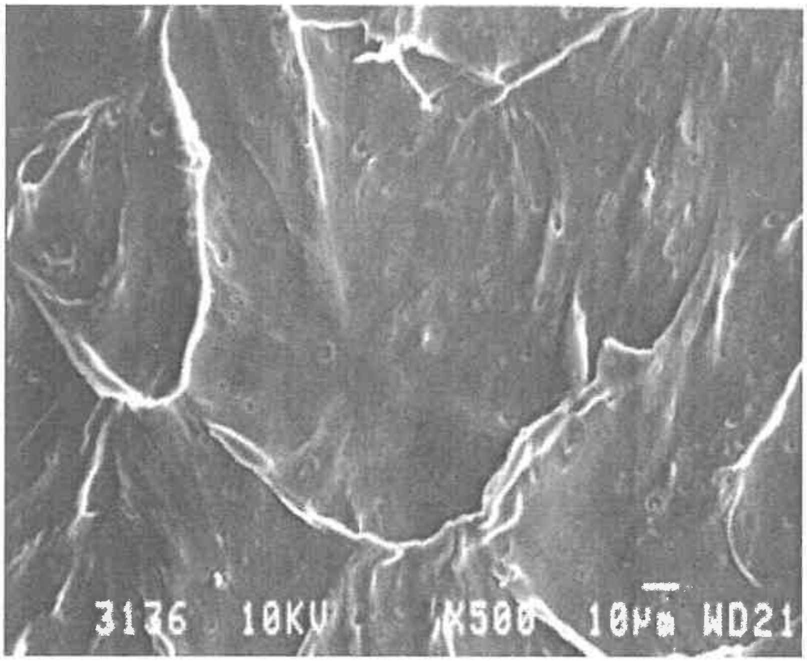

Figure 4.49: Fatigue crack propagation at higher crack propagation rate in the specimen shown in Figure 4.46 (crack propagation from bottom to top).

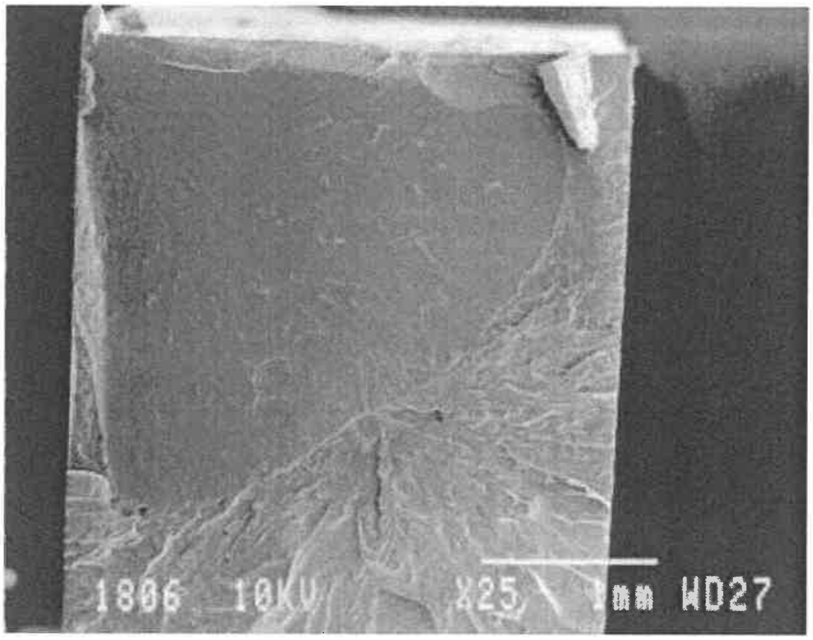

Figure 4.50: Complete region of fatigue crack propagation in a PA6 specimen from batch 3 (PA23): maximum stress 57 MPa, 3321 kilocycles to fracture.

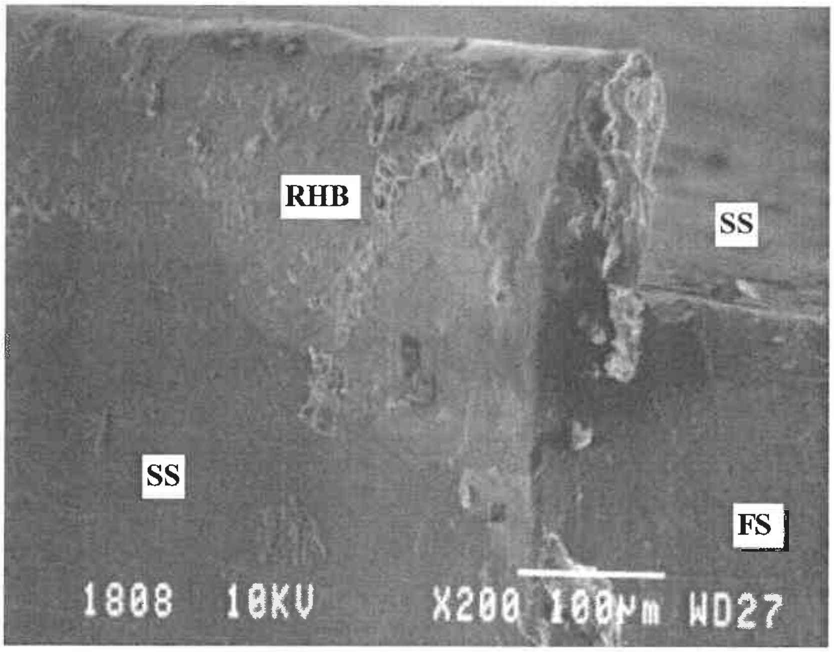

Figure 4.51: View of the specimen surfaces (SS) and fracture surface (FS) near the crack initiation site in the same specimen as in Figure 4.50 (Note region of higher brightness, labeled RHB, on the specimen surface).

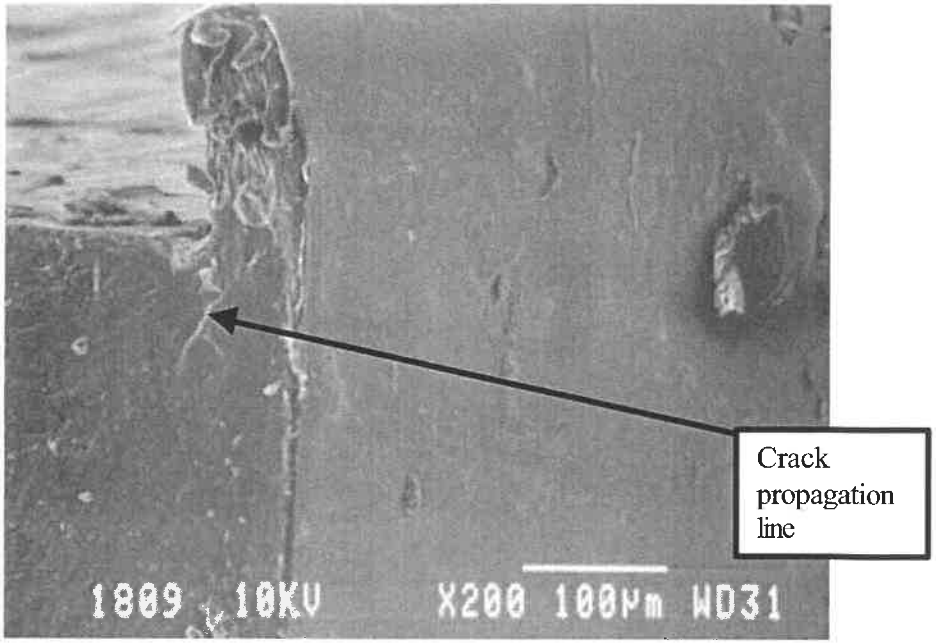

Figure 4.52:View of the specimen surfaces (upper left; right) and fracture surface (bottom left) near the crack initiation site in the same specimen as in Figure 4.50 (Note the absence of region of higher brightness on the specimen surface).

In a specimen from batch 3 (PA23), which failed after 3321 kilocycles at a maximum cyclic stress of 57 MPa, the divergence of the crack propagation lines suggested that crack initiation occurred very close to the external surface of the specimen (Figure 4.50). Since the fracture surfaces were damaged due to rubbing effects between the opposite surfaces, it was not possible to pinpoint the exact position of crack initiation. The presence of a large crack propagation (or ridge) line at the position indicated in Figure 4.52 suggests that crack initiation and propagation occurred from at least two distinct sites. On the specimen external surface, a region of higher brightness was observed on one side of the fracture surface plane (Figure 4.51) but not on the other (Figure 4.52). The zone of higher brightness could be due to the presence of impurities in the melt but also to a damage created to the specimen before or after fracture.

4.4 MORPHOLOGY OF THE DAMAGE ZONE

Observations on a cross-section containing the macroscopic crack propagation direction and the loading direction and intersecting the fracture surface of a FCP specimen of PNC were carried out following the methodology described in section 3.7. As shown in Figure 4.53, these observations were made at 12 mm from the razor blade cut and at 1.5 mm from the lateral surface of specimen ncd3. The macroscopic crack propagation rate (da/dN) was approximately 10^{-4} mm/cycle and the range of stress intensity (ΔK) was approximately 1.5 $\mathrm{MPa.m^{1/2}}$.

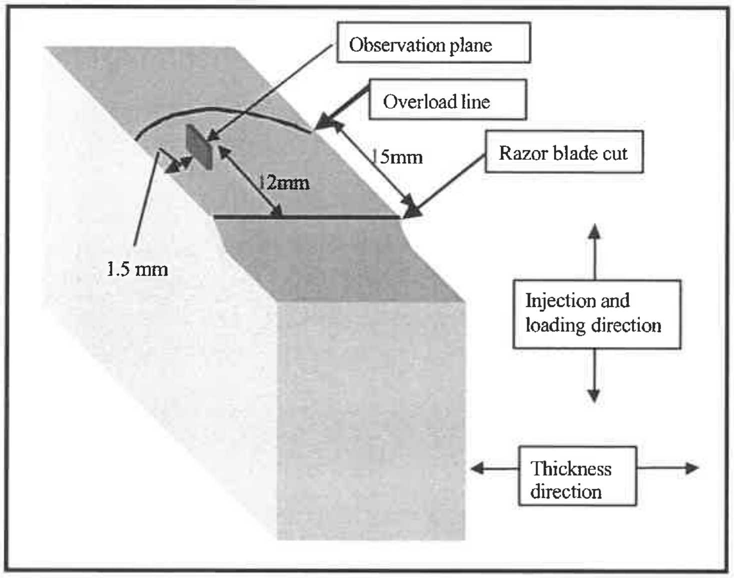

Figure 4.53: Position of the cross-section observation plane relative to the FCP specimen ncd3 and to the loading conditions.

Figure 4.54 presents a low magnification view obtained during these observations. The labels A and B are positioned over the fracture surface, which is inclined at more than 80° relative to the observation plane. Very near the inclined fracture surface, there is a zone of important deformation and of approximately constant thickness. In the bulk material, a small region located in the bottom right corner appears brighter than the average. As seen at higher magnification (Figure 4.55), this region contains cavities of approximately 1 μm in size. This observation suggests the presence of a high density of intercalated clusters in this small region.

When the region surrounding the highly deformed zone was observed at higher magnification (Figure 4.56), the damage zone appeared to have a constant morphology throughout its thickness of approximately 4 μm. Also, there was little or no gradient in the morphology of the bulk material located at more than 8 μm from the crack plane, suggesting that this material had not been strongly deformed. Between the deformation zone and the relatively non-deformed bulk material, an interface appeared present where the surface density of voids was larger than in the two other regions (Figure 4.57). At a magnification of 40000X (Figure 4.58), voids of very different sizes were observed. The bottom of several of these voids appeared relatively flat (e.g. that in the bottom right corner of Figure 4.58), which could suggest the presence of intercalated clusters of clay.

At least in one area, there was no highly deformed zone between the crack plane and the relatively non-deformed bulk material (Figure 4.59). In these areas, the crack might have propagated at the interface between the highly deformed zone and the relatively non-deformed bulk. In another area, it was possible to observe secondary cracking as well as a large fibril attached to the fracture surface (Figure 4.60). At high magnification, the surface of this large fibril appeared to contain sub-micron fibrils (Figure 4.61). The presence of secondary cracks within the deformed layer suggests that this layer does not have a higher resistance to crack propagation than the interface between the deformed layer and the non-deformed bulk material. Therefore, it is expected that crack propagation generally occurred in the middle of this deformed layer.

Finally, an attempt was made to observe the fatigue damage just below the fracture surface of one axial fatigue specimen (test PNC42, maximum cyclic stress of 85 MPa, 4 seconds of rest between each set of five loading cycles, macroscopically brittle fracture, fatigue life of 36.5 kilocycles) by TEM. The samples used for these observations were produced by ultra-microtomy at low temperature. A thin palladium coating was to be added to the fracture surface before ultra-microtomy, but this was not been done. Unfortunately, all the samples became highly rolled around themselves and it was not possible to determine the distance from the fracture surface at which the observations were made. These observations did not allow to observe any gradient in deformation nor to reveal any voided structure. They will not be further considered.

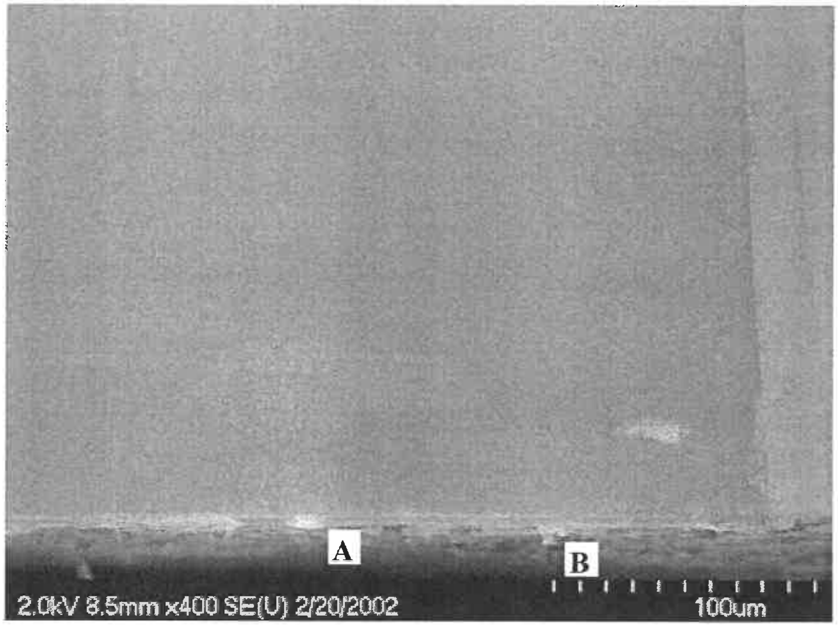

Figure 4.54: Low magnification view indicating a relatively constant width of the deformation zone (crack propagation direction is horizontal; references A and B for the next figures).

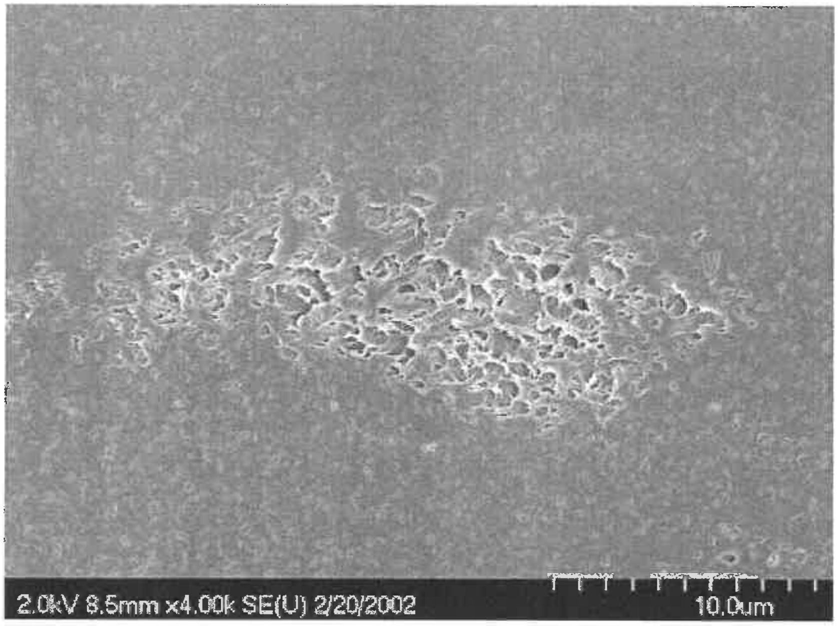

Figure 4.55: Zone of cavitation located in the bulk (c.f. right bottom corner of Figure 4.54).

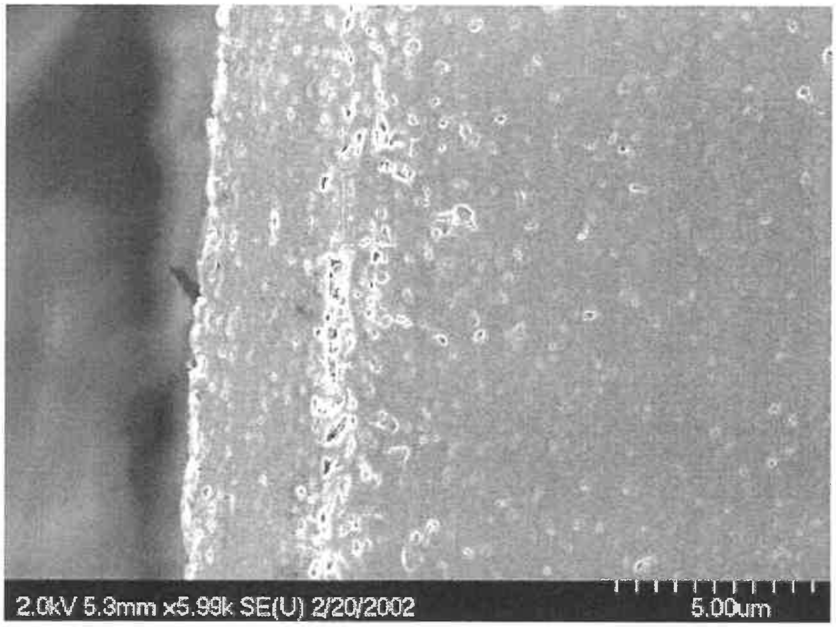

Figure 4.56: From left to right: fracture surface, relatively highly deformed zone, interface containing microvoids, and bulk material (crack propagation direction is vertical; observations between regions labeled A and B in Figure 4.54).

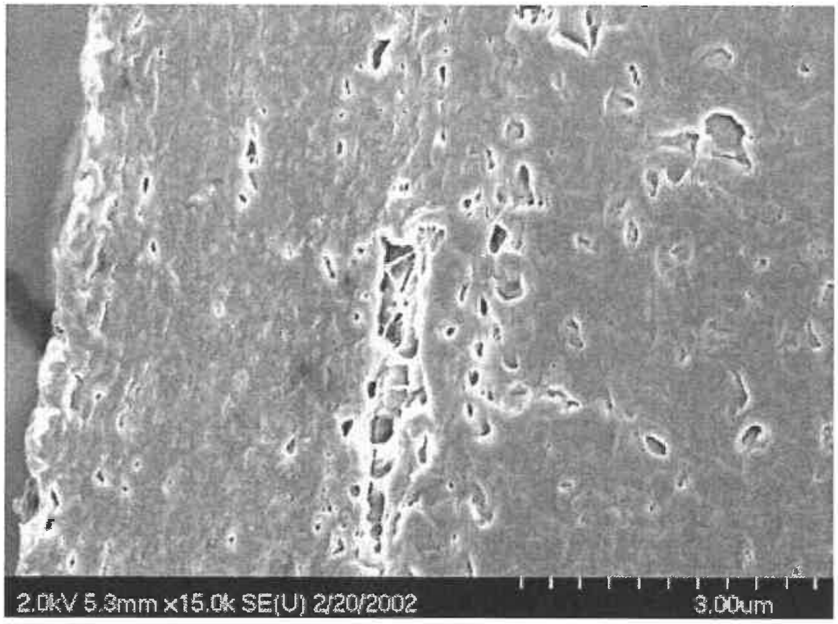

Figure 4.57: Higher magnification view of Figure 4.57 (region near the center).

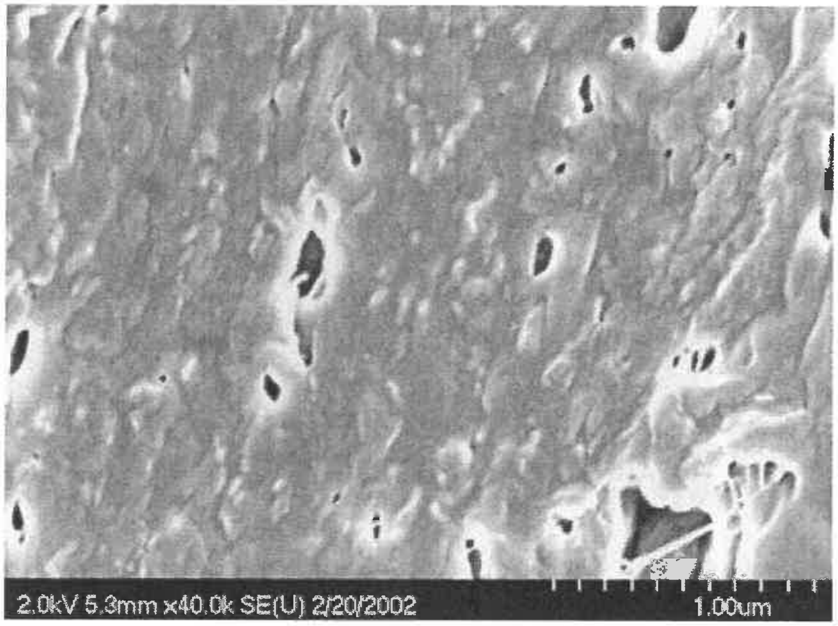

Figure 4.58: Higher magnification view of Figure 4.57 (region near the center).

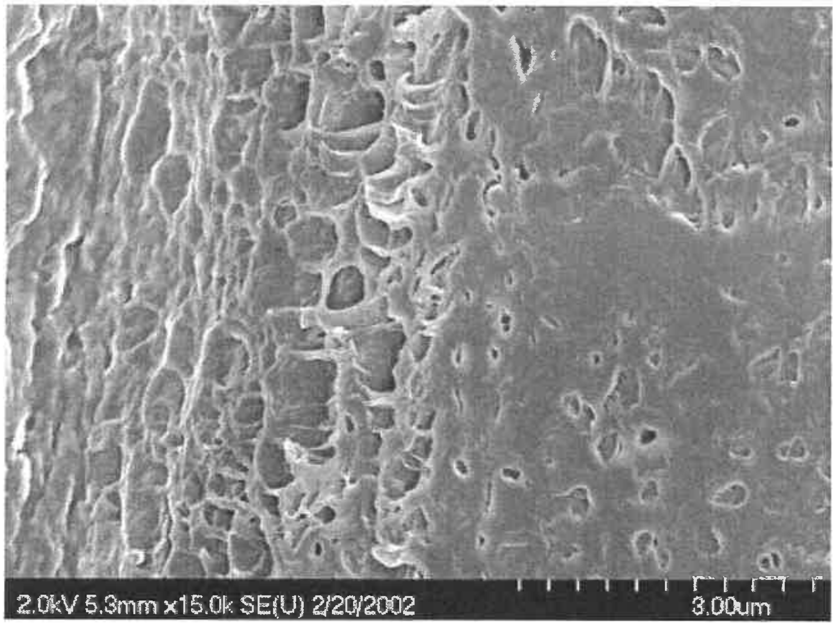

Figure 4.59: Region where the zone of important deformation between the fracture surface and the bulk appears absent (crack propagation direction is vertical; observations slightly to the left of the region labeled A in Figure 4.54).

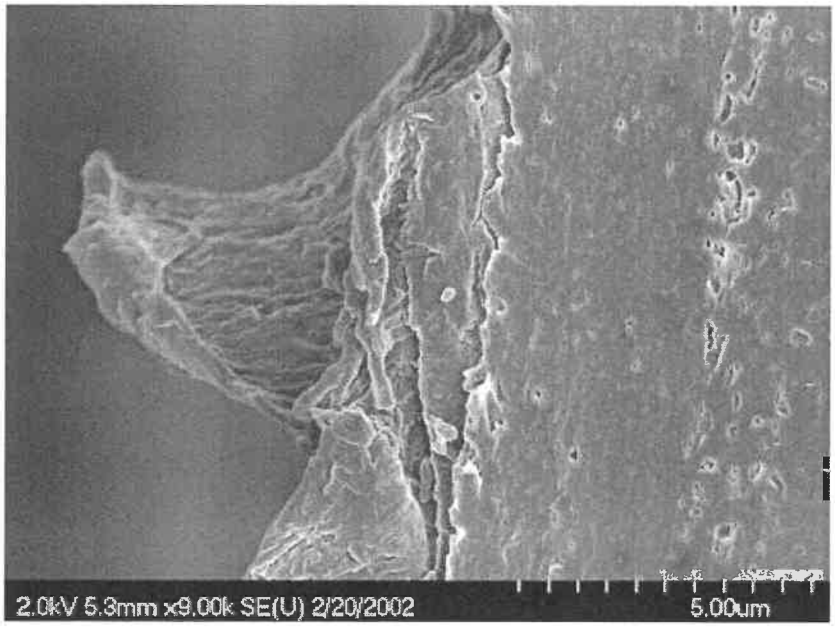

Figure 4.60: Region where a large fibril attached to the fracture surface is located near the cross-section plane (crack propagation direction is vertical; observations slightly to the left of the region labeled B in Figure 4.54).

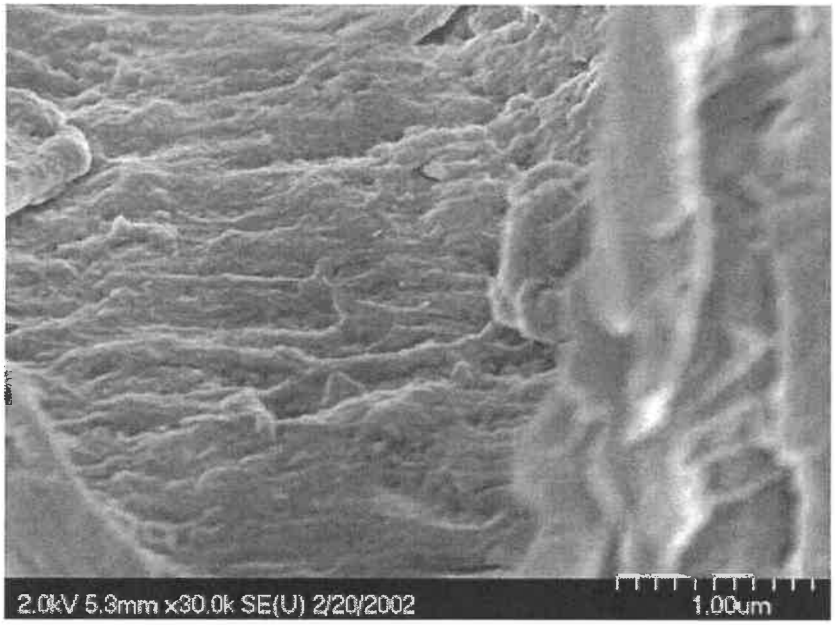

Figure 4.61: Surface morphology of the large fibril observed in Figure 4.60.

5 GENERAL DISCUSSION

The fractographic and morphological observations performed permitted to characterize partially the damage introduced in a small proportion of the specimen volume during crack propagation. Fatigue propagation tests permitted to characterize the resistance of the materials to such confined damage. The stress-strain-time response obtained from the axial fatigue tests enabled to characterize the damaging processes occurring at lower local strain and in a higher proportion of the specimen volume. The fractographic observation of the fracture surfaces of the axial fatigue specimens permitted to identify the fatigue crack initiation sites.

5.1 MACROSCOPICALLY HOMOGENEOUS DAMAGE PROCESSES

The preliminary results on specimens from batch 2 revealed the absence of correlation between the site of crack initiation (or the fatigue lifetime) and the accumulated strain response (c.f. section 4.1.2). Therefore, the strain response measurements are not sensitive to the events related to macroscopic crack initiation and early propagation. The analysis of the accumulated strain and of the accumulated volume variation of the specimens from batch 3 extended this finding by indicating that the regime III is not a direct consequence of macroscopic strain localization. Accordingly, it appears reasonable to consider that the three regimes of the stress-strain-time response characterize transitions in processes occurring macroscopically homogeneously throughout the whole gauge section of the specimens.

5.1.1 Significance of the Transitions in the Response

The three regimes defined in section 4.1.4 are not necessarily exclusive. The transitions observed in the response may correspond to the inhibition of previously activated molecular events rather than the occurrence of new events. This proposition is supported by the evolution of the rate of strain accumulation (Sherby-Dorn type of plot)., The rate of strain accumulation decrease throughout regimes I and II, which suggests the inhibition of some of the molecular events occurring during fatigue. In fact, the overall accumulated strain response could be represented by a dashpot in series with other dashpot and spring units. For the concepts attached to these terms, the reader is referred to the appendix (section A.1). Based on such a model, the deformation of the polymer in regime III would be controlled only by the molecular processes of viscous flow.

5.1.2 Hypothesis on the Nature of Molecular Events

Some information on the nature of the molecular events can be obtained from the experimental results and from the literature review. The accumulation of strain can be expected to result from viscoelastic alignment of the molecular segments by migration of molecular kinks or reptation (c.f. appendix, section A.2.2) along the tensile direction. A certain reversibility of the accumulated strain was observed when the tests were interrupted (c.f. section 4.1.5), which can be explained by a reversibility of the migration of the molecular kinks. In regime I, the accumulation of strain was largely reduced when the loading mode was changed to tension-compression (c.f. section 4.1.6). This can be attributed to an important effect of the maximum stress in activating the above-mentioned mechanisms or to the occurrence of the same mechanisms (in the opposite direction) during the compressive part of the cycle. By analogy to the explanation for the behavior in creep (c.f. appendix, section A.1.2.5), the transition from regime I to regime II could correspond to an increase in the activation volume for a molecular event. Finally, the accumulated strain in regime III could result from disentanglement and reptation only.

The general effect of cycling in regime I is a decrease in E' that is stress amplitude (c.f. section 4.1.6) controlled and irreversible (c.f. section 4.1.5). This decrease could result from an increase in the proportion of free volume in the molecular network. However, one would expect any increase in the proportion of free volume to be relatively quickly recovered during test interruption, which was not the case (c.f. section 4.1.6). As an alternative explanation, the decrease in E' could be attributed to a more homogeneous distribution of the stress resulting from deformation events involving the chain segments that were initially stressed at a level higher than the average. This proposed process of stress redistribution may be completed when the structure reaches a certain arrangement, which may constitute the beginning of regime II. It is suggested that the increase in E' in regime II results from the orientation of chain segments or from crystallization. These proposed mechanism could also be activated in regime I. Finally, the decrease in E' in regime III is likely to be a consequence of void or craze nucleation and growth.

The evolution of the parameter tan δ did not appear to be affected by the mean stress (c.f. section 4.1.6) and appeared to be largely reversible at least in regime I (4.1.5). The accumulation of reversible strain energy could explain the initial decrease in the damping capacity. On the other hand, an increase in the free volume could explain the subsequent increase in the damping capacity. A competition between these two mechanisms would explain the positive inflection in regime I. In regime II, the inflection becomes negative and a decrease in the damping capacity is observed at 57 MPa of maximum cyclic stress. Upon cycling, the reversible strain energy and the free volume can be expected to reach constant values. The decrease in the damping capacity in regime II could be a consequence of local alignment of mobile chain segments in the loading direction, thus enhancing the elastic mobility. As well, the final regime where the damping capacity increases could originate from the presence of voids for which the damping capacity is increased by surface tension effects.

From the above propositions, the following molecular events could explain the behavior of the material:

- accumulation of reversible strain energy (characterized by the decrease in tan δ);
- irreversible homogenization of the stress applied in each chain segment (characterized by a decrease E');
- reversible increase in the free volume (characterized by the increase in tan δ);
- mostly reversible viscoelastic elongation of the specimen (characterized by the accumulated strain);
- inhibition of the above mentioned mechanisms (mark the end of regime I);

- orientation of the chain segments (characterized by the increase in E' and the decrease in tan δ);
- viscoelastic elongation of the specimen by molecular events having increasing activation volumes (characterized by the accumulated strain in regime I);
- inhibition of the above mentioned mechanisms (marked by the end of regime II);
- nucleation and growth of voids or procrazes (characterized by the decrease in E', the change in the accumulated volume variation and the increase in tan δ).

As discussed in section 5.1.1, the molecular events occurring in regimes II and III might also be effective in regime I. For example, viscoelastic elongation by molecular events having high activation volumes may occur in regime I without having a significant effect on the accumulated strain.

5.1.3 Hypothesis on Factors Controlling the Molecular Events

Even if the molecular events leading to the evolution of the different parameters are likely to be somewhat different, there are certainly interactions between these events. This statement is supported by the correlation between the number of cycles at which transitions are observed in the accumulated strain, the E' and the tan δ responses. Since variations in E' and tan δ occur in regime I even under conditions for which there is no accumulation of strain (c.f. section 4.1.6), these variations are not dependent on this latter parameter. Also, the molecular events leading to variation in the parameters E' and tan δ can be expected to be more a consequence of the cyclic nature of loading than those leading to variations in the accumulated strain.

In general, the molecular processes leading to the variations in the stress-strain-time response in regimes I and II can be expected to involve the relative movement of chain segments over short distances. A controlling parameter for this displacement could be the intrinsic stiffness of the macromolecules in the amorphous phase, which can be characterized by the characteristic ratio C_∞ (c.f. appendix, section A.2.1). After a sufficient number of loading cycles, this displacement could be completed, leaving reptation and chain disentanglement as the principal deformation mechanisms. The resistance of the material to homogeneous damage in regime III can be expected to be controlled by the molecular weight and the entanglement density (c.f. appendix, section A.2.1). If one employs the macroscopic strain response of non-notched specimens to characterize the material resistance to the initiation and growth of intrinsic procrazes or voids, materials should be compared from their response in regime III.

5.2 HETEROGENEOUS DAMAGE DURING THE AXIAL FATIGUE TESTS

Based upon the literature review on heterogeneous deformation in semicrystalline polymers (c.f. section 2.1.3), craze-like features formed in PA6 at room temperature and in the absence of solvent should be in the category of fibrillated deformation zones rather than low temperature crazes. By their growth mechanism, low temperature crazes should have induced a network of interconnected voids. In the experiments on non-notched specimens of PNC, a network of interconnected fibrils has been observed in the low FCP rate regime (c.f. section 4.3.1). Also, a large fibril formed in the intermediate FCP rate regime was found to contain sub-micron fibrils lying parallel to each other (c.f. section 4.4). The presence of these small fibrils suggests that the deformation process leading to the craze-like morphology involved micronecking. In this manner, the extension of each fibril could be viewed as the process of transformation during tensile drawing of a non-notched specimen (c.f. model of Peterlin described in section 2.1.2.5). The fractographic observations and the literature review fully support the proposition that the craze-like features that grew ahead of the fatigue crack tip in PNC were fibrillated deformation zones.

A network of interconnected fine fibrils similar to those observed on the fracture surface of the PNC specimens has also been reported in a polyacetal copolymer (Hertzberg, 1987) and in a POM (Runt and Gallagher, 1991). This analogy suggests that the nanoparticles do not necessarily have an important effect on development of fibrillated deformation zones in the low FCP rate regime. As the FCP rate increases, the large lamellar fibrils were found to be preferentially oriented perpendicularly to the local crack propagation direction (c.f. section 4.3.1). This type of orientation of lamellar fibrils has already been reported in compression-molded and injection-molded PE (c.f. section 2.3.1.2) as well as in PBT (Yeh and Runt, 1989). Accordingly, the presence of lamellar fibrils is expected to be a consequence of a plane stress effect in the vicinity of the crack tip rather than a consequence of the anisotropy of the microstructure. From the observation of the fracture surface, it cannot be concluded that the nanoparticles play a direct role in the nucleation and growth of fibrillated deformation zones.

The increase in the size of the fibrils that was noted up to more than half of the distance between the crack initiation site and the final fracture line (c.f. section 4.3.1) could originate from the increase in ΔK. As ΔK increases, the process of extension of the fibrils can accelerate more rapidly than the process of fibril breakdown. At a larger distance from the initiation site, the size of the fibrils was found to decrease (c.f. section 4.3.1). This transition to a decreasing size of the craze fibrils which occurred at up to 300 μm from the final fracture line can be interpreted in two different manners. The process of fibril breakdown may have accelerated more rapidly than the processes resulting in the growth of the fibrillated deformation zone, thus resulting in a decrease in the distance between the front of the fibrillated deformation zone and the crack front. This explanation is consistent with the gradual transition to a mechanism of surface separation where no cavitation appears to occur (c.f. section 4.3.1). Alternatively, the transition may be associated with the formation and growth of a blunting zone prior to final fracture. Because of the gradual transition between the two mechanisms of surface separation, there should be similarities and a certain complementarily between the mechanism of FCP through a fibrillated deformation zone and the process of crack blunting occurring prior to the final fracture.

Just below the FCP fracture surface in PNC, a layer of material apparently stretched along the crack propagation direction was observed (c.f. section 4.4). In that layer, there was no apparent effect of the distance to the crack plane on the morphology, suggesting that the layer has been uniformly deformed. Uniformly deformed material has also been suggested to result from fatigue crack propagation in PC (c.f. section 2.3.1.1). At least in PC where fibrillation is unlikely to occur, it can be expected that the deformation leading to a deformed layer would occur by shear. As discussed in the literature review on heterogeneous deformation in amorphous polymers (c.f. appendix, section A.2.4.2), shear banding is found to occur by the displacement of the interface between a uniformly deformed and the bulk non-deformed polymer. The formation of a deformed layer by the displacement of the interface is the only deformation process found in the literature that can lead to a uniformly stretched material by heterogeneous deformation without the formation of voids. By assuming that the apparently uniformly deformed layer found in PNC has been formed by shear localized at the interface between a non-deformed bulk material and a homogeneously deformed material, the process of crack propagation can be expected to occur as shown in Figure 5.1. The material is uniformly deformed near the crack separation plane and well in front of the blunted crack tip as a result of shear forces acting on the interface at that location. At the same time, voids are formed and begin to grow along or very close to the crack separation plane. The nucleation and growth of these voids can be expected to facilitate the advance of the crack by reducing crack tip blunting and the thickness of the uniformly deformed layer, which certainly reduces the energy required for crack propagation. However, the nucleation and growth of these voids is not a necessary condition for crack tip advance. As the crack advances, the uniformly deformed layer is rotated by stress relaxation to lie parallel to the fracture surface.

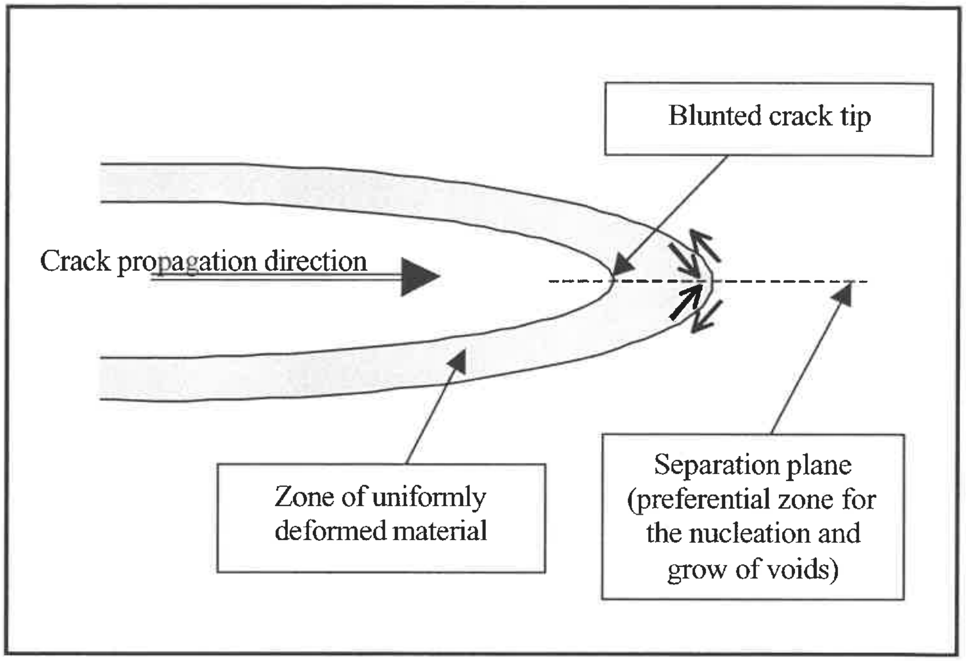

Figure 5.1: Expected heterogeneous deformation process accompanying fatigue crack propagation when a zone of uniformly deformed material is observed below the fracture surface. There is no fibrillated deformation zone schematized.

5.3 FACTORS CONTROLLING THE LIFETIME OF NON-NOTCHED SPECIMENS

The axial fatigue specimens failed as a result of localized deformation, crack initiation and fatigue crack propagation. At a maximum cyclic stress of 57 MPa, the average fatigue life of the PNC specimens was found to be more than twice that of the PA6 specimens (c.f. section 4.1.7). Four different parameters have been identified as having an effect on the relative fatigue life of PNC and PA6. These parameters are listed in Table 5.1 along with a brief summary of the discussion on their expected effect. They can be separated in two different categories. The first category is associated with the size and morphology of the heterogeneity at the crack initiation site and the position of the crack initiation site. These parameters are extrinsic to the material but intrinsic to the specimen. Since the same processing technique was employed for the production of all the specimens from batch 3, the heterogeneities contained in the non-filled PA6 specimens are expected to be also present in the PNC specimens. As found during the fractographic observations, PNC contains additional inorganic inclusions that are likely to originate from the addition of the clay. Since crack initiation occurred at these inclusions rather than at the organic inclusions which were significantly larger, the inorganic inclusions are likely to be more deleterious to the resistance to fatigue crack initiation. Therefore, the size and morphology of the heterogeneity at the crack initiation site is expected to be a parameter enhancing preferentially the fatigue life of the PA6 specimens. Crack initiation in PA6 occurred nearer to the lateral surfaces. The stress intensity factor is higher at the tip of a crack growing from or near an external surface. Accordingly, the position of the crack initiation site is expected to be a parameter enhancing preferentially the fatigue life of the PNC specimens.

The second category is associated with the resistance of the material to extrinsic crack initiation and to fatigue crack propagation. Since the fatigue life was increased significantly by a reduction of the size of the heterogeneities at the crack initiation site, the material resistance to extrinsic crack initiation can be expected to have an important effect on this life. Because of its higher stiffness, the PNC was subject to a lower strain amplitude. However, the exfoliated nanoparticles present in its structure could act as preferential sites for the nucleation of voids. For these reasons, it cannot be predicted if PNC presents or not a higher resistance to extrinsic crack initiation. However, the experimental measurements (c.f. section 4.2) indicate that PNC presents a lower resistance to fatigue crack propagation.

From the above discussion, it can be proposed that the enhancement in the fatigue life resulting from the addition of nanoparticles can originate either from a change in the position of the crack initiation site or from an enhanced resistance of the material to extrinsic crack initiation. The change in the position of the crack initiation site could be related to the effect of adding nanoparticles on the gradient of structure between the skin and core regions of the injection-molded specimens (c.f. section 2.2.3).

Table 5.1: Potential effect of specimen and material parameters on the fatigue life of PNC and PA6 specimens.

Parameter	Type of parameter	Discussion	Enhance preferentially the fatigue life of
Size and morphology of the heterogeneity at the crack initiation site	Extrinsic to the material (intrinsic to the specimen)	The heterogeneities in PA6 are also contained in PNC (same processing). PNC contains additional inorganic heterogeneities.	PA6
Position of the crack initiation site	Extrinsic to the material (intrinsic to the specimen)	Crack initiation near the surface (case of PA6) can be expected to cause a more rapid increase in stress intensity than bulk crack initiation.	PNC
Material resistance to extrinsic crack nucleation	Intrinsic to the material	The strain amplitude is lower in PNC but PNC may contain additional preferential sites for the nucleation of voids	Unknown
Material resistance to fatigue crack propagation	Intrinsic to the material	As measured	PA6

5.4 EFFECT OF NANOPARTICLES ON THE MECHANISMS OF DAMAGE

The addition of nanoparticles was found to affect differently the mechanism of macroscopic strain accumulation and that of fatigue crack propagation. At a given maximum cyclic stress, the addition of nanoparticles reduced the rate of strain accumulation in the regimes I and II of accumulation of macroscopic strain. This reduction is expected to be a consequence of the increase in the stiffness of the material, which causes a reduction in the strain amplitude at a given stress amplitude. In regime III, the material became viscous and appeared to have lost most of the reinforcement effect of the nanoparticles on the rate of strain accumulation.

The addition of nanoparticles induced the nucleation and growth of a fibrillated deformation zone ahead of the crack tip. This change in the mechanism of FCP can be a consequence of one of the following favors:

- enhanced intrinsic void nucleation due to the presence of exfoliated nanoparticles (direct effect);
- change in the supermolecular structure of PA6 (indirect effect);
- increase in the yield stress of the material (indirect effect).

Exfoliated nanoparticles could induce a distribution of zones of stress concentration in which intrinsic void nucleation might occur under a lower nominal stress. However, non-filled semicrystalline polymers already contain zones of stress concentration such as at spherulite radii, small voids at interspherulitic boundaries and interfaces between the crystallites and the amorphous phases. Also, the presence of nanoparticles is not found to change markedly the final morphology of the network of fibrils (c.f. section 5.2). For these reasons, the eventual direct stress concentration effect of the nanoparticles is not expected to be the principal origin of the change in the mechanism of FCP.

As established in the literature review (c.f. section 2.1.3.2), the growth of craze-like features can be affected by the supermolecular structure. For instance, the equatorial disks of the spherulites (c.f. section 2.1.1) are found to be zones of structural weakness (c.f. section 2.1.3.2d). The morphological investigation carried out on PA6 and PNC suggested the absence of a spherulitic arrangement in PNC (c.f. section 3.3). As mentioned in section 2.2.3, thermodynamic and kinetic calculations suggested that exfoliated clays in PE induce a bi-dimensional crystallization process. Also, crystallites in injection-molded PA12-based PLCNC are found to be preferentially oriented perpendicularly to the injection molding direction. By assuming that this type of orientation also prevails in the axial fatigue and FCP specimens of PNC, there would be a preferential orientation of the crystallite length perpendicularly to the macroscopic tensile loading direction. In such a structure, there is no region, such as the 45° domains of the spherulites, where plastic instability can be initiated by the intercrystallite shear deformation (c.f. section 2.1.1 for the structure and section 2.1.2 for the inelastic deformation mechanisms in semicrystalline polymers). Consequently, such a different supermolecular structure can be expected to have a relatively high yield stress.

Even though there is an effect of the supermolecular structure on the growth of craze-like features (c.f. section 2.1.3.2), the supermolecular structure does not necessarily control directly the transition between crack propagation by shear deformation to propagation by shear deformation assisted by the advance of a fibrillated deformation zone. In the latter case, void reinitiation occuring near the separation plane before, at or after the interface between the uniformly deformed material and the bulk non-deformed matrix can be expected to be the controlling parameter for the development of the fibrillated deformation zone. This void reinitiation process can be expected to be controlled by a combination of maximum stress and time effects. The maximum local cyclic stress near the separation plane is largely governed by the yield stress of the material.

From the above discussion, it is proposed that the transition in the FCP propagation mechanism is an indirect effect of the nanoparticles on the yield stress. The increase in the yield stress could originate from either or both a change in the supermolecular structure of the semicrystalline polymer resulting from a change in the crystallization process or a direct reinforcing effect or the nanoparticles resulting from a strong particle-matrix interaction. In the literature (c.f. section 2.2.3), the increase in the yield stress associated with the presence of exfoliated nanoparticles is generally attributed to the strong particle-matrix interaction. Such an interaction is apparently necessary in other to promote exfoliation (Simha, Utracki and Garcia-Rejon, 2001).

In glass bead-filled PP, for which the particle-matrix interaction is relatively weak, an increase in Young's modulus is not accompanied by an increase in yield stress; whereas, in glass bead-filled PA6, for which the particle-matrix interaction is expected to be higher, an increase is noted on both the Young's modulus and the yield stress (Meddad and Fisa, 1997). If one could find a way to reduce the particle-matrix interaction after the exfoliation process, it might become possible to increase the stiffness of polymers without increasing the yield stress. In such a case, the fracture toughness resistance would most probably be enhanced. However, a reduction in the strength of the particle-matrix interface may promote cavitation if a static or cyclic stress is applied over a sufficient period of time to activate the nucleation and growth of microvoids, which could result in a decrease in the resistance to FCP.

The addition of rubber particles in the PNC could be considered as an alternative solution to decrease the yield stress. A proper distribution of rubber particles into PA6 is found to greatly enhance the resilience at low temperature and high strain rate (Wu, 1988; Muratoglu, Argon, Cohen and Weinberg, 1995). However, the weakness of the particle-matrix interface in that system may promote cavitation if stresses are applied over a sufficient period of time. From this discussion, it appears that decreasing the yield stress could probably increase the ductility and fracture toughness but not necessarily the resistance to FCP.

Particles presenting a sufficient size, ductility and adhesion to the matrix can promote an increase in the resistance to FCP by bridging effects. This improvement has been reported in PE/PS bends (Bureau, Dickson and Denault, 1998). Bridging effects have also been reported in glass fiber-filled PA6 (c.f. section 2.3.3.1) conditioned at 50% RH but not in dried glass fiber-filled PA6 (Horst and Spoormaker, 1996 and 1997). From the results published for glass fiber-filled PA6 and for PE/PS blends, bridging occurs under conditions of relatively high ductility of one polymeric phase. When the particles are not ductile, the occurrence of bridging effects could be limited to conditions where the ductility of the matrix is relatively high and where the length of the particles is greater than the radius of curvature of the crack tip. Bridging effects may additionally require a sufficient strength of these particles. Increasing the resistance to FCP of a semicrystalline polymer such as dry PA6 by the addition of particles would probably be more difficult than increasing other properties.

5.5 SUGGESTIONS FOR FUTURE RESEARCH

This research project leaves a number of questions unanswered. Based upon some of these questions, suggestions for future research can be made. The first category of questions considered here concerns the mechanisms of fatigue damage associated with regime III of the macroscopic strain response. Since it appears that a loss in the reinforcement effect of the nanoparticles occur in this regime, one can also expect any direct reinforcing effect of the crystallites. From this hypothesis, it is proposed that the effect of crystallinity on the accumulated strain behavior would result from a change in the volume fraction of the amorphous phase. This hypothesis could be verified by producing specimens of similar overall crystallinity employing different molding and crystallization treatment conditions. Since the macroscopic response in regime III is viscous, it has been proposed that reptation and chain disentanglement could control the rate of damage (c.f. section 5.1.3). Providing that the hypothesis on the effect of the crystallites is verified, this second hypothesis could be tested by varying M_w and adjusting the overall crystallinity to the same level through adjustments in molding and/or crystallization treatment conditions.

In regime III of the macroscopic strain response, nucleation and growth of voids has been proposed to occur throughout the gauge section of the specimen (c.f. section 5.1.2). Event if the observations made by TEM in this research project did not allow to reveal any voided structure other than near the fracture surface (c.f. section 4.4), such a structure could possibly be revealed by improving the experimental technique. At least one additional consideration may need to be addressed in order to observe a voided structure by TEM. Any void or craze-like feature can be expected to recover when the macroscopic stress is removed because this recovery reduces the surface tension energy. To bypass this issue, efforts should be made to maximize the size of the void or craze-like feature and to minimize the time between fatigue test and the TEM observations. Attaching thin samples on a copper grid and stretching this copper grid during TEM observations could also be considered. During stretching, any closed microvoid or craze-like feature should reopen. Finally, efforts could be made to increase the lifetime of the axial fatigue specimens by improving the preparation technique for the specimens. Such an increase could also allow to determine if a viscous flow regime can be obtained with PA6 specimens.

It could also be of interest to further characterize the mechanisms of fatigue crack propagation. In section 5.2, it is proposed that crack propagation in PNC is accompanied by the displacement of an interface between a relatively non-deformed matrix and a relatively highly deformed layer. The presence of such an interface in front of the crack tip could be confirmed through direct observations by the method, which is briefly described in section 3.7, employed to obtain the results presented in the first part of section 4.4. It could be of particular interest to interrupt an FCP test, to polish or microtome a small transverse cross-section area containing the crack front, to install the prepared FCP specimen in an SEM and to observe the void reopening process induced by applying *in-situ* tensile force on the specimen. In section 5.4, it is proposed that the change in mechanism of fatigue crack propagation caused by the addition of nanoparticles results is an indirect effect of the increasing the yield stress. This hypothesis could be partially verified by increasing the yield stress of PA6 through a crystallization thermal treatment. If such a treatment could result in a change in the mechanism of fatigue crack propagation in non-filled PA6, it could be of interest to characterize the fracture surfaces.

As mentioned in section 5.4, promoting bridging effects appears as an efficient manner to increase the resistance of a material to FCP. It could be envisaged to employ particles thicker and longer than those employed in this research project in order to favor such a bridging effect. Material development efforts could also be concentrated in increasing the resistance of material to the nucleation and growth of voids ahead of an advancing fatigue crack.

6 CONCLUSIONS

Since both axial fatigue and FCP tests have been carried out during this research project, a few comments can be made on the information that can be obtained from each of these tests. Axial fatigue tests carried out with non-notched specimens enabled to characterize the overall resistance of the specimens and the macroscopic stress-strain-time response. It is concluded that this latter response characterizes the fatigue damage processes which occur macroscopically homogeneously throughout the whole section of the specimen.

The dominant damage processes leading to strain accumulation are strain amplitude controlled during the initial regimes; whereas, those occurring during the final regime are maximum stress controlled. Based upon the proposition that cavitation becomes a more dominant mode of change in structure in the final regime, it is concluded that any characterization of the resistance of a material to the initiation of a crack employing the macroscopic strain response should be concentrated in that regime.

From the correlation between the size of the inclusions at the crack initiation site and the fatigue life, it can be concluded that this life is characterized by the resistance of the specimen to the initiation of a crack from a microscopic zone of stress concentration. On the other hand, the fatigue crack propagation tests provided information on the resistance of the material to the growth of an existing crack. This latter type of test is expected to be much less affected by the presence of inclusions.

The research project allowed to determine some of the effects of the addition of layered crystals on the fatigue behavior of PA6. In the initial regimes of accumulation of macroscopic strain during axial fatigue tests, the addition of nanoparticles reduces the rate of strain accumulation because of a decrease in the strain amplitude resulting from the increase in stiffness. However, there is no such reinforcing effect of the nanoparticles in the final regime of the macroscopic response where the behavior of the materials becomes viscous. The principal material parameters that are expected to control the resistance of the material to this viscous-like strain accumulation process are the entanglement density, the molecular weight and the volume fraction of the amorphous phase.

It is concluded that the addition of nanoparticles induced a change the mechanism of fatigue crack propagation. This transition is proposed to be an indirect effect of the nanoparticles on the yield stress. Increasing the yield stress can have a deleterious effect on the resistance to FCP through an increase in the local stress near the surface separation plane where voids can nucleate and growth if a substantial static or cyclic stress is applied over a sufficient period of time. It is proposed that FCP in PNC is accompanied by the displacement of an interface between a relatively non-deformed matrix and a relatively highly deformed layer and by the development and growth of a fibrillated deformation zone near the surface separation plane.

The fatigue properties of PA6 and PNC have also been evaluated and compared. It is concluded that this increase could originate from an increase in the resistance of the material to extrinsic crack nucleation or to a change in the position of the crack initiation site, which could result from an effect of the nanoparticles on the structure gradient between the skin and core regions of the injection-molded specimens.

As mentioned in the introduction, an advantage of adding layered crystals in a polymer is to increase its stiffness with a very small volume fraction of nanoparticles. In the system studied, the benefit of adding exfoliated nanoparticles to improve the mechanical properties appeared limited to that increase in stiffness. For instance, the addition was accompanied by an increase in the yield stress, a reduction in ductility and a reduction in the resistance of the material to FCP.

Reducing the yield stress of PNC by decreasing the strength of the nanoparticle-matrix interface or adding rubber particles would probably enhance the ductility and fracture toughness of PNC but not necessarily the resistance to fatigue crack propagation. Promoting bridging effects through a proper selection of particle size and interface strength can be viewed as a promising way to enhance the resistance of the material to FCP. However, the occurrence of bridging effects may require a certain ductility of one of the two components. In this thesis, suggestions for future research are presented at the end of the general discussion.

REFERENCES

ADAMS, W.W., YANG, D. and THOMAS, E.L. (1986). Direct visualization of microstructural processes in polyethylene. J. Mater. Sci., 21, 2239-2253.

AKKAPEDDI, M.K. (1999). Glass fiber reinforced polyamide 6 nanocomposites. Polymer Composites '99 : SPE topical conference : International Symposium on Polymer Composites Science and Technology. Lac Delage October 6-8 1999, SPE, 169-182

ALEXANDRE, M. and DUBOIS, P. (2000). Polymer-layered silicate nanocomposites: preparation, properties and uses of a new class of materials. Mater. Sci. Eng. Report, 28, 1-63.

ANDREWS, E.H. and WALKER, B.J. (1971). Fatigue fracture in polyethylene. Proc. R. Soc. London, A325, 57-70.

ARGON, A.S.(1980). Inelastic deformation and fracture in oxide, metallic and polymeric glasses. Glass science and technology, 5, 79-132.

ARGON, A.S. and BESSONOV, M.I. (1977). Plastic flow in glassy polymers. Polym. Eng. Sci., 17, 174-182.

ARGON, A.S. and HANOOSH, J.G. (1977). Phil. Mag., 36, 1195.

ARGON, A.S., HUTNIK, M., MOTT, P. and SUTER, U.W. (1991). Molecular view of plastic deformation and precursor processes of crazing in glassy polypropylene and polycarbonate. Interim Technical Report No. 33, Massachusetts Institute of Technology, Cambridge.

ASTM. (1998). Standard practice for strain-controlled fatigue testing. Annual Book of ASTM Standards, E 606-92.

ASTM. (2000). Standard test method for measurement of fatigue crack growth rates. Annual Book of ASTM Standards, E 647-00.

ASTM. (2002). Standard test method for tensile properties of plastics. Annual Book of ASTM Standards, E 638-02.

BARRY, D. and DELATYCKI, O. (1987). Static fatigue fracture of polyethylene: a morphological analysis. J. Polym. Sci. Part B: Polym. Phys., 25, 883-899.

BARTCZAK, Z., ARGON, A.S., COHEN, R.E. and WEINBERG, M. (1999). Toughness mechanism in semicrystalline polymer blends: I. High density polyethylene toughened with rubbers. Polymer, 40, 2331-2346.

BARTCZAK, Z., ARGON, A.S., COHEN, R.E. and WEINBERG, M. (1999). Toughness mechanism in semicrystalline polymer blends: II. High density polyethylene toughened with calcium carbonate filler particles. Polymer, 40, 2347-2365.

BERGER, L.L. and KRAMER, E.J. (1988). The effect of temperature on the transition from crazing to shear deformation in crosslinked polystyrene. J. Mater. Sci., 23, 3536-3543.

BOTSIS, J., CHUDNOVSKY, A. and MOET, A. (1987). Fatigue crack layer propagation in polystyrene. Int. J. Fract., 33, 263-276.

BOUDA, V., ZILVAR, V. and STAVERMAN, A.J. (1976). The effect of cyclic loading on polymers in a glassy state. J. Polym. Sci.: Polym. Phys. Ed., 14, 2313-2323.

BOWMAN, J., HARRIS, N. and BEVIS, M. (1975). An investigation of the relationships between processing conditions, microstructure and mechanical properties of an injection molded semi-crystalline thermoplastic. J. Mater. Sci., 10, 63-76.

BRADY, T.E. and YEH, G.S.Y. (1973). Similarities between craze morphology and shear-band morphology in polystyrene. J. Mater. Sci., 8, 1083-1094.

BRETZ, P.E., HERTZBERG, R.W. and MANSON, J.A. (1979). Fatigue crack propagation in crystalline polymers: effect of moisture in nylon 66. J. Mater. Sci., 14, 2482-2492.

BRETZ, P.E., HERTZBERG, R.W. and MANSON, J.A. (1981a). Mechanisms of fatigue damage and fracture in semi-crystalline polymers. Polymer, 22, 1272-1278.

BRETZ, P.E., HERTZBERG, R.W. and MANSON, J.A. (1981b). Influence of absorbed moisture on fatigue crack propagation behaviour in polyamides: Part 2 Fractography. J. Mater. Sci., 16, 2070-2078.

BRETZ, P.E., HERTZBERG, R.W. and MANSON, J.A. (1981c). Influence of absorbed moisture on fatigue crack propagation behaviour in polyamides: Part 1 Macroscopic response. J. Mater. Sci., 16, 2061-2069.

BRETZ, P.E., HERTZBERG, R.W. and MANSON, J.A. (1982). The effect of molecular weight on fatigue crack propagation in nylon 66 and polyacetal. J. App. Polym. Sci., 27, 1707-1717.

BROWN, H.R. (1991). A molecular interpretation of the toughness of glassy polymers. Macromolecules, 24, 2752-2756.

BUREAU, M.N., DENAULT, J., COLE, K.C. and ENRIGHT, G.D. (2001). The role of crystallinity and reinforcement in the mechanical behavior of polyamide-6/clay nanocomposites. Polymer Nanocomposites 2001, Montreal September 17-19 2001, Society for Plastics Engineers, Paper #5.

BUREAU, M.N., DENAULT, J. and GLOWACZ, F. (2001). Mechanical behavior and crack propagation in injection-molded polyamide 6/clay nanocomposites. ANTEC 2001: conference proceedings, Dallas May 6-10 2001, Society for Plastics Engineers, 2125-2129.

BUREAU, M.N., DICKSON, J.I. and DENAULT, J. (1998). Comparison of the fatigue propagation behaviour of polystyrene and 95/5 polystyrene/polyethylene blends. J. Mater. Sci., 33, 1591-1606.

BUREAU, M.N., DICKSON, J.I. and DENAULT, J. (1998). Fatigue propagation behaviour of polystyrene/polyethylene blends. J. Mater. Sci., 33, 1405-1419.

BUREAU, M.N. (2001). IMI-CNRC, Personal communication.

BUREAU, M.N. (2002). IMI-CNRC, Personal communication.

CHAN, M.K. and WILLIAMS, J.G. (1983). Slow crack growth in high density polyethylenes. Polymer, 24, 234-243.

CHUDNOVSKY, A., MOET, A. and TAKEMORI, M.T. (1983). Effect of damage dissemination on the crack propagation in polypropylene. J. Appl. Phys., 54, 5562-5567.

CRAWFORD, R.J. and BENHAM, P.P. (1974a). Cyclic stress fatigue and thermal softening failure of a thermoplastic. J. Mater. Sci., 9, 18-28.

CRAWFORD, R.J. and BENHAM, P.P. (1974b). A comparison of uniaxial and rotating bending fatigue tests on an acetal co-polymer. J. Mater. Sci., 9, 1297-1304.

CRAWFORD, R.J. and BENHAM, P.P. (1975). Some fatigue characteristics of thermoplastics. Polymer, 16, 908-914.

DETTENMAIER, M. (1983). Intrinsic crazes in polycarbonate: Phenomenology and molecular interpretation of a new phenomenon. Advances in Polymer Science, 52/53, 57-104.

DOI, M. and EDWARDS, S.F. (1986). The theory of Polymer Dynamics, Oxford University Press, New York, 391 pages.

DÖLL, W. and KÖNCZÖL, L. (1990). Micromechanics of fracture under static and fatigue loading: Optical interferometry of crack tip craze zones. Advances in Polymer Science, 91/92, 137-214.

DONALD, A.M. and KRAMER, E.J. (1981). Phil. Mag., A43, 857.

DONALD, A.M. and KRAMER, E.J. (1982). Deformation zones and entanglements in glassy polymers. Polymer, 23, 1183-1188.

DOYLE, M.J. (1982). J. Mater. Sci., 17, 760.

DUAN, D.M. and WILLIAMS, J.G. (1998). Craze testing of tough polyethylene. J. Mater. Sci., 33, 625-638.

EGAN, B.J. and DELATYCKI, O. (1995). The morphology, chain structure and fracture behaviour of high-density polyethylene Part II Static fatigue fracture testing. J. Mater. Sci., 30, 3351-3357.

FAVIER, V., GIROUD, T., STRIJKO, E., HIVER, J.M., G'SELL, C., HELLINCKX, S. and GOLDBERG, A. (2002). Slow crack propagation in polyethylene under fatigue at controlled stress intensity. Polymer, 43, 1375-1382.

FERREIRO, V., PENNEC, Y., SEGUELA, R. and COULON, G. (2000). Shear banding in polyamide 6 films as revealed by atomic force microscopy. Polymer, 41, 1561-1569.

FLORY, P.J. and YOON, D.Y. (1978). Molecular morphology in semicrystalline polymers. Nature, 272, 226-229.

FOOT, J.S. and WARD, I.M. (1972). The fracture behaviour of polyethylene terephthalate. J. Mater. Sci., 7, 367-387.

FRIEDRICH, K. (1983). Crazes and shear bands in semi-crystalline thermoplastics. Advances in Polymer Science, 52/53, 225-274.

GALESKI, A. and PIORKOWSKA, E. (1983a). Localized volume deficiencies as an effect of spherulite growth. I. The two-dimensional case. J. Polym. Sci. Polym. Phys. Ed., 21, 1299-1312.

GALESKI, A. and PIORKOWSKA, E. (1983b). Localized volume deficiencies as an effect of spherulite growth. II. The three-dimensional case. J. Polym. Sci. Polym. Phys. Ed., 21, 1313-1322.

GALESKI, A., ARGON, A.S. and COHEN, R.E. (1998). Changes in morphology of bulk spherulitic nylon 6 to plastic deformation. Macromolecules, 21, 2761-2770.

GALESKI, A., ARGON, A.S. and COHEN, R.E. (1991b). Morphology of bulk nylon 6 subjected to plain strain compression. Macromolecules, 24, 3953-3961.

GALESKI, A., ARGON, A.S. and COHEN, R.E. (1987). Morphology of nylon 6 spherulites in bulk. Makromol. Chem., 188, 1195-1204.

GALESKI, A., ARGON, A.S. and COHEN, R.E. (1991a). Deconvolution of X-ray diffraction data to elucidate plastic deformation mechanisms in the uniaxial extension of bulk nylon 6. Macromolecules, 24, 3945-3952.

GALESKI, A., BARTCZAK, Z., ARGON, A.S. and COHEN, R.E. (1992). Morphological alterations during texture-producing plane strain compression of high-density polyethylene. Macromolecules, 25, 5705-5718.

GENSLER, R., PLUMMER, C.J.G., KAUSCH, H.H. and MUNSTEDT, H. (1997). Thin film and bulk deformation behaviour of poly(ether ether ketone)/poly(ether imide) blends. J. Mater. Sci., 32, 3037-3042.

GIANNELIS, E.P., KRISHNAMOORTI, R. and MANIAS, E. (1999). Polymer-silica nanocomposites: model systems for confined polymers and polymer brushes. Adv. Polym. Sci., 118, 108-147.

GLOAGUEN, J.M. and LEFEBVRE, J.M. (2001). Plastic deformation behaviour of thermoplastic/clay nanocomposites. Polymer, 42, 5841-5847.

HAHN, M.T., HERTZBERG, R.W. and MANSON, J.A. (1986). Effects of rubbery phase and absorbed water on impact-modified nylon 66: Part 2 Fratography. J. Mater. Sci., 21, 39-45.

HAHN, M.T., HERTZBERG, R.W., MANSON, J.A. and SPERLING, L.H. (1986). The influence of temperature and absorbed water on the fatigue crack propagation in nylon-6,6. Polymer, 27, 1885-1888.

HARCUP, J.P., DUCKETT, R.A., WARD, I.M. and CAPACCIO, G. (2000a). Fatigue crack growth in polyethylene: material dependence. I. Tension/compression loading. Polym. Eng. Sci., 40, 627-634.

HARCUP, J.P., DUCKETT, R.A., WARD, I.M. and CAPACCIO, G. (2000b). Fatigue crack growth in polyethylene: material dependence. II. Effect of time "off-load". Polym. Eng. Sci., 40, 635-644.

HEIKENS, D., SJOERDSMA, S. and COUMANS, W.J. (1981). A mathematical relation between volume strain, elongational strain and stress in homogeneous deformation. J. Mater. Sci., 16, 429-432.

HERTZBERG, R.W. (1987). Fracture surface micromorphology in engineering solids. Fractography of modern engineering materials: composites and metals. ASTM STP, 948, 5-36.

HERTZBERG, R.W. and MANSON, J.A. (1980). Fatigue of Engineering Plastics, Academic Press, New York, 275 pages.

HERTZBERG, R.W., SKIBO, M.D. and MANSON, J.A. (1978). Fatigue crack propagation in polyacetal. J. Mater. Sci., 13, 1038-1044.

HEYMANS, N. (2000). A novel look at models for polymer entanglement. Macromolecules, 33, 4226-4234.

HOBBS, J.K. and BARHAM, P.J. (1999). Fracture of poly(hydroxybutyrate). Part III. Fracture morphology in thin films and bulk systems. J. Mater. Sci., 34, 4831-4844.

HORST, J.J. and SPOORMAKER, J.L. (1996). Mechanisms of fatigue in short glass fiber reinforced polyamide 6. Polym. Eng. Sci., 36, 2718-2726.

HORST, J.J. and SPOORMAKER, J.L. (1997). Fatigue fracture mechanisms and fractography of short glass fiber reinforced polyamide. J. Mater. Sci., 32, 3641-3651.

HRISTOV, H.A., YEE, A.J. and GIDLEY, D.W. (1994). Fatigue craze initiation in polycarbonate: Study by transmission electron microscopy. Polymer, 35, 3604-3611.

HUNT, D.G. and DARLINGTON, M.W. (1978). Accurate measurement of creep of nylon-6,6 at constant temperature and humidity. Polymer, 19, 977-983.

HUNT, D.G. and DARLINGTON, M.W. (1979). Prediction of creep of nylon-6,6 at constant stress, temperature and moisture content. Polymer, 20, 241-246.

JANG, B.Z., UHLMANN, D.R. and VANDER SANDE, J.B. (1985). Crazing in polypropylene. Polym. Eng. Sci., 25, 98-104.

JINEN, E. (1986). Accumulated strain in low cycle fatigue of short carbon-fibre reinforced nylon 6. J. Mater. Sci., 21, 435-443.

JINEN, E. (1987). Creep properties of fatigued short carbon fibre reinforced nylon 6 plastics. J. Mater. Sci., 22, 1956-1962.

JO, N.J., TAKAHARA, A. and KAJIYAMA, T. (1994). Effect of crystalline relaxation on fatigue behavior of the oriented high-density polyethylene based on nonlinear viscoelastic measurements. Polym. J., 26, 1027-1036.

JONES, M.A., CARRIERE, C.J., DINEEN, M.T. and BALWINSKI, K.M. (1997). Failure and deformation studies of syndiotactic polystyrene. J. App. Polym Sci., 64, 673-681.

JONES, N.A. and LESSER, A.J. (1998). Morphological study of fatigue-induced damage in isotactic polypropylene. J. Polym. Sc. Part B: Polym. Phys., 36, 2751-2760.

KADOTA, K., CHUM, S. and CHUDNOVSKY, A. (1993). Bridging the PE lifetime under fatigue and creep conditions with its crystallisation behavior. J. App. Polym. Sci., 49, 863-875.

KALGAONKAR, R.A. and JOG, J.P. (2001). A study of static and dynamic mechanical properties of poly(butylene terephthalalte)-layered silicate nanocomposites: effect of quaternary ammonium modified bentonites. Polymer Nanocomposites 2001, Montreal September 17-19 2001, Society of plastics engineers, Paper #20.

KARBHARI, V.M. and DOLGOPOLSKY, A. (1990). Transitions between micro-brittle and micro-ductile material behaviour during FCP in shrot=fibre reinforced composites. Int. J. Fatigue, 12, 51-56.

KASAKEVICH, M.L., MOET, A. and CHUDNOVSKY, A. (1990). Comparative crack layer analysis of fatigue and creep crack propagation in high density polyethylene. Polymer, 31, 435-439.

KAUSCH, H.H. (1987). Polymer Fracture (2nd edition), Springer-Verlag, Berlin, 456 pages.

KAUSCH, H.H., GENSLER, R., GREIN,C., PLUMMER, C.J.G. and SCARAMUZZINO, P. (1999). Crazing in semicrystalline thermoplastics. Journal of Macromolecular Science Physics, B38, 803-815.

KAUSCH, HH, PLUMMER, C.J.G. and TEZ, L. (1994). The influence of the structure of physical networks on the properties of glassy polymers. Phys. Scr., T55, 216-218.

KAWABE, H., NATSUME, Y., HIGO, Y. and NUNOMURA, S. (1992). Micromechanism of a deformation process before crazing in a polymer during tensile testing. J. Mater. Sci., 27, 5547-5552.

KAWAGOE, M. and KITAGAWA, M. (1981). J. Polym. Sci. Polym. Phys., 19, 1423.

KIM, G.M., LEE, D.H., HOFFMANN, B., KRESSLER, J. and STOPPELMANN, G. (2001). Influence of nanofillers on the deformation process in layered silicate/polyamide-12 nanocomposites. Polymer, 42, 1095-1100.

KOJIMA, Y., USUKI, A., KAWASUMI, M., OKADA, A., FUKUSHIMA, Y., KURAUCHI, T. and KAMIGAITO, O. (1993). Mechanical properties of nylon 6-clay hybrid. J. Mater. Res., 8, 1185-1189.

KRAMER, E.J. (1975). The growth of shear bands in polystyrene. J. Polym. Sci. Polym. Phys. Ed., 13, 509-525.

KRAMER, E.J. (1983). Microscopic and molecular fundamentals of crazing. Advances in Polymer Science, 52/53, 1-56.

KRAMER, E.J. and HART, E.W. (1984). Theory of slow, steady state crack growth in polymeric glasses, Polymer, 25, 1667-1678.

KRAMER E.J. AND BERGER L.L. (1990). Fundamental processes of craze growth and fracture. Advances in Polymer Science, 91/92, 1-68.

KRISHNA, N .R., BULAKH, N. and JOG, J.P. (2001). Effect of clay treatment on mechanical properties of polypropylene based composites. Polymer Nanocomposites 2001, Montreal September 17-19 2001, Paper #18.

KUNG, T.M. and LI, J.C.M. (1987). Recovery processes in amorphous polymers. J. Mater. Sci., 22, 3620-3630.

LANG, R.W., MANSON, J.A. and HERTZBERG, R.W. (1987). Mechanisms of fatigue fracture in short glass fibre-reinforced polymers. J. Mater. Sci., 22, 4015-4030.

LAZZERI, A., MARCHETTI, A. and LEVITA, G. (1997). Fatigue and fracture in polyacetal resins. Fatigue and Fracture of Engineering Materials and Structures, 20, 1207-1216.

LEE, J.A., GOPAKUMAR, T.G., KONTOPOULOU, M. and PARENT, J.S. (2002). Polyolefin nanocomposites using maleic anhydride modified polyolefins. ANTEC 2002, San Francisco May 5-8 2002, Society for plastics engineers, Paper #1056.

LESSER, A.J. (1995). Changes in mechanical behaviour during fatigue of semicrystalline thermoplastics. J. App. Polym. Sci., 58, 869-879.

LESSER, A.J. (1996). Effective volume change during fatigue and fracture of polyacetal. Polym. Eng. Sci., 36, 2366-2374.

LIN, J.H. and YANG, A.C.M. (2001). Crazing micromechanism in glassy atactic polystyrene and its blends with Poly(2,6-dimethyl-1,4-diphenyl oxides) by AFM. Macromolecules, 34, 3698-3705.

LIN, L. and ARGON, A.S. (1994). Review: Structure and plastic deformation of polyethylene. J. Mater. Sci., 29, 294-323.

LIN, L. and ARGON, A.S. (1992). Deformation resistance in oriented nylon 6. Macromolecules, 25, 4011-4024.

LIU, L., ZONGNENG, Q.I. and ZHU, X. (1999). Studies on nylon 6/clay nanocomposites by melt-intercalation process. J. App. Polym. Sci., 71, 1133-1138.

LIU, L.B., GIDLEY, D. and YEE, A.F. (1992). Effect of cyclic stress on structural changes in polycarbonate as probed by positron annihilation lifetime spectroscopy. J. Polym. Sci. Polym. Phys. Ed., 30, 231-238.

LU, X. and BROWN, N. (1987). Effect of thermal history on the initiation of slow crack growth in linear polyethylene. Polymer, 28, 1505-1511.

LU, X., MCGHIE, A. and BROWN, N. (1992). The dependence of slow crack growth in a polyethylene copolymer on test temperature and morphology. J. Polym. Sci. Polym. Phys., 30, 1207-1214.

LU, X., QIAN, R. and BROWN, N. (1991). Discontinuous crack growth in polyethylene under a constant load. J. Mater. Sci., 26, 917-924.

MANGION, M.B.M., CAVAILLE, J.Y. and PEREZ, J. (1992). A molecular theory for the sub-t sub-g plastic mechanical response of amorphous polymers. Philosophical Magazine A (UK), 66, 773-796.

MARANO, C. and RINK, M. (2001). Shear yielding threshold and viscoelasticity in an amorphous glassy polymer: a study on a styrene-acrylonitrile copolymer. Polymer, 42, 2113-2119.

MASCIA, L. (1989). Thermoplastics: materials engineering, Elsevier Applied Science, New York, 537 pages.

MEDDAD, A. and FISA, B. (1997). Stress-strain behavior and tensile dilatometry of glass bead-filled polypropylene and polyamide 6. J. App. Polym. Sci., 64, 653-665.

MEDELLIN-RODRIGUEZ, F.J., BURGER, C., HSIAO, B.S., CHU, B., VAIA, R. and PHILIPS, S. (2001). Time-resolved shear behavior of end-tethered nylon 6-clay nanocomposite followed by non-isothermal crystallization. Polymer, 42, 9015-9023.

MICHLER, G.H. (1986). Colloid & Polymer Sci., 264, 522.

MINDEL, M.J. and BROWN, N. (1973). J. Mater. Sci., 8, 863.

MINDEL, M.J. and BROWN, N. (1974). The relationship of creep, recovery and fatigue in polycarbonate. J. Mater. Sci., 9, 1661-1669.

MIZUNO, W., KAWAGOE, M., QUI, J. and MORITA, M. (1997). Fatigue fracture and morphology in injection molded polyacetal. Deformation, Yield and Fracture of Polymers, Cambridge, 431-434.

MIZUNO, W., KAWAGOE, M., QUI, J. and MORITA, M. (1997). Fatigue fracture and morphology in injection molded polyacetal. Kobunshi Ronbunshu Japanese Journal of Polymer Science and Technology, 54, 333-343.

MORE, A.P. and DOMALD, A.M. (1992). The effect of metal halides on the deformation mechanism of thin films of nylon. Polymer, 33, 4081-4086.

MOREL, D.E. and GRUBB, D.T. (1984a). Craze behaviour in isotactic polystyrene: 1. Craze-spherulite interaction. Polymer, 25, 417-429.

MOREL, D.E. and GRUBB, D.T. (1984b). Observation of order in craze fibrils of isotactic polystyrene by electron diffraction. J. Mater. Sci. Lett., 3, 5-8.

MORELLI, T.A. and TAKEMORI, M.T. (1984). Fatigue crack advance mechanisms in polymers: Part 2 Semicrystalline polymers for T less than Tg (polybutylene terephthalate). J. Mater. Sci., 19, 385-395.

MUCCIGRESSO, J. and PHILLIPS, P.J. (1978). IEEE Trans El. Insult, EI-13, 172.

MURATOGLU, O.K., ARGON, A.S., COHEN, R.E. and WEINBERG, M. (1995). Microstructural processes of fracture of rubber-modified polyamides. Polymer, 36, 4771-4786.

NAIR, S.V., GOETTLER, L.A. and LYSEK, B.A. (2001). Toughening behavior of nanoscale and multiscale polymer composites. Polymer Nanocomposites 2001, conference in Montreal September 17-19 2001, Paper #47.

NAQUI, S.I. and ROBINSON, I.M. (1993). Review: Tensile dilatometric studies of deformation in polymeric materials and their composites. J. Mater. Sci., 28, 1421-1429.

NARISAWA, I. and ISHIKAWA, M. (1990). Crazing in semicrystalline thermoplastics. Advances in Polymer Science, 91/92, 353-392.

OKADA, A. and USUKI, A. (1995). The chemistry of polymer-clay hybrid. Mater. Sci. Eng., C3, 109-115.

OLEINIK, E.F., SHENOGIN, S.V., PARAMZINA, T.V., RUDNEV, S.N., SHANTAROVICH, V.P., AZAMATOVA, Z.K., PAKULA, T and FISCHER, E.W. (1998). Molecular mobility in plastically deformed glassy polymers. Polymer Science (Russia) Series B, 40, 1187-1202.

OLF, H.G. and PETERLIN, A. (1974). Crazing and fracture in crystalline, isotartic polypropylene and the effect of morphology, gaseous environment, and temperature. J. Polym. Sci. Polym. Phys., 12, 2209-2251.

PARSONS, M., STEPANOV, E.V., HILTNER, A. and BAER, E. (1999). Correlation of fatigue and creep slow crack growth in a high density polyethylene. J. Mater. Sci., 34, 3315-3326.

PARSONS, M., STEPANOV, E.V., HILTNER, A. and BAER, E. (2000a). Correlation of fatigue and creep slow crack growth in a medium density polyethylene pipe material. J. Mater. Sci., 35, 2659-2674.

PARSONS, M., STEPANOV, E.V., HILTNER, A. and BAER, E. (2000b). Effect of strain rate on stepwise fatigue and creep slow crack growth in high density polyethylene. J. Mater. Sci., 35, 1857-1866.

PARSONS, M., STEPANOV, E.V., HILTNER, A. and BAER, E. (2001). The damage zone ahead of the arrested crack in polyethylene. J. Mater. Sci., 36, 5747-5755.

PECORINI, T.J. and HERTZBERG, R.W. (1993). The fracture toughness and fatigue crack propagation behaviour of annealed PET. Polymer, 34, 5053-5062.

PEGORETTI, A., GUARDINI, A., MIGLIARESI, C. and RICCO, T. (2000). Investigation of nonelastic response of semicrystalline polymers at high strain levels. J. App. Polym. Sci., 78, 1664-1670.

PERRIN, F. (2002). IMI-CNRC, Personal communication

PETERLIN, A. (1975). Plastic deformation of polymers with fibrous structure.Colloid Polym. Sci., 253, 809-823.

PETERLIN, A. (1975). Structural model of mechanical properties and failure of crystalline polymer solids with fibrous structure. International Journal of fracture, 11, 761-780.

PETERLIN, A. (1973). Mechanisms of deformation in polymeric solids. Polymeric Materials, American Society for Metals, 175-238.

PLUMMER, C.J.G. and DONALD, A.M. (1989). J. Polym. Sci. Polym. Phys., 27, 325.

PLUMMER, C.J.G. and KAUSCH, H.H. (1993a). Deformation in thin films of amorphous and semicrystalline isotactic polystyrene. Polymer, 34, 1972-1974.

PLUMMER, C.J.G. and KAUSCH, H.H. (1993b). Deformation of thin films of poly(ether ether ketone). Polymer, 34, 305-311.

PLUMMER, C.J.G., CUDRE-MAUROUX, N. and KAUSCH, H.H. (1994). Deformation and entanglement in semicrystalline polymers. Polym. Eng.Sci., 34, 318-329.

PLUMMER, C.J.G., MENU, P., CUDRE-MAUROUX, N. and KAUSCH, H.H. (1995). The effect of crystallization conditions on the properties of polyoxymethylene. J. App. Polym. Sci., 55, 489-500.

PLUMMER, C.J.G. and KAUSCH-H.H. (1996a). Deformation and entanglement in semicrystalline polymers. Journal of Macromolecular Science Physics, B35, 637-657.

PLUMMER, C.J.G. and KAUSCH, H.H. (1996b). Micronecking in thin films of isotactic polypropylene. Macromol. Chem. Phys., 197, 2047-2063.

PLUMMER, C.J.G., SCARAMUZZINO, P., KAUSCH, H.H. and PHILIPPOZ, J.M. (2000). High temperature slow crack growth in polyoxymethylene. Polym. Eng. Sci., 40, 1306-1317.

PLUMMER, CJG, GOLDBERG, A. and GHANEM, A. (2001). Micromechanisms of slow crack growth in polyethylene under constant tensile loading. Polymer, 42, 9551-9464.

QUINSON, R., PEREZ, J., RINK, M. and PAVAN, A. (1996). Components of non-elastic deformation in amorphous glassy polymers. J. Mater. Sci., 31, 4387-4394.

RABINOWITZ, S. and BEARDMORE, P. (1974). Cyclic deformation and fracture of polymers. J. Mater. Sci., 9, 81-99.

REMMERSWAAL, J. (1992). The effect of waveform on low cycle fatigue of PC. Low cycle fatigue and elasto-plastic behaviour of materials--3, Berlin September 7-11 1992, Elsevier Applied Science, New York, 37-42

REYNAULD, E., JOUEN, T., GAUTHIER, C., VIGIER, G. and VARLET, J. (2001). Nanofillers in polymeric matrix: a study on silica reinforced PA6. Polymer, 42, 8759-8768.

RUNT, J. and GALLAGHER, K.P. (1991). Influence of microstructure on fatigue crack propagation in polyoxymethylene. J. Mater. Sci., 26, 792-798.

RUNT, J. and JACQ, M. (1989). Effect of crystalline morphology on fatigue crack propagation in polyethylene. J. Mater. Sci., 24, 1421-1428.

SALAMATINA, O.B., HOHNE, G,W,H., RUDNEV, S.N. and OLEINIK, E.F. (1994). Work, heat and stored energy in compressive deformation of glassy polymers. Thermochim Acta, 247, 1-18.

SAUER, J.A. and CHEN, C.C. (1983). Crazing and fatigue behavior in one- and two-phase glassy polymers. Advances in Polymer Science, 52/53, 169-224.

SAUER, J.A. and MARA, M. (1990). Effect of molecular variables on crazing and fatigue of polymers. Advances in Polymer Science, 91/92, 69-118.

SCHULTZ, J.M. (1984). Microstructureal aspects of failure in semicrystalline polymers. Polym. Eng. Sci., 24, 770-785.

SEHANOBISH, K., HADDAOUI, N. and MOET, A. (1993). Effect of thickness on ductile fatigue crack propagation in polycarbonate. J. Mater. Sci., 28, 1360-1366.

SHAH, A, STEPANOV, E.V., CAPACCIO, G., HILTNER, A. and BAER, E. (1998). Stepwise fatigue crack propagation in polyethylene resins of different molecular structure. J. Polym Sci. Polym. Phys., B36, 2355-2369.

SHAH, A, STEPANOV, E.V., HILTNER, A., BAER, E. and KLEIN, M. (1997). Correlation of fatigue crack propagation in polyethylene pipe specimens of different geometries. Inter. J. Fract., 84, 159-173.

STREBEL, J.J. and MOET, A. (1991). Accelerated fatigue fracture mechanism of medium density polyethylene pipe material. J. Mater. Sci., 26, 5671-5680.

STREBEL, J.J. and MOET, A. (1995). The effect of annealing on fatigue crack propagation in polyethylene. J. Polym. Sci. Polym. Phys., 33, 1969-1984.

TAKEMORI, M.T. (1990). Competition between crazing and shear flow during fatigue. Advances in polymer science, 91/92, 263-300.

TEH, J.W., WHITE, J.R. (1979). Fractures surfaces produced by monotomic and cyclic loading of low-density polyethylene. J. Polym. Sci. Polym. Lett. Edn., 17, 737-742.

TEH, J.W., WHITE, J.R and ANDREWS, E.H. (1979a). Fatigue of viscoelastic polymers: 1. Crack-growth characteristics. Polymer, 20, 755-763.

TEH, J.W., WHITE, J.R and ANDREWS, E.H. (1979b). Fatigue of viscoelastic polymers: 1. Fractography. Polymer, 20, 764-771

TON-THAT, M.T., PERRIN, F., LACAND, P., COLE, K.C., DENAULT, J. and ENRIGHT, G. (2001). Preparation and performance of nanocomposites based on polypropylene and layered nanoclays. Polymer Nanocomposites 2001, Montreal September 17-19 2001, Society for Plastics Engineers, Paper #49.

TROTIGNON, J.P., DEMDOUM, L. and VERDU, J. (1992a). Effect of mineral fillers in low concentration on the mechanical properties of polymeric materials: Part 1 Static and fatigue fracture of polypropylene, qualitative aspect. Composites, 23, 313-318.

TROTIGNON, J.P., DEMDOUM, L. and VERDU, J. (1992b). Effect of mineral fillers in low concentration on the mechanical properties of polymeric materials: Part 2 Fatigue of polypropylene, kinetic aspects. Composites, 23, 319-325.

TROTIGNON, J.P., DEMDOUM, L. and VERDU, J. (1993). Fatigue behavior of mineral filled polyamide 6-6. Advanced composites '93, Wollongong February 15-19 1993, TMS, Warrendale, 573-577.

TROTIGNON, J.P. and VERDU, J. (1987a). Skin-core structure-fatigue behavior relationships for injection-molded parts of polypropylene - I. Inflence of molecular weight and injection conditions on the morphology. J. App. Polym. Sci., 34, 19-36.

TROTIGNON, J.P. and VERDU, J. (1987b). Skin-core structure-fatigue behavior relationships for injection-molded parts of polypropylene - II. Morphology-fatigue behavior relationships. J. App. Polym. Sci., 34, 19-36.

TROTIGNON, J.P., VERDU, J., MARTIN, C.H. and MOREL, E. (1993). Fatigue behaviour of some temperature-resistant polymers. J. Mater. Sci., 28, 2207-2213.

USUKI, A., KOJIMA, Y., , KAWASUMI, M., OKADA, A., FUKUSHIMA, Y., HURAUCHI, T. and KAMIGAITO, O. (1993). Synthesis of nylon 6-clay hybrid. J.. Mater. Res., 8, 1179-1183.

SIMHA, R., UTRACKI, L.A., GARCIA-REJON, A. (2001). Pressure-volume-temperature relations of a poly- epsilon -caprolactam and its nanocomposite. Composite Interfaces, 8, 345-353

VARGA, J. (1992). Review Supermolecular structure of isotactic polypropylene. J. Mater. Sci., 27, 2557-2579.

VARLOT, K., REYNAUD, E., KLOPPFER, M.H., VIGIER, G. and VARLET, J. (2001). Clay-reinforced polyamide: preferential orientation of the montmorillonite sheets and the polyamide crystalline lamellae. J. Polym. Sci. Part B: Polym. Phys., 39, 1360-1370.

WARD, I.M. and D.W. Hadley (1993). An Introduction to the Mechanical Properties of Solid Polymers, John Wiley & Sons, New York, 334 pages.

WAY, J.L., ATLINSON, J.R., NUTTING, J. (1974). ?, J. Mater. Sci., 9, 293-

WU, S. (1988). A generalized criterion for rubber toughening: the critical matrix ligament thickness. J. Appl. Polym. Sci., 35, 549-561.

WU, S. (1992). Control of intrinsic brittleness and toughness of polymers and bends by chemical structure: a review. Polym. Int., 29, 229-247.

YAMASHITA, A., HIGASHI, S., KOMATSU, S.T., TAKAHARA, A. and KAJIYAMA, T. (1998). Fatigue analyses of short glass fiber reinforced nylon 6 on the basis of dynamic viscoelastic measurements under cyclic fatigue. Key Engineering Materials, 137, 147-154.

YAMASHITA, A., TAKAHARA, A. and KAJIYAMA, T. (1999). Aggregation structure and fatigue characteristics of (nylon 6/clay) hybrid. Compos. Interf., 6, 247-258.

YANG, F., OU, Y. and YU, Z. (1998). Polyamide 6 / silica nanocomposites prepared by in situ polymerization. J. App. Polym. Sci., 69, 355-361.

YEE, A.F., PLUMMER, C.J.G., SOLES, C.L., XIAO, C., WU, J. and KAUSCH, H.H. (1995). Effect of limiting chain mobility on the yielding and crazing behavior of bisphenol-A polycarbonate derivatives. Macromolecules, 28, 7157-7164.

YEH, J.T. and CHEN, C.Y. and HONG, H.S. (1994). Static fatigue behaviour of linear low-density polyethylenes. J. Mater. Sci., 29, 4104-4112.

YEH, J.T. and RUNT, J. (1989). Fatigue crack-propagation in annealed poly(butylene terephthalate. J. Mater. Sci., 24, 2637-2642.

ZERDA, A.S. and LESSER, A.J. (2001). Intercalated clay nanocomposites: morphology, mechanics and fracture behavior. J. Polym. Sci. Part B: Polym Phys, 39, 1137-1146.

ZHOU, H. and WILKES, G.L. (1998). Orientation-dependent mechanical properties and deformation morphologies for uniaxially melt-extruded high-density polyethylene films having an initial stacked lamellar texture. J. Mater. Sci., 33, 287-303.

ZHOU, Y. and BROWN, N. (1989). Fatigue behaviour of notched polyethylene as a function of R. J. Mater. Sci., 24, 1458-1466.

ZHOU, Y. and BROWN, N. (1992). Evaluating the fatigue resistance of notched specimens of polyethylene. J. Polym Sci Part B: Polym Phys., 30, 477-487.

ZHOU, Y., LU, X. and BROWN, N. (1993). A fatigue test for controlling the quality of polyethylene copolymers. Polym. Eng. Sci., 31, 711-716.

ZHOU, Y. and BROWN, N. (1994). Slow crack growth of bends of high density and linear low density polyethylenes as influenced by morphology. Polymer, 35, 3619-3623.

ZHOU, Y. and BROWN, N. (1995). Anomalous fracture behaviour in polyethylenes under fatigue and constant load. J. Mater. Sci., 23, 6065-6069.

ZHOU, Y., BROWN, N. and CRIST, B. (1995). Slow crack growth in blends of HDPE and model copolymers. J. Polym. Sci. Polym. Phys., 33, 1047-1051.

ZOK, F. and SHINOZAKI, D.M. (1987). Dilatational damage accumulation during fatigue of polypropylene. J. Mater. Sci., 22, 3995-4001.

ZOK, F. and SHINOZAKI, D.M. (1994). Environmental fatigue crack growth in spherulitic polyethylene. J. Mater. Sci. Lett., 13, 940-943.

APPENDIX

A.1 GENERALITIES ON POLYMERIC MATERIALS

Derived from the Greek, the term "Polymer" refers to organic macromolecules that contain many similar repeating units (Mascia, 1989). If these units are linked into a three dimensional network fashion, the polymer is called a cross-linked polymer or a thermoset. If the units are arranged sequentially to form long linear chain molecules, the polymer is called a linear polymer or a thermoplastic. After their polymerization, thermoplastics can be melted while thermosets undergo thermal degradation of their molecular structure. Industrial thermoplastic materials can be in two different states of supermolecular arrangement: the amorphous state and the semicrystalline state. In the amorphous state, which is the supermolecular state of polycarbonate (PC) and polystyrene (PS), the macromolecular chains remain disoriented upon cooling. This type of behavior can be associated with either or both a high melt viscosity and a low thermodynamic stability of the potential ordered structure. The melt viscosity is affected by average molecular weight and molecular weight distribution of the polymer as well as by the presence of the lateral groups. The thermodynamic stability of the potential ordered structure depends largely on the relative positions of the lateral groups (e.g. isotactic, syndiotactic or atactic configurations) and also on their size.

In the semicrystalline state, which is the supermolecular state of polypropylene (PP) and PA6, a part of the polymer chain segments are aligned along their length and they form crystals. The level of crystallinity can vary from zero to approximately 90% (Mascia, 1989). All semicrystalline polymers contain amorphous phase regions and crystalline phase regions. In that sense, non-reinforced semicrystalline polymers can be considered as composites. Their properties are highly affected by the arrangement of and the bonding between the amorphous phase and the crystalline phase regions. This composite structure and its effect on the deformation behavior is described in details in section 2.1.

A.1.1 Polymeric Materials Processing

After being produced from different polymerization processes, thermoplastic polymers are usually solidified in the form of pellets. In order to produce a component or a test specimen from the pelletized polymer, many forming processes can be employed. Only two basic direct molding techniques using pellets are considered here: compression molding and injection molding.

In compression molding, the pellets are melted in an open-die mold where a compression force is applied. In injection molding, the pellets are melted in a screw or a twin-screw melting unit before being injected in a closed-die mold. For both compression and injection molding, the resulting microstructure depends on many molding parameters. A major difference exists between compression molding and injection molding: in the latter, local viscous flow of the polymer associated with a shear couple along the local flow direction induces local macromolecular chain orientation. The materials employed in this M.A.Sc. project were injection-molded.

A.1.1.1 Processing Parameters and Chain Orientation

The rheology of a polymer melt is quite complex. A highly simplified approach will be employed here: the polymer will be considered as a Newtonian fluid. For this simplest type of fluid, the occurrence of either a lamellar or a bulk turbulent flow depends on the Reynolds's number (Re) (Bird, Stewart and Lightfoot, 1960). Bulk turbulent flow is generally accompanied by a lamellar film near the walls. Bowman, Harris and Bevis (1975) have shown that the microstructure of etched injection-molded semicrystalline polymer tensile bars contained basically two types of regions. X-ray diffraction results reported in the form of pole figures indicated that the two different types of regions corresponded to different degrees of macromolecular chain orientation: relatively non-oriented zones and highly oriented zones. In all cases, a region near the surface was found to have a large amount of macromolecular chain orientation along the molding direction. This region is called the subskin.

The extent of lamellar flow and it location depend on the processing conditions. Under intermediate processing conditions, a sandwich-like stacking of two oriented and two non-oriented regions through the thickness from the surface to the mid-thickness, as shown schematically in Figure A.1, can be obtained (Bowman, Harris and Bevis, 1975). At times when the melt temperature was particularly high, the second oriented band seen in moving away from the specimen surface was narrow (about 300 to 400 μm), near the specimen mid-thickness, with macromolecular preferential chain orientation perpendicular to the injection molding direction. These particular processing-induced microstructures indicate that the microstructure of an injection-molded sample cannot always be divided in only the subskin and core components.

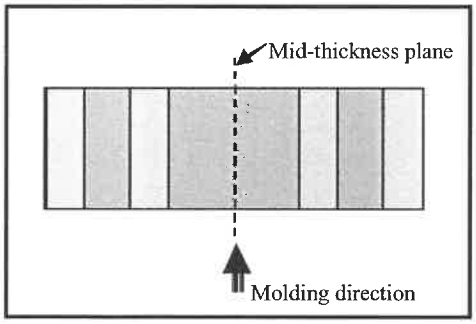

Figure A.1: Sandwich-like stacking of oriented (dashed) and non-oriented (gray) regions in an injection-molded sample.

Results have shown that the proportion of oriented regions increases as the mold temperature decreases. The effect on this proportion of other molding parameters such as the mold temperature, the polymer flow rate and the final injection pressure appears more difficult to generalize (Bowman, Harris and Bevis, 1975). The processing induced microstructure cannot be predicted easily from the pellet material rheology and the processing parameters.

A.1.1.2 Chain Orientation and Characterization of Structure and Properties

The chain orientation effect has an important consequence on the local polymer structure and on the polymer properties. Chain orientation affects the overall polymer crystallinity (Trotignon and Verdu, 1987). Bowman, Harris and Bevis (1975) measured higher microhardness values and higher indentation anisotropy in the oriented zones. It is important to note that the orientation varies through the specimen thickness and that a detailed characterization of the microstructure of a test specimen should be made where the properties are evaluated. Depending where crack initiation occurs, the detailed characterization of the morphology and of the fatigue-induced damage must be performed at different locations. The variations of the morphology through the specimen thickness can allow in theory a comparison of the fatigue-induced damage occurring prior to crack initiation under different material morphology conditions.

A.1.2 Mechanical Behavior of Thermoplastics

Generalities of on the viscoelastic behavior, the tensile inelastic stretching behavior and the creep behavior of polymers will be presented in the present section.

A.1.2.1 Models for the Viscoelastic Behavior of Polymers

The viscoelastic behavior is a general term that generally refers to the influence of time and temperature on the mechanical response of materials. Since most of the current knowledge regarding the phenomenology of the viscoelastic behavior of polymers has been developed for amorphous polymers, the following discussion is initially limited to such polymers. If the total deformation of a polymer can be considered as the sum of independent elastic (Hookean) and viscous (Newtonian) components, the polymer has a linear viscoelastic behavior. In such a case, the Boltzman superposition principle (c.f. below) can be applied. Linear viscoelasticity is dominant up to about 1 % of strain in most useful plastics (Ward and Hadley, 1993). When the independence between the deformation components is not respected, the polymer has a non-linear viscoelastic behavior. The description here will be first restricted to the linear viscoelastic behavior.

For the most general case of a linear viscoelastic solid, the total deformation induced by the application of a constant load can be divided into an immediate elastic deformation, a delayed elastic deformation and a Newtonian flow (Ward and Hadley, 1993). Two mechanical analogue models for the linear viscoelastic behavior are shown in Figure A.2. The model in Figure A.2a is called the standard linear solid (SLS). This model provides an approximate representation of the observed behavior of polymers in their viscoelastic range (Ward and Hadley, 1993). In the SLS model, a spring of modulus E_a is in parallel with a Maxwell unit, which is a unit consisting of a spring and a Newtonian dashpot in series. A Newtonian dashpot is a cylinder system in which a piston moves at a rate proportional to the viscosity of the oil and proportional to the applied stress.

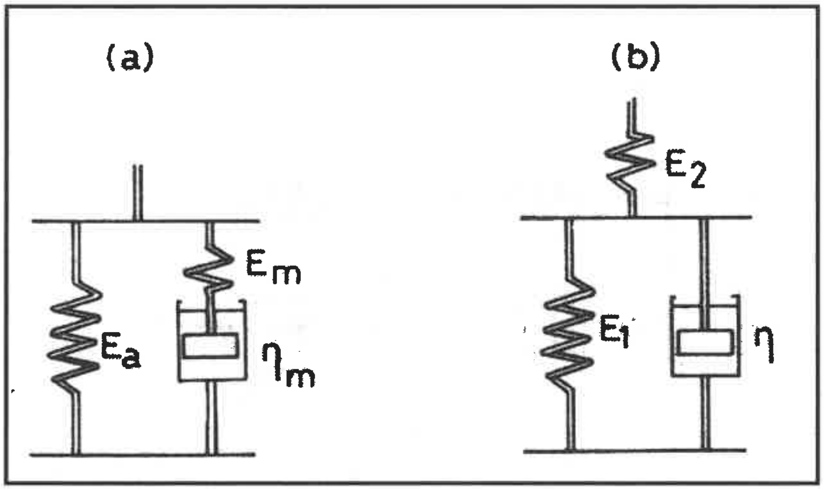

Figure A.2: Mechanical analogue models for the linear viscoelastic behavior where (a) is called the standard linear solid (SLS) model (from Ward and Hadley, 1993).

The following discussion is based upon the SLS model. In creep, which is a constant stress static loading mode, the spring of modulus E_a extends as a result of load transfer from the Maxwell unit. Load transfer from the Maxwell unit to the spring of modulus E_a occurs by time dependent extension of the dashpot unit. In stress relaxation, which is a constant strain static loading mode, the extension of the spring of modulus E_a remains constant while the extension of the spring of the Maxwell unit decreases as a result of time dependent extension of the dashpot. For both creep and stress relaxation loading, the extension of the dashpot of the Maxwell unit cannot be recovered instantaneously upon unloading. Upon unloading, one can expect to have a residual elongation of the spring of modulus E_a and a residual contraction of the spring of modulus E_m. A potential energy is associated with these residual spring elastic strains. This potential energy can be a driving force for recovery after unloading. The recovery will occur by viscous flow in the dashpot. The degree of extension of the dashpot at a given time directly affects deformation behavior of the system. This degree of extension depends on the loading history.

The conclusion, derived from the SLS model, that the loading history affects the deformation behavior of the system was proposed by Boltzmann for creep in 1876 (Ward and Hadley, 1993). From the independence of the elastic (Hookean) and viscous (Newtonian) components, Boltzmann also proposed a superposition principle: each loading step makes an independent contribution to the final deformation. Returning to the SLS model, the superposition principle has the following consequence: the total extension of the dashpot is the summation of the extension induced by each successive loading step, and is therefore dependent on the loading history. This also implies that one can predict the creep deformation resulting from loading at a stress of 2σ by multiplying by two the creep deformation resulting from loading at a stress of σ. In other words, the viscoelastic deformation is independent of the total instantaneous stress. As it will be shown below, this independence in creep is dubious since the creep deformation is thermally activated.

However, in most practical cases the viscoelastic response of a polymer cannot be considered as linear. In non-linear viscoelasticity, no general approach is considered entirely satisfactory (Ward and Hadley, 1993). However, there is experimental evidence that the creep deformation of polymers is thermally-activated. By assuming that the deformation of a polymer is a thermally activated process involving the motion of segments of macromolecules over potential barriers, Eyring *et al.* (1945) developed a theoretical equation in order to describe the macroscopic deformation behavior.

The development of the Eyring equation for non-linear viscoelasticity is based upon the assumptions that the applied stress produces linear shifts $\beta\ \sigma$ (where β is the activation volume for the molecular event and σ is the stress) of the energy barriers ΔH in a symmetrical way manner that the net flow of segments of macromolecules over the energy barriers is linearly related to the macroscopic deformation rate. Before the application of a stress, the number of chain segments moving in one direction ν_1 is balanced by β is the activation volume for the molecular event so that the system is in equilibrium and the values of ν_1 and ν_2 are given by Equation A.1. When a load is applied in the same direction as the direction of the ν_1 chain movement, the value of ν_1 is given by Equation A.2, the value of ν_2 is given by Equation A.3 and the overall deformation rate is given by Equation A.4. Equation A.4 will be called the Eyring equation of polymer non-linear viscoelasticity. According to this equation, the deformation rate of the polymer depends exponentially on the stress applied. This characteristic contrasts with the linear dependence between the strain rate and the stress in Newton's viscous flow law. The SLS model of linear viscoelasticity can be adapted to non-linear viscoelasticity by saying that the movement of the dashpot is governed by a thermally-activated process (Ward and Hadley, 1993).

Equation A.1:

$$\nu = \nu_0 \exp\left[-\frac{\Delta H}{RT}\right]$$

Equation A.2:

$$\nu_1 = \nu_0 \exp\left[-\frac{(\Delta H - \beta\sigma)}{RT}\right]$$

Equation A.3:

$$\nu_2 = \nu_0 \exp\left[-\frac{(\Delta H + \beta\sigma)}{RT}\right]$$

Equation A.4:

$$\frac{de}{dt} = \dot{e} = \dot{e}_0 \exp\left[-\frac{\Delta H}{RT}\right]\left\{\exp\left[\frac{\beta\sigma}{RT}\right] - \exp\left[-\frac{\beta\sigma}{RT}\right]\right\}$$

In viscoelasticity, the deformation rate at low stress may follow Newton's viscous flow law but the deformation rate at high stress varies exponentially with the applied stress. Experimental results have shown that the viscoelastic deformation of polymers at high stress is a thermally activated process (Ward and Hadley, 1993), which explains the dependence of the viscoelastic behavior on temperature. The driving force for recovery after unloading is due to the presence of an internal potential energy. Using the SLS model, the internal potential energy after a creep experiment comes from the residual contraction in the spring in series with a dashpot and the residual tension in the other spring. The molecular processes that may lead to the accumulation of internal potential energy or to a decrease in the entropy of the system will be further discussed in section 1A.2.2.

A.1.2.2 Delayed Deformation Response and Relaxation Transitions

A practical consequence of viscoelasticity in cyclic loading is the delay of the strain response to an applied load. Three parameters are employed to characterize the polymer viscoelastic response upon continuous sinusoidal cycling. Expressions for the applied stress of Equation A.6 and for the delayed strain response of Equation 7.5 are employed to define the phase lag (δ). The expression for the applied stress of Equation A.6 can be divided (following trigonometric relationships) into a stress component in phase with the strain ($\sigma_o \cos \delta \sin \omega t$) and a stress component out of phase with the strain ($\sigma_o \sin \delta \cos \omega t$), as shown in Equation A.7. The stress-strain relationship can also be expressed by two components, as shown in Equation A.8, employed to derive expressions of the storage modulus E' (Equation A.9) and the loss modulus E'' (Equation A.10). Combining Equation A.9 with Equation A.10, the tangent of the phase lag ($\tan \delta$) can be expressed as the ratio between the loss modulus and the storage modulus (Equation A.11). The $\tan \delta$ is the third parameter often employed to characterize the polymer viscoelastic response to continuous sinusoidal cycling.

Equation A.5: $$e = e_0 \sin \omega t$$

Equation A.6: $$\sigma = \sigma_0 \sin (\omega t + \delta)$$

Equation A.7: $$\sigma = (\sigma_0 \cos \delta) \sin \omega t + (\sigma_0 \sin \delta) \cos \omega t$$

Equation A.8: $$\sigma = e_0 E' \sin \omega t + e_0 E'' \cos \omega t$$

Equation A.9: $$E' = \sigma_0 / e_0 \cos \delta$$

Equation A.10: $$E'' = \sigma_0 / e_0 \sin \delta$$

Equation A.11: $$\tan \delta = E'' / E'$$

The parameters E', E'' and δ are employed to characterize the relaxation transitions in polymers. On a tan δ versus temperature scan, the peaks in the value of tan δ are associated with molecular relaxation transitions and are customarily labeled α, β, γ, δ, etc. in alphabetical order with decreasing temperature. The peak labeled α, which is the highest temperature peak, is called the glass transition temperature (T_g). In general, the stiffness of polymers varies significantly near this T_g. The T_g value, measured using viscoelastic response of the polymer upon continuous sinusoidal cycling, varies with the time-scale of the experiment, which is related to the loading frequency.

Dilatometric measurements at different temperatures is a second method employed to determine a T_g for a given polymer. The dilatometric T_g is defined as the temperature at which there is a discontinuity in the slope of the relationship between the density and the temperature. The discontinuity in the curve is expected to originate from a difference in the relationship between the free volume fraction and the temperature. Below the critical temperature, the free volume fraction is expected to be independent of temperature, while above this temperature, the free volume fraction is expected to increase with temperature (Ward and Hadley, 1993). The dilatometric T_g is slightly dependent on the rate of heating, which can be considered as the time-scale of the experiment. The dilatometric T_g itself is not considered as a thermodynamic transition temperature. However, the temperature $T_2 = T_g - 52.6^{\circ}C$ could correspond to a secondary order thermodynamic transition temperature (Ward and Hadley, 1993). The value of

52.6°C has been established by applying the Williams-Landel-Ferry equation to the experimental data obtained with a variety of polymers. The dilatometric T_g and the T_g measured by continuous sinusoidal cycling testing are transition temperatures at which the time-scale for certain molecular processes, which are not thermally activated below T_2, is comparable with the time-scale of the experiment.

The macromolecular chain structure, the molecular mass and the presence of plasticizing agents are among the principal factors that affect the T_g of amorphous polymers. In semicrystalline polymers, the glass transition temperature usually exists, but the extent of variation with temperature in the polymer stiffness increases as the proportion of the amorphous phase increases. As in the case of amorphous polymers, the T_g in semicrystalline polymers is associated with a change in the thermally activated molecular processes governing the deformation of the amorphous phase. It is frequently possible to attribute the other relaxation peaks (β, γ, δ, etc.) to either the amorphous or the crystalline component (Ward and Hadley, 1993). The analysis of the polymer viscoelastic response upon continuous sinusoidal cycling can be employed as a tool to determine which molecular processes are likely to occur upon deformation at a given temperature and experiment time-scale.

A.1.2.3 Inelastic Deformation during Tensile Elongation

The term inelastic deformation refers to the strain component that is not instantaneously recovered upon unloading. Accordingly, one can divide the strain response of a thermoplastic into two components: an elastic deformation component and an inelastic deformation component. In the previous subsection, the macroscopic behavior of thermoplastics subjected to a low strain was considered. Under those conditions, most of the deformation is elastic. When a thermoplastic is subjected to a high strain, the inelastic component of the deformation becomes dominant. The present and the next (section A.1.2.4) sections will consider the macroscopic deformation response to such higher amplitude strain.

The engineering tensile stress-elongation curves of semicrystalline polymers often present a point over which the load borne by the specimen decreases as the elongation increases. However, the deformation of semicrystalline polymers does not give rise to intrinsic softening of the material when the applied specimen elongation rate is low enough that no excessive specimen temperature increase occurs. This is shown in Figure A.3a where the true stress versus true strain relationships are plotted for different semicrystalline polymers. Another characteristic of semicrystalline polymers subjected to tensile elongation is that the strain hardening rate increases after a certain amount of deformation (c.f. Figure A.3a).

Step-like variations of the specimen elongation rate induce discontinuities in the true stress versus true strain relationship as shown in Figure A.3b. When the strain rate is increased rapidly, the stress increases rapidly and then decreases or increases but at a lower rate than before the strain rate increase. This behavior can be attributed to a time-delayed deformation. The opposite phenomenon occurs when the strain rate is decreased rapidly. The time-delayed deformation induced when the strain rate is increased or decreased indicates that the viscoelastic properties of polymers may affect their inelastic deformation behavior at least in the cases where variations in the true strain rate occurs. However, the memory of the previous strain rate history is retained only during a transient period.

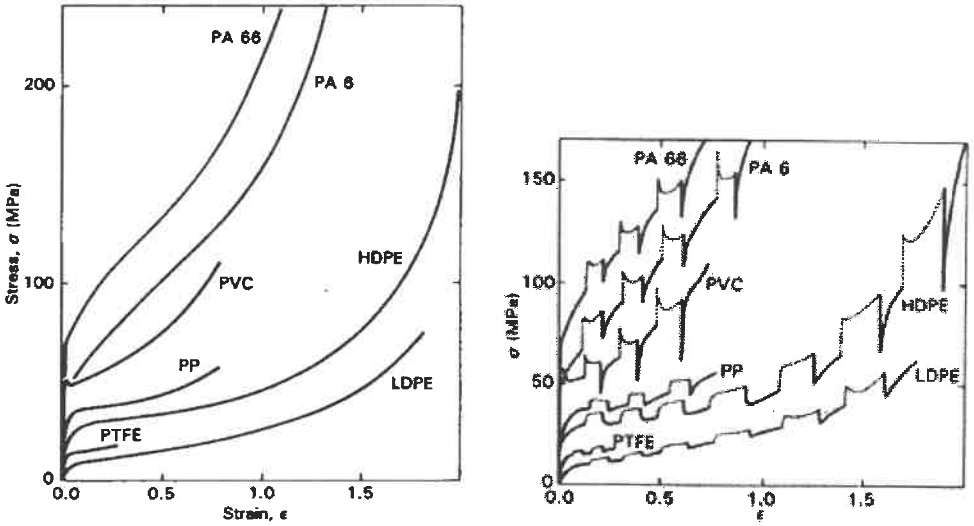

(a) (b)

Figure A.3: Tensile behavior of semicrystalline polymers: (a) True stress-strain curves at a true strain rate of 0.1%/s; (b) Effect of repetitive true strain rate variation from 0.1%/s (continuous curved segments) to 1%/s (dashed segments) (from Lin and Argon, 1992).

During tensile testing, the relative volume variation of the specimen gauge section can be called the volume strain ($\Delta V/V$). The measurement of the volume strain can provide some insight regarding the nature of the deformation. One can divide the volume strain of a tensile specimen into three components according to Equation A.12: an elastic component ($\Delta V_{EL}/V$), a deviatoric component ($\Delta V_{DEV}/V$) and a dilatational component ($\Delta V_{DIL}/V$). By measuring the longitudinal strain (ε_L) and long-transverse strain (ε_W), an experimental volume strain can be computed according to Equation A.13. In the development of Equation A.13, it is assumed that the strain in the thickness direction is the same as that in the width direction. According to Equation A.14, the volume increase associated with the elastic component is related to the fact that the axial specimen elastic elongation is not fully compensated by the lateral contraction. In other words, the Poisson's ratio (ν) is less than 0.5. There is no volume variation associated with the deviatoric component (Equation A.15). The volume increase associated with the dilatational component (Equation A.16) is related to the formation of voids, crazes and/or cracks.

Equation A.12 $$\frac{\Delta V}{V} = \frac{\Delta V_{EL}}{V} + \frac{\Delta V_{DEV}}{V} + \frac{\Delta V_{DIL}}{V}$$

Equation A.13 $$\frac{\Delta V}{V} = (1+\varepsilon_L)(1-\varepsilon_W)^2 - 1$$

Equation A.14 $$\frac{\Delta V_{EL}}{V} = (1+\varepsilon_L)(1-\nu * \varepsilon_L)^2 - 1$$

Equation A.15 $$\frac{\Delta V_{DEV}}{V} = 0$$

Equation A.16 $$\frac{\Delta V_{DIL}}{V} = \frac{\Delta V}{V} - \frac{\Delta V_{EL}}{V}$$

Naqui and Robinson (1993) have reviewed the tensile dilatometric studies of deformation in polymers and polymer blends/composites. The addition of particles in a non-reinforced polymer matrix can influence the proportion of each volume strain component. The proportion of each volume strain component can also vary with temperature and strain rate.

In their experimental study, Naqui and Robinson (1993) compared the experimental volume strain (calculated using Equation A.13) with the predicted dilatational component of volume strain (calculated using Equation A.14) as a function of the axial strain. This comparison allows to determine the axial strain beyond which the deviatoric component of the material deformation becomes significant. However, the technique does not allow to determine which proportion of the axial strain is the result of constant volume deformation mechanisms and which is the deviatoric component of the axial strain.

Heikens, Sjoerdsma and Coumans (1981) have proposed a model that enables to decompose the axial strain into three components of deformation by using the dilatometric results, Young's modulus and Poisson's ratio of the polymer. Their model is based upon the two following hypotheses:

- the elastic component of the axial strain is Hookean and linear elastic with a stiffness constant equal to Young's modulus,
- there is no transverse strain associated with the dilatational component of the axial strain.

The former hypothesis leads to Equation A.17 while the latter leads to Equation A.18. The elastic component of the axial strain (ε_{EL}) can be calculated when Young's modulus of the material is known. The dilatational component (ε_{DIL}) can be calculated from the dilatometric results and the deviatoric component (ε_{DEV}) can then be calculated according to Equation A.19.

Equation A.17: $$\varepsilon_{EL} = \sigma / E$$

Equation A.18: $$\varepsilon_{DIL} = \frac{\Delta V_{DIL}}{V}$$

Equation A.19: $$\varepsilon_{DEV} = \varepsilon_L - \varepsilon_{EL} - \varepsilon_{DIL}$$

Dilatometric tensile test results have been reported by Gloaguen and Lefebvre (2001) using the model of Heikens, Sjoerdsma and Coumans (1881). The results, shown in Figure A.4a for 50% RH conditioned PA6 and in Figure A.4b for 50% RH conditioned PA6NC, indicate that the addition of montmorillonite in the PA6 matrix leads to significant increases in the dilatational component of the axial strain upon tensile deformation near or above the T_g. This result is further discussed in section 2.2 of the thesis.

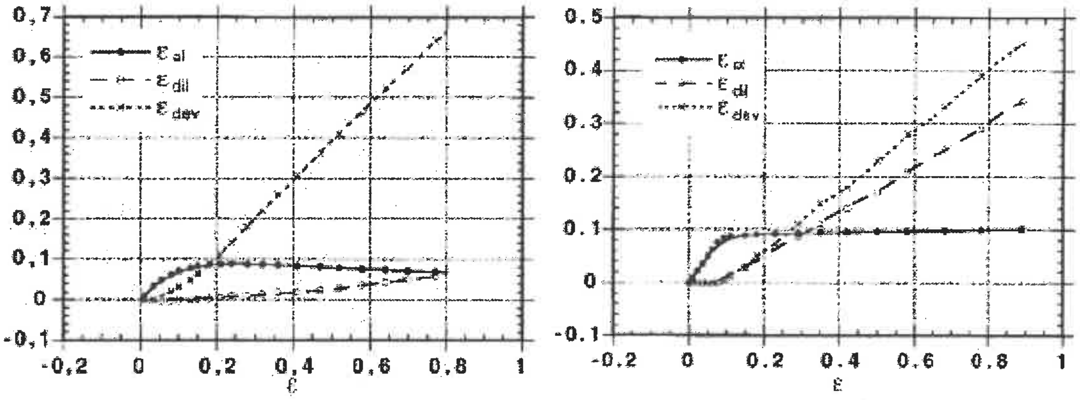

(a)

(b)

Figure A.4: Elastic, deviatoric and dilatational components of the axial strain for (a) 50% RH conditioned PA6 and (b) 50% RH conditioned PA6NC (Gloaguen and Lefebvre, 2001).

A.1.2.4 Reversibility of the Inelastic Deformation

Great care must be taken when qualifying the nature of the inelastic strain. One can distinguish two components of inelastic strain: an anelastic component and a plastic component. The anelastic component can be recovered with time, whereas the plastic component is considered permanent if the temperature is maintained constant. In the case of amorphous polymers (PS, PC and PMMA) strained in compression up to 15-20% (Quinson, Perez, Rink and Pavan, 1996) and up to 50-55% (Kung and Li, 1987), it has been shown that most of the inelastic strain is recovered upon heating up slightly above T_g. Pegoretti, Guardini, Migliaresi and Ricco (2000) studied the strain recovery behavior of semicrystalline polymers as a function of the recovery time and temperature. Films of dried PA6 where strained up to 20% at room temperature and than unloaded. Upon unloading, the non-recovered strain of the PA6 films in those experiments was approximately 8%. The variations of that non-recovered strain as a function of the recovery time and temperature is shown in Figure A.5. After temperature exposure to 75°C for 1000 seconds, the non-recovered inelastic strain fell below 0.2%. The measured T_g of the PA6 films was 69°C. Based on this result, as in the case of amorphous polymers, almost all of the inelastic deformation of semicrystalline polymers can be recovered when the strained sample is exposed to a temperature near the glass transition temperature.

The reversibility of the inelastic deformation is a common characteristic of amorphous and semicrystalline polymers. For amorphous polymers, the nucleation and growth of shear microdomains (SMDs) are expected to be the principal deformation mechanism responsible for the accumulation of anelastic strain (Mangion, Cavaille, and Perez, 1992; Quinson, Perez, Rink and Pavan, 1996). Salamatina, Hohne, Rudnev and Oleinik (1994) also expected an important role of the SMDs in the accumulation of potential energy in the amorphous polymer structure upon deformation. It should however be considered that the complete recovery state corresponds to the state of maximum entropy (Argon, 1980). Above T_g, the entropy barrier might be low enough that thermal activation could induce recovery even in absence of stored elastic or viscoelastic energy.

Oleinik, Shenogin, Paramzina, Rudnev, Shantarovich, Azamatova, Pakula and Fischer (1998) have measured and compared the E’ and E’’ moduli of non-deformed and deformed (by axial compression to 40-45%) PMMA and PC specimens. Deformation was found to decrease the storage modulus (E’) and to increase the lost modulus (E’’). However, annealing the material caused strain recovery and partial recovery of the original viscoelastic properties. They concluded that all changes in the dynamic modulus were due to the anelastic component of the specimen residual strain. However, their work did not attempt to cover the behavior of semicrystalline polymers.

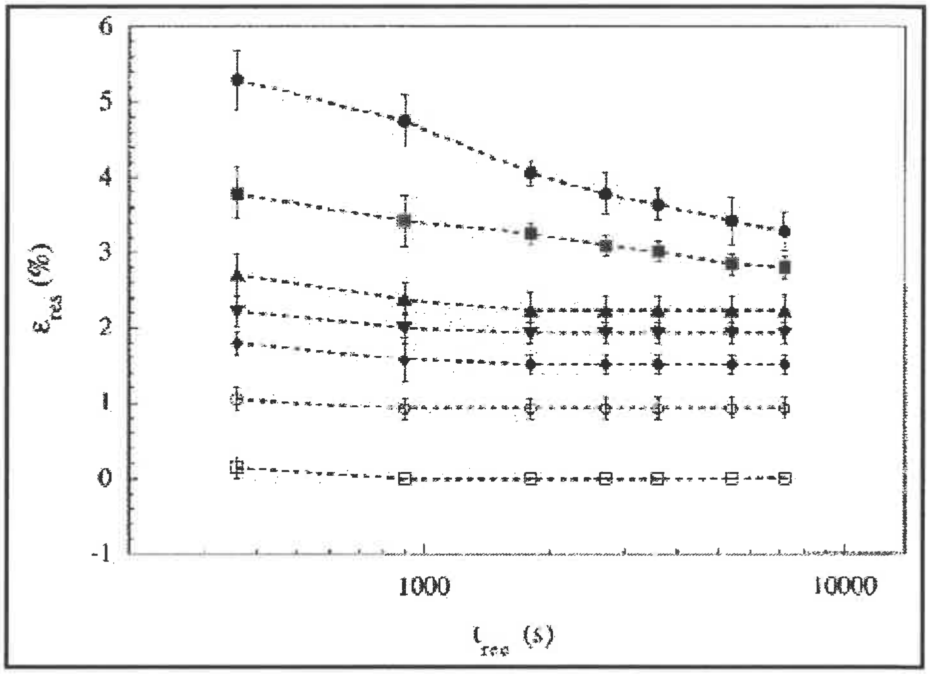

Figure A.5: **Recovery of the residual strain as a function of the recovery time in dried PA6 films (T_g of 69°C) strained up to 20% for recovery temperatures of 25, 30, 50, 55, 60, 70 and 75°C (from top to bottom) (adapted from Pegoretti, Guardini, Migliaresi and Ricco, 2000).**

During interrupted tensile tests performed by Pegoretti, Guardini, Migliaresi and Ricco (2000), the stress – strain curve showed a positive slope up to 20% of strain, strain at which the specimens were unloaded. This result suggests that no specimen necking occurred. Necking leads to a localized a high strain, which induces an important rearrangement of the crystalline phase (section 2.1.2.5). This important rearrangement is most probably an irreversible process. Thus, the plastic component of the inelastic strain would have been of higher magnitude if necking had occurred.

A.1.2.5 Creep Behavior

In characterizing the creep of thermoplastics, a linear relationship between the strain and the time under load is often observed on a log – log scale. Such a linear relationship has been reported for PP tested at 60°C (Ward and Hadley, 1993) and 50% room humidity conditioned PA6 tested at room temperature (Jinen, 1986; Jinen, 1987). However, for 29% room humidity conditioned PA6 tested at room temperature, a transient regime has been reported before the occurrence of a linear relation on a log – log scale (Hunt and Darlington, 1978). A testing temperature below the glass transition temperature might be the reason for this different creep deformation behavior. The linearity on a log – log scale is in accordance with the Eyring equation for non-linear viscoelasticity (Equation A.4). Thus, the creep defromation is a thermally activated process. The strain versus time under load curves of PP tested at 60°C shown in Figure A.6 present two successive stages where linear relationships are observed. This behavior can be explained by the occurrence of two different thermally activated deformation mechanisms coupled in parallel and having different activation volumes. Hunt and Darlington (1979) reported multistage curves for PA66.

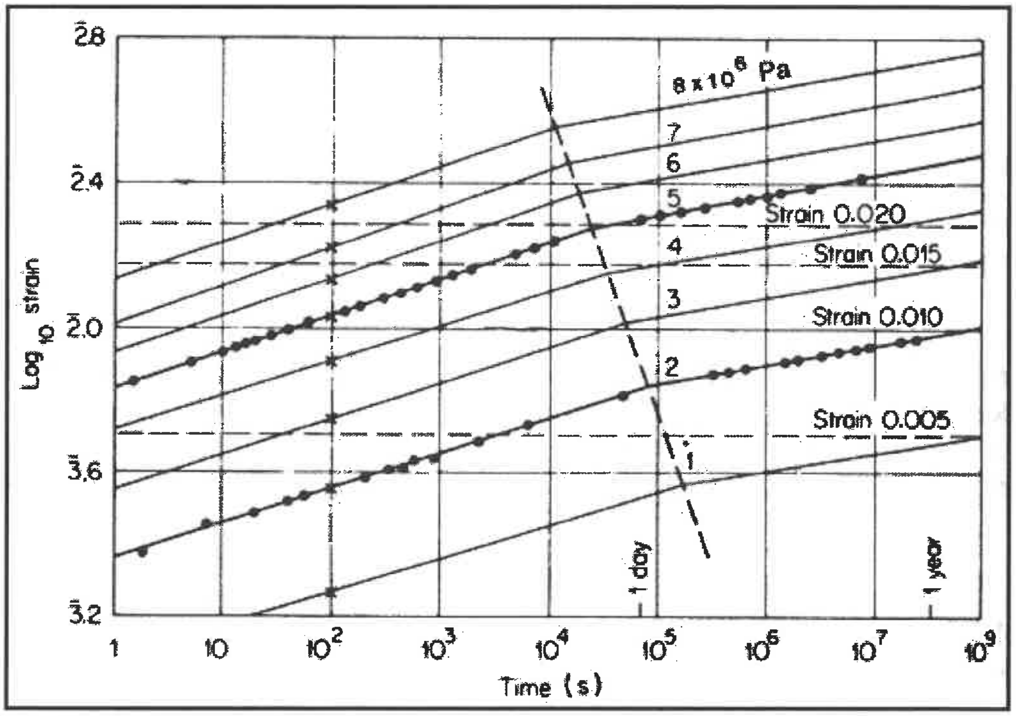

Figure A.6: Tensile creep of PP at 60°C, experimental data obtained for stress levels of 2 and 5 MPa (from Ward and Hadley, 1993).

A.2 AMORPHOUS POLYMERS

The inelastic deformation mechanisms induced by the application of an external force and/or by the presence of an internal viscoelastic energy can be classified by two main categories: viscoelastic deformation processes and plastic deformation processes, with plastic deformation referred to as the deformation that is not recovered after a long post-stressing relaxation time at the testing temperature. A knowledge of the structure of amorphous polymers is a prerequisite to the understanding of all inelastic deformation mechanisms.

A.2.1 Structure of Amorphous Polymers

The amorphous state is characterized by the absence of regular organization at long distance. It is then the opposite to the crystallized state. However, when applied to thermoplastic polymers, the common definition of the amorphous state may include the state where short distance order is present. Although this local order has been observed in low molecular weight amorphous substances, several experimental results suggest that this type of order is absent at higher molecular weight (Kausch, 1987).

When macromolecules are free to move, they adopt the configuration that minimize their free energy, which is the sum of the internal energy and of the energy related to the entropy of the system (degree of disorder). By neglecting the interactions between chain segments as well as intermolecular interactions, the minimal internal energy of a macromolecule corresponds to any condition where the distance between adjacent atoms and the angle between primary bonds are at their equilibrium values. In these conditions of minimal internal energy, a minimization of the free energy requires to maximize the entropy. The entropy is maximized when the set of chain conformations is the most probable statistically. Since there are few specific chain conformations that can lead to highly extended chains, this type of conformation is not dominant in melt solidified polymers. In the absence of strain-induced preferential orientation, the macromolecules are folded and the square root of the mean square end-to-end distance

($<r^2>^{1/2}$) is much lower than the sum of the chain segments. From the unperturbed chain model of Flory (Dettenmaier, 1983), $<r^2>^{1/2}$ is given by

Equation A.20: $$<r^2>^{1/2} = \beta M^{1/2} \quad ;$$

where β is a constant for a given molecular structure and M is the molecular weight of the macromolecules or chain segments. This model was found to agree with the experimental results at least in the case of PC (Dettenmaier, 1983).

Chain entanglement is an important concept employed to explain the deformation behavior of polymers. Heymans (2000) reviewed the current models of entanglement of flexible chains and compared their ability to predict the effects of the macromolecular structure on the level of entanglement. The experimental data employed for comparison were obtained from melt elasticity and viscosity measurements on several polymers. The model that best describes the behavior are different for elasticity and for viscosity. For elasticity, the packing model seems the more appropriate. This model considers as a single important parameter the ratio of the pervaded volume to the occupied volume of the chain, which is proportional to the molecular weight. The pervaded volume is assumed proportional to r_s^3, where r_s is the root-mean-square chain end-to-end distance. For viscosity, the Colby-Rubinstein model seems the more appropriate. This model considers the ratio of the pervaded volume to the occupied volume of the chain multiplied by the number of binary contacts in the pervaded volume. A binary contact occurs when two chain segments are in their immediate neighborhood.

In the solid state, the view employed by several authors (Plummer, Menu, Cudre-Mauroux and Kausch, 1995; Kramer and Berger, 1990; Kausch, 1987; Dettenmaier, 1983; Treloar, 1975) to describe the effect of chain entanglement on the deformation behavior is to consider a network of interconnecting elastic nodes (Figure A.7). The portions of macromolecules constituting this network are those offering the greatest resistance to an imposed large strain. These portions of macromolecules, each of average mass M_e, are retained at their extremity with other similar entities. As a simplified view, an entanglement can be considered as a temporary cross-link between backbone chains and can be visualized as hooks, knots or local interactions such as hydrogen bonding.

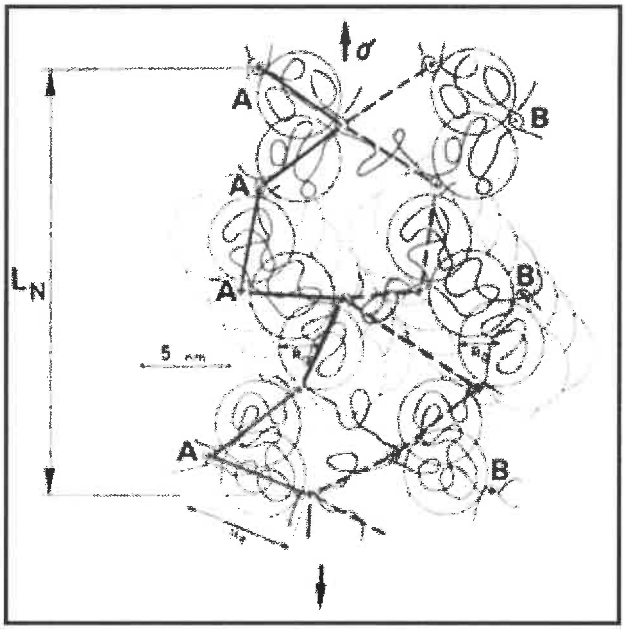

Figure A.7: Schematic view of sequences of entanglement points: each "+" symbol represents an entanglement point, the large solid lines represents a sequence (namely A) of entanglement points that are aligned nearly parallel to the tensile force σ and located in the plane of the figure, the large dotted lines represent a similar sequence (namely B) but located out of the plane of the figure, the distance R_g is the radius of gyration between entanglement points, the distance R_e is the distance between entanglement points, and the distance L_N represents the end-to-end distance of a sequence of a sequence of entanglement points (from Kausch, 1987).

The knots in the solid state are assumed to be the same as those present in the melt and in the rubbery state. No conformational change is expected upon cooling. In the rubbery state, the knots affect the elastic properties in a similar way as the cross-links in rubbers. The most common technique to characterize the level of entanglement is to evaluate the parameter M_e, defined as the molecular weight between entanglement points (usually in g/mol), from the following relation (Kramer, 1983):

Equation A.21: $$M_e = \frac{\rho R T_A}{G^o_N} \quad ;$$

where ρ is the density of the polymer, R is the universal gas constant, T_A is the absolute temperature, and G^o_N is the shear modulus at the rubbery plateau. According to Heymans (2000), the characterization of the chain entanglement by the parameter M_e is oversimplified. Since there is no experimental observation of elastic knots, these knots may or may not have any specific physical representation. However, the parameter M_e is widely employed in the literature on deformation in solid polymers and it allows to explain differences in the behavior between different polymers. M_e will be prime parameter employed in the present text to characterize the entanglement network.

From the above development, a characterization of the structure of an amorphous polymer at the network level must include the molecular weight between entanglements M_e and the average molecular weight of the macromolecules (M_w). In the glassy state, the structure at the network level is expected to have an important effect only at large local deformations (Dettenmaier, 1983; Kausch, Plummer and Teze, 1994). One of these important effects will be discussed in the section on heterogeneous deformation (section A.2.4).

At lower strain and also in the glassy state, the resistance to the relative movement of molecular chains can be expected to be largely controlled by the rigidity of the chains. Experimental evidence of this effect is discussed in the section on homogeneous deformation (section A.2.3). The characteristic ratio of the macromolecular chain, C_∞, is employed to characterize the intrinsic rigidity of a coiled chain. This characteristic ratio is defined by (Wu, 1992)

Equation A.22: $$C_\infty = \lim_{n_v \to \infty} \frac{<r^2>}{n_v <l_v^2>} \quad ;$$

where $<r^2>$ is the mean square end-to-end distance, n_v is the number of statistical skeletal units in a chain and $<l^2_v>$ is the mean square length of such a unit. If the unperturbed chain model applies (c.f. Equation A.20), the value of C_∞ would be unity. As the flexibility of the chains is reduced (by the presence of lateral groups and intermolecular interactions), the value of C_∞ increases.

A.2.2 Viscoelastic Deformation Mechanisms

Below the macroscopic yield stress, Doi and Edwards (1986) have proposed a two step model for the viscoelastic deformation of macromolecules at large strains (Ward and Hadley, 1993). In this model, the original assumption is that the rapid movement of the chain segments of a macromolecule is confined within a tube such as the one presented in Figure A.8. According to this model, the two categories of molecular motion are molecular extension within the tube by migration of molecular kinks along the tube axis, somewhat similar to the movement of dislocations in metals, and lateral movement of the entire tube through a phenomenon called reptation. Reptation requires the migration of entanglements. The characteristic time required for the migration of molecular kinks is much shorter than that required for the migration of entanglements leading to reptation. This difference in the characteristic time required for the activation of the different types of molecular motion can explain that axial contraction of the tube (Figure A.9c) will occur prior to its lateral migration (Figure A.9d) during stress relaxation after a large step strain (Figure A.9). It may also explain the presence of two regimes during creep deformation of PP (c.f. Figure A.6 in appendix A).

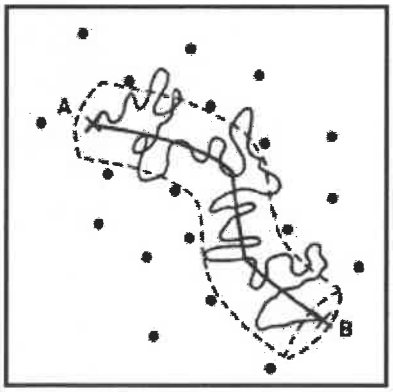

Figure A.8: Confinement of viscoelastic molecular motion within a tube (Ward and Hadley, 1993).

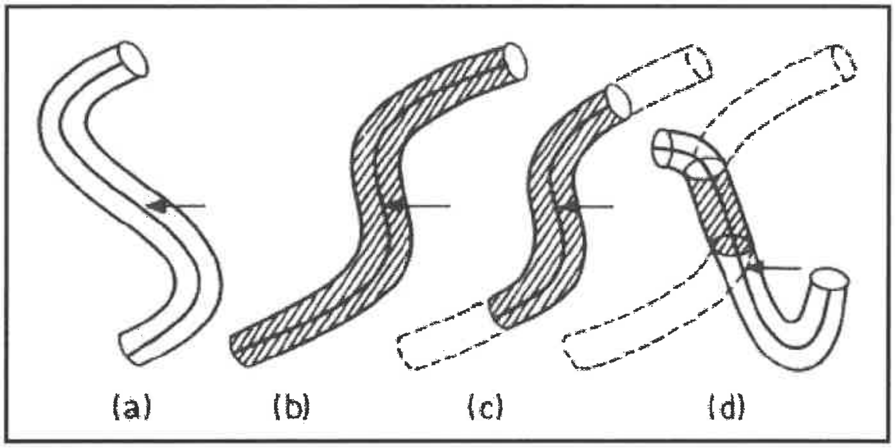

Figure A.9: Model for the sequence of events during stress relaxation: (a) equilibrium conformation before deformation, (b) conformation tube immediately after a large step deformation, (c) conformation after relaxation within the tube by migration of molecular kinks, and (d) conformation after lateral displacement of the tube by reptation (Ward and Hadley, 1993).

A.2.3 Homogeneous Shear Yielding

During loading the combination of external forces and of internal energy stored in the polymer network, as a result of previous deformation, enables deformation processes that were not mechanically and/or thermally activated at lower applied external forces. With the potential exception of chain scission, all deformation mechanisms in polymers can be expected to be thermally activated. The deformation can occur homogeneously (at the micrometer scale) or heterogeneously. Homogeneous inelastic deformation is generally referred to as shear yielding.

Shear yielding in a glassy amorphous polymer is thought to be a non-specific and non-localized event (Argon, 1980). According to computer simulations (Argon, Hutnik, Mott and Suter, 1991), the volume over which a coherent plastic relaxation event occurs would be approximately 67 nm^3 (equivalent of a sphere with a diameter of 5 nm) in PP at low temperature (-40°C). This event would occur through a series of torsion angle changes along the backbone of each molecule (Argon, Hutnik, Mott and Suter, 1991). In

PC, the activated configuration for shear yielding would consist of four molecular segments (Argon and Bessonov, 1977).

In his review on brittleness and toughness of polymers, Wu (1992) presented an experimental correlation between the characteristic ratio of the macromolecules C_∞ (c.f. Equation A.22) and the macroscopic yield stress. Based on this correlation and on the assumption that the molecular parameter controlling the onset of shear yielding is torsion angle changes, the parameter C_∞ appears to be a primary parameter controlling the activation energy for plastic deformation.

In an experimental study in which the yield point of a styrene-acrylonitrile copolymer was measured (in tensile loading, stress relaxation and creep), Marano and Rink (2001) suggested that the anelastic strain, the anelastically stored energy and the viscoelastic energy reached a threshold value at the yield point. Although these parameters might be more relevant than stress and strain by taking into account the time variable, the scatter in the data of Marano and Rink (2001) clearly appeared non-random in nature. It appears that a reliable generalized criteria for the onset of shear yielding under different loading condition does not yet exist in the open literature.

A.2.4 Heterogeneous Deformation

Either before or after the onset of homogenous inelastic deformation, localized or heterogeneous deformation can occur. The occurrence of heterogeneous deformation is a direct consequence of the fact that a polymer is not a continuum of matter. Heterogeneous deformation is often a precursor to crack initiation and propagation.

A.2.4.1 Crazing

A craze is a network of interconnected voids located in a plane that is generally perpendicular to the maximum principal tensile stress. It is similar to a crack with the difference that the opposite surfaces are held together by craze fibrils, which are highly strained ligaments (Kausch, 1987; Kramer, 1983). After its nucleation, a craze will grow in thickness, width and/or length while remaining perpendicular to the maximum principal tensile stress. When the local stress, strain and/or strain rate at the craze tip reach a critical level, craze breakdown occurs by facture in the fibrils or at the interface between the fibrils and the non-crazed matter.

a) Craze Nucleation

Kausch (1987) proposed that the nucleation of a craze depends simultaneously on three groups of variables: the macroscopic state of strain or stress, the nature of defects or heterogeneities in the matrix, and the molecular behavior of the polymer. Craze nucleation (and growth) is favored by a multi-axial tensile stress or, in more general terms, by hydrostatic tension (Kramer, 1983). This effect can account for the formation and growth of crazes from a notch in a semicrystalline polymer tested above its T_g while the same material would not craze in the presence of a hydrostatic compression or in the absence of a notch (Narisawa and Ishikawa, 1990). Since it reduces the mobility of the chains, increasing the local strain rate can be considered to have an indirect effect on the molecular behavior.

As shown by Argon and Hannoosh (1977), there is a time delay between the application of a stress and the moment when a craze can be detected. In most practical cases, crazes initiate at surface defects or near the surface of internal secondary phase particles. In such cases, the surface density of crazes increases almost linearly with time on a log-log scale before reaching a saturation value (Argon and Hannoosh, 1977). This saturation of the surface density of crazes can be interpreted as the saturation of the most favorable set of heterogeneous craze nucleation sites.

A second type of crazes, usually referred to as crazes II or intrinsic crazes, have been reported to nucleate at an extension ratio of 2.1 during tensile elongation of PC at 10-15°C below T_g (Dettenmaier, 1983). A similar behavior have been reported at an extension ratio of 2.7 in PMMA (De Brossin, Dettenmaier and Kausch, 1982). In an attempt to correlate the nucleation of intrinsic crazes and the instability of the entanglement network (c.f. section A.2.1), Dettenmaier (1983) defined λ^e as the maximal extension ratio of strands between entanglement points, which can be estimated by

Equation A.23

$$\lambda^e = \frac{l_e}{R_e} = \frac{M_e}{M_o}\frac{l_o}{R_e} \quad ;$$

where R_e is the root-mean-square end-to-end distance of unperturbed segments (calculated from Equation A.20), l_e is the length of a completely elongated segment, M_e is the molecular weight of entanglement, M_o is the molecular weight of the monomer unit, and l_o is the length of the projection of the monomer unit on the chain axis. A segment is here defined as a chain of entanglement molecular weight joining two entanglement points. By replacing R_e by

Equation A.20, Equation A.23 becomes

Equation A.24

$$\lambda^e = \frac{l_0}{M_o \beta} M_e^{1/2} \quad .$$

Dettenmaier (1983) found agreement between the calculated value of λ^e (for PC and PMMA) and the extension ratio at which intrinsic crazing occurs during tensile testing, which suggests that intrinsic crazing occurs at the onset of instability in the entanglement network at large strain.

In a study of Dettenmaier (1983) different degrees of pre-orientation were induced by deformation at approximately 10°C above T_g. When the pre-oriented samples were loaded in tension below T_g with the tensile axis parallel to the pre-orientation axis, the extension ratio at which intrinsic crazing occurred was found to decrease with an increase in the molecular degree of pre-orientation. However, the stress at which intrinsic crazing occurred increased with the degree of pre-orientation. The logarithm of the total extension ratio at intrinsic craze nucleation, which is the sum of the inelastic deformation induced by pre-orientation and the deformation induced during the tensile test, was found to increase linearly with the extension ratio induced by pre-orientation. Dettenmaier

(1983) suggested that, during pre-orientation above T_g, chain slippage and disintegration of entanglement points were effective mechanisms, which further supported the suggestion that intrinsic crazing occurs at the onset of instability in the entanglement network at large strain.

The remainder of the present section be limited to extrinsic crazes. Kausch (1987) proposed that the dominant mechanism in extrinsic craze nucleation is an unstable reorientation of segments (again, a segment is defined as a chain of entanglement molecular weight joining two entanglement points), a reorientation which seems to preserve the entanglements previously existing in that direction. This proposition is supported experimentally by the independence of the critical stress (or strain) for craze nucleation with the molecular weight, reported for example in PS (Kausch, 1987) for $M_w > 2\ M_e$. Below T_g, the segments have a small internal mobility (segment elongation) and also small external mobility (segment motion). During elastic straining, local stresses develop between segments and the local stresses are not evenly distributed. At some point, a reorganization of the segments becomes inevitable. This reorganization requires local inelastic deformation which may occur by either dilatation or shear. An initial moderate inelastic dilatational deformation process may elongate the segments along the direction of principal tensile stress by the rupture of secondary bonds while maintaining the integrity of the network itself. This does not produce any void and the deformation mode may still change to shear. However, if the anelastic shear deformation is still inhibited, pre-craze surface flaws or internal voids are eventually formed. The pre-crazes or voids will grow and eventually lead to microscopic crazes. From the above model, the effect of several molecular parameters can be understood. A craze will nucleate under conditions where the molecular mobility is sufficiently low to inhibit local shear deformation processes up to a point where unstable reorientation of segments is required but is sufficiently high to promote the growth of the voids formed.

Argon and Hannoosh (1977) proposed that the formation of voids could occur at the end of shear patches formed by thermal activation. On the contrary, Kawagoe and Kitagawa (1981) proposed that their formation could occur by the mechanical interaction between shear bands at their intersection. From velocity measurements of surface acoustic waves and from crystallinity measurements by X-ray diffraction, it has been proposed that local and heterogeneous textures were developed in PMMA and PC by plastic deformation prior to craze initiation during tensile tests (Kawabe, Natsume, Higo and Nunomura, 1992). In all three cases, a precursor to the formation of voids would be heterogeneous plastic deformation.

The presence of a minimum particle size for craze nucleation at or near the particle/matrix interface in a rubber particle filled PS clearly suggests that the zone of stress concentration must have a critical size to induce heterogeneous craze nucleation. Independently of the diameter of the particles, the stress concentration factor at the rubber matrix interface is expected to be 2 (Kramer, 1983). However, craze nucleation does not occur in PS around rubber particles of diameter less than 1μm. Since theoretically the local stress concentration factor is expected to fall from 2 to 1.5 within one tenth of the particle diameter, Kramer (1983) estimated at 75 nm the critical size of a craze nucleus in PS.

b) Craze Growth

Craze tip advance, craze thickening and breakdown of the craze fibrils are precursors to the advance of a crack when cracking is assisted by crazing. As shown in Figure A.10, these three steps occur sequentially between the craze front and the crack front. The craze front and the crack front may or may not have the same velocity. Most of the following interpretation is based upon experimentation carried out employing thin films. Craze tip advance may occur by a meniscus instability mechanism or by a craze reinitiation mechanism. The meniscus instability mechanism shown in Figure A.11 has been observed by TEM in a variety of glassy amorphous polymers (Donald and Kramer, 1981). The craze reinitiation mechanism has been observed experimentally by Michler (1986) in samples which were microtomed into thin films. According to Kramer and Berger (1990), the apparent reinitiation process observed by Michler (1986) could be a reopening of voids and crazes formed during sample preparation.

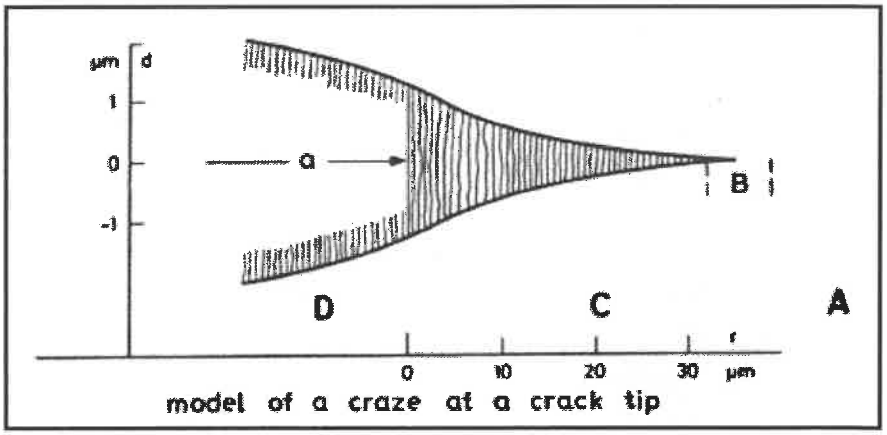

Figure A.10: Steps in the process of complete surface separation through crazing: elastic and/or anelastic deformation (zone A), craze tip advance (zone B), craze growth or thickening (zone C) and craze breakdown (zone D) (Kausch, 1987).

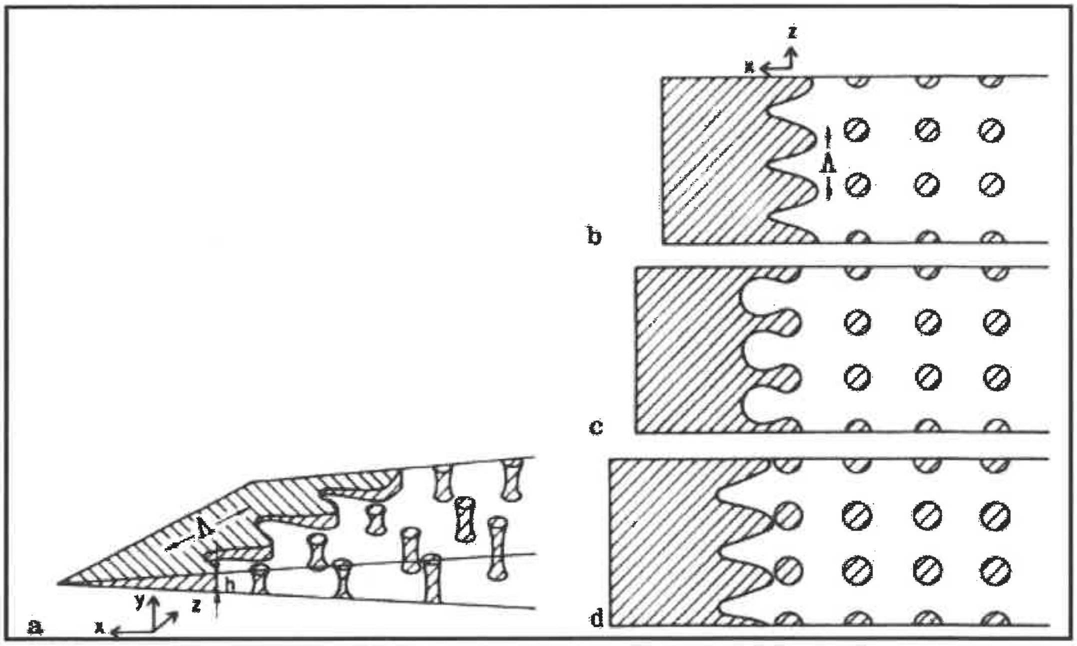

Figure A.11: Craze tip advance through a meniscus instability mechanism: The "y" direction represent the direction of principal maximum tensile stress (Kramer, 1983).

The increase in the thickness of a craze is mainly an effect of fibrillation of matrix material rather than an increase in the fibril extension (Kausch, 1987; Kramer and Berger, 1990). For instance, Lanterwasser and Kramer (1979) have shown that the volume fraction of polymer in the craze is approximately constant during thickening. As a result, the deformation occurs in active zones between the bulk non-deformed polymer and the extended fibrils (Figure A.12). The thickness of the active zone has been reported to increase from approximately 20 to 80 nm in the temperature range from 23 to 93°C (Kramer and Berger, 1990).

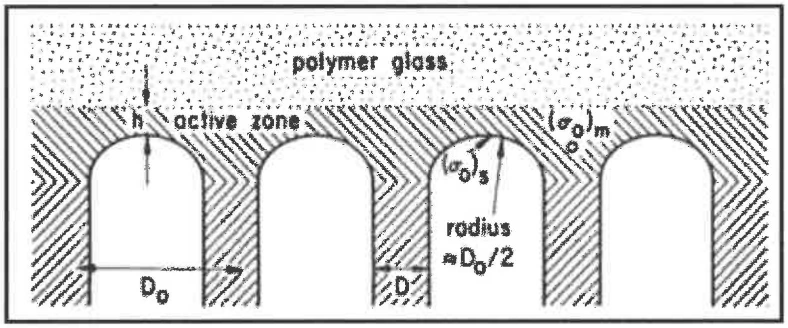

Figure A.12: Mechanism of craze thickening (Kramer and Berger, 1990).

For a variety of polymers, the maximum extension along the drawing direction of the entanglement network, λ_e from Equation A.24, as been reported to be almost equal to the extension ratio of craze fibrils for specimens tested under the same conditions (Kramer and Berger, 1990). However, in the range from approximately 10 to 30°C below T_g for PS, Berger and Kramer (1988) reported an increase of the extension ratio of craze fibrils with temperature, suggesting a partial disentanglement of the entangled chain segments oriented parallel to the tensile stress direction. By assuming that the extension ratio of craze fibrils is equal to λ_e, which is the case at lower temperature, the final thickness of a fibril, D, can be estimated from

Equation A.25: $$D = D_o \lambda_e^{-1/2} \quad ;$$

where D_o is the distance between the center of the fibrils (or the initial diameter of a fibril). From theoretical considerations, Kramer and Berger (1990) proposed that the equilibrium value of D_o is proportional to Γ, the surface tension of the void surface. The value of Γ depends on the mechanism by which free surfaces are created and by which entanglements in the transverse direction are lost. During fibrillation of PS at room temperature, conditions for which the fibril extension equals λ_e and the mechanism of lost of entanglement points is chain scission, a lost of entanglement density in the range of 25 to 50% has been measured (Henkee and Kramer, 1986). At least in this case, it can be assumed that the transformation of the matrix bulk material in craze fibrils retains the entanglement segments along the tensile direction while destroying a significant proportion of those initially oriented at significant angles relative to the tensile direction.

The free surfaces are created after separation of the polymer along planes of separation, such as that shown in Figure A.13a. Separation occurs by relative movement in opposite directions of macromolecular segments along the local direction normal to the separation plane (Figure A.13b). This relative movement requires disentanglement of the chains, which is time-dependent. If the time or stress required to induce disentanglement is too high, chain scission will occur. In an intermediate situation, both disentanglement and chain scission can be effective (Figure A.13c). In such a case, the mechanism of separation of a particular macromolecule may depends on its fractional length x, which is the ratio of its length located on one side of the separation plane to its total length. Disentanglement crazing is reported to become effective at a temperature of or lower than approximately T_g-100°C in thin films of different polymers having an entanglement density in the same range as PC (Plummer and Donald, 1989).

Chain scission or chain disentanglement along the plane of separation can be inhibited if the local resistance to these processes of lost of entanglements is higher than the average due to microstructural anisotropy (Figure A.14a). This inhibition results in the formation of cross-tie fibrils (Figure A.14b). When the distance between the cross-tie fibrils and the active zone increases, a relaxation in the cross-tie fibrils can promote a local reorientation of the principal fibrils (Figure A.14c).

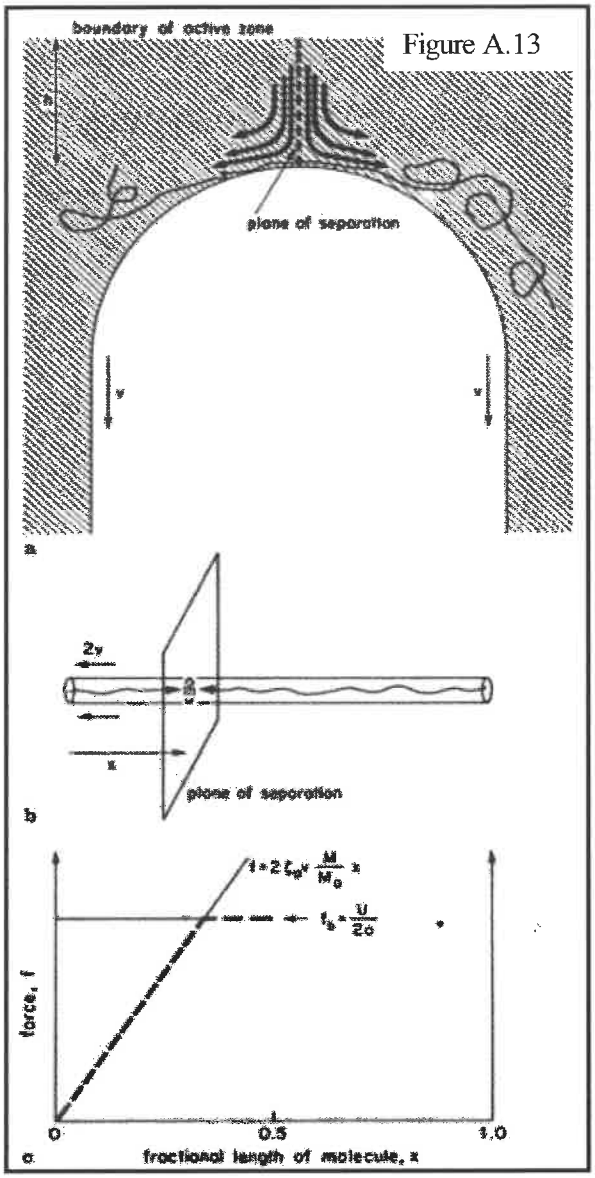

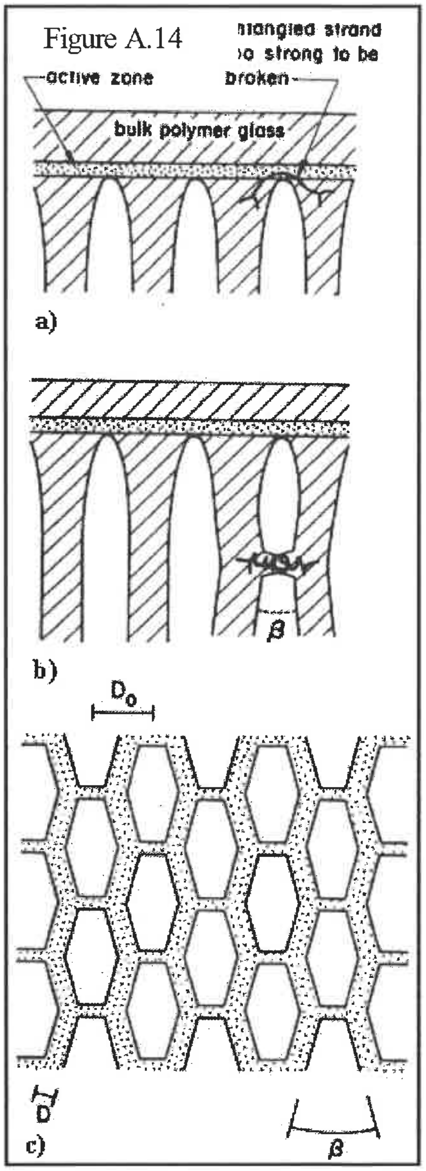

Figure A.13: Molecular separation in the active zone of the craze: a) overview indicating the crack separation plane and the velocity vector of fibril thickening (v); b) molecular motion perpendicularly to the separation plane; c) Force required for relative motion by chain disentanglement (f) or chain scission (f_b) as a function of the fractional length of molecules (x) (Kramer and Berger, 1990).

Figure A.14: Formation of a cross-tie fibril structure: a) Inhibition of the separation; b) Relaxation of the cross-tie fibril inducing local reorientations of principal fibrils; c) Resulting structure. (Kramer and Berger, 1990).

Lin and Yang (2001) employed observations by atomic force microscopy (AFM) and mechanical models to determine the local stresses and strains during crazing. Their results indicate that the local deformation rate attains a maximum value at the boundaries between the matrix and the craze fibrils and that most of the deformation is concentrated near these boundaries. They also showed that the craze fibril extension ratio varies with the entanglement density and is independent of the molecular weight. These results are consistent with a mechanism of craze thickening by complete extension of the segments of the entanglement network initially orientated along the tensile direction and by destruction of segments initially perpendicular to the tensile direction.

Kramer and Berger (1990) derived that the stress required for a craze to grow, S, can be expressed as

Equation A.26

$$S \propto \left[\frac{2(n+2)v}{\sqrt{3}\,\dot{\varepsilon}_f h}\right]^{\frac{1}{2n}} \sqrt{\frac{\sigma_{fc}\Gamma}{h}} \quad ;$$

where v is the velocity of displacement of the surface of the active zone of the craze, h is the thickness of that active zone and Γ is the surface tension of the void surface, and the parameters $\dot{\varepsilon}_f$, σ_{fc} and n are characteristics of the material in the active zone. The factor n in the exponent is usually much greater than 1 for glassy polymers and σ_{fc} may be considered as the flow stress of a non-Newtonian fluid at a strain rate of $\dot{\varepsilon}_f$. It is important to note that the term Γ includes the energy required for chain scission or chain disentanglement.

For shear yielding, the critical stress can be expressed as

Equation A.27

$$\sigma_y = \sigma_{yo}\left(\frac{\dot{\varepsilon}}{\dot{\varepsilon}_y}\right)^{1/n_y} \quad ;$$

where σ_{yo} is the yield stress at a strain rate of $\dot{\varepsilon}_y$, and n_y is a material parameter. Even if the properties of the material in the active zone (σ_{fc} and n) and in the bulk (σ_{yo} and n_y) are possibly different, they can be assumed identical for qualitative comparison.

As discussed in section A.2.3, shear deformation appears to maintain the entanglement network to a large extent. On the contrary, crazing requires relative motion between chain segments higher than that allowed by the entanglement network. Chain scission or chain disentanglement are thought to be the only mechanisms allowing this relative movement (Kausch, Plummer and Teze, 1994). As the entanglement density increases (M_e becomes smaller), this relative motion becomes increasingly difficult since the energy required for chain scission or chain disentanglement increases, which can explain why a transition from crazing to shear deformation is observed as the entanglement density increases (Kramer and Berger, 1990).

c) Craze Breakdown

A critical molecular weight M_c for the occurrence of physical entanglements appears to exist. The value of M_c can be determined from viscosity measurements. When the molecular weight is below M_c, fibrils will break before any significant thickening of the craze (Kramer and Berger, 1990). Accordingly, there is a minimum level of entanglement required for a craze to thicken and grow in a stable manner. Even well above M_c, a strong dependence of the molecular weight (M_w) on the craze fibril stability is observed (Kramer and Berger, 1990). This dependence is observed even when the dominant craze fibril formation mode is chain scission. Accordingly, chain disentanglement is expected to be an important mechanism associated with the breakdown process.

In cast thin films subjected to monotonic loading, cracks are found to initiate at the boundary between the active zone (c.f. Figure A.12) and the craze fibrils (Kramer and Berger, 1990). Kramer and Berger (1990) suggested to explain this preferential site for crack nucleation that the fibrils physically aged after there formation, thus reducing the mobility that is required for chain disentanglement. The craze stability is highly reduced by the presence of dust particles induced during casting and acting as stress concentrators (Kramer and Berger, 1990).

After its initiation in a bulk specimen during a fracture toughness test, a crack will generally grow through the center of the craze. Time under load or creep concepts were previously employed to discuss fibril breakdown (Kramer and Hart, 1984). However, these concepts are unable to explain the independence of the maximum craze width on the crack velocity (Brown, 1991). Brown (1991) proposed a model to explain the fracture toughness in which tie-molecules have an important effect in the crack advance mechanism. When a first fibril breaks near it interface with the active zone, the cross-tie fibrils can accelerate the breakdown process and relocate it to the craze midrib by transferring the load from the broken fibril that tends to recover to the adjacent fibrils. The resistance to crack propagation associated with crazing depends on several molecular and intermolecular parameters. At the macroscopic level, this resistance will be increased if several crazes are growing on parallel but different plans at the crack tip (Doyle, 1982). This effect on the resistance to crack propagation will be discussed in section 2.3.1.1. The influence of crystallinity on the process of crazing will be addressed in section 2.1.3.2.

A.2.4.2 Shear banding

Shear banding is an heterogeneous inelastic deformation which tends to become localized along the planes of principal maximum shear stresses on which it has initiated. This strain localization effect is generally observed at low temperatures and high strain rates. In these conditions, the local state of reduced coordination or of excess in free volume that is associated with an initial event of coherent plastic deformation cannot be diffusively dispersed before the onset of a subsequent event of coherent plastic deformation (Argon, 1980). For this reason, the subsequent event is likely to occur at the position of the initial event since the barrier energy for a coherent plastic deformation at that position is temporary reduced. Previously, strain softening was attributed to an adiabatic temperature rise at the shear band tip. However, Kramer (1975) showed that shear bands can propagate under isothermal conditions. Under these conditions, the growth of the shear band was found to be controlled by the local strain rate at the interface.

Brady and Yeh (1973) have shown that the morphology of shear bands is not a strong function of molecular weight. Within a shear band, Donald and Kramer (1982) showed that the polymer extension ratio is constant and approximately equal to 0.6 of λ^e (maximal extension ratio of the entanglement network, c.f. Equation A.23). Therefore, the loss of entanglements required for the formation of shear bands is lower than for crazing. Also, the growth of a shear band occurs by localized deformation at the interface between this band and the non-deformed matrix.

A.2.5 Summary

The solid structure of amorphous polymers of high molecular weight is likely to be characterized by the absence of regular organization at long as well as at short distance. In this structure, the macromolecules are folded and entangled with each other. It is generally considered that this structure contains a network, of macromolecule segments connected at entanglement points, offering the greatest resistance at high plastic strain. The average molecular weight of the macromolecule segments between the entanglement points (M_e) is generally employed to describe this network.

When this structure is strained in the viscoelastic regime, the model of Doi and Edwards (1986) postulates that molecular extension by migration of molecular kinks and reptation requiring the displacement of the entanglement points are the two types of molecular motion that can occur. Others processes are activated when the strain, strain rate and/or stress are increased. If the deformation remains homogeneous, the deformation process is generally called shear yielding. Shear yielding is thought to be a non-specific and non-localized event involving a series of torsion angle changes along the backbone of each molecule. The rigidity of the macromolecules, which can be estimated by their characteristic ratio C_∞, is an important factor determining the resistance to homogeneous shear yielding. If the deformation becomes heterogeneous, two distinct processes called shear banding and crazing are generally observed.

A shear band is formed when the activated configuration that allows the first shear yielding event is not dissipated before the second event, which favors strain localization. During the growth of a shear band, the deformation is concentrated at the interface with the bulk material. The extension ratio within the band was found constant but lower than in craze fibrils. In several polymers and conditions, the extension ratio of craze fibrils equals the maximum extension ratio of the macromolecule segments between the entanglement points that are oriented in the drawing direction. Such extension requires the lost of connections between the entanglement points in the transverse direction. This lost can occur by chain scission or chain disentanglement. Due to it nature, chain disentanglement is highly sensitive to molecular weight.

Intrinsic craze initiation results from an instability in the entanglement network at large homogeneous macroscopic strain. Even though extrinsic crazes are formed at lower macroscopic strain, they are also expected to be a consequence of this instability. The conditions for instability are not dependent on molecular weight. According to different models, heterogeneous or localization deformation would be a precursor to the formation of voids. It appears to have a critical size for a craze nucleus to grow. Craze thickening occurs by fibrillation of further material from the active zone. The stress required for a craze to growth increases with the energy consumed for the formation of the surfaces and with the velocity of displacement of the surface of the active zone but decreases with the thickness of the active zone. On it side, the stress required for shear yielding depends primarily on the strain rate. The energy consumed for the formation of surfaces increases as the entanglement density increases, which can explain the transition from crazing to shear yielding as M_e decreases. Even when the mechanism of lost of connections between the entanglement points in craze thickening is chain scission, chain disentanglement is expected to be an important mechanism associated with fibril breakdown. Fibril breakdown can initiate in the active zone at small heterogeneities. The cross-tie fibrils can accelerate the process and relocate it to the craze midrib by transferring the load from the broken fibrils that tends to recover to the adjacent non-broken fibrils.